University of Strathclyde

Department of Civil and Environmental Engineering

The role of accessory minerals in inhibiting bentonite erosion in the geological disposal of higher activity radioactive waste.

by

Christopher Peter Reid

A thesis presented in fulfilment of the requirements for the degree of Doctor of Philosophy

July 2016

Declaration of Originality

This thesis is the result of the author's original research. It has been composed by the author and has not been previously submitted for examination which has led to the award of a degree.

The copyright of this thesis belongs to the author under the terms of the United Kingdom Copyright Acts as qualified by University of Strathclyde regulation 3.50. Due acknowledgement must always be made of the use of any material contained in, or derived from, this thesis.

Signed:

Date:

Acknowledgements

Firstly, I'd like to thank my supervisor Rebecca Lunn for the multiple opportunities, support and counsel she's afforded me throughout the early stages of my career. For always being approachable and letting me know when I needed to 'stop flapping'.

I'd also like to thanks my supervisor Grainne El Mountassir for her support, time and advice over the last 6 years, from undergraduate through to postgraduate.

My final supervisor, Alessandro Tarantino, thanks for your help over the years. I particularly enjoyed our progress meetings at 9pm in the pub in the early days.

I'd like to thank Patrik Sellin and Kari Koskinen, for welcoming me into BELBaR group to participate in their workshops and meetings. Also, Tim Schatz from the BELBaR group, for the advice he's given me over the course of my PhD on this subject and samples of materials with which to work.

My peers, who commenced their PhDs at the same time as me, Ian Murray and Erica McLachlan; thanks for giving me your time to teach me how to use a particular piece of equipment or advice on something I wasn't familiar with. Particularly considering you had plenty of your own work to be getting on with at the time.

Thanks to the SAFE barriers research group and Simon Norris in particular for the interesting discussions and sharing of knowledge on the subject of radioactive waste disposal.

My mum, Rita, and brother, Paul. Thanks for understanding when I might not have been the most fun person to be around recently.

Lastly, I'd like to thank Sandra Currie for the patience she's shown me throughout the course of, and particularly towards the end of, my PhD. Her nature in sympathising with me when she was experiencing the same herself is something I'll always be grateful for.

Abstract

The chemical erosion of bentonite buffer material, during periods of glaciation, is a point of concern in the approval of safety cases for disposal of radioactive waste in crystalline rock. Currently, quantitative mass loss assessments are based on a 100% montmorillonite buffer and lead to unacceptable mass loss predictions. In practice however, the buffer will be comprised of ≈80% montmorillonite and ≈20% accessory minerals. A better understanding therefore of the role accessory minerals play in the erosion process is required to inform more realistic mass loss assessments. As indeed is the presence of fracture aperture variability on the extrusion / erosion process, as almost exclusively, research carried out to date has been in uniform aperture fracture flow cells.

Four month duration erosion experiments were undertaken, designed to mimic groundwater flow through, and buffer extrusion / erosion into, a fracture intersecting a deposition hole in the KBS-3V disposal concept upon contact with dilute water. Purified montmorillonite in a planar aperture fracture was examined, as was the reference bentonite buffer material for the KBS-3V concept, MX80 (with accessory minerals), in both planar and naturally variable aperture fractures.

In line with work by other researchers, the purified montmorillonite exhibited a steady mass loss throughout the experiment, with no mechanism in place to attenuate mass loss. Data correlated for the experiments with MX80 to reveal an erosion mechanism in which the accessory minerals serve to inhibit erosion when deposited at the extrusion / groundwater interface at a critical thickness. Irrespective of whether a variable or planar aperture fracture was used. Aperture variability plays a role in that, after deposition of the minerals at a critical thickness and subsequent decrease in mass loss from the system, force chain development in the accessory minerals against the variable aperture wall facilitated a rise in swelling pressure, resulting in breach of the accessory mineral barrier. An erosive period ensues, during which the breach is healed and the barrier regains its integrity.

Simplified assessments, scaling the experiments to a repository scenario by incorporating the mitigating effect of the presence of accessory minerals into current quantitative mass loss assessments, predict mass loss over the course of a repository assessment period to be within acceptable limits.

Contents

Chapter 1 Introduction.

The United Kingdom, in concert with 24 international counterparts, are currently pursuing a programme of deep geological disposal, married with secure interim storage, for its inventory of intermediate and high level radioactive waste and any such waste which may be generated in the future. Demonstrating the practicability and safety of geological disposal facilities has been the subject of worldwide research and development programmes for over three decades; pioneered by Finland, France, Switzerland and Sweden.

The Swedish geological disposal concept for a facility in crystalline rock is being used by the UK disposal Agency, Radioactive Waste Management Ltd (RWM), as one of three reference disposal concepts for the UK (the other two being in clay rock and in salt). In 2011, Sweden submitted a license application (including an accompanying environmental safety case) to construct a deep geological repository for high level waste in crystalline rock underlying Forsmark; the outcome of the license application is due in 2017. The Swedish safety case is based on their KBS-3V 'multi-barrier' concept, which relies upon a series of engineered and natural barriers to partition the waste from the biosphere, until such time as the natural radioactive decay process has reduced its activity to that of a natural ore. One constituent of this multi-barrier system is a highly compacted series of discs and rings of the clay bentonite, termed the 'bentonite buffer', which envelops the waste canisters within the 1.75m diameter, 9m deep vertical 'deposition holes'. It is the long-term performance of this bentonite buffer that is the subject of this Thesis.

A preliminary review of Sweden's safety case in 2012, while commending its competency in demonstrating the safety of the disposal concept, concluded that there were areas in which further clarification and confidence in the understanding of specific processes was required (NEA-RWMC 2012). One such area was the erosion of the bentonite buffer, which is foreseen as being a hazard in any crystalline rock concept for a deep geological repository during periods of glaciation, due to unfavourable chemical interactions between the buffer and potentially dilute groundwater. This erosion process may result in the safety functions of the buffer being impaired and may potentially facilitate the transport of radionuclides to the surface.

The aim and objectives of this PhD thesis relate to the erosion of bentonite buffer material, and were guided by the outcome of the Swedish preliminary license review and by previous research in the field of bentonite buffer erosion.

This research aims to develop a predictive understanding of the mechanisms that control the erosion of the bentonite buffer material. Specific objectives are to:

- Determine the effect of inherently present impurities or 'accessory minerals' within the bentonite on the erosion of buffer material within a fractured crystalline rock environment.
- Investigate the effect of fracture aperture variability on the erosion of buffer material within fractures intersecting a deposition hole.

These aims and objectives are addressed through a series of laboratory based experiments in flow-through cells, similar in design principle to those employed by Vilks and Miller (2010), Matsumoto and Fujita (2011) and Schatz et al (2013), to study the process of buffer erosion from horizontal rock fractures intersecting deposition holes. With the notable difference that, in this thesis, bespoke cells were constructed using a methodology developed in by the author that mimics flow through fractures with naturally varying apertures. In addition, whereas previous researchers investigated erosion of pure montmorillonite, the experiments described here use the Swedish and Finnish reference buffer bentonite, MX80, that contains a small percentage of natural accessory minerals.

Multiple orientations of natural rock fracture might be expected to intersect a deposition hole, ranging from horizontal to sub-horizontal and vertical, as is illustrated in Figure 3.22. The extrusion and erosion behaviour of buffer in fractures of various orientation might be expected to be different, as demonstrated by Schatz et al (2013). Horizontal rock fractures were chosen as the topic of interest in this thesis, due to the wealth of work undertaken previously by other researchers on horizontal fractures, against which this work could be compared and the fact that the current quantitative approach to quantifying buffer loss in SKB's 2012 safety case is based on a horizontal rock fracture.

Three long-term (3 – 4 months) flow through tests were undertaken in total. Two tests were undertaken with MX80, one in a variable aperture flow cell and one in a uniform aperture flow cell. A complimentary test was undertaken in a uniform aperture flow cell with montmorillonite procured from research consultants B+Tech in Finland. All tests were undertaken at an equal hydraulic aperture and constant flow rate with deionised water as a proxy for glacial melt water. Gravimetric analysis of the effluent was undertaken daily from each cell to determine mass loss rates, the swelling pressure of the bentonite specimens was monitored throughout and quantitative image analysis of the extrusion and erosion process was also undertaken.

A detailed description of the need for this research, the approach to meeting the aims and objectives and the thesis outcomes are delivered within the following structure:

Chapter 2, introduces deep geological disposal as the internationally recognised, best practice method of addressing the issue of long-lived, high level radioactive waste. It describes the international landscape, in terms of stages of implementation of national policy with regard to the disposal of high level radioactive waste and outlines the leading generic disposal concepts for a range of host geologies. Finally, the specific problem of bentonite buffer erosion is introduced, in the context of the KBS-3V disposal concept of high level radioactive waste disposal in crystalline rock.

Chapter 3, the literature review, firstly presents theory relevant to bentonite chemistry, mineralogy and colloid chemistry. All of which underpin the way in which bentonite interacts with changing geochemical environments and in turn, the bentonite erosion process. Subsequently, all past research relevant to the field of bentonite erosion is examined. Chapter 3 concludes with an examination of the quantitative treatment of buffer erosion in SKB's 2011 safety case.

Chapter 4 outlines the prescriptive process which was followed in order to achieve each of the aims and objectives. This includes the construction of the experimental apparatus, preparation of bentonite samples and the experimental protocol which was carried out prior to, during and upon completion of each experiment. Additionally, other details relevant to the understanding of the data analysis, including X-Ray Diffraction (XRD) and Image analysis are also described.

Chapters 5, 6, 7 and 8 describe the results of the suite of bentonite erosion experiments which were undertaken. Specifically these were: erosion of MX80 bentonite in both variable aperture and planar aperture fracture flow cells and the erosion of purified montmorillonite in a planar aperture fracture flow cell. Two further experiments: a static extrusion test with purified montmorillonite and an experiment with MX80 in which initial saturation was conducted with a saline solution are also discussed.

Chapter 9 presents a new mechanism for MX80 bentonite erosion from a fracture intersecting a deposition hole. The wider implications of the results i.e. scaling to a full scale repository scenario, under the geological time scale throughout which the repository will operate, and the way in which the mechanism may be engineered are also addressed in chapter 9.

Finally, chapter 10 contains the research conclusions and chapter 11 the recommendations for future research.

Chapter 2 Geological disposal of radioactive waste

The United Kingdom is pursuing a programme of deep geological disposal married with secure interim storage for high and intermediate level radioactive waste. Internationally, significant volumes of research have been conducted, over a period of nearly 30 years, to develop locally appropriate designs for geological disposal facilities and to demonstrate their long-term safety. International research has ranged from relatively short-duration bench scale experiments up to full scale experiments in Underground Rock Laboratories (URLs) lasting decades. These experimental programmes have been designed to simulate the interactions between repository design elements, their surrounding geosphere and the changing environmental scenarios that will take place during a typical repository lifecycle.

The environmental safety case for a geological disposal facility must demonstrate satisfactory performance over hundreds-of-thousands to millions of years. Consequently, the extent to which experimental work can be relied upon to verify a safety case is limited. Such experimental work however, when coupled with a proven theoretical understanding, can provide robust predictions of repository performance over long timescales by the use of constitutive and numerical modelling. Further to this, the study of natural analogues of geological processes, lend confidence to these predictions of long-term safety.

Research to-date has led to generic disposal concepts for three main types of host geology: crystalline, clay and salt rock. The first two of these are perhaps most significant when considered in the context of the United Kingdom. Sweden and Finland have jointly developed the KBS-3 disposal concept for crystalline environments. France and Belgium on the other hand have geared their research programmes towards refining disposal concepts in clay host geologies. Each concept is unique and tailored to site specific requirements however; the employment of the swelling clay bentonite in some capacity is a factor which is consistent throughout.

Bentonite, like all other design elements of a repository, will be subject to temporal changes in chemical and physical environment and these changes will affect the extent to which the clay is able to perform its required functions. The erosion of bentonite from the repository is

one potential consequence of being subjected to environmental changes and is specific to crystalline disposal concepts. Its occurrence, even to a relatively small extent, could undermine repository safety.

2.1 Policy and progress

2.1.1 UK high level radioactive waste policy 2008-2013

Radioactive waste is generally graded on specified levels of radioactivity and the waste's ability to generate heat. The current UK radioactive waste inventory comprises of low level, intermediate level and high level waste.

Low level waste typically comprises of redundant infrastructure from nuclear power plant decommissioning and wastes from medical and research applications. Intermediate level waste typically has radioactivity which exceeds the specified levels for low level waste but doesn't generate heat. This waste typically comprises of reactor components etc. High level waste generates significant heat because of its radioactivity and in the U.K. it is predominantly comprised of a vitrified nitric acid solution containing fission products, a by-product from spent fuel reprocessing. High level waste disposal is the focus of this thesis.

High level waste currently accounts for less than 0.1% by volume of the UK's radioactive waste inventory however it accounts for 95% of the radioactivity of the nation's legacy waste (DEFRA & NDA 2010). High level waste is currently in interim storage at 36 sites around the UK, the majority of which is at Sellafield in Cumbria.

The UK's[1] modern policy on dealing with higher activity legacy waste was originally set forth in the 2008 white paper: Managing radioactive waste safely (MRWS) – A framework for implementing geological waste disposal (DEFRA et al 2008). The stepwise MRWS process of community volunteerism, consultation, desk and field based studies and construction set forth in the white paper is detailed in Figure 2.1.

---

[1] The Scottish government has an independent stance and policy on higher activity radioactive waste arising in Scotland. Upon reflection on CORWM's 2006 report and a round of public consultation, the Scottish Government adopted the stance that deep geological disposal was not, at the time of consideration, deemed to be a "reasonable alternative" to interim storage. Such waste is stored in surface facilities at the point of source in Scotland (Scottish Government 2011).
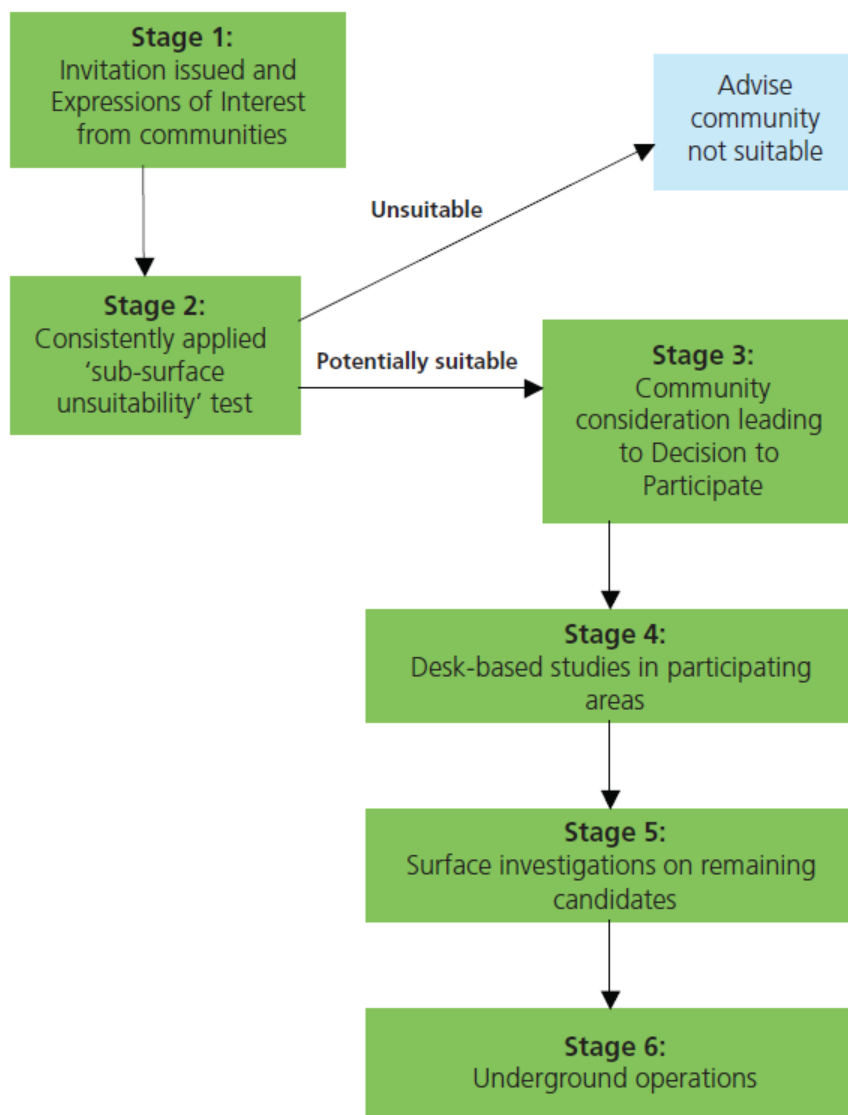
Figure 2.1: Stages in the MRWS site selection process (DEFRA 2008)

The responsibility for execution of the above policy lay with Radioactive Waste Management Directorate, a branch of the Nuclear Decommissioning Authority (NDA).

Prior to publication of the 2008 MRWS White Paper, the independent advisory body, Committee on Radioactive Waste Management (CoRWM), was set up by the government to consider potential management options and provide recommendations on the best course of action for dealing with radioactive waste. CoRWM published their findings in 2006 and the 2008 MRWS White Paper was a result of government's reflection on CORWM's recommendations.

The projected date for a geological disposal facility (GDF) to be ready to receive waste is stipulated in the MRWS White Paper as 2040 (NDA 2008) and cost estimates vary between 12 and 20 billion pounds sterling, depending on such factors as the nuclear inventory, the host-rock type and the depth of construction (West Cumbria: MRWS 2012). The cost of nuclear decommissioning, including the construction of a GDF will be met by a combination of the nuclear energy producers and the U.K. taxpayer. To date, 8.96 billion pounds sterling has been deposited in the nuclear liabilities fund in order to deal with legacy waste and future nuclear operators also have to make provision for any such waste requiring disposal from new nuclear power plants (DECC 2011). The responsibility for management of nuclear decommissioning and delivery of a GDF ultimately lies with the NDA. Naturally, the commissioning of any such facility would also have to be sanctioned by the appropriate legislative regulators in the Environment Agency and the Office for Nuclear Regulation, a division of the Health and Safety Executive.

Following publication of the 2008 White Paper, a siting process for a Geological Disposal facility was initiated. Between 2008 and 2013, as part of the MRWS process, three communities expressed an interest in hosting a GDF[2]; the boroughs of Allerdale and Copeland, in which Sellafield is situated, and Cumbria County Council. As part of this consultation process, the West Cumbria MRWS Partnership was set up as an advisory body to facilitate a framework for discussion and fact-finding between the residents and learned experts in fields relevant to deep geological disposal. The West Cumbria MRWS Partnership also commissioned research and invited opinions from independent experts.

Between March and May 2012, a survey was commissioned by the West Cumbria MRWS Partnership to gauge public opinion and assess public awareness. Over 1000 residents were approached in each area and, of the respondents, approximately 80% were aware of the regions involvement in the MRWS process and 53% thought the councils should participate in the search for a suitable site (Welch and Neville 2012).

In September 2012, despite a majority of public support, whilst Copeland and Allerdale borough councils both voted to continue to the next stage of the MRWS process, Cumbria

---

[2] Supplementary to the ~6km^2 underground footprint a GDF may occupy, associated surface facilities such as a waste encapsulation plant, construction support and repository operational infrastructure would also be situated in any host district. (DEFRA 2008).

county council, whose jurisdiction encompasses both Copeland and Allerdale borough councils ultimately decided to withdraw. This effectively resulted in an end to the 2008 siting process.

2.1.2 UK high level radioactive waste policy 2013-2016.

In July 2014, the UK Government issued a revised White Paper, Implementing Geological Disposal – A framework for the long-term management of higher activity radioactive wastes (DECC 2014). The essence of the original 2008 White Paper is consistent with the revised White Paper in that the government continues to be committed to a volunteerism approach and expects to commence formal dialogue with potential new host communities in 2016.

The revised paper lays out a number of initial actions to be implemented, resulting from the consultation process: the establishment of the policy framework for planning decisions in England[3], developing a new process for working with communities and conducting a national geological screening exercise. These actions are to be led by both the UK government and Radioactive Waste Management Ltd, a new subsidiary of the NDA, which has been formed from the Radioactive Waste Management Directorate and is now responsible for delivering a GDF in the UK and will be the site licence holder.

2.1.3 International Progress in Geological Disposal

The international experience garnered from both successes and failures in the repository siting process has demonstrated that stakeholder engagement is key in realising a successful programme and, although the UK has adopted and is currently implementing this strategy, it is somewhat lagging behind the Nordic forerunners of Finland and Sweden and indeed France. Finland and Sweden are proposing to construct geological disposal facilities in granitic rock. Posiva is the organisation responsible for the implementation of a GDF in Finland. Posiva were granted a licence to construct their final disposal facility in November 2015 and are currently expanding their rock characterisation facility (RCF) at Onkalo into a GDF.

Sweden plan to commence the decade-long construction process of a GDF in the granitic rock of Söderviken in Forsmark in 2020. Their radioactive waste disposal organisation, SKB, submitted a safety case in 2011, which is currently under review by The Swedish Radiation

---

[3] As the siting of a GDF is a devolved issue, any potential GDF to be sited out with England i.e. in Wales or Northern Ireland would be subject to their respective national planning laws.

Safety Authority (SSM). SSM have produced an initial review into the safety case and an overall assessment regarding SKB's licence application. The latter of which was published in June 2016 and endorsed SKB's licence application with the proviso that further work will be undertaken around a number of technical issues relating to long term safety. Which SSM will ultimately have to pass judgement on at a later stage in the process.

SSM expect to submit its recommendations to government in 2017. After which, the government will consult with the localities in which the facilities (both the GDF and waste encapsulation plant) are to be built, who interestingly still possess the right to reject the facilities, before arriving at a final decision (SKB 2015).

France also expects to be emplacing waste in the clay-rock of the Meuse/Haute-Marne region (ANDRA 2012) in 2025.

2.2 Geological disposal concepts

As mentioned previously, research has been undertaken at laboratory bench scale up to full scale in underground facilities in order to replicate the processes and conditions which may be expected in a deep geological repository. Research in both crystalline and clay rock geologies has given birth to two of the generic disposal concepts which the UK could decide to adopt, and tailor to site specific requirements.

2.2.1 KBS-3V disposal concept for crystalline rock.

The Finnish and Swedish radioactive waste management organisations of Posiva and SKB have jointly developed the KBS-3V disposal concept for high level waste as illustrated in Figure 2.2. This concept has undergone testing and refinement in the Onkalo underground rock characterisation facility in Finland and the Äspö hard rock laboratory in Sweden.
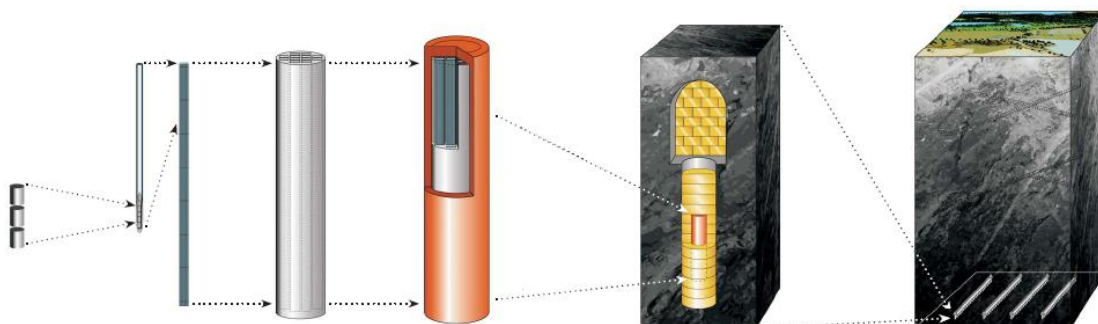

Figure 2.2: KBS-3V engineered barrier system (Posiva 2011).

Current design standards for a typical deep geological disposal facility in crystalline rock comprise emplacing the waste at a depth of between 200m and 1000m depending on the

suitability of the host rock. Suitability is determined based on factors such as the presence of structural discontinuities in the rock and the hydrogeology of the area. The proposed repositories are constructed by excavating a helical access tunnel and ventilation shafts to the required depth. A further network of deposition tunnels are then branched off horizontally into the host rock from which vertical deposition holes will be drilled. These vertical deposition holes, 1.75m in diameter and 9m deep, are drilled at approximately 6m intervals for emplacement of the waste which will be contained within 1.05m diameter, 50mm thick, copper canisters.

Depending on radioactive waste inventory, and the ability to locate a suitably large rock volume, the Swedish repository may have the capacity for 6000 canisters (SKB 2012). The KBS-3V disposal concept depicted in Figure 2.2 revolves around an engineered barrier system (EBS) whereby the waste is isolated from the biosphere until such time when the decay process has returned its radioactivity to that of its natural ore. Isolation is achieved through a series of engineered barriers acting in unison though designed to function independently should one or more fail:

- The first barrier is created by vitrifying the high level waste by conversion from a liquid into ceramic form with a high resistance to dissolution. The glassified waste pellets are arranged in vacuum sealed, highly corrosion resistant zirconium alloy assemblies which are supported by a cast iron lattice tube.

- The assemblies are then sealed in a 50 mm thick copper canister, highly corrosion resistant in the oxygen free conditions expected in the repository environment.

- This canister is then emplaced into one of the deposition holes where it is isolated from the host-rock by 350mm of pre-compacted bentonite clay discs and rings. This portion of the engineered barrier system is referred to as the 'buffer'. Transport processes through the clay buffer are designed to be diffusive, resulting in canister protection and radionuclide migration retardation.

- Deposition tunnels are then filled with highly compacted clay blocks and the interface between clay blocks and the tunnel wall filled by centrifugally emplaced clay pellets. This portion of the engineered barrier system is termed the 'backfill'. The end of the tunnel is sealed with the in-situ casting of a concrete plug.

- The crystalline host-rock is ultimately the last line of defence in preventing radionuclide transport back to the biosphere by providing a stable hydrogeochemical environment for the bentonite and potentially possessing the capacity for free radionuclide sorption (Garcia-Garcia 2010).

2.2.2 Disposal concepts in argillaceous rock.

Argillaceous bodies of rock are also under examination at the Mont Terri rock laboratory in the Opallinus clay of Switzerland and the Bure underground research laboratory in the Callovo-Oxfordian clay formations of the Meuse/ Haute-Marne district of France. Indeed, at Cigar Lake in Canada, there exists a Uranium ore deposit at 430m depth, overlain by a clay layer, yet no sign of this is evident at the surface (NAWG 2012). Thus demonstrating the suitability of clay as a buffer, and host rock, in waste isolation.

ANDRA, the French waste management organisation (WMO), have developed a concept for disposal of high level waste within argillaceous rock, which involves emplacing the waste at a depth comparable to that in the KBS-3V concept. In the French concept however, the waste is isolated from the host geology by stainless steel waste canisters whose purpose is to delay release of radionuclides to the host rock for several centuries. The host-rock is foreseen to be the main barrier in this concept (Pusch 2008) because of its low hydraulic conductivity, homogeneous pore size and ability to self-seal (Wilson et al 2011).

ANDRA's concept, as illustrated in Figure 2.3, is distinct in that waste canisters are deposited in horizontal boreholes, up to 40m in length. Each borehole has capacity for 6 to 20 canisters, depending on heat output. Boreholes are lined with a stainless steel sleeve to aid canister insertion and possible retrieval. Canisters are inserted into the holes aided by ceramic skids and each borehole is then sealed with swelling bentonite and concrete plugs (ANDRA 2005). Disposal shafts may then be sealed with the excavated argillaceous material.
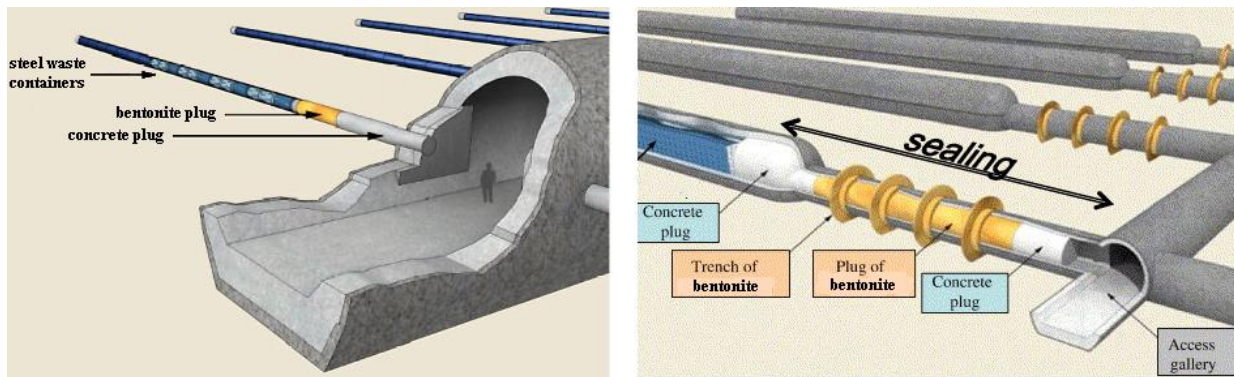
Figure 2.3 Andra disposal concepts in Argillaceous rock for spent fuel (LHS) and intermediate level waste (RHS) Andra (2005).

In ANDRA's clay concept, the main factor inhibiting water circulation around the waste is the geological formation. Because of the low hydraulic conductivity of these specific clay rock bodies and diffusive transport conditions of 2-3 cm per 100,000 years in the case of the French host rock, Callovo-Oxfordian clay (ANDRA 2005), radionuclide migration in the host rock is extremely slow. Indeed, upon excavation of the Mont Terri rock laboratory in the Opallinus clay of Switzerland, neither dripping water nor any moist spots were observed on any of the tunnel walls, even in areas with a high number of rock discontinuities (Nagra 2012).

2.2.3 The role of bentonite in geological disposal concepts.

Bentonite clay barriers play an integral role in partitioning radionuclides from the biosphere until the radiation from the waste has decayed to harmless levels. This decay process occurs over geological timeframes, within which the bentonite will be subject to temporal changes in the chemical and physical environment in the repository. Clays currently under consideration for buffer material in the Nordic KBS-3V concepts are IBECO-RWC, a high grade calcium bentonite from the island of Milos in Greece and the current reference material MX-80, a natural sodium bentonite from Wyoming, USA.

Current materials proposed for tunnel backfill blocks vary somewhat between current SKB reference material IBECO-RWC-BF (a lower grade Ca-bentonite), and POSIVA's reference material Friedland ton, a German mixed-layer clay. There also remains the potential for mixes in various proportions, of those mentioned and any crushed excavated material; reducing the need to dispose of tonnes of excavated rock.

Bentonite in the KBS-3V disposal concept

In the KBS-3V concept, both the buffer and backfill combined are required to inhibit the release of radionuclides into the host rock for approximately 10,000 years (Juvankoski & Marcos 2010). The backfill is designed to restrict the advective movement of groundwater and maintain the buffer in the deposition hole by providing 0.2 MPa swelling pressure when saturated (Keto et al 2009). The buffer, in contrast, is required to perform a number of functions. Bentonite buffer discs and rings are compacted at 100 MPa compaction pressure to an initial dry density of approximately 1700 kg/m^{-3} (SKB 2012) and are required to:

- Restrict transport processes to and from the canister to being diffusive only. Bentonite compacted to this degree exhibits a hydraulic conductivity in the region of 10^{-14} m/s, preventing corrosive chemicals such as sulphides reaching the canister. This also retards the release of any radionuclides in the opposite direction, as a result of to the sorptive properties of the bentonite.
- Provide a plastic environment for the canister to buffer against any tectonic activity.
- Generate a swelling pressure of between 2 and 10 MPa in order to suppress sulphate reducing microbial activity. These bacteria may be indigenous to the bentonite or indeed harboured in groundwater. A swelling pressure <2 MPa and use of an energy source such as H_2 from decaying waste (Juvankoski & Marcos 2010) may allow such bacteria to flourish, resulting in bio-mobilisation of radionuclides and bio-corrosion of the copper canister.

Structural and cation exchange properties of montmorillonite (the chief constituent mineral of bentonite which gives it its unique properties) enable the above functions to be fulfilled. After initial emplacement of the buffer discs and rings; a nominal gap, whose inclusion aids the emplacement of the discs and rings, will remain. There are a number of possible options for filling this interface between the buffer rings and the host-rock. Current reference designs for both SKB and POSIVA involve filling the 50mm gap between the host rock and buffer with bentonite pellets emplaced with the aid of gravity. Other, less likely designs involve leaving a gap of approximately 30mm and allowing water to ingress gradually filling the gap/ saturating the buffer simultaneously or placing the copper canister surrounded by bentonite rings in a perforated 'super-canister' and immersing this in a bentonite mud in the

deposition hole, aiding the hydration process of the pre-compacted rings. Achieving the detailed target swelling pressures relies on saturation of the backfill and buffer from the ingress of groundwater from the host rock to a target saturated density of ~2000 kg.m^{-3} (Apted et al 2010).

Early in a repository evolution, a temperature gradient will exist across the buffer, with an initial canister temperature of up to 100°C; a temperature gradient of 0.34^{o}C/cm radially can be expected to have developed across the buffer after approximately 2 years (Pusch 2008).

Bentonite in Argillaceous concepts.

Fewer requirements are placed on bentonite in argillaceous disposal concepts than in those with crystalline host rocks. NAGRA, the organisation responsible for implementing Swiss radioactive waste disposal policy, have defined the following functions which it requires of the bentonite buffer in an argillaceous GDF concept (Wilson et al 2011):

- Confine any released radionuclides due to the associated long re-saturation time and self-sealing capacity owing to the plasticity of the clay.
- Attenuate any radionuclide release due to sorption and diffusion dominated transport process in the clay.

Within NAGRA's disposal concept, in a similar capacity to the French disposal concept, waste canisters are deposited into horizontal drifts. The canisters are positioned at the centre of the drifts by their emplacement on pedestals made from compacted bentonite blocks. The annular gap between the canister and the host rock is then filled with a granular bentonite as illustrated in Figure 2.4.
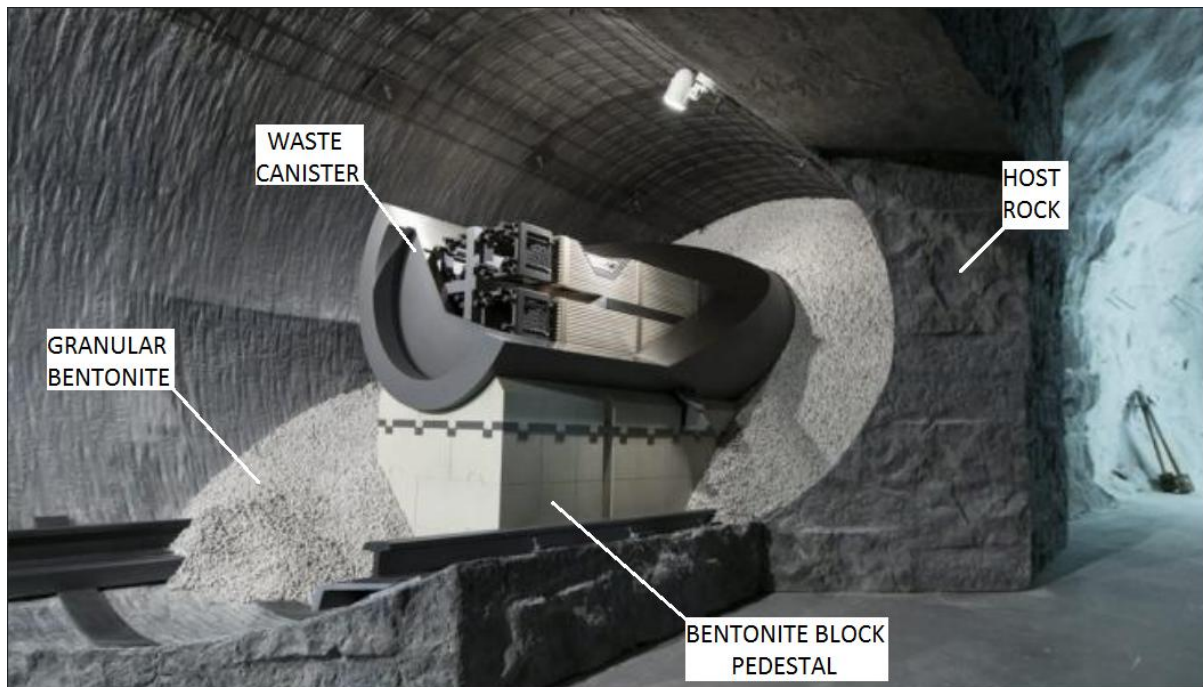
Figure 2.4: Swiss high level waste disposal concept (Nagra 2011)

ANDRA adopt a similar stance to NAGRA, relying more heavily on the host rock (Wilson et al 2011).

In argillaceous disposal concepts, during the operational phase, excavation and ventilation will de-saturate the host rock in contact with air several centimetres into the rock face. Upon repository closure, the rock will re-saturate towards the repository by diffusion, including saturation of the bentonite. In the French argillaceous concept, full re-saturation is expected to take in the order of 100,000 to 200,000 years (ANDRA 2005), this is in stark contrast to crystalline concepts, where buffer saturation is expected to take in the order of decades to a couple of hundred years (Pusch 2008). Indeed, in argillaceous concepts, should the water content of the compacted bentonite be above that of the clay host rock, water migration from the bentonite to the host rock may initially be anticipated in order to attain hydraulic equilibrium.

Bentonite in other disposal concepts.

Bentonite barriers are also proposed in ANDRA's disposal concept for intermediate level waste (ILW). In this case, bentonite is proposed for use as a 2m deep cut off-wall, designed to mitigate water circulation in the engineered damage zone (EDZ) surrounding tunnels and

shafts. The EDZ is the zone of damage that forms at the periphery of excavated tunnels, vaults and boreholes created through the use of invasive excavation techniques such as tunnel boring and drilling. During EDZ formation, existing discontinuities may be extended and/or new ones created due to the redistribution of stresses in the host rock as detailed in Figure 2.5. To inhibit groundwater flow along the EDZ (parallel to the tunnel) and to mitigate against any further damage, cut-off walls are proposed to be cut perpendicular to the tunnel face using a purpose built saw and filled with compacted bentonite, as also shown in Figure 2.5.
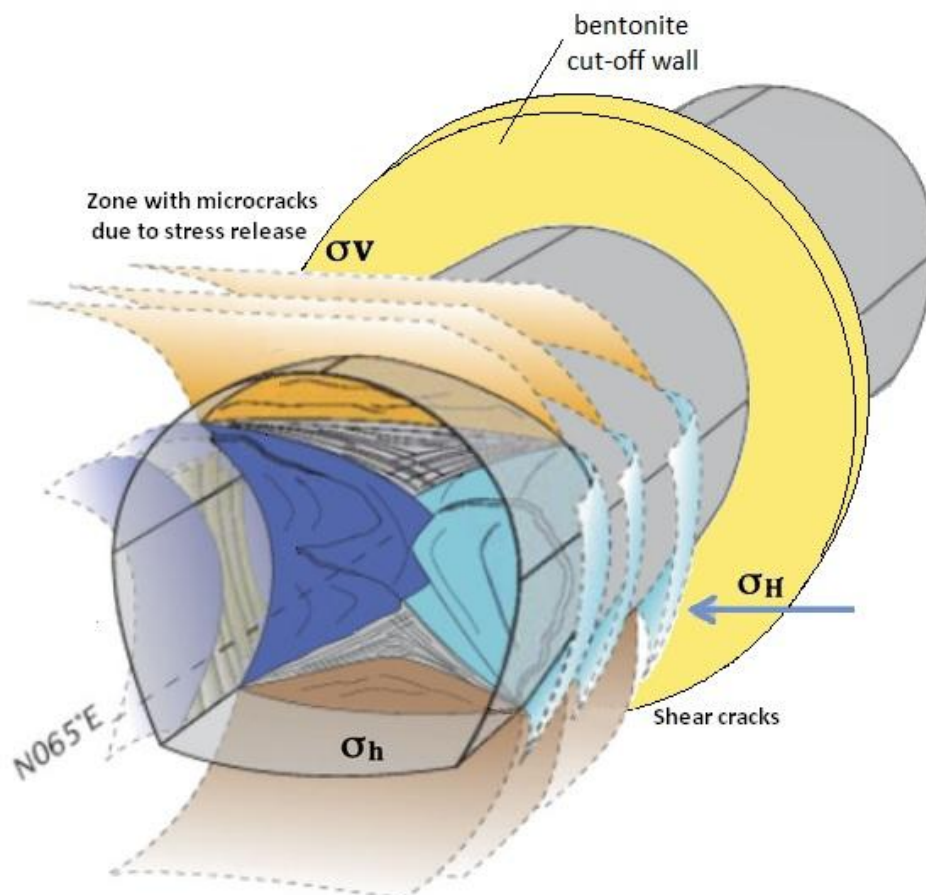
Figure 2.5: Depiction of EDZ and bentonite cut-off wall. Adapted from Zaoui, A. & Sekkal, W. (2014)

As outlined above, the host rock is foreseen to be the main barrier in the clay concepts and less onerous requirements are placed on bentonite in these concepts. Bentonite erosion is not foreseen to be a problem in the clay concepts due to the lack of transmissive water features and diffusion dominated hydrogeological flow regimes. In the crystalline concepts however, bentonite buffer material is likely to erode during glacial melting, when low salinity groundwater may be circulating at depth. Hence, for these concepts, there is a need

to show that bentonite erosion rates are sufficiently low as to not compromise repository safety.

A summary of the uses of bentonite in the various international disposal concepts is given in Table 2.1.

Nation	*Organisation*	*Geology*	*Reference bentonites*	*Purpose*
Sweden	SKB	Crystalline	MX-80, IBECO-RWC-BF	MX-80 - compacted buffer rings and blocks/ pellets for interface between blocks/rings and host rock. IBECO-RWC-BF - tunnel backfill blocks.
Finland	Posiva	Crystalline	MX-80, Friedland ton	MX-80 - compacted buffer rings and blocks/ pellets for interface between blocks/rings and host rock. Friedland ton for tunnel backfill blocks.
France	Andra	Clay	MX-80	Sealing plugs at the end of horizontal HLW/ILW drifts. Cut-off walls at the end of ILW drifts.
Switzerland	Nagra	Clay	MX-80, IBECO-RWC	IBECO-RWC - compacted support pedestals for waste canisters. MX-80 – pellet filling remainder of horizontal drift

Table 2.1 **Summary table of bentonite roles in various disposal concepts**

2.3 The problem of bentonite erosion.

Maintenance of bentonite buffer and backfill performance characteristics is inextricably linked to the preservation of bentonite in the repository. While loss of some bentonite mass over the course of many millennia is inevitable, a better understanding of the coupled processes bentonite may be subjected to over a typical repository evolution will be crucial in the mitigation of bentonite erosion. The erosion of bentonite from a repository has two main implications for the safety case. Firstly, most, if not all, of the functions which the buffer is required to perform are directly or indirectly linked to achieving its target homogenized and saturated bulk density of approximately 2000 kg/m^{-3}. Any loss of bentonite mass would result in a drop in density and negate the capacity of the barrier to perform these functions.

Secondly, the erosion of even a small mass may not be permissible when considering the scenario in which a waste canister is compromised and radionuclides are adsorbed into the interlayer space of clay platelets within the bentonite buffer. In this scenario, there persists the potential for radionuclides to migrate, by diffusion, across the main body of the buffer in the deposition hole and any buffer potentially extruded into any fractures intersecting the deposition hole. From the canister to the buffer/groundwater interface. Here, erosion of the bentonite harbouring the radionuclides into the groundwater filled fractures that intersect the deposition holes may facilitate the transport of radionuclides back to the biosphere as illustrated in Figure 2.6.
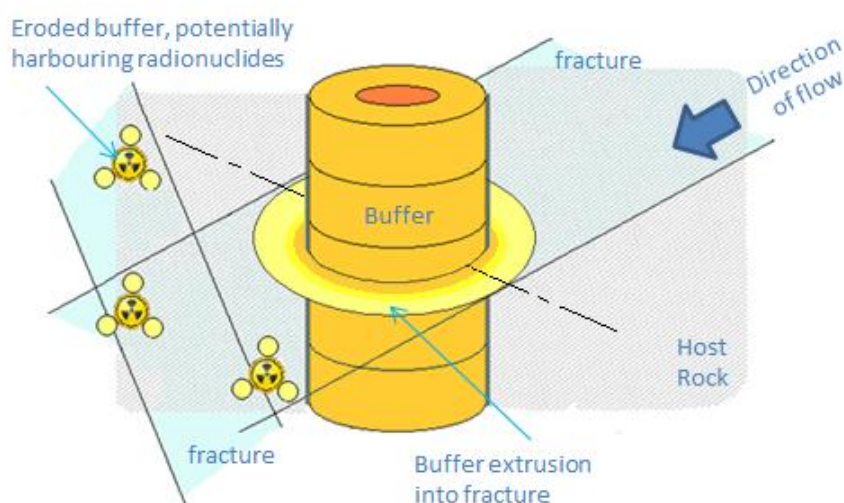
Figure 2.6: Transmissive fracture intersecting deposition hole and radionuclide transport.

'Erosion of bentonite' is a somewhat ambiguous phrase in that bentonite comprises a range of minerals in various proportions. The most abundant of these minerals, which is responsible for making bentonite suitable as a buffer material, is the clay mineral montmorillonite, which typically constitutes 80% of the buffer by weight. All constituents of bentonite are 'erodible' depending on the hydrogeochemical conditions, however, it is the erosion of the montmorillonite constituent that occurs most readily and is a critical factor in the development of long-term safety cases for geological disposal.

Chapter 3 Literature

In order to fully appreciate the coupled chemical and physical process affecting bentonite buffer erosion, it is important to consider the microstructure and chemistry of bentonite, in particular its primary constituent, montmorillonite. The commercially available bentonite MX80, from Wyoming in the USA, shall be the main focus of this study. It is comprised of approximately 80% of the clay mineral montmorillonite and 20% detrital material. Relevant research in the field of buffer erosion to date has also been examined in order to identify the areas in which further research is required.

3.1 Clay Mineralogy, Chemistry and Structure.

3.1.1 Tetrahedral and octahedral structural units

For continuity, henceforth a '*sheet*' will refer to the tetrahedral and octahedral structural units which form a montmorillonite '*layer*'. Each '*stack*' of montmorillonite layers shall be referred to as such and the term '*aggregate*' shall be used to describe a cluster of montmorillonite stacks.

One of the rudimentary structural units of the ideal clay mineral is the silica tetrahedral sheet, constructed from SiO_4^{4-} tetrahedra consisting of oxygen (O^{2-}) anions occupying each vertex and the central cavity being occupied by the silicon (Si^{4+}) cation. These tetrahedra are connected to form a hexagonal network by the sharing of three of the four oxygens present and having apical oxygen tips all pointing in the same direction as illustrated in Figure 3.1.
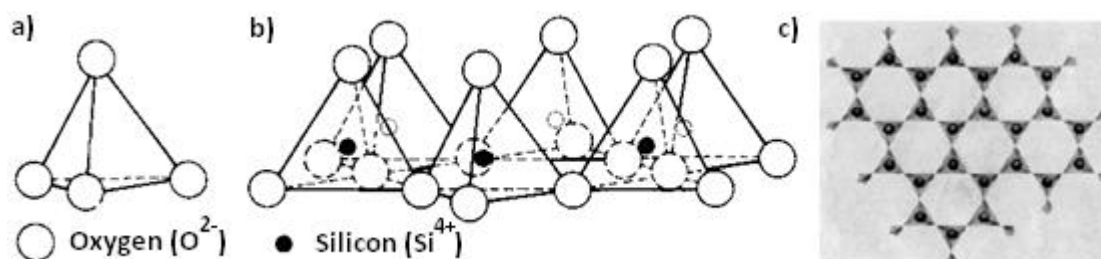

Figure 3.1: Tetrahedral arrangement and hexagonal network in plan view. Adapted from Mitchell & Soga (2005) and Holmboe (2010).

This tetrahedral sheet is complimented by an octahedral sheet which consists of two planes of hydroxyl (OH$^-$) ions within which lie a plane of either aluminium (Al^{3+}) or magnesium (Mg^{2+}) ions in an ideal clay mineral, named the gibbsite and brucite octahedral sheets respectively. The octahedral sheet may accommodate three cations depending on their charge and in the case of the brucite sheet; all three of these positions are normally filled due to the magnesium having a charge of 2+. The brucite sheet is therefore termed trioctahedral. In the gibbsite sheet however, aluminium having a charge of 3+ normally results in only two of the three possible cation sites being filled and the gibbsite sheet is therefore termed dioctahedral. The gibbsite sheet is depicted in Figure 3.2.
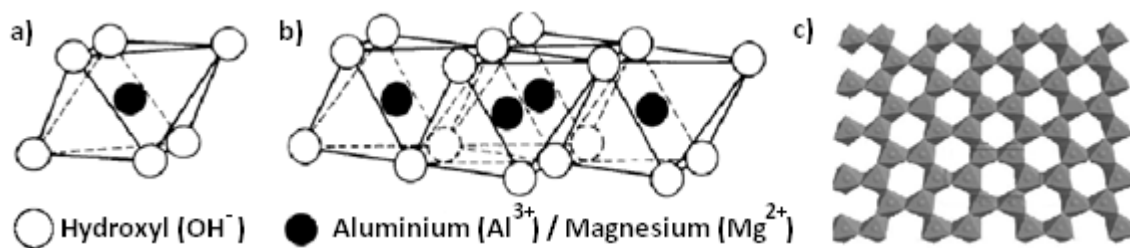

Figure 3.2: Octahedral arrangement and network in plan view. Adapted from Mitchell & Soga (2005) and Holmboe (2011)

A tetrahedral and an octahedral sheet may combine to form a 1:1 clay mineral which consist of successive layers of one sheet joined to the other, such as in the minerals kaolinite (gibbsite octahedral sheet) or serpentine (brucite octahedral sheet). They may also combine to form a 2:1 clay mineral with the layers consisting of an octahedral sheet being sandwiched by two tetrahedral sheets such as in the minerals smectite and illite. Indeed, many clays are comprised of both 2:1 and 1:1 minerals mixed.

3.1.2 Bonding in clay minerals

What sets each of the clay minerals apart is their distinct thermal, hydrological, mechanical and chemical properties. These distinct properties are caused by the presence of different cations in the tetrahedral and octahedral sheets, the space between successive layers and the various types of bonding present between the layers. The bonding present within the tetrahedral and octahedral sheets is of covalent nature and very strong, indeed when these sheets combine, the oxygen tips of the tetrahedral sheets obtrude into the plane of

hydroxyls in the octahedral sheet, replacing two thirds of the hydroxyls (Weaver & Pollard 1973).

Bonding between the layers in comparison is relatively weak and is more readily susceptible to changes in the environment of the clay. The molecular units bound to the surface of the clay mineral layers at their periphery are the reactive components of the mineral and dictate the sorption properties of the clay and bonding present between clay mineral layers (Sparks 1995). In the case of clay minerals these functional groups are the plane of oxygen atoms bound to silicon in the tetrahedral sheet and the plane of hydroxyls bound to octahedral sheets.

Bonding between layers is formed in order to maintain electrical neutrality and may be present in the form of hydrogen bonding and Van der Waals forces between electrically neutral layers such as in pyrophyllite and talc (Meunier 2005).

3.1.3 Isomorphous substitution

In many of the clay minerals however, an overall negative layer charge results from isomorphous substitution within the tetrahedral and octahedral sheets. Isomorphous substitution is the process by which aluminium and magnesium in the octahedral sheets and silicone in the tetrahedral sheet may be replaced by a different cation of similar cationic radius without unsettling the mineral's crystal structure. It usually occurs during initial formation or subsequent weathering of the mineral (Mitchell & Soga 2005) and is highly dependent on the formation environment.

In reality therefore, the ideal unit structures of 1:1 and 2:1 clay minerals, $Si_4{}^{IV}Al_4{}^{VI}O_{10}(OH)_8$ and $Si_8{}^{IV}Al_4{}^{VI}O_{20}(OH)_4$ respectively, rarely, if ever, exist. Take for instance the formula for the 1:1 mineral kaolinite, $Si_4{}^{IV}Al_4{}^{VI}O_{10}(OH)_8$ (ideal as there is negligible isomorphous substitution in kaolinite), the charge distribution across the unit cell is:

$4 \times Si^{4+} = 4 \times 4+ = 16+$

$4 \times Al^{3+} = 4 \times 3+ = 12+$

$10 \times O^{2-} = 10 \times 2- = 20-$

$8 \times OH^- = 8 \times 1- = 8-$

Total = 16 + 12 − 20 − 8 = **0**

The charge distribution across the unit cell is therefore neutral and bonding between the layers in kaolinite is of the hydrogen bonding and van der Waals type.

In the case of a 2:1 clay mineral, which has undergone isomorphous substitution however, such as smectite, a net negative charge will result in the layers. Smectite is also comprised of a further subset of minerals having undergone various forms of isomorphous substitution, which includes the mineral montmorillonite, the chief constituent of bentonite.

3.2 The clay mineral Montmorillonite

Montmorillonite is formed due to isomorphous substitution of magnesium and iron for aluminium in the octahedral sheet, it is almost exclusively dioctahedral (Mitchell & Soga 2005). This net negative charge facilitates the adsorption of cations and polar molecules such as water into the interlayer space to maintain electrical neutrality, resulting in interlayer expansion (clay swelling) and low bond strength between layers. The degree to which water adsorption may be possible is dependent on the interlayer cations present, temperature and confining pressure (Pusch 08).

3.2.1 Negative layer surface charges

The net negative charge across an interlayer can be demonstrated by the charge distribution calculation across the ideal half-cell unit formula (full unit cell formula / 2) of montmorillonite, $Al_{1.67} (Fe^{2+}$ or $Mg^{2+})_{0.33} Si_4 O_{10} (OH)_2$:

0.33 x (Fe^{2+} or Mg^{2+}) = 0.33 x $2+$ = $0.66+$

1.67 x Al^{3+} = 1.67 x $3+$ = $5.01+$

4 x Si^{4+} = 4 x $4+$ = $16+$

10 x O^{2-} = 10 x $2-$ = $20-$

2 x OH^- = 2 x $1-$ = $2-$

Total = $0.66 + 5.01 + 16 - 20 - 2$ = **0.33 −**

The charge distribution is calculated across the half-cell unit formula to demonstrate a neutral charge on the tetrahedral sheet and a negative charge of 0.33 on the octahedral sheet, making possible the ingress of hydrated cations into the interlayer space which

results in the balanced half-cell unit formula: $M_{0.33}$ H_2O $Al_{1.67}$ (Fe^{2+}, Mg^{2+})$_{0.33}$ Si_4 O_{10} $(OH)_2$, with M denoting any cations balancing the charge.

Naturally, with this unit formula being 'ideal' there will be a high degree of variability in practice, indeed, most montmorillonites display a small degree of isomorphous substitution of aluminium for silicon in the tetrahedral sheet also (Weaver & Pollard 1973). This will result in different layer charges for variations of the mineral. However, an analysis of layer charge of 101 montmorillonites from a various sources by Weaver & Pollard (1973) revealed a distinct mode of 45% of the values within the range 0.30 to 0.35.

Montmorillonite is composed of a further subset of minerals, so named depending on the cation present in the highest proportion in the interlayer space balancing the charge. Calcium (Ca^{2+}) montmorillonite and sodium (Na^+) montmorillonite are the two major smectite minerals, though magnesium (Mg^{2+}), iron (Fe^{2+}/Fe^{3+}), lithium (Li^+) and Aluminium (Al^{3+}) montmorillonite are also naturally occurring smectites and have the common names saponite, nontronite, hectorite and beidelite respectively (Murray 2007).

3.2.2 Positive layer edge charges

As illustrated in Figure 3.1 and Figure 3.2 above, the tetrahedral and octahedral sheets have a planar structure. In three dimensions these sheets form irregular edged disc-shaped crystals, which have a tendency to extend from 10 nm to 10 µm in diameter (Velde & Meunier 2008). Where these layers ultimately terminate, broken bonds results in –OH functional groups being susceptible to protonation or deprotonation as detailed below (Sparks 1995):

$M\text{-}OH + H^+ \longleftrightarrow S\text{-}OH_2^+$

$M\text{-}OH \longleftrightarrow S\text{-}O^- + H^+$
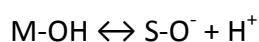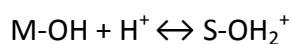
(M being any tetrahedral/ octahedral cation). These reactions, which are strongly pH dependant, may result in +ve edge charges on clay mineral layers, which can have implications when considering the colloidal behaviour of montmorillonite suspensions due to +ve edge/ -ve face interactions (Mitchell & Soga 2005). These are discussed in section 3.7.

3.2.3 Montmorillonite stack structure

The 2:1, tetrahedral:octahedral montmorillonite mineral structure with cations and water molecules residing in the interlayer space for electrical neutrality is illustrated in Figure 3.3. The way in which positively charged cations balance the charge of the negatively charged montmorillonite layers shall be discussed in more detail in 3.3.
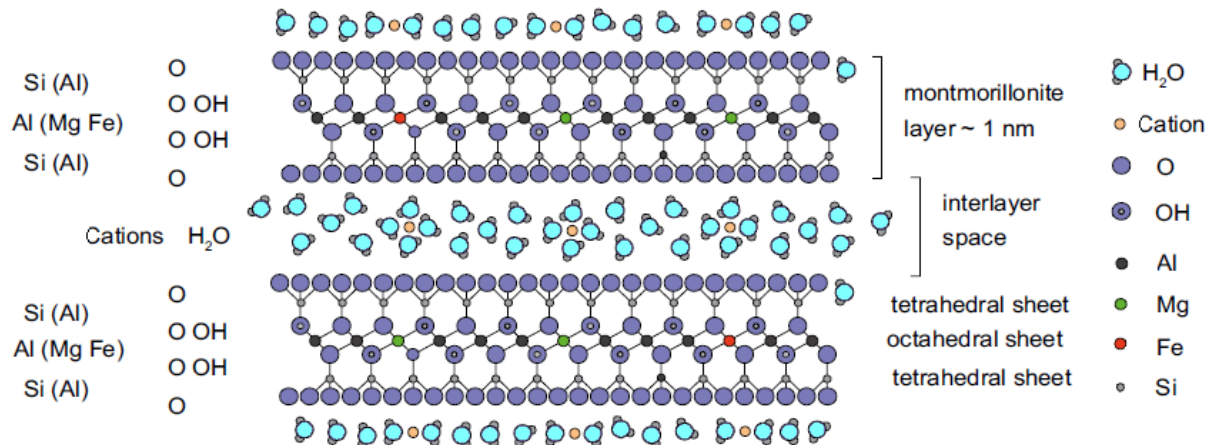

Figure 3.3: Edge view of two montmorillonite layers. Adapted from Karnland (2010). Water molecule orientation not random in reality.

To reiterate, the valence of cation present in this interlayer space governs the clay's behaviour in terms of ability to swell etc. and typically, sodium montmorillonites have one connected molecular water layer and a basal spacing of 1.23 nm. Calcium montmorillonites generally have two connected water layers with an associated basal spacing of 1.42 nm (Murray 2007), the basal spacing being the thickness of the approximately 1 nm-thick montmorillonite layer + interlayer space.

3.2.4 Formation and dominant exchangeable cations in montmorillonite

Montmorillonite is formed by the weathering of igneous rock, which may occur in a variety of environments. Keller (1964) suggested a correlation between depositional environment and the dominant exchangeable cation present in montmorillonites, however, it is also linked to a number of other factors such as post-depositional leaching, original type of clay/ cation present and time. Keller (1964) noted that in the oldest montmorillonites, Na^+ seems to be the dominant exchangeable cation. In montmorillonite that has been in equilibrium with fresh water, Ca^{2+} seems to predominate, whereas in those clays which have been in equilibrium with saline water, Mg^{2+} dominates.

3.3 Surface complexation

Bonding in clay minerals may be present in two forms between the interlayer cations and the negatively charged layers.

3.3.1 Outer-sphere complexes

Outer-sphere complexes are those that form when there is a water molecule present between the cation and the surface functional group on the clay mineral layer, as is the case for montmorillonite, illustrated in Figure 3.4a. This type of bonding occurs relatively quickly and the electrostatic forces present are weak in comparison to those bonds formed in inner-sphere complexation, which are usually covalent or ionic and formed in the absence of water.

3.3.2 Inner-sphere complexes

Inner-sphere complexes form relatively slowly and are irreversible, in contrast to outer-sphere which are reversible (Sparks 1995). One example of inner sphere complexation is in the clay mineral illite as depicted in Figure 3.4b, in which potassium (K^+) is present in the inter-layer space.

3.3.3 Illitisation

Under specific conditions of temperature, pH and in an abundance of potassium, montmorillonite may be converted to illite i.e. from a) to b) in Figure 3.4. An undesirable reaction in the context of radioactive waste disposal (Cuadros 2008), as it would negate many of the buffer's functions which rely on its ability to swell.
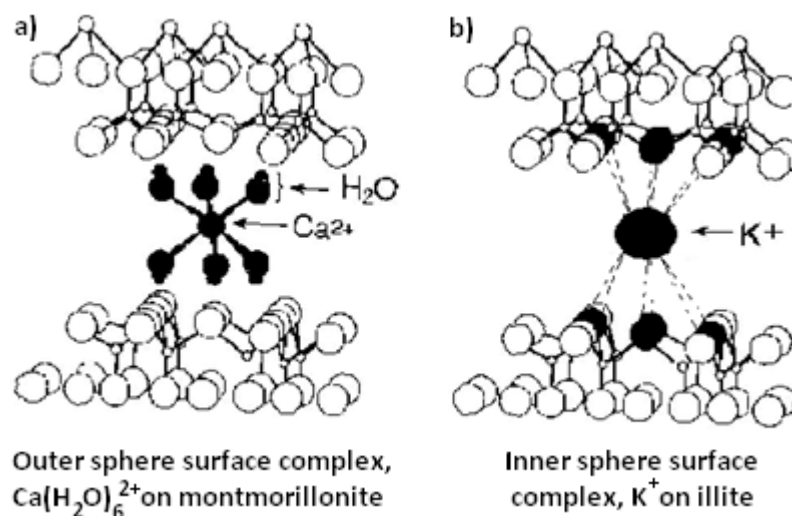

Outer sphere surface complex, $Ca(H_2O)_6^{2+}$ on montmorillonite

Inner sphere surface complex, K^+ on illite

Figure 3.4: Examples of inner and outer-sphere surface complexes on 2:1 clay minerals (Sparks 1995).

3.4 Bentonite

Very rarely in nature does one find a homogenous deposit of one pure mineral such as montmorillonite, due to the high degree of spatial variability in natural weathering and transportation conditions. Bentonite is the name assigned to clay comprising predominantly montmorillonite, the remainder of which is made up of accessory minerals such as other clay minerals, feldspar, quartz and precipitated salts of those cations not required for electrical neutrality (Mitchell & Soga 2005). Typically, high-grade bentonites being considered for use as buffer material in a nuclear repository have montmorillonite contents in the range of 75 to 90% (Karnland 2010). The montmorillonite constituent of MX80 bentonite, the Swedish and Finnish reference buffer bentonite and focus of this study, has Na^+ as the dominant exchangeable cation. Lower quality backfill candidates have montmorillonite contents in the region 50 to 70% (Olsson & Karnland 2009).

3.4.1 Bentonite interactions with geochemical environment.

Quarried, raw bentonite will contain adsorbed cations and a small degree of residual water between the montmorillonite mineral layers. When dispersed in solution, however, this may cause the dissolution of any soluble accessory minerals present in the bentonite and create a suspension of cations in the pore water surrounding the montmorillonite particles. Indeed, any cations already present in solution will have the same effect. This will cause the cations present in the interlayer space to try and diffuse from the interlayer into the surrounding fluid and indeed those in the surrounding fluid in the opposite direction in order to equilibrate cation concentrations throughout the suspension. This tendency to equilibrate is opposed by the Coulombic attraction from the negatively charged clay surface (Mitchell & Soga 2005).

3.4.2 Diffuse double layer

The Gouy & Chapman diffuse double layer charge distribution model has been used extensively and built upon to best describe these interactions. Taking for instance a negatively charged clay particle surface (1/2 of the montmorillonite structure illustrated in Figure 3.5a dispersed in water:
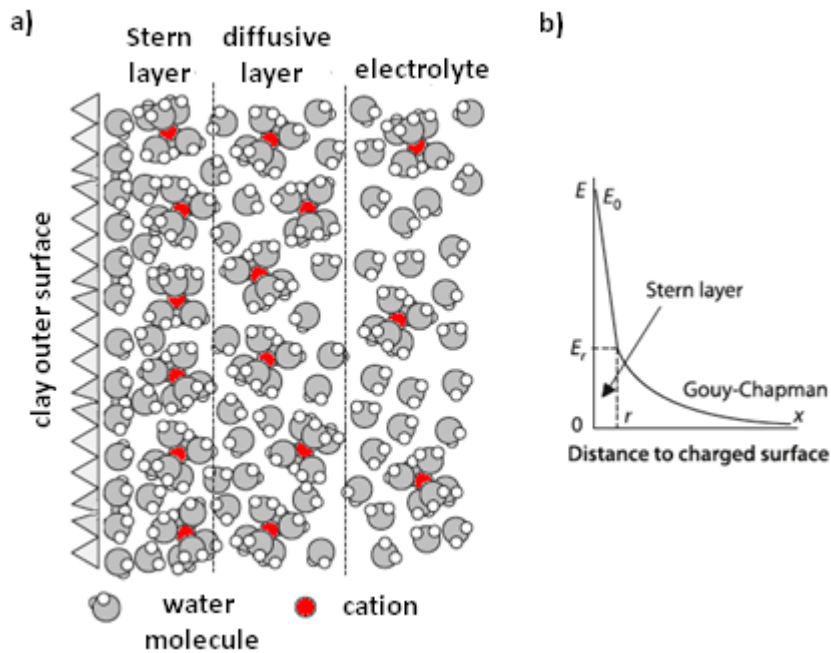
Figure 3.5: Idealised demonstration of diffuse double layer and cation concentrations in adjacent solution (anions omitted). Adapted from Velde and Meunier (2008).

Gouy & Chapman initially proposed that the concentration of cations varies exponentially from the negatively charged clay particle surface. Stern (1924) modified this model, however, to take into account the effect of cation crowding near the clay particle surface, making the surface less accessible for other cations (Mitchell & Soga 2005). Stern (1924) proposed that the concentration of cations actually exhibits a linear concentration profile within a region equal to the ionic radius of the cation attracted to the surface, as depicted by the Stern layer in Figure 3.5b.

The Gouy and Chapman model is traditionally applicable to clay suspensions and montmorillonite colloidal behaviour. It can also be used to describe the bonding in montmorillonite stacks discussed in section 3.2.3 however in that, when two clay particles are brought together, the diffuse, repulsive layers overlap causing a redistribution of cations in the interlayer, resulting in an attractive force which binds the layers together as detail in Figure 3.6.
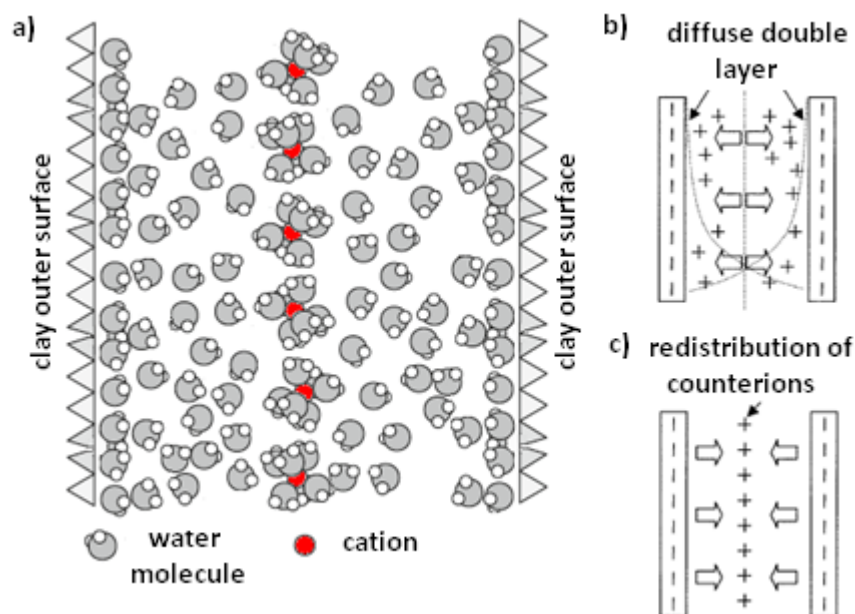
Figure 3.6: Depiction of overlapping diffuse double layers and cation redistribution. Adapted from Velde and Meunier (2008) and Mitchell and Soga (2005). Water molecule orientation will not be random in reality.

3.4.3 Ion exchange phenomena.

As discussed in 3.3, outer-sphere surface complexes, commonly found in montmorillonite, are reversible processes. Cation exchange phenomena, in those cations bound by outer-sphere surface complexes, may occur in montmorillonite whereby exchange may take place between a cation adsorbed on a negatively charged surface of a clay particle and a cation introduced into a diffuse cloud surrounding the clay particle caused by changes in the environment.

In the context of radioactive waste disposal, this cation may be introduced in a number of ways: as a solute in contacting groundwater; as dissolved accessory minerals already present in the bentonite; or as the release of radionuclide species, most of which are positively charged. The process is usually reversible, driven by diffusion and is governed by a number of factors such as temperature, pH, pressure, chemical and biological composition of the pore water (Mitchell & Soga 2005).

Cation exchange capacity

Stoichiometry dictates that a cation must be displaced by an equivalent charge (one or more cations) in order to maintain electrical neutrality. The extent to which this may occur is

quantified by the *cation exchange capacity (CEC)* of the clay mineral, measured in mol $_c$ / kg or moles of charge per kg. In order to demonstrate the use of these units in a cation exchange scenario, consider the problem:

Q. What mass of $CaCl_2$ would be required to replace 4 mol $_c$ of K^+ in a clay?

A. K^+ is replaced with Ca^{2+} in the clay

1 mol of Ca^{2+} = 2 mol $_c$

1 mol of $CaCl_2$ = 2 mol $_c$ = 111g

1 mol of K^+ = 1 mol $_c$

4 mol of K^+ = 4 mol $_c$ = 156.4g

Mass of $CaCl_2$ required = 2 x 2 mol $_c$ = 2 x 111g = 222g

The CEC of a clay is usually determined by washing off all excess salts and accessory minerals until only the clay mineral remains; montmorillonite in the case of bentonite. The clay mineral would then be immersed in a solution of excess concentrations of an index cation such as Mg^{2+} at pH 7 and room temperature. Excess quantities of the index cation are then removed from the solution and the index cation is displaced by another cation such as Ca^{2+}. The amount of excess cation displaced can then be measured and the CEC calculated (Sparks 1995). This exchange would take place by the following reaction, where *X* represents negatively charged mineral exchange sites:

$CaCl_2(sol) + MgX \leftrightarrow MgCl_2(sol) + CaX$

For instance, if 300 mg of Ca^{2+} was displaced from 200g of a clay:

1 mol of Ca^{2+} = 2 mol $_c$

40g of Ca^{2+} = 2 mol $_c$

300 mg of Ca^{2+} = 0.015 mol $_c$ in 200g clay

CEC = 0.075 mol $_c$ / kg or 7.5 cmol $_c$ / kg

Typical values of the CEC for montmorillonites are in the range 80 – 120 cmol $_c$ / kg (Velde & Meunier 2008).
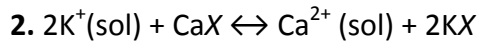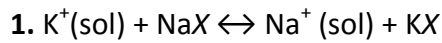
Cation selectivity

Cation exchange involves the selectivity of one cation over another, and generally depends on the hydrated radius, valence and concentration of ions present. These factors can be demonstrated by a few 'rules of thumb', which exist for clay minerals. For instance, for cations of the same valence from the same group of the periodic table, the cation with the smallest hydrated radius will be preferred: $Cs^+ > Rb^+ > K^+ > Na^+ > Li^+ > H^+$. For a group of cations with different valence, the cation with the highest valence will usually be preferred: $Al^{3+} > Ca^{2+} > Mg^{2+} > K^+ = NH_4^+ > Na^+$ (Sparks 1995). In practice, the above rules will exhibit a broad degree of variability and a cation of low valence such as Na^+ may replace a cation of higher valence such as Ca^{2+} if the concentration of the lower valence ion in solution is high in relation to the higher valence cation.

Interestingly, and significant in the context of radioactive waste disposal, as early as 1964 Hanshaw noted that the cation selectivity is also dependent upon whether the clay is compacted or dispersed, both of which conditions may exist in and around a deposition hole. Hanshaw (1964) found that the cation selectivity in compacted montmorillonite is of the order: $K^+ > Na^+ > H^+ > Ca^{2+} > Mg^{2+}$. A notion confirmed by Weaver and Beck (1976) who agreed that in dispersed marine clays, in which Mg^{2+} predominates throughout the initial sedimentation, Na^+ will begin to replace the Mg^{2+} during compaction. The rate at which these exchange processes occur is highly variable and is dependent on a number of factors including temperature, pH, solution concentrations and mineral type. Montmorillonite, in comparison to other minerals, exhibits longer time frames for exchange owing to the inaccessibility of exchange sites between layers (Mitchell & Soga 2005).

Selectivity coefficients

The selectivity clay minerals exhibit for one cation over another can be demonstrated by the selectivity coefficient. Many efforts have been made to establish a relationship between the concentration of ions in solution and those adsorbed to a mineral surface. One such relationship, and perhaps the most widely used is that proposed by Gaines and Thomas (1953). It may be used to describe the selectivity in homovalent cation equilibrium systems and indeed heterovalent (monovalent over divalent and vice-versa) equilibrium systems,

considering the following homovalent and heterovalent cation exchange reactions, again *X* denoting the clay mineral:

1. $K^+(sol) + NaX \leftrightarrow Na^+ (sol) + KX$

2. $2K^+(sol) + CaX \leftrightarrow Ca^{2+} (sol) + 2KX$

The Gaines-Thomas selectivity coefficients for the above reactions would be defined as:

1. $K_{GT} = \dfrac{\{KX\}.[Na^+]}{\{NaX\}.[K^+]}$

2. $K_{GT} = \dfrac{\{KX\}^2.[Ca^{2+}]}{\{CaX\}.[K^+]^2}$

If the value of K_{GT} is greater than 1 in either case, this signifies that K is preferred over Na^+ & Ca^{2+} and the opposite is true for values of K_{GT} less than 1. Karnland et al (2011) used the Gaines-Thomas convention to calculate the selectivity coefficient for $Ca^{2+} - Na^+$ exchange in a highly compacted bentonite for various concentrations of potentially infiltrating groundwater. The bentonite was washed of soluble accessory minerals to avoid their dissolution and any effect on exchange processes. The resultant montmorillonite was then purified into homoionic Ca^{2+} and Na^+ form and exchange undertaken across a range of concentrations of the corresponding ion in solution. The dry density of each clay was also varied.

In general, the dry density was shown to have an effect on the rate of cation exchange with higher dry densities resulting in slower exchange processes though the same equilibrium was eventually reached. Those clays that started off as Ca-montmorillonite were also found to be closer to equilibrium at the start as uptake of Na^+ was not as significant as uptake of Ca^{2+} in the corresponding test. In summary, the K_{GT} values were found to be similar to those previously calculated for high water-to-solid ratios, with the clay showing a distinct affinity for Ca^{2+} over Na^+, contrary to Hanshaw's (1964) earlier postulation. Considering this in the context of radioactive waste disposal, higher dry densities will only serve to slow down the process of the clay equilibrating with a groundwater solution.

Anion exchange capacity

Similar to the cation exchange capacity, montmorillonite will also exhibit an anion exchange capacity due to the small number of positively charged mineral layer edges as discussed in section 3.2.2. The combined anion and cation exchange capacity constitute the total exchange capacity of the clay mineral. Due to the variable nature of the +ve edge charges however and the large specific surface area attributed to negatively charged faces in montmorillonite, the vast majority of a montmorillonite's exchange capacity will be due to cation exchange.

The permanent charge between clay mineral layers is predominantly where cation exchange occurs in montmorillonite, although the variable charge at mineral layer edges may also undergo exchange processes accounting for up to 20% of the exchange capacity of smectites (Mitchell and Soga 2005).

3.5 Bentonite Fabric.

Consideration of the bentonite fabric and physical properties is central to bentonite erosion as it will govern the way in which remaining clay is redistributed upon the loss of some material (Robinson & Bath 2010). As mentioned previously, bentonite consists of the mineral montmorillonite (75 to 90%, high grade), other clay minerals and detritus such as quartz grains and precipitated salts such as gypsum.

3.5.1 Bentonite aggregates

In the raw, quarried state, bentonite consists of grain sizes in the range of 10 to 5000 µm, depending on the processes involved in quarrying. These grains consist of aggregates of montmorillonite stacks (Figure 3.8B). Stacks are typically between 3 and 30 layers in thickness (Pusch 2008) and between 10 and 100 nm in diameter (Ichikawa et al 2004).

Accessory minerals and detritus, or macrograins, are generally larger and their diameter falls within the micrometer scale, though naturally these characteristics will vary between different bentonites. The way in which these stacks interweave and accommodate accessory minerals in a compacted bentonite is illustrated in Figure 3.7, which shows an SEM image of the pure montmorillonite stacks (Figure 3.7A) alongside images in which the stacks contain precipitates of NaCl and Gypsum in MX80 bentonite, Figure 3.7B and Figure 3.7C respectively.
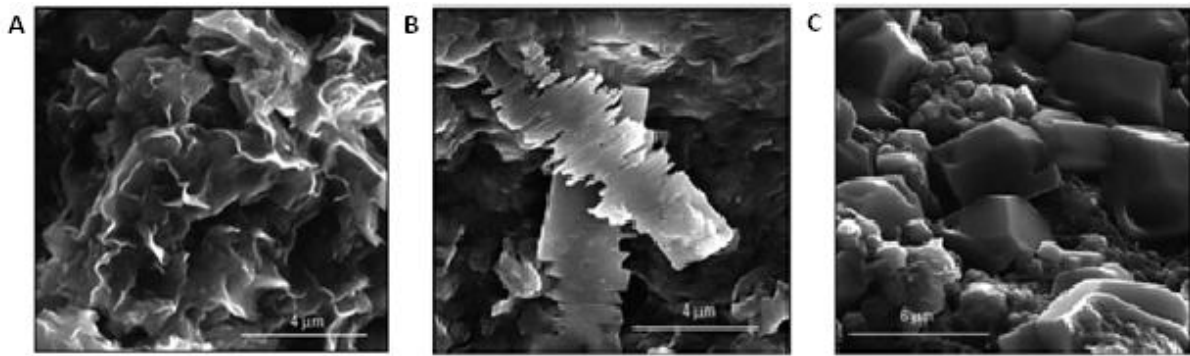
Figure 3.7: SEM images of A. Interwoven montmorillonite stacks in MX80, B. Precipitated NaCl in the clay matrix and C. Precipitated gypsum in the matrix (Pusch 2008)

3.5.2 Porosity in bentonite

Un-compacted bentonite has been observed to contain three types of porosity (Pusch 2008): micropores between individual montmorillonite layers (Figure 3.8A); mesopores within individual aggregates (Figure 3.8B) and macropores between particles (Figure 3.8C).

This model can be further simplified to a double porosity model whereby micropore porosity represents 'internal' water and meso-to-macro-scale pores represent 'external' water (Apted et al 2010). The respective volume of each type of porosity is dependent upon the degree of compaction of the clay; as compactive effort increases, the macroporosity (external water) is reduced via diffusion and the proportion of interlayer water in the system begins to dominate. This ultimately results in the low hydraulic conductivity of highly compacted bentonite.
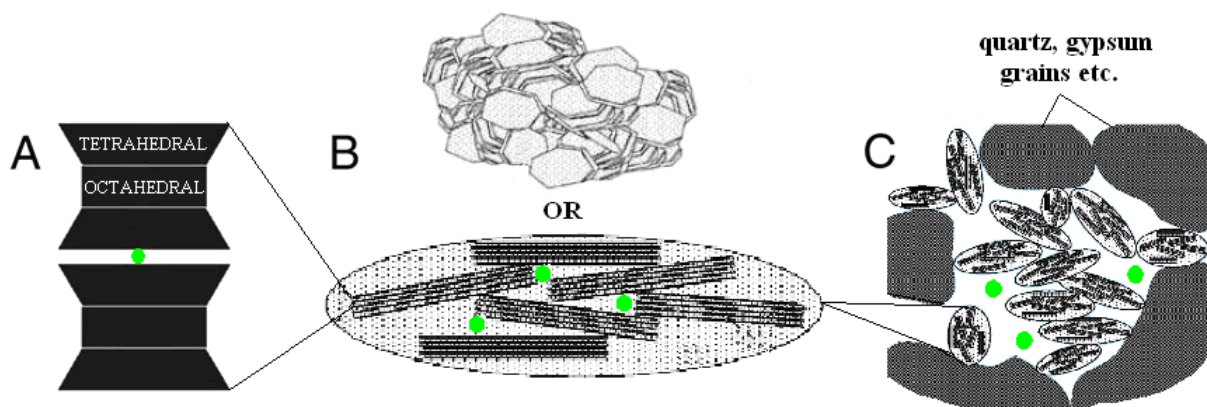

Figure 3.8: Conceptual model of hierarchal porosity in bentonite. Pore location indicated by green dots. Adapted from Ichikawa et al (2004), Pusch (2008) & Prikryl & Weishauptova (2010).

3.6 Bentonite buffer candidates (grain size and mineralogy).

In order to demonstrate the variability between different bentonite deposits, consider the two reference buffer bentonites proposed for use in the SKB KBS-3V repository concept: MX80, the natural sodium bentonite from Wyoming and its counterpart IBECO-RWC, a natural calcium bentonite from the island of Milos in Greece.

Figure 3.9 illustrates the mineral composition by weight and the grain size distribution of either material in the 'as-delivered' state. It is apparent that there is a broad degree of variability in grain size between MX80 and IBECO RWC bentonites in the 'as-delivered' state with ~20% of the grains in the IBECO RWC being larger than the largest grain size of 2mm in the MX80. The varying mineral composition between the two deposits will also have implications for ion exchange processes and in-turn for the erosion characteristics of either material.

a)

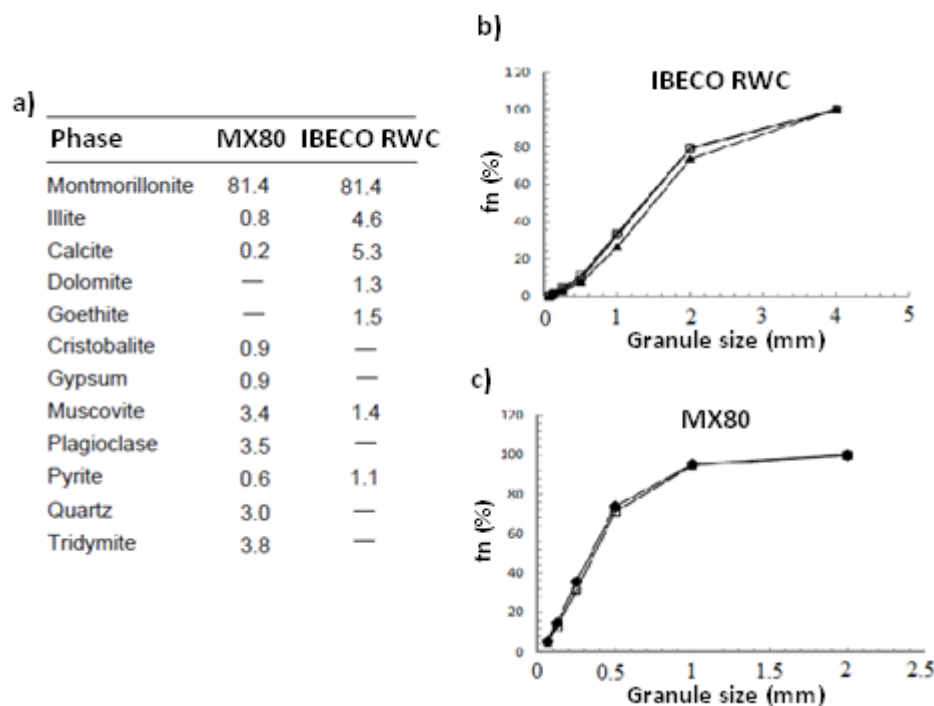| Phase	MX80	IBECO RWC
Montmorillonite	81.4	81.4
Illite	0.8	4.6
Calcite	0.2	5.3
Dolomite	—	1.3
Goethite	—	1.5
Cristobalite	0.9	—
Gypsum	0.9	—
Muscovite	3.4	1.4
Plagioclase	3.5	—
Pyrite	0.6	1.1
Quartz	3.0	—
Tridymite	3.8	—

Figure 3.9: Mineral constitution (%) and grain size distribution (dry sieving) of MX80 and IBECO-RWC bentonites. Adapted from Karnland (2010) and Kiviranta & Kumpulainen (2011).

3.7 Montmorillonite colloid chemistry.

Clay colloid chemistry is concerned with clay particle interaction on a microscopic scale, the analysis of the forces acting between clay particles in suspension, and how the type and arrangements of ions and molecules on the clay surface influence these forces (Van Olphen

1966). The study of clay particles in suspension is pertinent to understanding the interaction between clay minerals and pore water in soil systems, and any effect the chemistry of infiltrating solutions to the soil system may have. The diffuse double layer, and ion exchange phenomena discussed in sections 3.4.2 to 3.4.3. are particularly relevant to clay colloid chemistry.

An appreciation of these interactions is central to the investigation of bentonite erosion - considering the compacted buffer to be the clay soil system and the groundwater the infiltrating solution. Initially, prior to wetting, the buffer may be considered to have a high solid to water ratio. However, it is at the buffer/groundwater interface where erosion may take place; here there is a high liquid-to-solid ratio. Once in suspension, colloids are potentially mobile through any host rock where the pore size is considerably larger than the colloids and the hydrogeological environment is dominated by advective transport, i.e. in higher strength crystalline and sedimentary host rocks.

In terms of bentonite erosion, colloidal behaviour will be significant with respect to predicting the quantity of montmorillonite colloids released in various groundwater chemistries, their mobility and the likelihood of them remaining in suspension (stability). Upon the selection of any site, characterisation of the local groundwater for current colloid stability and transport will provide an analogue for predicting the fate of bentonite colloids in the far field. If erosion rates and transport properties are unfavourable, this would imply significant risk to radionuclide transport to the biosphere (Figure 3.10).
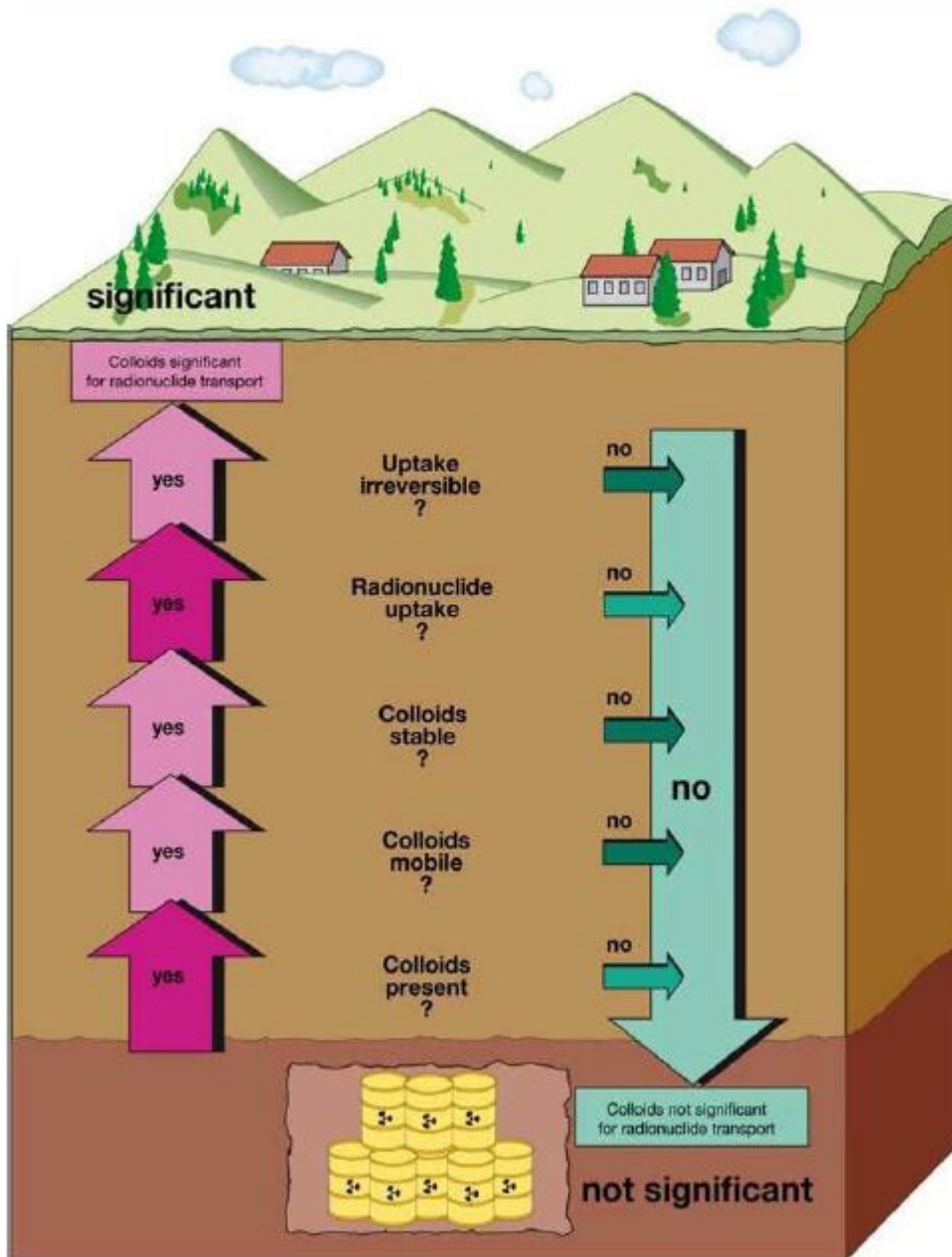
Figure 3.10: The colloid ladder (Beard 2013)

Colloid generation in lower strength sedimentary rocks such as the Opalinus clay of Switzerland and the Callo-Oxfordian clay in the French concept are currently not considered significant in either the near field or host rock due to the lack of transmissive features, diffusion dominated flow regimes and the rock's unique plasticity and ability to self-seal (Serco 2012).

As detailed in section 3.4.2 electro-neutrality is maintained in bulk soil systems, yet on a micro-scale there is a real heterogeneity in electrical charge. The binding of clay mineral

particles has been demonstrated from the overlapping of diffuse double layers and the presence of hydrated cations in the interlayer space. The ability of this interlayer to hydrate is controlled by confining conditions and the valence and concentration of interlayer cations; associated swelling decreases with increasing charge and concentration of cations.

3.7.1 Buffer saturation and swelling

The focus will be centred on the KBS-3V concept, which is currently being employed by the U.K. as a reference concept for scoping studies, colloid generation is foreseen to be a potential problem in this concept (Alexander & Neall 2011). During buffer saturation, bentonite exposed to groundwater at the host rock interface will be free to swell, firstly to fully accommodate the deposition hole and subsequently into any fractures intersecting the deposition hole, depending on the groundwater chemistry as detailed in Figure 3.11.
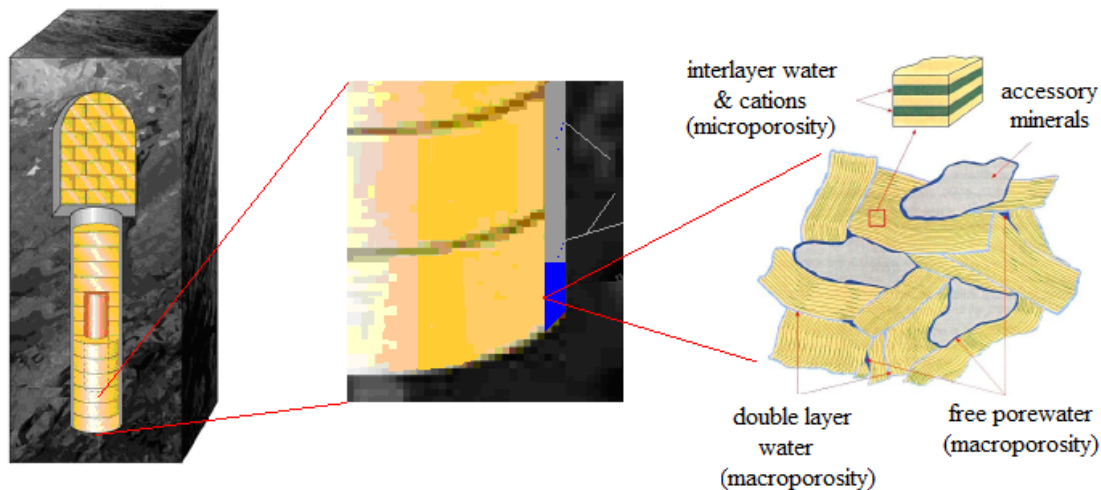

Figure 3.11: Illustration of deposition hole and compacted bentonite fabric at buffer / host-rock interface. Adapted from Posiva (2011) and Apted et al (2010)

As detailed in section 3.6, SKB have specified the Sodium dominated MX-80 as their reference buffer material, however, the calcium dominated IBECO-RWC has also been extensively researched and both will exhibit different swelling behaviour in varying groundwater chemistries. Ca montmorillonite does not have the same ability to swell as Na montmorillonite and, with higher swelling pressure, more colloids may be generated due to higher repulsion between mineral layers in Na montmorillonite (Missana et al 2003). In the case of sodium montmorillonite, four layers of water molecules may be accommodated

between clay layers before the positive and negative attractive forces of overlapping diffuse double layers and interlayer cations equilibrate.

3.7.2 Colloid generation.

At this point, in unfavourable groundwater chemistry i.e. low ionic strength, cations may diffuse out of the interlayer space into solution and negative, repulsive forces will prevail between montmorillonite layers. This results in colloidal suspensions of montmorillonite layers (Figure 3.12a) and stacks (Figure 3.12b), between 1nm and 1µm in size (Holmboe 2010).
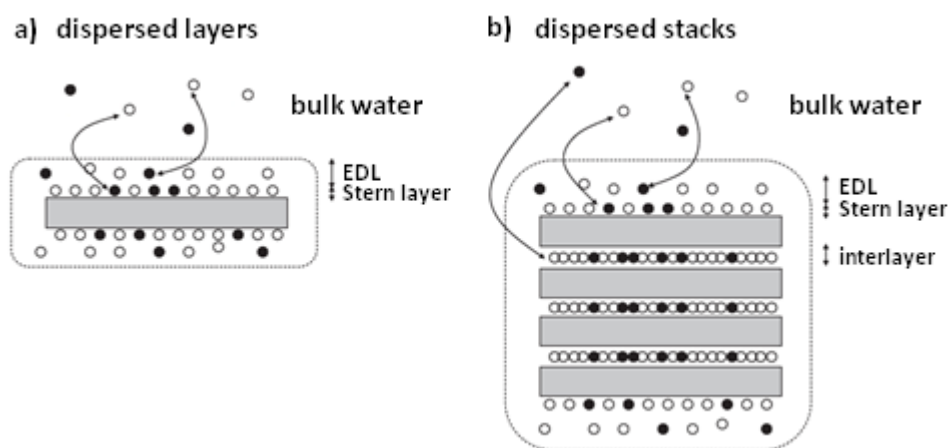

Figure 3.12: Exchange processes involved in aqueous clay / electrolyte interactions. a) dispersed layers b) dispersed stacks. (Tournassat et al 2011).

Figure 3.12 depicts the negatively charged clay layer surfaces attracting an equivalent opposite charge from the bulk solution, this opposite charge constitutes the counterions in the Stern layer and the diffuse layer. The concentration of counterions gradually decreases from the clay particle surface until equalling that of the bulk solution. In stagnant conditions, these particles remain stable in suspension by Brownian motion. Adjacent particles move in various directions and velocities and this irregular motion is the outcome of net forces on the particles resulting from collisions (Van Olphen 1963). The stability of these colloid suspensions, i.e. the tendency to remain in the peptized (dispersed) state rather than flocculate (come out of suspension), is important in bentonite erosion, as a stable colloidal suspension is more likely to lead to a higher degree of bentonite erosion.

3.7.3 DLVO theory.

The stability of bentonite colloids can be quantified in principle by DLVO theory, so named after Derjaguin & Landau (1941) and Verway & Overbeek (1948) who extended the Gouy-Chapman theory (discussed in section 3.4.2) to describe the interaction forces between colloidal particles and predict their stability (Mitchell & Soga 2005). This theory describes the interaction between charged mineral surfaces as the energy that results (V_T) from the interaction due to repulsion (V_R) and the attraction energy (V_A) due to Van der Waals forces (Holmboe 2010), where h is the distance between particles:

$$V_T = V_R(h) + V_A(h)$$

For spherical particles of radius *r*, the attractive and repulsive energies can be described as:

$$V_R(h) = 4\pi\varepsilon\varepsilon_r(\frac{k_B T}{ze})\frac{r^2}{h+2r}\Psi_s^{\ 2}e^{-kh}$$

$$V_A(h) = -\frac{Ar}{12h}$$

Where ε & ε_r = dielectric constants for a vacuum and water.

k_B = Boltzmann constant

z = Ion valency

e = elementary charge

k^{-1} = Debye length (thickness of double layer)

ψs = surface potential

A = Hamaker constant. Represents attraction due to Van der Waals forces

An example of DLVO interactions between two colloidal particles is detailed in Figure 3.13. $V_{T,max}$ is the maximum barrier height and what governs the rate of aggregation between colloidal particles. In typical systems, if:

$V_{T,max}$ > 25 $k_B T$. The dispersion will remain stable for months.

0 < $V_{T,max}$ < 15 $k_B T$. Aggregation will occur over shorter time periods.

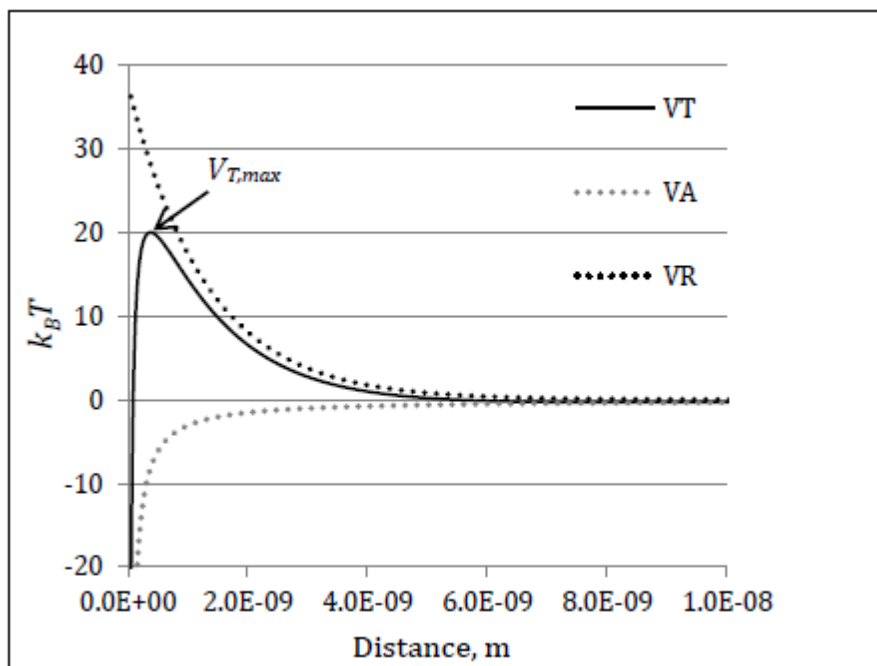$V_{T,max}$ < 0. Every collision will result in aggregation and the system will be unstable.

Figure 3.13: DLVO interaction example between two colloids (Holmboe 2011).

3.7.4 Colloid cycle

As more and more particles collide and aggregates are formed, as governed by DLVO theory, gravity will begin to dominate over Brownian motion and the particles will sediment out of suspension. A cyclical process of colloid generation, aggregation and sedimentation ensues in static systems as detailed in Figure 3.14. In the context of bentonite erosion however, this equilibrium may never be reached if aggregation rates are suitably slow or advection rates suitably high to facilitate transport of the colloidal solution out of the cycle before sedimentation can occur.
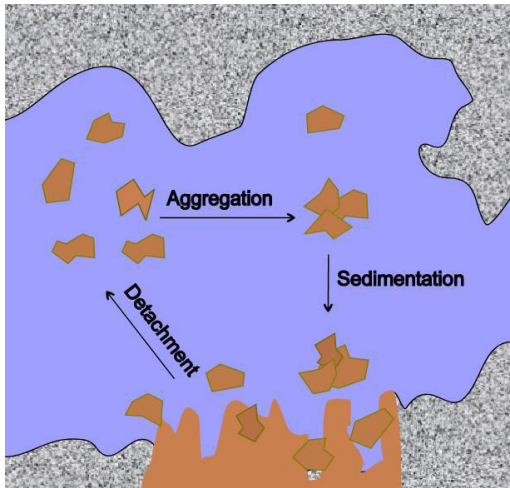
Figure 3.14: Colloidal life cycle (Garcia-Garcia 2010).

3.7.5 Montmorillonite particle associations in clay suspensions

Future intrusion from glacial melt water, discussed in more detail in section 3.8.3, is one such scenario in which groundwater depleted in electrolytes may contact the clay and cause colloid formation and a stable colloidal suspension (Apted et al 2010). Generally speaking, the higher the ionic strength of intruding water, the less stable colloids will be. This can be demonstrated by the way in which clay particles may interact when in suspensions of various ionic strength as proposed by Van Olphen (1963):
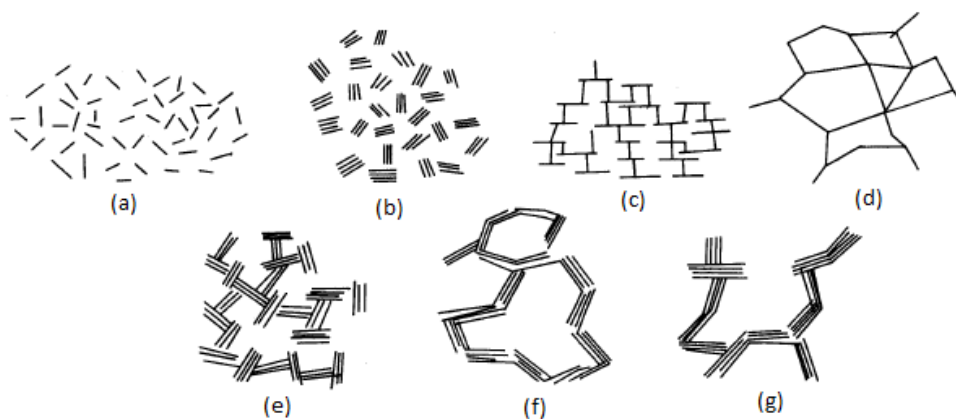

Figure 3.15: Particle associations in clay suspensions (a) dispersed (b) face to face (c) edge to face (d) edge to edge (e) edge to face stack (f) edge to edge stack (g) edge to face and edge to edge stack (Van Olphen 1963).

In electrolyte free systems, one might expect colloids in the nature of Figure 3.15(a) or (d) to prevail. Broken bonds at layer edges (both +ve & -ve charged) creating edge to edge interactions. As the concentration of electrolyte in solution increases though, double layers

on either side of individual clay particles become compressed and associations begin to favour edge to face interactions, or the 'card-house' structure such as in Figure 3.15(c). Card-house structures are voluminous though lack the mass which aggregates or floccs possess to sediment at a reasonable rate (Mitchell & Soga 2005).

Critical coagulation coefficient (CCC)

Increasing the concentration of electrolyte further still results in additional double layer compression to the point where face to face interactions become rapid and 'book-house' structures of the floccs dominate (Yariv & Cross 1979) and coagulation occurs. The concentration of electrolyte at which this occurs is the *critical coagulation coefficient* (CCC) of the particular clay mineral for a particular salt. The CCC is dependent on pH, due to the layer edge charge dependency on pH (Birgersson et al 2009), and occurs at lower concentrations of higher valence ions in solution. The CCC is only applicable however for a purified montmorillonite in a homoionic solution hence has limited applicability in the context of bentonite erosion from a GDF.

3.8 Bentonite erosion phenomena and research undertaken in field to date.

Bentonite erosion is understood to occur by chemical and physical/ mechanical processes.

3.8.1 Physical erosion

Physical bentonite erosion is the process whereby steep hydraulic gradients and rapidly flowing groundwater can cause shearing of bentonite particles from the surface of the compacted bentonite or indeed the stable gel of bentonite at any wetting front. Slip and breakage at the contacts between adjacent particles takes place at suitably high shear stresses (Pusch 2008).

Piping

Piping is one such physical erosion process, whereby the water pressure from a fracture is higher than the counteracting pressure by the clay; or the hydraulic conductivity of the clay is lowered suitably to facilitate water ingress into the clay, ceasing to resist the water pressure in the fracture (Wilson et al 2011). Erosion by such mechanical processes as piping have been demonstrated in ¼ scale (Riikonen 2009) and ½ scale (Dixon et al 2008) deposition tunnel experiments and also laboratory based (Sandén & Börgesson 2010) and full scale, in situ (Cuss et al 2010) deposition hole experiments. In the above work, water

inflow rates from point sources were varied in order to establish the effects of inflow rate on erosion. The process is perhaps more applicable to the tunnel backfill, as higher groundwater inflow rates are expected into depositional tunnels than deposition holes. Due to the fact that, should a deposition hole be excavated and be found to have an unsuitably high inflow rate, it may be abandoned and backfilled. It will be more difficult to avoid such water bearing discontinuities in the larger diameter deposition tunnels however.

Groundwater flow rates in the Swedish and Finnish disposal concepts

No limits have been set to date on maximum permissible inflow rates into deposition tunnels whereas in the case of deposition holes, erosion research to date has led to SKB imposing a preliminary maximum permissible cumulative inflow rate of 0.1 l/min in order to prevent physical buffer erosion during the installation phase, before backfill (Sandén & Börgesson 2010).

In the case of the Finnish repository, they have noted cumulative average inflow rates into deposition tunnels at their Onkalo site of 1 l/min per 100m (Hansen et al 2010), though naturally this will be site specific. Further to this, groundwater flows will be spatially and temporally variable, hence the possibility of such phenomena occurring in deposition holes throughout a repository evolution cannot be ruled out. Indeed, higher localised water velocities may occur in the smaller fracture apertures permissible intersecting deposition holes as opposed to the larger fractures intersecting the access tunnels; resulting in piped channel formation in the buffer.

Indeed, the shearing of any stable gels formed after swelling into a fracture, such as that depicted in Figure 3.16, may also result in physical bentonite erosion.
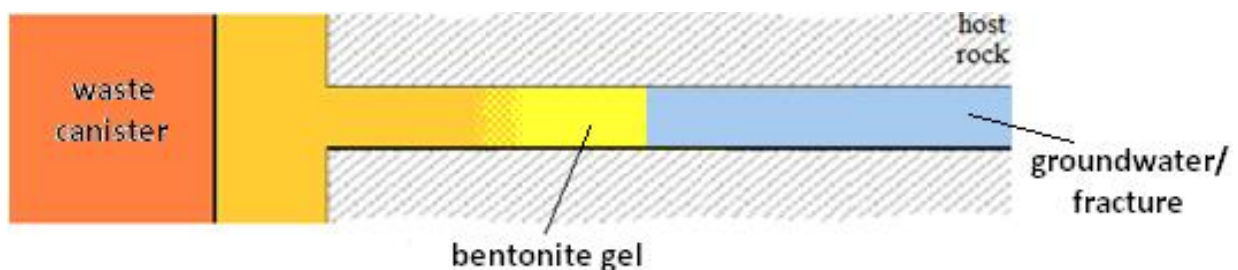

Figure 3.16: Conceptual model of stable bentonite swelling into a fracture (Adapted from Apted et al 2010).

3.8.2 Chemical erosion

The initial chemistry of the montmorillonite mineral and the chemistry of the encroaching groundwater both determine the type and strength of bonding between swelling montmorillonite layers as detailed previously.

Groundwater chemistry – Early in repository evolution.

Early in repository evolution, saline groundwater may be expected to prevail; with high enough dissolved salt concentrations to maintain a stable buffer saturation and swelling process into rock fractures intersecting the deposition holes. Supporting a cohesive montmorillonite gel at the wetting front. Groundwater investigations at the site of the Swedish repository in Forsmark have revealed chloride concentrations in the order of 2000 to 6000mg/l at repository depth (SKB 2011, Vol I).

In the context of the U.K., Bath et al (2006) has undertaken groundwater sampling in the Sellafield area of Cumbria and the composition of one representative borehole at 543m (approximate repository depth) in the Borrowdale volcanic group, test DET 10, is reported in Table 3.1:

Ion	mg/l	mass of 1 mol (g)	mol/l
Na^+	8000	23	0.347
K^+	102	39.1	0.0026
Mg^{2+}	82	24.3	0.00337
Ca^{2+}	685	40.1	0.0171
Sr^{2+}	15.4	87.6	0.000176
Cl^-	13000	35.5	0.3662
SO_4^{2-}	1060	96.1	0.011
HCO_3^-	86	61	0.0014
Br^-	23.6	79.9	0.000295

Table 3.1: Concentrations of various ions in solution from a borehole at 543m depth in the Borrowdale volcanic group, Cumbria (Bath 2010).

The ionic strength of the groundwater in test DET 10 (Table 3.1) can be calculated as:

$$I = \frac{1}{2} \sum c_i z_i^{\,2}$$

Where: c_i = molar concentration of ion i

z_i = charge of ion i

$$\therefore I = \frac{1}{2}[0.0171 \times (2^2) + 0.347 \times (1^2) + 0.0026 \times (1^2) + 0.00337 \times (2^2) + 0.000176 \times (2^2) +$$

$$0.3662 \times (-1^2) + 0.011 \times (-2^2) + 0.0014 \times (-1^2) + 0.000295 \times (-1^2)]$$

$$\therefore I = 0.422M$$

Which is two orders of magnitude higher than the ionic strength required to maintain a stable montmorillonite gel and avoid colloid generation, which shall be discussed further in section 3.8.4.

Further to likely high initial groundwater salinities, during the construction phase, ventilation in a similar capacity to the argillaceous concept, may de-saturate the rock. Salts present in the groundwater may build up in the form of precipitates on fracture surfaces and deposition hole/ tunnel walls as a result of evaporation. Upon re-saturation, the re-dissolution of these precipitates may result in their presence in far higher concentrations in the groundwater i.e. increasing the salinity of the groundwater that saturates the bentonite further still.

Groundwater chemistry – Intrusion of dilute groundwater during repository evolution.

As long as the groundwater remains sufficiently saline, the cations present between interlayer montmorillonite sheets, which act to maintain electrical neutrality, will be in equilibrium with those present in the groundwater. If the concentration of cations in the groundwater should fall below a critical threshold however, due to the intrusion of dilute groundwater for instance, cations will diffuse from the buffer to the groundwater due to the concentration gradient; allowing negative, repulsive forces to dominate between montmorillonite sheets.

Ultimately, this could lead to the dissociation of the montmorillonite mineral layers and the formation of a low shear strength colloidal sol at the buffer/ groundwater interface, which will be susceptible to erosion by the flowing groundwater as illustrated in Figure 3.17.
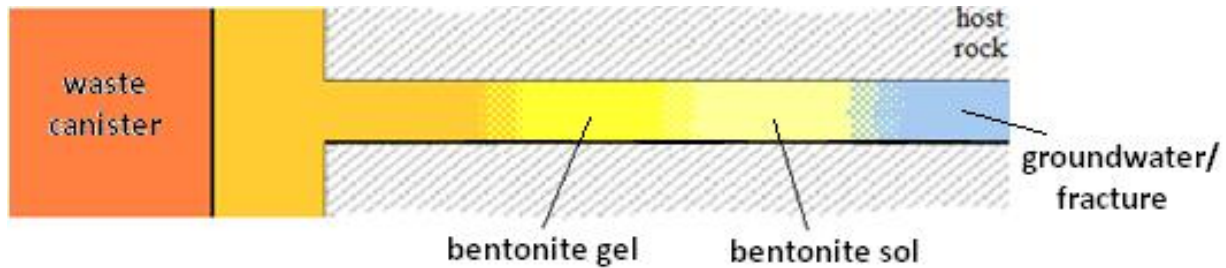

Figure 3.17: Conceptual model of unstable bentonite swelling into a fracture and colloidal sol formation. Adapted from Apted et al (2010).

One possible scenario, in which dilute groundwater intrusion may be initiated, is if the pore water trapped in the rock matrix, pre-dating that flowing in fractures, is more dilute in nature with respect to dissolved salts (Robinson & Bath 2010), thus facilitating the removal of dissolved salts from the groundwater into the rock matrix by diffusion. Construction of the repository and creation of the EDZ may perhaps cause equilibration between rock matrix and fracture water resulting in the dilution of fracture water over time.

3.8.3 Glaciation

Intrusion of dilute groundwater to repository depth is also possible during periods of glaciation, which may last many millennia and reoccur up to 8 times during the typical repository assessment period of 1,000,000 years (SKB 2011, Vol II).

Glacial meltwater is characterised by a low content of dissolved salts (Clark et al 2000) and a highly pressurised sub-glacial environment, which provides a driving force for freshwater circulation to repository depths (Figure 3.18). Glacially-driven freshwater circulation has been observed at the Forsmark site in Sweden, in which post-glacial meltwater penetration from 8800BC is recorded at a depth of 550m (SKB 2011, Vol II).
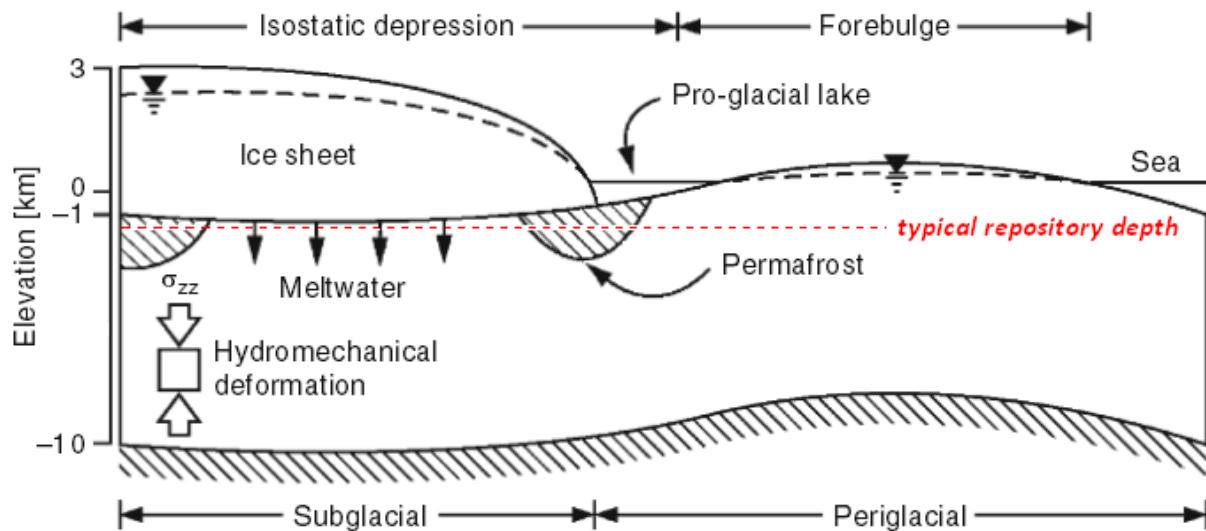
Figure 3.18: Conceptual model of potential mechanisms influencing groundwater during a period of glaciation. Adapted from Lemieux and Sudicky (2011).

The injection of pressurised sub glacial melt water may also serve to increase the velocity of groundwater flowing through a repository, which may increase the rates of buffer erosion. Physical erosion may be viewed as a physicochemical process, as chemical conditions will dictate the strength of bonding present and viscosity of the bentonite gel, with higher bond strength being able to withstand higher groundwater velocities. In the reference glacial cycle evaluated for the Forsmark site in Sweden, the buffer is exposed to glacial meltwater for 30,000 years (SKB 2011, Vol II).

Greenland Natural Analogue Project (GAP)

A joint project between Finland, Sweden and Canada is currently underway in order to better understand the potential ramifications of a period of glaciation on a GDF. A large degree of uncertainty regarding future groundwater compositions exists and as a result, a glacier in Greenland is currently under scrutiny as part of The Greenland Natural Analogue Project (GAP). In GAP, sub horizontal boreholes are being drilled under the glacier in order to gain an insight into the way in which glacial melt water and the existing groundwater system interacts.

3.8.4 Previous research in to chemical erosion of bentonite buffer.

Chemical erosion studies to gain an appreciation of the interactions between different bentonites and groundwater chemistries have been undertaken over a variety of scales. In

order to understand the generation and stability of bentonite colloids in various synthetic groundwaters (for example Missana et al 2003, Baik et al 2007, Jansson 2009 etc.), the effects of pH and temperature change on colloidal behaviour (Garcia-Garcia 2010) and to establish the CCCs of specific cations in solution for various montmorillonites (Jansson 2009).

This work has underpinned bentonite microstructure and colloidal behaviour theory in a number of ways. For instance, the concentration of divalent Ca^{2+} ions in solution has been found to be critical in preventing colloid formation. Jansson (2009) found that for sodium montmorillonite, 1-2mM of Ca^{2+} ions prevented dispersion. The concentration of Na^+ ions required in solution to prevent dispersion for the same clay was 100 times higher. The safety criteria set by SKB in their 2011 safety case application for based on such work is that no erosion of buffer shall occur for a groundwater total dissolved solids concentration of >4mM (SKB 2011).

Artificial fracture experiments

Considerable work has also been undertaken in order to simulate the process of bentonite expansion into a fracture intersecting a deposition hole and subsequent erosion by dilute groundwater (Figure 3.19a) (Jansson 2009, Vilks and Miller 2010, Matsumoto and Fujita 2011, Schatz et al 2012). This work has been undertaken almost exclusively around the same experimental design premise of a compacted bentonite pellet housed in a plexiglass flow cell. The pellet is intersected at its midpoint by a slit, designed to act as a fracture aperture, as detailed in Figure 3.19b.
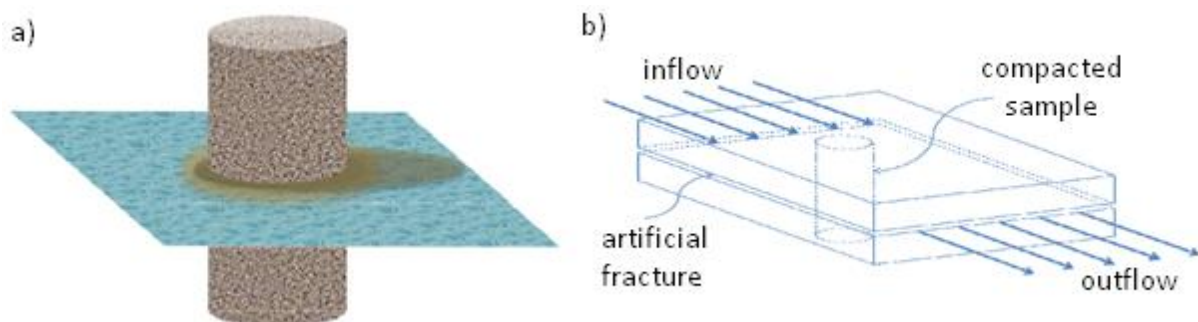

Figure 3.19: Conceptual model of buffer erosion from a fracture intersecting a deposition hole. b) Experimental design. Adapted from Schatz et al (2013).

Vilks and Miller (2010) examined bentonite expansion into fractures and erosion of various compositions of purified Na/Ca montmorillonite at a density of 2000kg/m^3 in both a uniform aperture artificial fracture and a natural fracture of variable aperture in a quarried block of granite. They studied the effects of both stagnant and flowing conditions, solution chemistry, fracture aperture and inclination. They found that results from the synthetic fracture correlated well with those of the natural fracture, providing supporting evidence for the viability of artificial fracture tests. The study found colloid generation and bentonite erosion were significantly higher with deionised water than with solutions containing millimolar concentrations of dissolved salts.

Schatz et al (2013) examined the extrusion behaviour and erosion rates of purified montmorillonites of various compositions with respect to Na/Ca content in an artificial, smooth walled fracture system with a 1mm aperture. This work was undertaken with a variety of solution chemistries and velocities and found purified Na and 50/50 Ca/Na montmorillonite to be erosive at solution chemistries of ≤ 0.25g/l NaCl. Erosion rates also correlated well with fluid velocities under the most dilute conditions of solution chemistry.

The work has also demonstrated that calcium bentonite exhibits little to no colloid formation in any type of groundwater until the proportion of sodium in exchange positions exceeds 20%, at which point the clay starts to behave like a sodium bentonite. A key point to consider is that, should the concentrations of Ca^{2+} ions in the saturating groundwater be sufficiently low as to facilitate unfavourable exchange reactions with the buffer during saturation, it could be foreseen that the bentonite may become more susceptible to erosion on later intrusion of dilute water.

Matsumoto and Fujita (2011) refined the experiment described in Figure 3.19, to incorporate a means to monitor the swelling pressure of the bentonite in the central compartment during the extrusion process into fractures of aperture 0.5, 1 and 1.5mm (Figure 3.20).
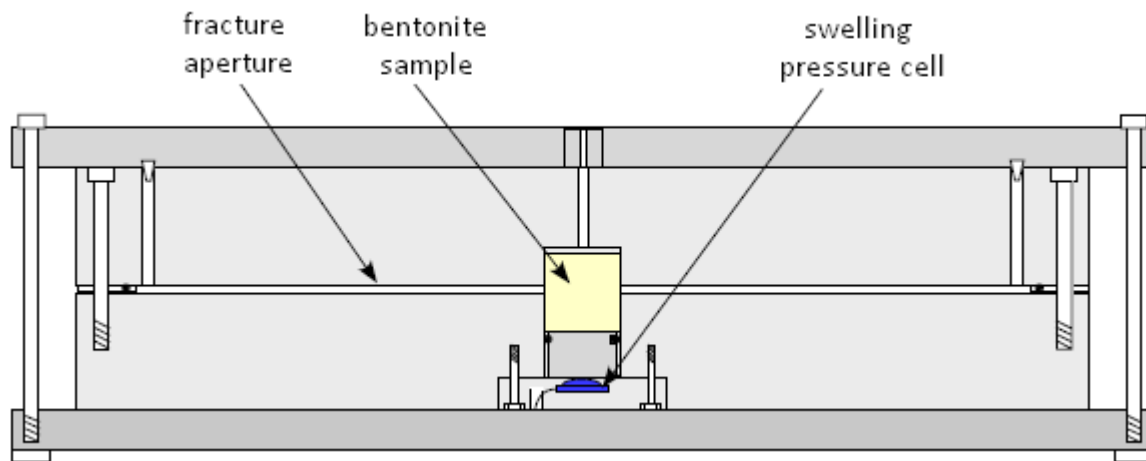
Figure 3.20: Erosion apparatus incorporating a device to monitor swelling pressure (Matsumoto and Fujita 2011).

Unfortunately, Matsumoto and Fujita (2011) is published in Japanese hence no definitive information on the quantitative aspects of erosion they examined can be drawn however, one aspect of this work which is consistent almost exclusively throughout the literature, is that the experiments use purified montmorillonite. The compacted montmorillonite is pre-prepared with various proportions of Ca^{2+} and Na^+ in exchange positions. In reality, and as mentioned previously, a bentonite is most likely to be employed in raw, quarried form. There is variability in the properties of the constituents of bentonite and between different types as indicated in Figure 3.9. Additional experimental limitations worth noting are that the plexiglass fractures do not provide the same frictional resistance to swelling as a natural fracture and the apertures investigated to-date are large in relation to the average size of aperture one might expect in a deposition hole.

Filter cake formation

One phenomenon, postulated as a result of observations from the limited erosion research on MX80 in synthetic fractures has been the filtering of clay colloids in the detrital material (commonly referred to as 'accessory minerals' in the literature) contained within the bentonite. For instance, Neretnieks et al (2009), in synthetic fracture glass slit tests, inferred that as the clay expands, the accessory minerals are transported with it, then as the gel density decreases, the detrital material remains at the gel/sol interface forming a potential filter cake. Similarly, Jansson (2009) observed in artificial fracture plexiglass tests, a dark rim of accessory minerals (mainly feldspar) evident at the gel/sol interface. There has, however,

been limited subsequent research to analyse the rate of filter cake formation and determine its effect on bentonite erosion (Apted et al 2010). Schatz & Kanerva (2012) investigated the formation of accessory mineral filter beds by the addition of various accessory minerals to purified montmorillonite but found no reduction of mass loss from the system upon deposition of these minerals at the extrusion / erosion interface.

Pre-formed filter experiments

Building on these observations, Richards & Neretnieks (2010) conducted a series of experiments to gain a better understanding of the potential for colloid filtration using pre-compacted beds of various accessory minerals. They found that kaolin filter beds exhibited some potential, though the experimental conditions of their preformed filter cakes and the pressure gradient placed across them, weren't representative of repository conditions.

Work on the filtration of montmorillonite colloids has also been undertaken by Birgersson et al (2009) using various metal porous discs from 0.2 to 100 μm pore size in combination with fillers such as kaolinite in a test cell with deionised water as circulating fluid. They revealed a pore size of <0.5 μm stopped colloid release for homoionic sodium montmorillonite and pore size <100 μm (largest tested) stopped colloid release for homoionic calcium montmorillonite. Although results from fillers weren't conclusive they also revealed the potential for material with a grain size of <10 μm to be used as colloid filters.

The above work highlights the possibility of utilising natural filtration to prevent erosion from buffer expansion into fractures by the formation of a filter cake within the fracture or indeed by the prevention of colloid transport into fractures during the saturation phase by the mechanism of arch formation over the fracture's opening, as depicted in Figure 3.21. This latter research also raises the possibility of installed filters, providing they don't impair the wider functionality of the bentonite buffer.
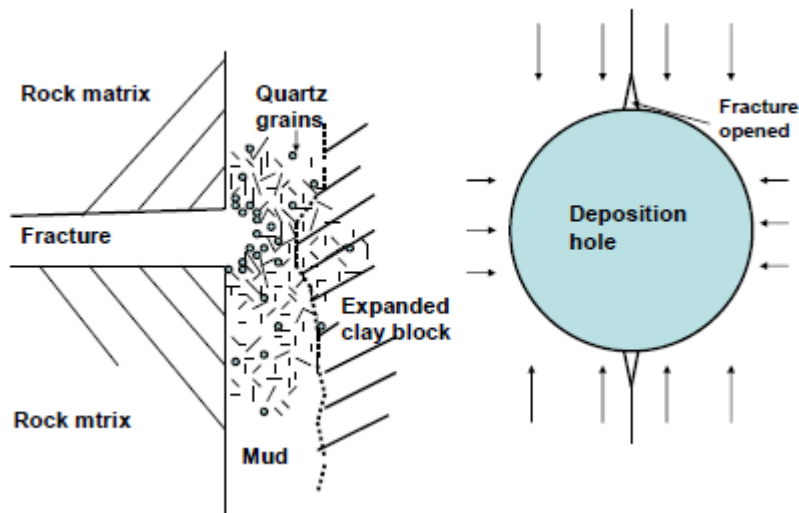
Figure 3.21: Detritus forming a filter arch over a transmissive fracture (Wilson et al 2011).

3.9 Quantitative assessment of buffer erosion in SKB's safety case.

Following from the above research and specifically that of Birgersson et al (2009), and assuming that when equilibrated with groundwater the buffer will have a Ca^{2+} concentration of ≥ 20% in exchange positions; SKB have established a groundwater ionic strength of 4 mM charge equivalents, above which chemical erosion of buffer can be neglected. The possibility of a small number of deposition holes experiencing conditions more dilute than this, due to glacial melt water intrusion, cannot be ruled out however. As such, in the safety case currently under review, SKB have included a quantitative model to evaluate buffer erosion from a fracture intersecting a deposition hole. The model was developed by Neretnieks et al (2009) and incorporates much of the theory laid out earlier in this chapter. The model is based on the buffer comprising 100% purified sodium montmorillonite depleted of Ca^{2+} ions, contacted with a saturating solution of concentration < 4 mM. The swelling process of the montmorillonite into the fractures is calculated using DLVO theory, by adapting a force-balance model for spherical colloids to the parallel flat charged surfaces of montmorillonite layers. The model of swelling was calibrated using bentonite free swelling tests. This swelling model is then combined with a viscosity model for the repulsive montmorillonite sol at the edge of the extruded material and the Darcy equation for two dimensional flow in a planar fracture at the groundwater/ sol interface, where the sol concentration is sufficiently low as to facilitate erosion. The montmorillonite release rate is calculated as:

$$R_{Erosion} = A \times \delta \times v^{0.41}$$

Where: $R_{Erosion}$ = release rate (kg/year), A = constant 27.2, δ = fracture aperture (m) and v = groundwater velocity (metres/year). The assessment does allude to the possibility that erosion may be mitigated by the presence of accessory minerals, though the mechanism is not accommodated in the quantitative calculations (SKB 2011, vol II) due to a lack of empirical data demonstrating under what conditions it occurs. Example calculations of the application of the model to a 1mm fracture aperture detailed are reproduced in Table 3.2.

Water velocity, [m/yr]	Smectite release for 1 mm fracture aperture, [g/yr]	Penetration into the fracture at the centre, [m]
0.10	11	34.6
0.32	16	18.5
0.95	26	11.5
3.15	43	7.0
31.50	117	2.1
315.00	292	0.5

Table 3.2: Montmorillonite erosion rates from a 1mm fracture aperture intersecting a deposition hole (Neretnieks et al 2009)

SKB's safety criterion dictates that a loss of 1,200kg of montmorillonite from a deposition hole is sufficient to drop the dry density of the buffer to the point where advective flow conditions are induced (SKB 2011, Vol III). Thus negating its function as a diffusive barrier. Considering a period in which the buffer is subjected to 30,000 years of exposure to dilute glacial melt water, this equates to a loss of only 40g of buffer per year over that time period, neglecting subsequent glacial cycles. To put this into perspective, this is the equivalent of the weight of 1/2 an apple every year from approximately 20 tonnes of buffer. Given that the release rates detailed in Table 3.2 are for a single fracture intersecting a deposition hole, very low rates of buffer erosion may prove an issue, since in reality multiple transmissive fractures will intersect a single hole. For example, Figure 3.22 shows a map of transmissive, water bearing fractures (dark lines) in a test deposition hole at 420m depth at the at the Äspö URL in Sweden.

Figure 3.22: Geological mapping of the deposition hole DA3147G01 in Äspö. Drilled for a large scale gas injection test (LASGIT). Cuss et al (2010)

3.10 Need for further research

It is apparent from the research presented in this chapter that the current quantitative approach to assessing buffer loss, combined with the effect of multiple glacial cycles and multiple fractures intersecting individual deposition holes, may lead to predictions of unacceptable mass loss in some areas of the repository. The current model, however, is highly conservative, since it is based on 100% purified Na^+ montmorillonite and uses 1mm fracture apertures that are far higher than those likely to be permitted to intersect the deposition holes.

As a consequence, to be confident that erosion rates are in fact acceptable, a better understanding of the erosion behaviour of *as delivered* MX80 bentonite would be very valuable. Indeed, SKB concede directly:

''As mentioned in the reference evolution, the buffer colloid release/erosion process is poorly understood and leads already in the reference evolution to loss of buffer mass to the extent that advection cannot be ruled out for a few deposition holes during the first glacial cycle.'' (SKB 2011, Vol III)

Further to this, and as described in the introductory chapter to this thesis, an international peer review team working on behalf of SSM and appointed by the Organisation for Economic Co-operation and Development (OECD), conducted a preliminary review in 2012 into SKB's 2011 safety case application, *Long-term safety for the final repository for spent nuclear fuel at Forsmark*. While the review team commended the overall competency of SKB in demonstrating the safety of their concept for a repository, one area which was deemed to be insufficiently understood was the erosion of bentonite buffer.

3.10.1 Thesis aims and objectives

The aims and objectives to be addressed within this PhD thesis in relation to the erosion of bentonite buffer material were thus structured around these concerns and the previous research in the field of bentonite buffer erosion outlined in this chapter. These were constructed with a view to understanding the mechanisms that control the erosion of MX80 buffer material, specifically to:

- Determine the effect of the presence of inherently present impurities or 'accessory minerals' within MX80 bentonite and the effect they have on the erosion rate of the buffer from a fracture intersecting a deposition hole for disposal concepts in fractured crystalline rock.
- Investigate the effect of fracture aperture variability on the erosion process of MX80 buffer material from a fracture intersecting a deposition hole.

Chapter 4 Methodology

This chapter outlines the stepwise process which was undertaken for each of the experiments undertaken. Specifically, the manufacture of each piece of experimental apparatus, sample preparation, the experimental procedure and data acquisition and processing.

4.1 Materials

Two materials were procured for the purpose of these tests. One raw, quarried bentonite in MX80 (including accessory minerals) and one processed, sodium bentonite in Nanocor-PGN (devoid of accessory minerals).

4.1.1 MX80

MX80 bentonite was chosen as the material which would be tested: it is the reference material for both the Swedish and Finnish radioactive waste disposal organisations and there exists a wealth of research which has been undertaken on MX80 in the context of the KBS-3 disposal concept. MX80 is distributed by Cetco minerals in the UK and 50kg was procured from this distributor. Upon receipt, it was characterised in terms of its water content, Atterberg (liquid and plastic) limits and particle size distribution to establish its parameters in relation to Posiva and SKB bentonite buffer acceptance standards (Kiviranta and Kumpulainen 2011). British standard methods were used for each of the above tests. The material was also subject to XRD analysis, as shall be discussed in section 5.1.2.

A supplementary method was also used for determination of the liquid limit, as set forth in Kiviranta and Kumpulainen (2011). This method differs slightly from the British standard in that, in Kiviranta and Kumpulainen's method, samples are prepared 24 hours in advance, prior to cone penetration testing. I.e. samples are prepared at 5 water contents, placed in cups and the cups sealed and left for 24 hours. Each cup containing a sample is then subject to the British standard method of cone penetration testing. Penetration depth is plotted against water content for each dish and the liquid limit is given as the water content corresponding to 20mm penetration depth. This method produces a higher estimation of liquid limit than the British standard method due to the increase in shear strength of bentonite that occurs with ageing.

4.1.2 Nanocor-PGN

Nanocor PGN, a commercially available sodium montmorillonite, was procured from B+Tech research consultants in Finland, who have extensive experience in testing the erosion characteristics of montmorillonite. The extraction of montmorillonite from MX80 and homoionisation (replacing all interlayer cations with a single cation) to a pure sodium montmorillonite is a labour intensive process and, having tested both purified montmorillonite from MX80 and Nanocor PGN side-by-side, B+Tech found the erosion characteristics of either material to be similar. Hence Nanocor PGN is employed as a proxy for purified montmorillonite from MX80 in their tests conducted on behalf of Posiva, and indeed as a benchmark material to assess the erosion characteristics of sodium montmorillonite in the European wide project BELBaR (Bentonite Erosion: effects on the Long term performance of the engineered Barrier and Radionuclide transport). A BELBaR benchmark test was also undertaken as part of this thesis, data for which is presented in the appendix, and the results of which are discussed briefly in the discussion chapter of this thesis. No characterisation of the geotechnical parameters of this material were undertaken, as it was procured directly from researchers undertaking tests against which the work undertaken in this thesis would be compared. It was however subject to XRD analysis, which shall be discussed in section 4.7.

4.2 Experimental apparatus

To examine the effect of aperture variability on the extrusion and erosion behaviour of buffer into a fracture intersecting a deposition hole it was decided that, if possible, a fracture with a naturally varying aperture profile would be deployed. Contact was made with numerous granite suppliers with a view to using their waste material for this purpose. Kay's of Scotland, a curling stone manufacturer from Ayrshire was found to provide the most suitable material. Curling stones are manufactured from a micro granite sourced from Ailsa Craig, a volcanic plug off the west coast of Scotland. These stones are cored from granite slabs which have cleaved along natural fractures.

Any sections of core that contain natural fractures (Figure 4.1) are not suitable as curling stones and are, hence, considered as waste by the manufacturer. As a consequence, a stone was procured free of charge, which was selected to have a fracture which, when subject to mechanical force, would split resulting in a suitably large planar rough fracture face surface.
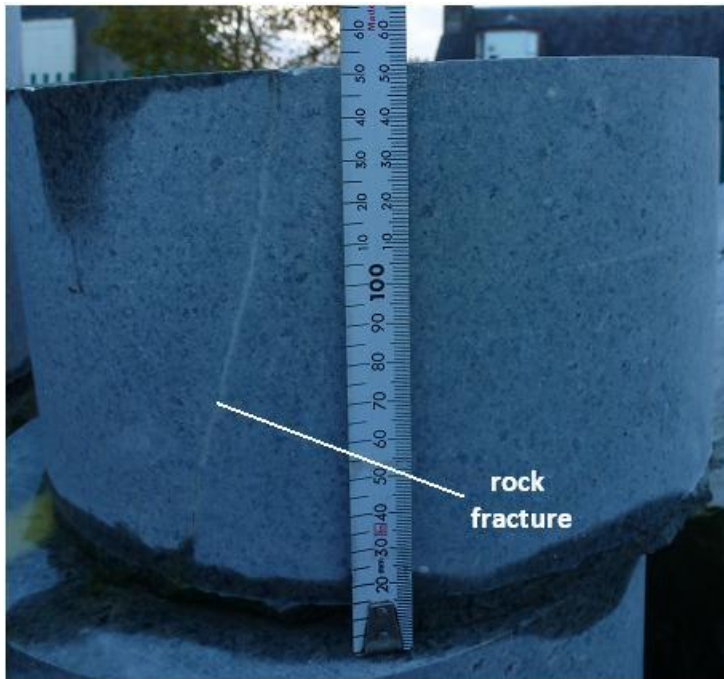
Figure 4.1: Image of curling stone with fracture and some mineral infill.

From this surface, a mould could be taken using clear, rigid, two-part epoxy resin (ABL Stevens resin supplies). Many experimental set-ups were considered prior to settling on one which bears some resemblance to experimental apparatus previously employed by Matsumoto & Fujita (2009), Vilks &Miller (2010) and Schatz et al (2013).

Figure 4.2 depicts this apparatus in which a compacted bentonite specimen, 2cm in diameter and 1cm in height is installed at the centre of a 26cm diameter flow cell, intersected at its midpoint by the fracture aperture. In line with previous work, this apparatus is designed to mimic a fracture intersecting a deposition hole in the KBS-3V concept. The sample has been illustrated larger relative to the cell geometry in Figure 4.2 for illustration purposes.
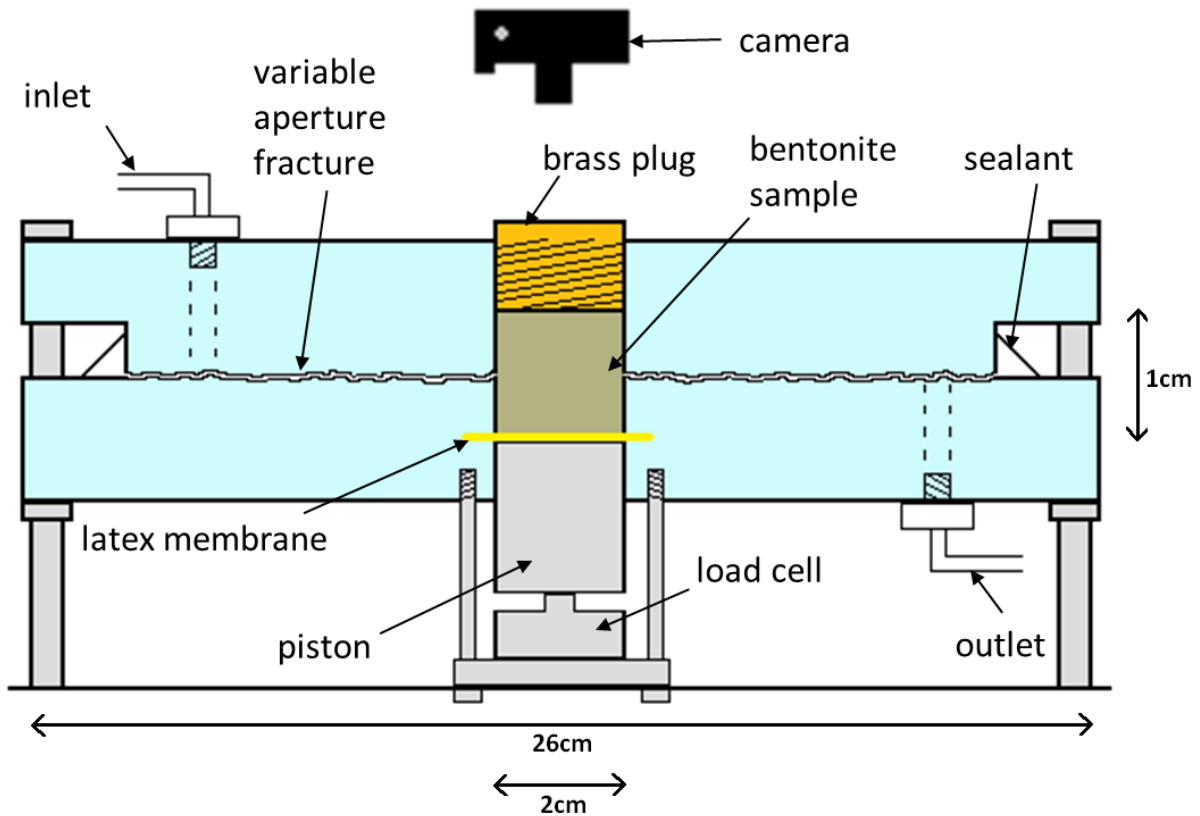
Figure 4.2: Vertical cross section of experimental design.

4.2.1 The fracture moulding process

A 26 cm diameter fracture flow cell (Figure 4.2), was constructed using moulds taken from the granite fracture face. The methodology for the process was as follows:

a) The natural fracture running through the curling stone was propped up horizontally. The level was checked in the North-South and East-West directions with a spirit level. As detailed in Figure 4.3.

b) A cylindrical mould, 26cm in diameter, was placed on top of the fracture and the interface between fracture and mould was sealed from the outside with a bead of silicone.

c) The fracture surface and inside surface of the mould were then coated with PVA release agent. Applied in a thin coat with the aid of a paint brush.
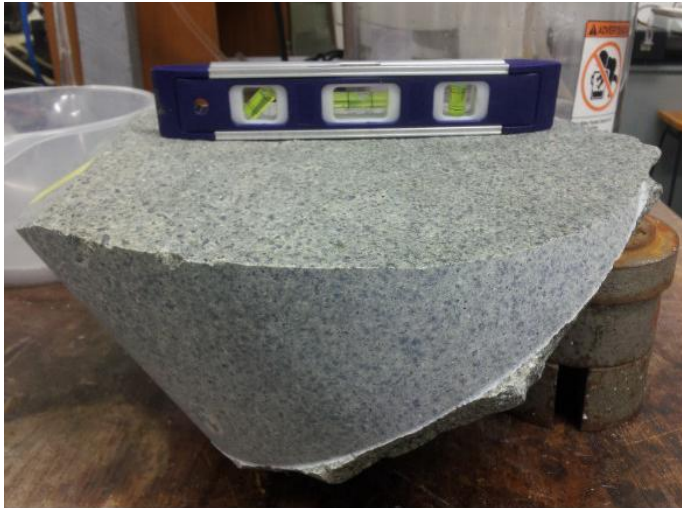
Figure 4.3: Levelling of fracture face.

d) The quantity of resin and hardener required to cast a fracture surface 26cm in diameter with an average thickness of 2cm was calculated as follows:

$$\rho_{hardener} = 1012\frac{kg}{m^3} \qquad\qquad \rho_{resin} = 1154\frac{kg}{m^3}$$

$$From\ manufacturer: 45g\ of\ hardener\ to\ 100g\ of\ resin$$

$$\therefore \rho_{mix} = 1154 * \frac{100}{145} + 1012 * \frac{45}{145} = 1109\frac{kg}{m^3}$$

$$Volume\ of\ fracture\ face = \pi * 0.13^2 * 0.02$$

$$= 0.00106m^3$$

$$Mass\ of\ fracture\ face = 0.00106m^3 * 1109\frac{kg}{m^3} = 1.177kg$$

$$\therefore Mass\ of\ resin = 1.177 * \frac{100}{145} = 0.811kg$$

$$\therefore Mass\ of\ hardener = 1.177 * \frac{45}{145} = 0.365kg$$

e) A glass beaker was placed on weighing scales and the scales tared. 0.365kg of hardener was then poured into the beaker.

f) The scale was tared again and 0.811kg of resin was poured into the beaker.

g) The mix was then thoroughly stirred manually beneath a fume hood to remove any streakiness and ensure a homogenous mix.

h) The mix was then poured into the mould on the granite fracture and allowed to cure for 3 days (Figure 4.4).

Figure 4.4: Resin curing in mould.

i) Once cured the cylindrical mould was released from the fracture face to leave the cured resin attached to the fracture surface as depicted in Figure 4.5:
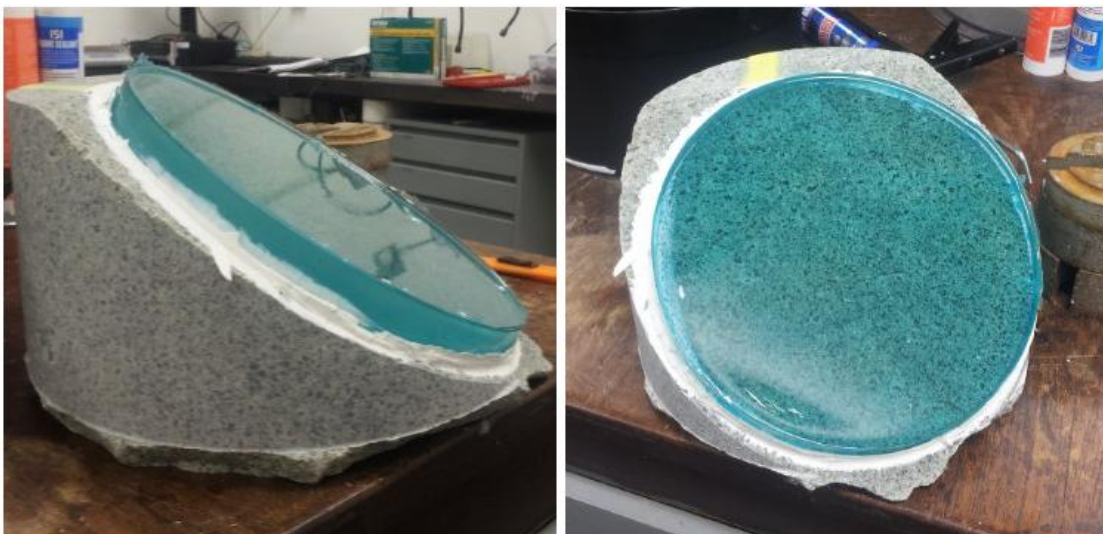
Figure 4.5: Cured resin attached to fracture face.

j) The resin was then prized from the fracture face by gently tapping at the resin/fracture interface with a hammer and chisel around the circumference of the resin until released.

k) The resin and granite fracture faces and the inside of the mould were then washed to remove all PVA release agent.

l) The resultant resin fracture face was placed fracture side up in the same mould and the interface between the mould and fracture was sealed with a silicone bead.

m) A silicone ring, 1.5cm by 1cm, was placed inside the mould around the circumference of the face to be cast.

n) Steps *c)* to *k)* were then repeated.

o) The silicone ring was removed from the fracture face with a safety knife to create a sealant gap.

p) 1/8" NPT threaded water inlet holes were then drilled and tapped in the top plate at 12 and 3 o'clock and effluent outlet holes in the underside of the bottom plate at 6 and 9 o'clock.

4.2.2 Manufacture of the flow-cell.

This fracture moulding process resulted in two epoxy resin plates, each 2 cm thick with complementary rough fracture faces which, when joined together, form a perfect union. From the resulting fracture faces, a flow cell was manufactured. This was achieved by the following methodology:

a) Blanks were screwed into the inlet and outlet ports of the two fracture plates before immersing the plates in water in a deep sink, ensuring no air bubbles were trapped between two. The top plate was then rotated through a fine degree, such that the directionality of features specific to the fracture were retained whilst creating a small hydraulic aperture. The two plates were secured in this position under water by clamps.

b) The sealant gap was then filled with *Evo-Stik serious stuff wet grab waterproof adhesive,* capable of curing under water.

c) Once the adhesive had set, the fracture - now filled with water- was moved to the bench and the inlet port was connected to deionised water source via an *Ismatec* peristaltic pump and a 0.79mm internal diameter flexible *EFL Tygon* tube. The same tubing was connected to the outlet port.

d) Standpipes off the inlet and outlet lines via T-pieces were attached to the wall.

e) The flow paths through the fracture cell were imaged using an overhead camera by carrying out a dye injection test. The flow area was then converted into an equivalent rectangular area of width, W and length, L to determine the equivalent hydraulic aperture:

f) The hydraulic aperture of the fracture was determined by pumping water through at a constant flow rate and measuring the drop in pressure across the flow cell using the standpipes:

$$Q = \frac{W\rho g b^3 \Delta h}{12 \mu L}$$

$Where: W = width\ of\ flow\ zone$

$\rho = density\ of\ water$

$g = acceleration\ due\ to\ gravity$

$b = fracture\ hydraulic\ aperture$

$Q = volumetric\ flowrate$

$\Delta h = head\ difference\ across\ system$

$\mu = viscosity\ of\ water$

$L = length\ of\ flow\ zone$

The standpipes were not positioned directly at the inlet and outlet ports of the cell, but were at some distance along the inlet and outlet pipes. In order to calculate the head loss between the standpipes and the inlet and outlet ports, and thus the actual drop in head

across the cell, the Hagen–Poiseuille equation for pressure drop in a fluid under laminar flow conditions, flowing through a cylindrical pipe of constant cross section was employed:

$$\Delta P = \frac{8\mu L Q}{\pi r^4}$$

$Where: \Delta P = pressure\ drop$

$\mu = viscosity\ of\ water$

$L = length\ of\ pipe$

$Q = volumetric\ flowrate$

$r = radius\ of\ pipe$

As $$P = \rho g h$$

and

$$Q = \frac{u}{cross\ sectional\ area}$$

head loss in the pipe,

$$h = \frac{32\mu L u}{\rho g d^2}$$

g) In the event that the fracture hydraulic aperture was too large i.e. > 0.1mm, steps a) to e) were repeated with a finer rotation of the plates, until a suitable experimental aperture was obtained.

h) Once a suitable fracture aperture i.e. ≤ 0.1mm had been determined, evenly-spaced holes were drilled through the sealant gap around the circumference of the fracture to accommodate bolts, ultimately locking the fracture in place at this aperture.

i) The fracture was then dismantled and cleaned of all silicone with a safety knife.

j) The fracture was then reassembled with the bolts in place and a hole drilled completely through the centre of both plates using a 19mm drill bit.

k) The plates were then dismantled once again and the hole in the centre of the top plate was threaded through.

l) On the underside of the bottom plate, a recess 40mm in diameter was milled concentrically over the initial hole in the centre of the plate, stopping 5mm from the fracture face.

m) A 40mm diameter piece of latex triaxial cell membrane (Figure 4.6) was cut and glued into the circular recess using *Evo-Stik serious stuff wet grab* waterproof adhesive.
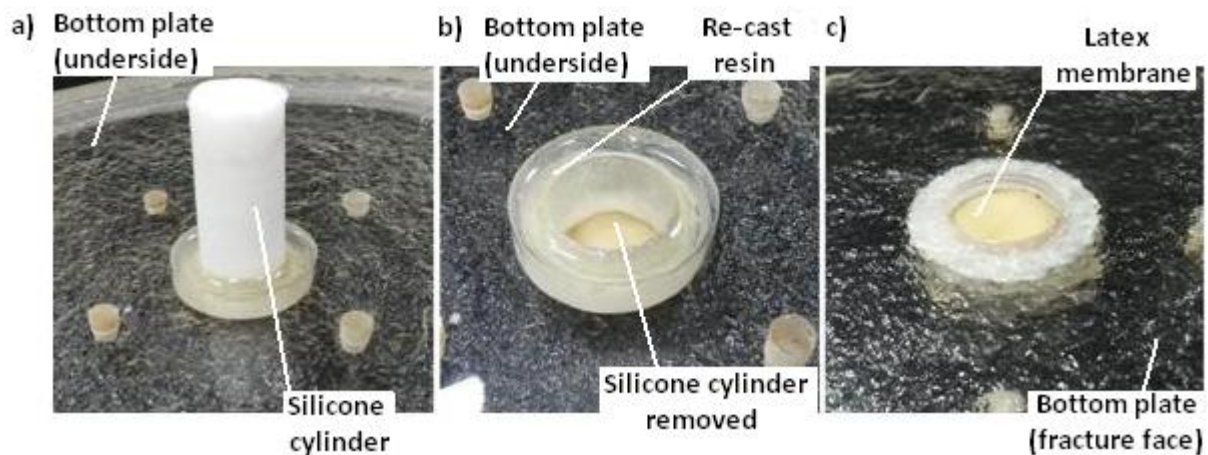
Figure 4.6: Images of central compartment to house sample, from underside and fracture side.

n) Once the adhesive had set, a 19mm diameter cylinder of RTV silicone, which had been cast from the mould used to make the bentonite pellets, was placed in the recess on top of the membrane, directly over the 19mm diameter hole still present beneath the membrane (Figure 4.6a). A thin smear of *Vaseline* was placed on the face of the silicone cylinder in contact with the latex membrane to prevent any ingress of clear rigid epoxy resin between the two.

o) The recess which was milled in j) was then recast around the silicone cylinder using clear rigid epoxy resin.

p) Once the resin had cured the silicone cylinder was removed and the resultant recess cleaned of any *Vaseline* or excess resin. This process, and the resultant compartment, are depicted in Figure 4.6.

q) A 70mm x 70mm square, 5mm thick steel plate was cut to accommodate an *Omega* LCM-302 2kN button load cell to be mounted on the underside of the bottom plate. 5mm diameter holes were drilled at the 4 corners of the plate and a 20mm diameter,

1mm deep recess cut in to the centre of the plate to provide a seat in which the 20mm diameter load cell would reside (Figure 4.7).
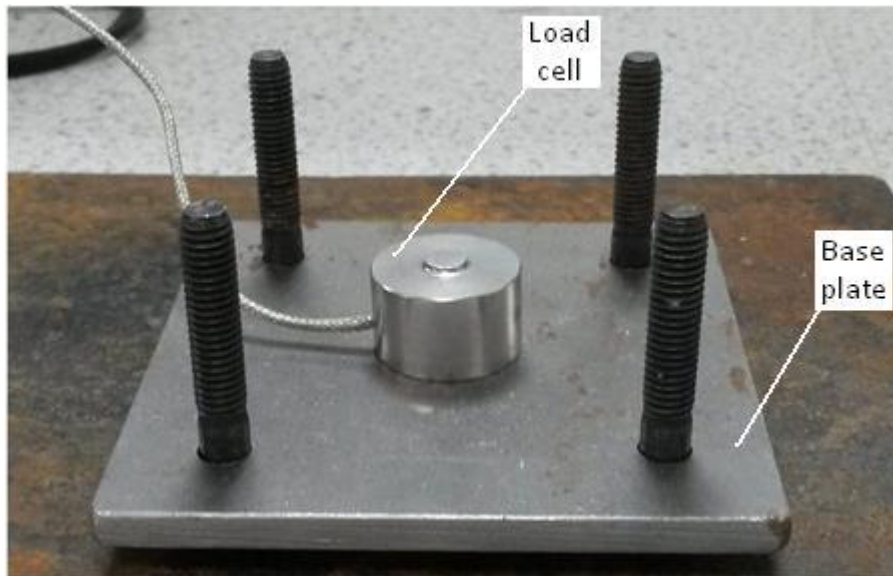
Figure 4.7: Base plate housing load cell and screws to attach to underside of fracture cell.

r) The steel plate was then placed centrally over the hole on the underside of the resin cast and 4 holes drilled through the holes at each corner of the plate into the resin. The drill holes in the resin were then threaded to attach the steel plate to the underside of the resin.

It should be noted that the hydraulic aperture of the fracture is not the same as the physical aperture. This is due to a number of factors. First, the surface is rough, and as a consequence, the flow lines may not follow all the surface indentations, resulting in regions of no-flow within indentations in the fracture surface. Second, the plates, when considered at a large scale, may not be flat; they are bolted together a four points around the perimeter, which may produce a flexure of the whole system. Third, the rough rock surface from which the plates were cast may have had a larger scale trend i.e. it may not have been approximately planar and flat. Indeed, upon inspection of the fracture cell after the casting process, there appeared to be a discernible bow in the fracture surface, i.e. it wasn't entirely planar. Finally, the inflow streamlines are not parallel, due to the presence of a point inflow and outflow, which means that the whole area of the plate is not subject to the same head

gradient, whereas the parallel plate law assumes it is. Hence the hydraulic aperture represents the equivalent aperture of a pair or parallel plates that would produce the same flow rate under the same head difference, in a one-directional system, with straight, parallel flow lines.

Complimentary to the calculation of hydraulic aperture, the original granite rock fracture was scanned using a *scan control, micro-epsilon 2700-100* laser scanner and the data processed using *imagej* software to reveal a standard deviation of 169 µm in the roughness of the fracture surface. Taking this into account and the points mentioned previously, it is the opinion of the author that the physical fracture aperture was more in line with this figure.

4.3 Sample preparation

For the purpose of manufacturing bentonite samples to be installed in the apparatus, SKB and Posiva reference buffer design literature were consulted. Both prescribe a compaction pressure of 100MPa as being required to compact buffer discs and rings, at 17 $^+/_-$ 1% water content, to the required bulk density. It was found however, after repeated trial and error with various masses of sample and compaction pressures, that 5.86 grams of material compacted to a load of 8kN resulted in a pellet of approximate dimensions 10mm height by 20 mm $\emptyset$ and a bulk density of 2000 $^+/_-$ 50kg/m^3. In accordance with SKB's buffer design standards of 2000 $^+/_-$ 20 kg/m^3 for disc blocks and 2070 $^+/_-$ 20 kg/m^3 for ring blocks (SKB 2011 Vol I).

This equated to a compaction pressure of approximately 28 MPa. It is thought that the reduced compaction pressure required may be attributable to scaling effects. As the 100MPa compaction pressure is prescribed for samples 1.5m in diameter and 500mm in height. Compaction equipment, specifically a mould and 3-part ram, were specially manufactured for this purpose and are detailed in Figure 4.8.

Figure 4.8: Specially manufactured compaction ram and mould.

It was apparent post compaction that some material remained inside the mould. The methodology for preparing the pellets is as follows:

a) 1kg of Cetco MX80 bentonite, initial water content 12%, is made up to 17 $^+/_-$ 1 % water in accordance with Posiva's initial reference buffer design (Juvankoski et al 2012).

<div style="display: flex; justify-content: space-between;">

i. <u>12% water</u>

$$w = \frac{m_w}{m_s} = 0.12$$

$$m_w + m_s = m_T = 1$$

$$\therefore 0.12 = \frac{m_w}{1 - m_w}$$

$$\therefore m_w = 0.11 kg$$

$$\therefore m_s = 0.89 kg$$

<u>17% water</u>

$$w = \frac{m_w}{m_s} = 0.17$$

$$\therefore \frac{m_w}{0.89} = 0.17$$

$$\therefore m_w = 0.151$$

$$Difference = 0.151 - 0.1$$

$$= 0.041 kg \ of \ water \ to \ add$$

</div>

b) 1 kg of as delivered MX80 was placed in a metal tray on weighing scales and the scales tared.

c) 0.041kg of water was added with the aid of a spray gun in 10g increments in order to bring the water content of the as delivered material up from 12% to 17%.

d) Upon the addition of each 10g increment of water, the bentonite wetted at the top of the sample appears to form a 'wetted mat' on top of the drier sample. Therefore, between each 10 g step, the bentonite is thoroughly mixed with two steel spatulas, working the water into the bentonite to ensure a homogenous mix.

e) The prepared material is stored in a vacuum sealed plastic bag ready for use.

f) 5.86g of the prepared material was weighed into an aluminium mould, ≈ 19.2 mm internal diameter. A specially manufactured ram was then placed inside the mould on top of the sample.

g) The apparatus containing the sample was then mounted on to a 50kN Wykeham Farrance 50kN loading frame and the platform raised until the compaction ram contacted the load button of a 50kN 'S' type load cell (Figure 4.9).
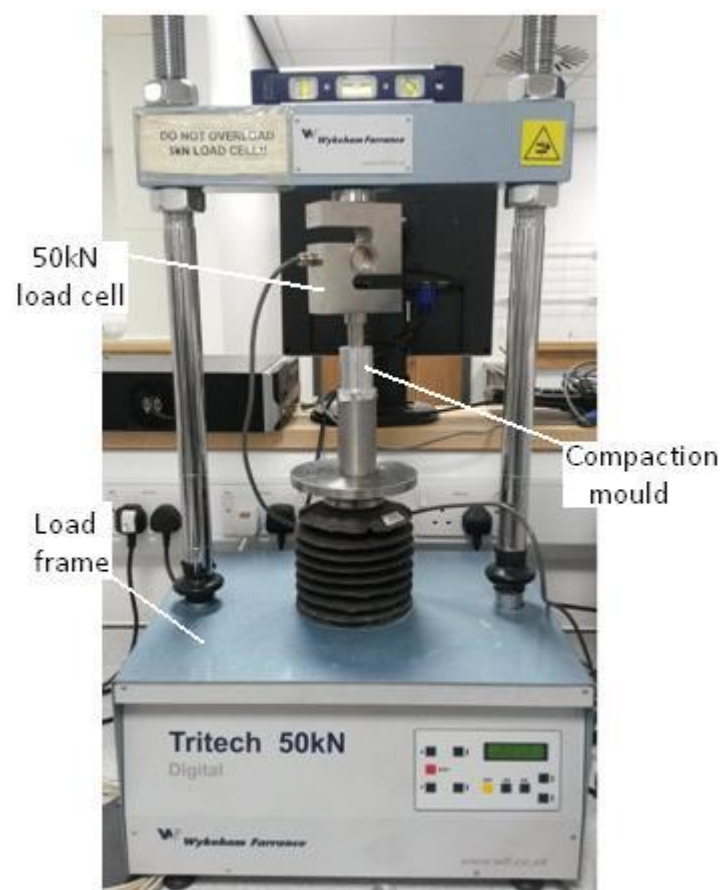
Figure 4.9: Loading frame and sample under compaction.

h) The loading frame was set to load the sample at a rate of 0.25mm/min, the time was noted and the machine set to run.

i) The sample was loaded to ≈ 8 kN, corresponding to ≈ 28 MPa compaction pressure.

$$Diameter = 0.0192m \qquad\qquad Pressure = \frac{Force}{Area}$$

$$Area = \frac{\pi * 0.0192^2}{4} = 0.000289m^2 \qquad = \frac{8000}{0.000289} = 27681661 \, Pa$$

j) Once unloaded, the sample was extruded from the mould at a rate of 0.5mm/min. This was achieved by propping the mould up and extruding the sample from the bottom.

k) Sample dimensions were then measured using digital Vernier callipers. Four measurements each of diameter and height were taken and the average calculated.

l) The water content was confirmed by oven drying a replica pellet (compacted under the same conditions and from the same sample) at 105°C for 24 hours.

m) The samples were then vacuum sealed in a plastic bag and all corresponding calculations of bulk density, dry density, etc. were performed.

Once prepared, the bentonite pellets had a diameter slightly larger than that of the central compartment in the fracture cell. Therefore, before a pellet could be installed in the fracture and the erosion experiment could commence, the diameter of the pellet had to be reduced. This was achieved by gently shaving the pellet around its circumference using a razor blade until it just passed through the top plate, at which point it was resealed in a vacuum bag.

4.4 Pre-test procedure

Prior to commencing the erosion test, a number of preparatory steps had to be undertaken as detailed below:

a) The fully machined, variable aperture fracture was immersed in water in a deep sink. Ensuring no air was trapped between the plates, the plates were screwed together via the bolt holes at the periphery and the plate was sealed using *Evo-Stik serious stuff wet grab waterproof adhesive.* Blanks were placed in the inlet and outlet ports and a brass plug used to seal the central compartment.

b) Once the adhesive had set, the fracture was moved to the bench and the inlet port was connected to a deionised water source via an Ismatec peristaltic pump and

0.79mm i.d. flexible *EFL Tygon* tubing. Deionised water was used as a proxy for dilute glacial melt water, in order to induce the most erosive conditions.

c) Tubing was also connected to the outlet port, running to a 2 litre conical flask to collect the effluent. The pump was set to run at a constant flow rate of 1ml/min. This flow rate corresponded to an average fluid velocity of approximately 0.5mm/s in the fracture, determined from a dye injection test using image analysis.

d) A pre-calibrated 2kN button load cell was mounted on the underside of the flow cell, in contact with the latex membrane via a 19mm diameter, 30mm long steel piston (Figure 4.10). The screws attaching the steel plate to the flow cell were adjusted to ensure the load cell wasn't placed under any stress prior to commencing the experiment whilst ensuring there was no slack to be taken by the piston upon the expansion of bentonite:
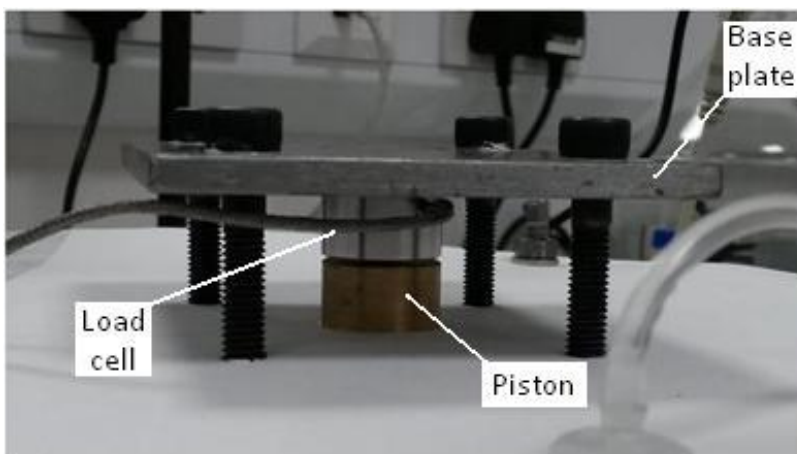
Figure 4.10: Underside of fracture cell showing load cell mounted on base plate and in contact with sample via piston.

e) The load cell was connected to a PC via *National Instruments* data acquisition hardware and *labview* software.

f) A *Nikon D3200* DSLR camera was mounted to a retort stand directly over the cell and controlled via the same PC using *candylabs videovelocity* image capture software

g) Before commencement of the erosion experiments, the radial extent of the flow pathways within the cell were once again imaged by dye injection and the elliptical area was converted into an equivalent rectangular area of width, W and length, L to determine the final equivalent hydraulic aperture.

4.5 Test procedure

The cell was now considered ready to begin the erosion experiment, according to the following methodology:

a) The brass plug was removed from the centre of the fracture cell and the bentonite sample from a) was gently pushed into the compartment in the centre of the cell until it was in contact with the latex membrane.

b) The compartment on top of the pellet was then filled with deionised water and the brass plug gently reinstalled in the cell until it was in contact with the bentonite pellet. This was discernible from the load cell registering a stress. The brass plug was then relaxed slightly so as not to have the bentonite sample under any mechanical stress and to ensure any load cell readings were solely due to swelling pressure generation.

c) No ptfe tape was used to seal the threads on the brass plug as it was found, through trial and error, that installing the brass plug slowly, without tape, allowed excess water to escape from the top of the sample, up through the threads during installation. The swelling pressure then generated by the sample ensured the plug sealed the compartment.

d) Upon reinstalling the brass plug, the time was noted and the erosion experiment was now considered to be underway. The camera was set to record an image every 30 minutes during the extrusion phase and every hour during the later stages of the experiment.

e) The effluent bottle was changed approximately every 24 hours with the time noted at the exact point of change. Upon changing the effluent bottle, it was weighed and the effluent outflow rate calculated over the 24 hour period as the volume of water collected/time period.

f) The effluent was then set to filter through a 47mm diameter, 0.2μm pore size *Whatman Nuclepore* filter paper. The filter paper had been oven dried at 105°C for 24 hours and weighed prior to filtration and was subject to the same drying process and weighing post-filtration. The mass of eroded bentonite could then be calculated for the 24 hour period, as could the average effluent solids concentration over the period and the mass loss rate. The erosion rate was for the 24 hour period was scaled and evaluated in terms of grams/year of buffer material eroded.

g) A 50ml sample of each filtrate was kept for Ion Chromatography analysis and each filtrand was also kept for mineralogical analysis.

h) The flow-through erosion experiment was terminated when no appreciable difference in sample extrusion was visually observed and the erosion of material from the fracture had ceased.

4.6 Termination procedure

a) Inlet and outlet ports were removed from the cell and the bead of sealant in the sealant gap was opened with a safety knife, the fracture was then left for a period of 2 weeks to allow water to evaporate from the cell and the sample. This was to minimise disturbance of the sample when separating the fracture plates.

b) When all water had evaporated from the cell, the bolts holding the cell together were removed and the top half of the cell carefully removed in order to cause minimal disturbance to the sample

c) For the purpose of post-test analysis, the fracture face was then sampled at various points of interest, I.e. points at which discernible changes in colour were apparent indicating deposition of specific minerals in different regions of the fracture face or potential changes in mineralogy.

d) Each sample was then subject to X-Ray Diffraction analysis to determine its mineralogy and optical microscopy in order to evaluate grain size and morphology.

4.7 XRD analyses.

To determine the differences in the mineralogy of those phases deposited on the fracture face to those initially installed in the cell and those eroding - XRD analysis was undertaken on a*s delivered* MX80 material, Nanocor PGN material, material isolated in section 4.6 and the eroded material filtered from the effluent of the cell.

A Bruker D8 advance XRD machine was used for the evaluation of the samples and the data analysed using *diffrac.eva* evaluation software. All samples were evaluated using a copper X-Ray source at a wavelength of 1.5406 Å, using a 0.6mm slit in Goebel mirror mode. Samples were scanned from 2 to 70° 2θ, using 0.02° counting steps at 1 second / step.

4.7.1 *'As-delivered'* material

In the case of the *as delivered* MX80 and Nanocor PGN material, and accessory minerals isolated from MX80, the sample holder was filled in the conventional manner, as depicted in Figure 4.11:

Figure 4.11: Sample holder full with 'as-delivered' material.

Prior to emplacing in the sample holder, *as delivered* MX80 material was hand ground in a mortar and pestle to a fine powder.

In the case of the accessory mineral analysis, and the eroded material present on each filter paper, an insufficient mass of sample was present in each case to fill the sample holder. An improvised set-up was used in either case.

4.7.2 Post-test fracture face samples

In the case of the samples described in section 4.6, the sample holder was flipped to its underside which was flat; a small sample of accessory minerals was then placed directly in the centre of the sample holder as illustrated in Figure 4.12:

Figure 4.12: Sample holder upturned with small sample from fracture face in centre.

In this instance, the sample holder was placed in the machine and scanned from 2-70° 2θ as noted above. Once the scan was complete, the sample was then rotated 90^0 in the sample holder and re-scanned. This was repeated for each sample twice more. So, in total, each sample was scanned 4 times, with the sample holder at 0°, 90°, 180°, and 270°. It was thought that scanning each sample multiple times would provide the best chance of identifying each mineral in the sample, due to exposing each sample to the X-Ray at a higher number of crystal orientations. The data was then analysed by overlaying the scan taken from each of the 4 sample holder orientations into one graph.

The sample holder was also scanned upturned without any sample present in order to establish a background reading for the sample holder. Despite the amorphous nature of the sample holder, its signature may be expected to contribute significantly to the reflection data from scanning the accessory mineral samples, due to the small quantities of sample present.

4.7.3 Eroded material

In the case of the eroded material, a filter paper, after oven drying, was applied to the flat surface of the underside of the sample holder using a thin smear of silicone grease as illustrated in Figure 4.13. The silicon grease was also amorphous and was not foreseen to be a problem with regard to a background signal because of the area of the sample holder covered by the filter paper.
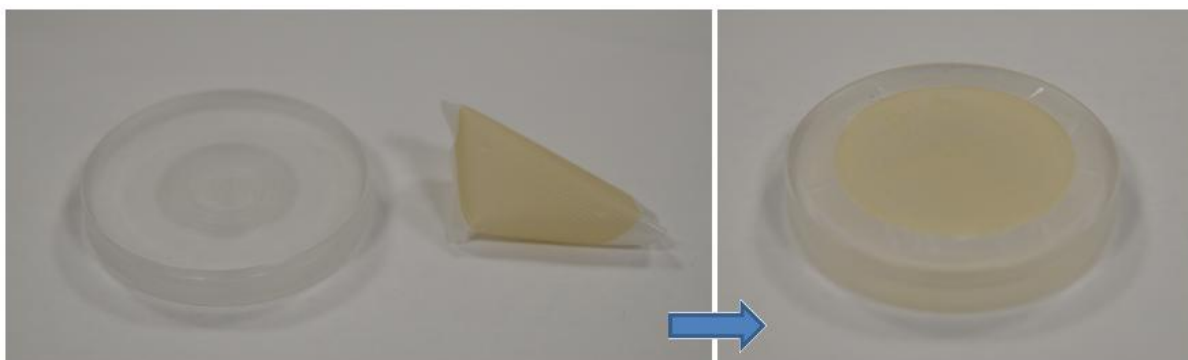
Figure 4.13: Sample holder / filter paper and filter paper applied using silicone grease

4.7.4 Evaluation of XRD data.

For the assessment of each of the scans, each scan was first imported into the diffract.eva software and the back ground removed. An example of this process is demonstrated in Figure 4.14, which depicts the original scan for *as delivered* MX80 in the full sample holder (in blue) and the background removed (in black).
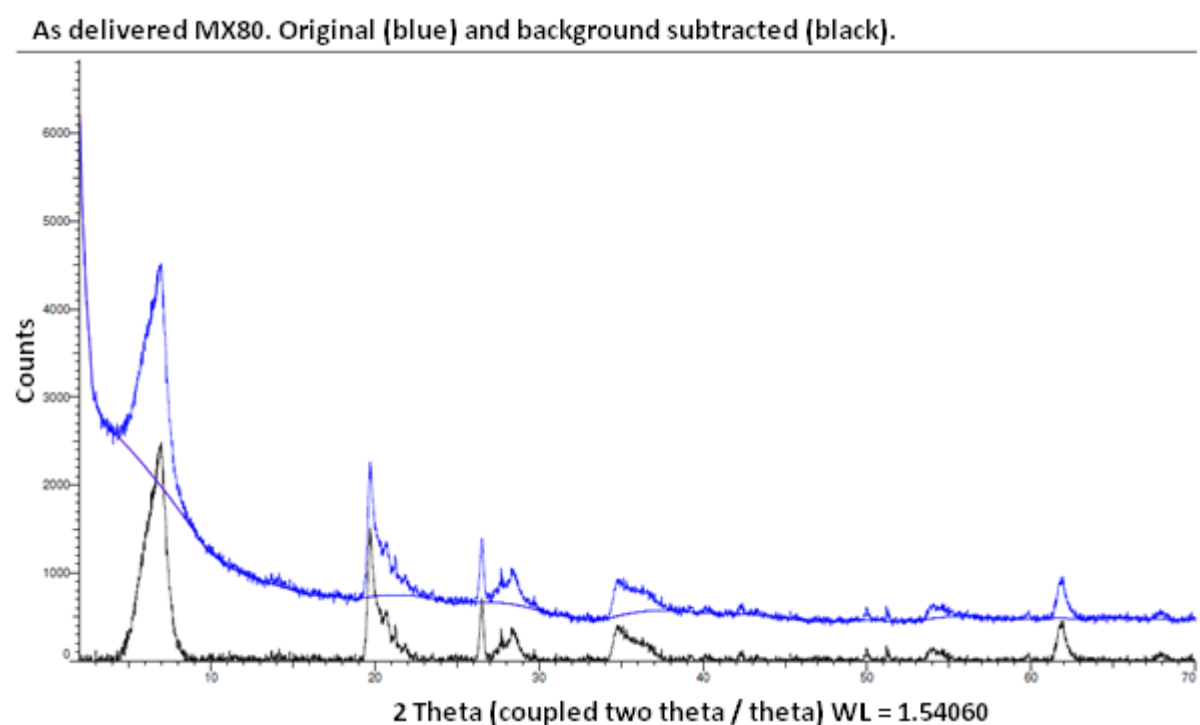
Figure 4.14: Original scan for MX80 (blue) and background removed (black).

Before attempting to match the scans with patterns found in the ICDD (International Centre for Diffraction Data) database, a chemical filter was first applied to the database in order to screen for the minerals which were most likely to be found in MX80. These were selected based on the mineralogical data for MX80 provided by the supplier of the material, Cetco minerals, from a test conducted by Macaulay Scientific Consulting Ltd in 2014 on behalf of Cetco, and data from Kiviranta and Kumpulainen (2010) in which minerals were identified by a combination of XRD and optical microscopy, also conducted on Cetco MX80.

Two data sets were used, as Kiviranta and Kumpulainen (2011) identified additional minerals through optical microscopy which neither party identified by XRD. The minerals which were expected to be found based on both data sets are detailed in Table 4.1:

Mineral	Identified by	
	Kiviranta & Kumpulainen 2010	*Macauley Consulting Ltd.*
Montmorillonite	yes	yes
Quartz	yes	yes
Plagioclase	yes	yes
K-Feldspar	yes	yes
Calcite	yes	yes
Pyrite	yes	yes
Gypsum	yes	yes
Opal-C / Cristobalite	yes	yes
Kaolinite	yes	yes
Biotite	yes (optical microscopy)	No
Hematite	yes (optical microscopy)	No
Apatite	yes (optical microscopy)	No
Zircon	yes (optical microscopy)	No

Table 4.1: Minerals identified through XRD / optical microscopy of Cetco MX80 from two sources.

The chemical filter facility in the software was, therefore, used to screen the database only for elements which are present in each of the above minerals. The search/ match feature of the software was then used to identify all potential mineral matches and those deemed the most likely matches of each peak in the data were assigned to those peaks.

The residual scan feature of the software was also used to identify minor phases, whose peaks may be obscured by larger peaks, this feature excludes the patterns already matched and increases the signature of the minor phases.

Further to this, XRD was also undertaken on accessory minerals and montmorillonite both isolated from *as delivered* MX80 by a series of centrifugations and separations. It was not possible to sample any material from the region of extruded material between the central compartment and the accessory mineral ring as only a fine film of material, which was presumably montmorillonite, was present and adhered to the fracture face.

4.7.5 Post-test optical microscopy.

The samples of material isolated in section 4.6 from the accessory mineral ring were examined by means of a *Nikon Eclipse LV100ND* optical microscope optical microscope, and the resulting images processed in *image j* software, in order to assess the particle sizes and morphology of those minerals being deposited in the fracture.

4.8 Quantitative image analysis.

Quantitative image analysis was used to determine the location of the extruded material within the fracture over time. This allowed the rate of extrusion of the sample and the relative areas of various regions of interest in the extruded material, specifically the discernible darker ring of 'accessory minerals' at the edge of the extruded material, to be calculated. The analysis was performed using the software, *imagej*, using the following methodology:

a) An image at the centre of the time series was arbitrarily selected. A length scale was then set on the image using a region of known dimensions i.e. the brass plug.

b) Colour thresholding techniques were then employed to isolate, by eye, the total extruded area (bounded by white in Figure 4.15**.** The threshold values selected were:

- Hue 0:0, Saturation 0:0 and Brightness 107:174
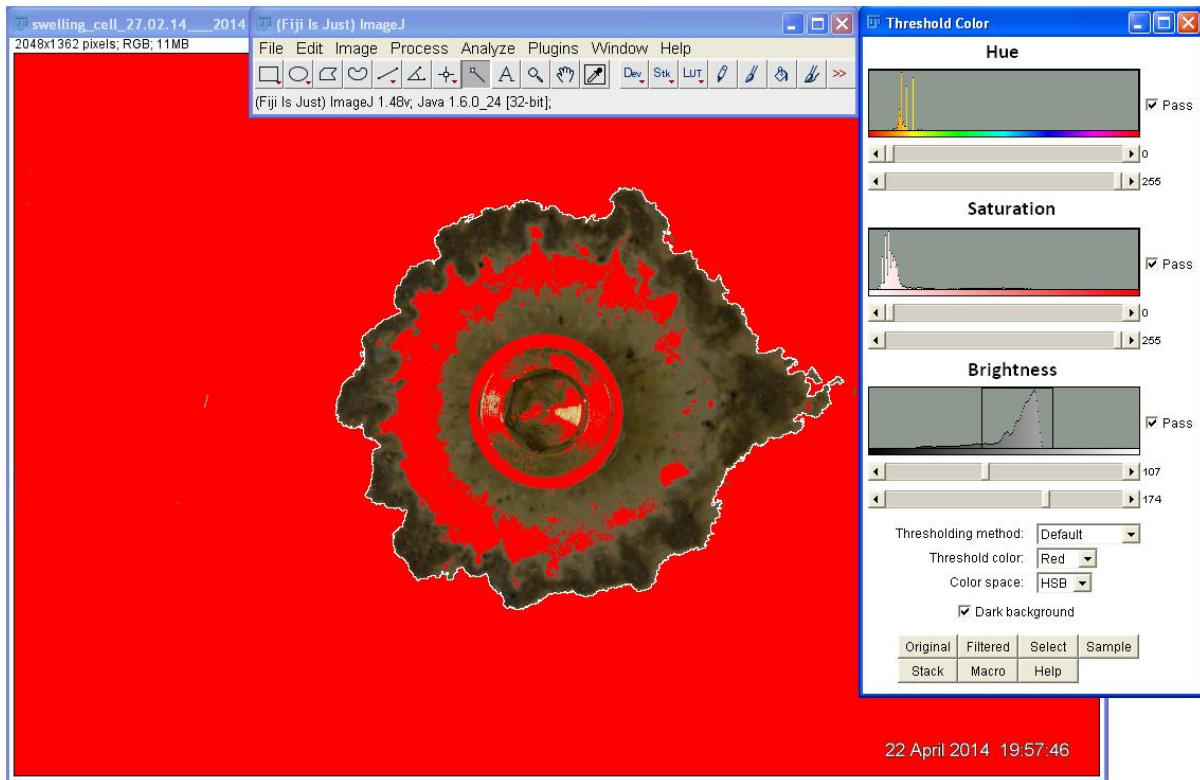
Figure 4.15: Image analysis technique for total extruded area, bounded by white.

c) Similarly, colour thresholding techniques were used to isolate the darker area of accessory minerals in the image (bounded by white in Figure 4.16). The threshold values selected were: Hue 0:0, Saturation 71:255 and Brightness 0:77. For the purpose of isolating the mineral ring, any area selected by the software out with the region of interest i.e. any area not forming part of the contiguous mineral ring at the edge of the extruded material, was manually removed prior to evaluating the area. Examples of such areas are apparent in Figure 4.16 around and inside the brass plug.
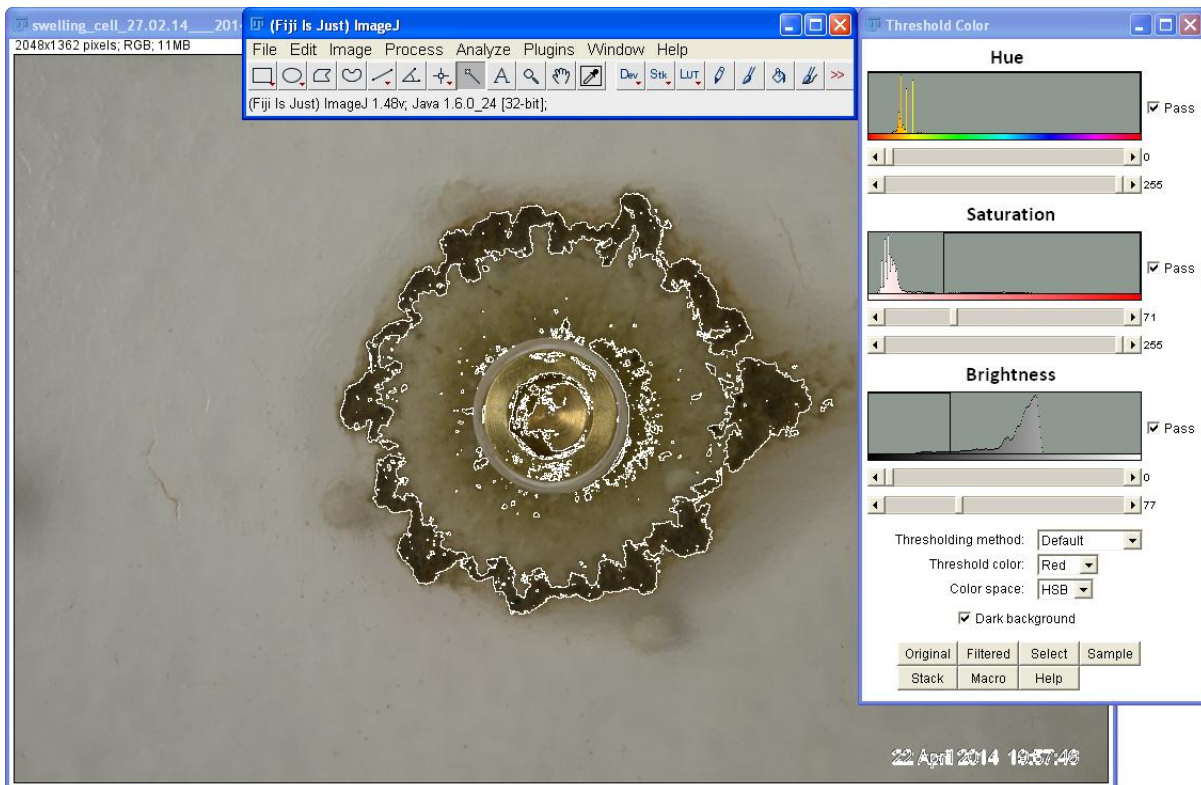
Figure 4.16: Image analysis technique for isolating regions of interest, bounded by white.

As lighting conditions were kept constant throughout the course of the experiment, the same threshold parameters were then applied to every image in the time series. Images were saved with the highlighted areas incorporated, for the purpose of constructing time lapse image videos to visually asses the way in which the area of interest evolved throughout the course of the extrusion and erosion process.

Data sets regarding erosion rate, swelling pressure, rate of extrusion and accessory mineral ring area were subsequently analysed with respect to time and each other.

4.9 Variations to the methodology for other tests in the suite

The above methodology is detailed for a test in which MX80 bentonite is installed in a variable aperture cell. For some tests, either a uniform aperture cell was deployed or the MX80 was replaced with a compacted plug manufactured from Nanocor PGN. In both cases, the same methodology was observed but with small differences.

4.9.1 Uniform aperture flow cell, MX80

In order to create a uniform aperture flow cell of similar hydraulic aperture to the variable aperture cell, the following changes to the methodology described in sections 4.2.1 and 4.2.2 above were made.

Using the same circular mould and quantities of resin, a uniform fracture face was moulded off of a piece of acetate on a horizontal surface instead of the rock fracture itself. Once cured, the acetate was peeled from the resin and the process repeated, including the addition of the sealant gap for the top plate. This resulted in two planar fracture faces, one with a gap in which the cell could be sealed.

An aperture was created by the inclusion of physical spacers between the plates, also made of acetate. The spacers were made from 4mm x 8mm pieces of acetate, which when folded in half made 4mm x 4mm spacers. The acetate has a thickness of 75 μm, which when folded gave the spacers a thickness of 150 μm. Initially, one 75 μm thick piece of acetate was trialled as the spacer. It was thought this thickness of spacer would provide an aperture similar to that of the previous experiment in the naturally variable aperture cell. It was found however that the 75 μm acetate folded over to 150 μm, revealed a hydraulic aperture closer to that of the variable aperture cell. The spacers were placed at evenly spaced intervals around the fracture face as detailed in Figure 4.17:
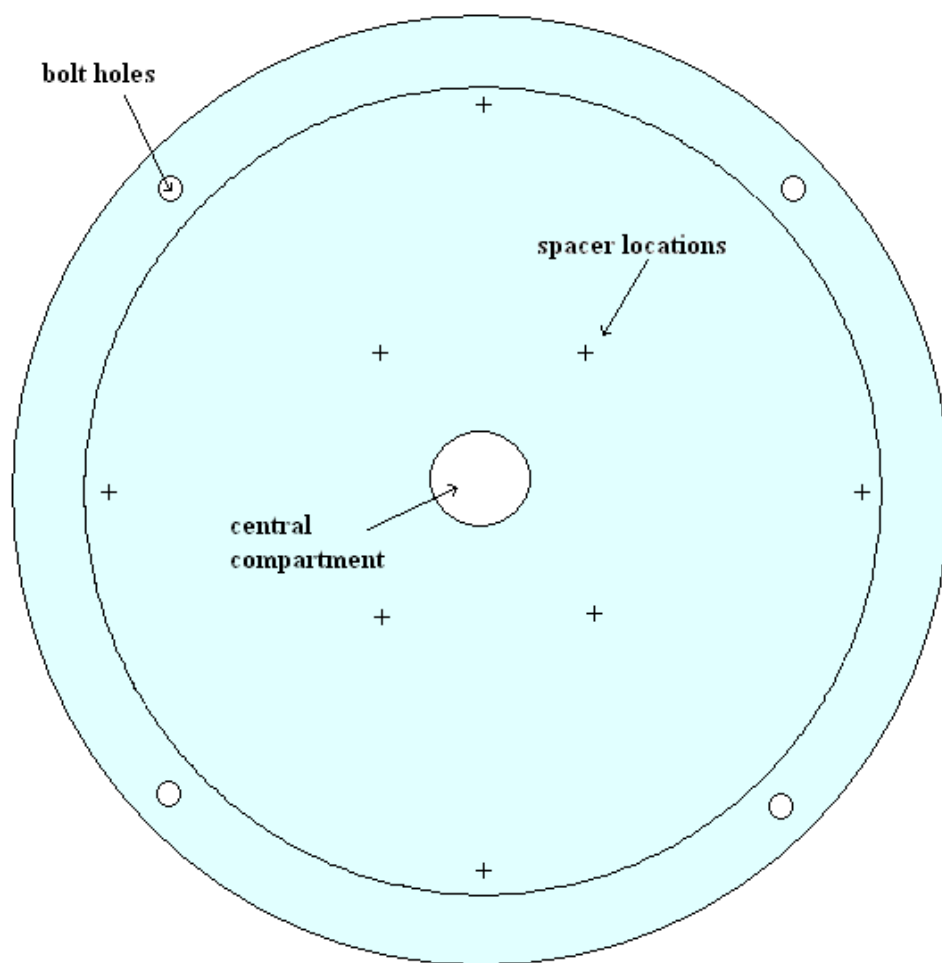
Figure 4.17: Plan view of spacer locations on uniform aperture fracture face.

Based on observations made in the previous test, the spacers were placed approximately 5 cm from the central compartment in order not to interfere with the extrusion of the sample. Spacers were also placed around the circumference of the cell.

4.9.2 Uniform aperture flow cell, Nanocor PGN.

The '*sample preparation*' methodology detailed in section 4.3 was followed for the preparation of Nanocor PGN purified montmorillonite, with the only exception that the as delivered material had an initial water content of 10% as opposed to the 12% of MX80.

Chapter 5 Bentonite Material Characterisation

Prior to discussing the experimental results, it is useful to present the bentonite mineral composition for use in subsequent chapters. This chapter describes the material characterisation undertaken at Strathclyde on both the as delivered Cetco MX80 and Nanocor PGN clays. Cetco and Nanocor are the respective suppliers of either clay, both of whom, at the time of commencing this thesis were subsidiaries of Amcol International Corporation, which has since been acquired by Minerals Technologies Inc. Less comprehensive characterisation was performed on Nanocor PGN as a result of having a limited quantity of this material with which to work.

5.1 MX80

5.1.1 Water content, dry-sieve grain size distribution and liquid limit

To ensure the buffer fulfils its specific performance requirements, a procedure for quality control upon buffer material acquisition is set forth in Kiviranta and Kumpulainen (2011), on behalf of Posiva. Three of the tests performed in this work as part of basic acceptance testing are the water content, liquid limit and grain size distribution by dry sieving of the MX80 material.

Kiviranta and Kumpulainen (2011) found Cetco MX80 had water content of 12.3 $^+/_-$ 0.1% and a liquid limit of 483 $^+/_-$ 6%. The grain size distribution tests on two samples of material performed by Kiviranta and Kumpulainen (2011) are depicted in Figure 5.1, which also shows the dry sieve grain size distribution of two samples of Cetco MX80 tested at Strathclyde for the purpose of this work.
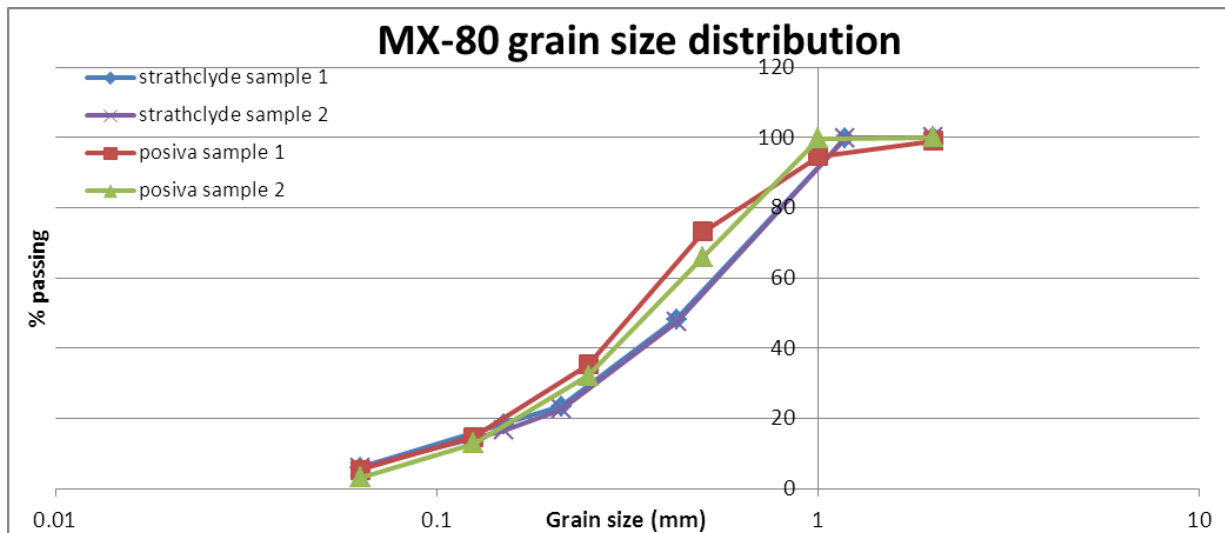
Figure 5.1: Comparison between dry sieve grain size distributions performed at Strathclyde and performed by Kiviranta and Kumpulainen (2011) on Cetco MX80.

It is apparent from Figure 5.1 that the material used by Posiva contains a higher degree of fines than the material procured for the purpose of this work. This however could be an artefact of the fact that different sieve sizes were used in either test. It was not thought that the small differences in grain size of the material would affect its erosion characteristics because the erosion tests were performed on highly compacted samples, within which the grains are essentially bonded.

Upon testing the water content of three samples from the batch of material procured at Strathclyde, it was found to have a water content of 11.6%.

Testing of the liquid limit was performed by two methods, the British standard method and the method set forth in Kiviranta and Kumpulainen (2011), as described in section 4.1.1. The results of which are illustrated in Figure 5.2:
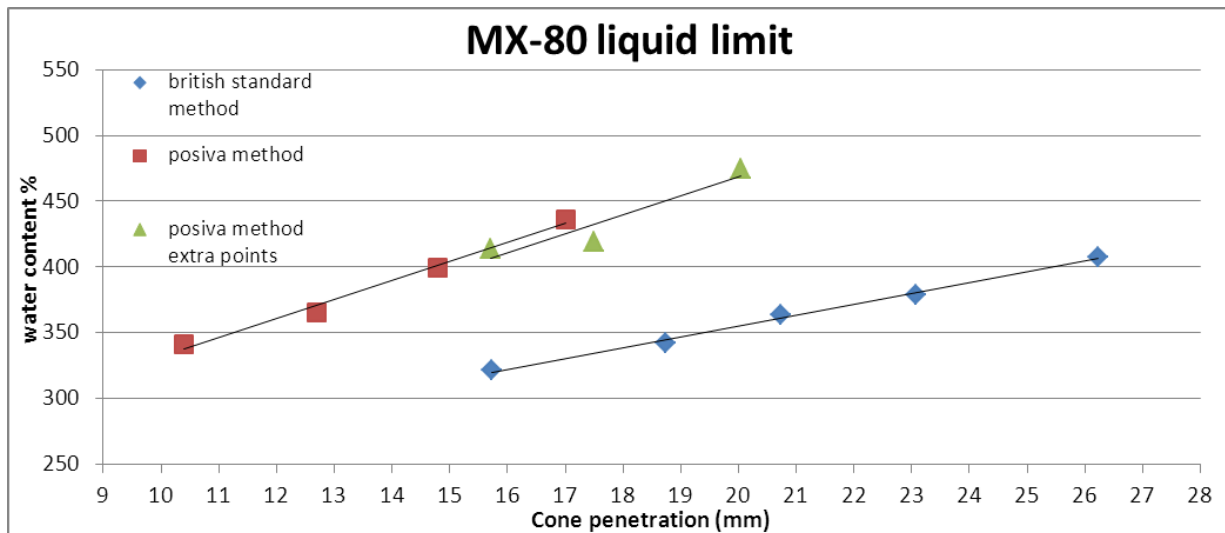
Figure 5.2: Comparison between methods for liquid limit testing on Cetco MX80 procured at Strathclyde, method outlined in Kiviranta and Kumpulainen (2011) for Posiva and British Standard method.

It is apparent from Figure 5.2 that two methods for liquid limit testing on the same material produce significantly different results. The British standard method reveals a liquid limit of approximately 360%, whereas the method employed by Kiviranta and Kumpulainen (2011) produces a liquid limit in the region of 475%. In either instance, the liquid limit corresponds to the water content at 20mm penetration of the cone.

The increase in the liquid limit between test methods is most likely attributable in some way to an increase in shear strength associated with ageing effects of bentonite, such as those described in Evans & Ryan (2005). In the British standard test method, samples are prepared at a specific water content and tested instantaneously. Whereas in Kiviranta and Kumpulainen's method, samples are prepared at specific water contents, sealed, left over-night and tested the following day. Hence, the cone is less able to penetrate samples at the same water content as the bentonite ages.

In any case, the measured liquid limit of 475% using Kiviranta and Kumpulainen's (2011) method (which defines Posiva's buffer acceptance standards), as well as the measured water content and grain size distribution are within the bounds of the buffer material acceptance standards.

5.1.2 X-Ray diffraction.
Qualitative mineralogy

The MX80 material used in this work was purchased from Cetco minerals in 2012 and, at the time of purchase, no XRD mineralogical data was provided by the supplier with the material. Upon contacting the supplier in 2015 requesting this data, XRD mineralogical data was provided from a test conducted by Macaulay Scientific Consulting Ltd in 2014 on Cetco's MX80 material. Hence, the test is likely to have been conducted on a different batch of material to that examined in this work.

In order to verify that the mineralogical data for the material provided by the supplier in 2015 was similar to the material procured in 2012, and indeed in line with the mineralogical data set forth in Kiviranta and Kumpulainen (2011) for buffer acceptance standards, the mineralogy of the MX80 material procured form Cetco was examined by X-ray diffraction according to the procedure set forth in section 4.7.1. The diffraction pattern for '*as delivered*' MX80 material procured for this work was analysed and compared with that of data provided by the supplier, Cetco minerals, for this material.

In the report by Phillips (2014), the material was prepared by being wet ground in ethanol in a McCrone mill and spray dried to produce a randomly oriented powder. Clay minerals have a tendency to orient preferentially and the sample preparation technique of McCrone milling and spray drying gives the best chance of obtaining accurate relative intensities of each peak in the diffraction pattern, which can only be achieved when the crystals are randomly oriented (Hillier 1997). The powder was then scanned using a cobalt kα X-Ray source from $2 - 75^{o}$ 2Θ with 0.02^{o} counting steps at 1 second/ step. The X-Ray diffraction pattern from the analysis undertaken by Philips (2014) is given in Figure 5.3a, along with the XRD scan for as-delivered Cetco MX80 undertaken for the purpose of this thesis at Strathclyde (Figure 5.3b). Corresponding peaks from either scan have been joined by coloured lines for illustration purposes.
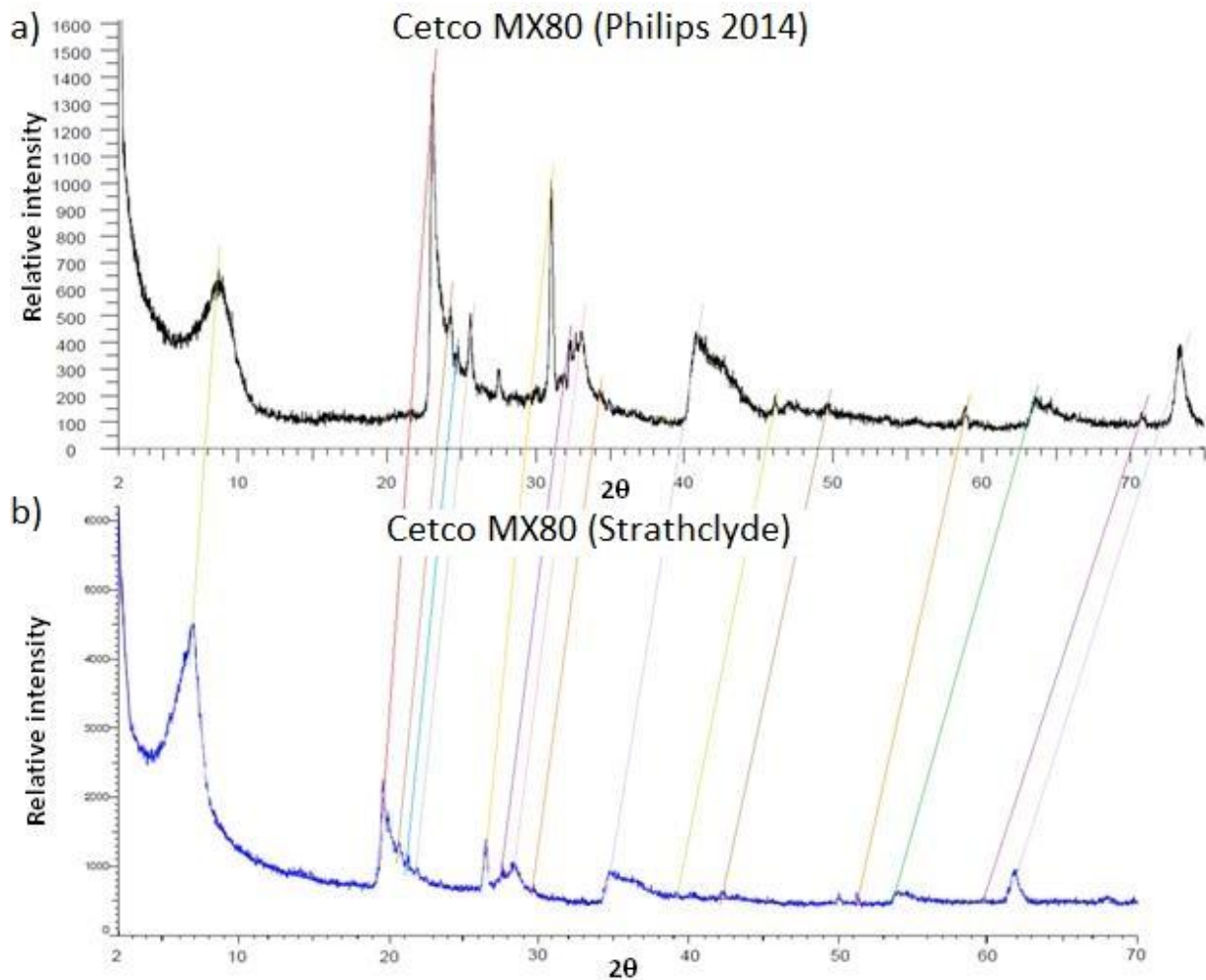
Figure 5.3: X-Ray diffraction data for as delivered Cetco MX80. a) Philips (2014) b) Strathclyde

In the analysis undertaken at Strathclyde, no sample preparation techniques were undertaken, due to not having the facilities to do so; the sample was simply ground gently in a mortar and pestle before filling the sample holder. Despite this, the X-Ray diffraction patterns for both batches are very similar, as such the phase structure of both batches should also be very similar. Discrepancies in the locations of the peaks between Figure 5.3a and Figure 5.3b, with regard to 2ϴ, are due to the difference in the wavelength of the X-Ray source used in either test. In the case of the supplier's data, the cobalt source has a larger wavelength at 1.79Å than the 1.54Å copper source used at Strathclyde, therefore the XRD pattern using a cobalt source will shift to higher angles and the distance between peaks will also be larger for cobalt. The minerals identified by the manufacturer and their relative proportions in MX80 are given in Table 5.1:

Quartz	Plagioclase	K-feldspar	Calcite	Pyrite	Gypsum	Opal-C/Cristobalite	Dioctahedral Smectite	Kaolinite	Total
4.2	1.8	2.0	0.1	0.2	trace	1.8	89.7	0.2	100

Table 5.1: Mineralogy, % by weight of as delivered Cetco MX80. Philips (2014).

Figure 5.4 shows the XRD diffraction pattern for MX80 undertaken at Strathclyde, annotated using a combination of the information on the minerals identified with regard to peak locations based on Philips (2014) and the search-match scan function on *diffract.eva* software. The first, broad peak at 7° 2Θ in Figure 5.4, corresponds to the primary peak for montmorillonite in the sample. Subsequent peaks are labelled and correspond mostly to the crystalline phases of quartz, albite (plagioclase feldspar) and microcline (K-feldspar).
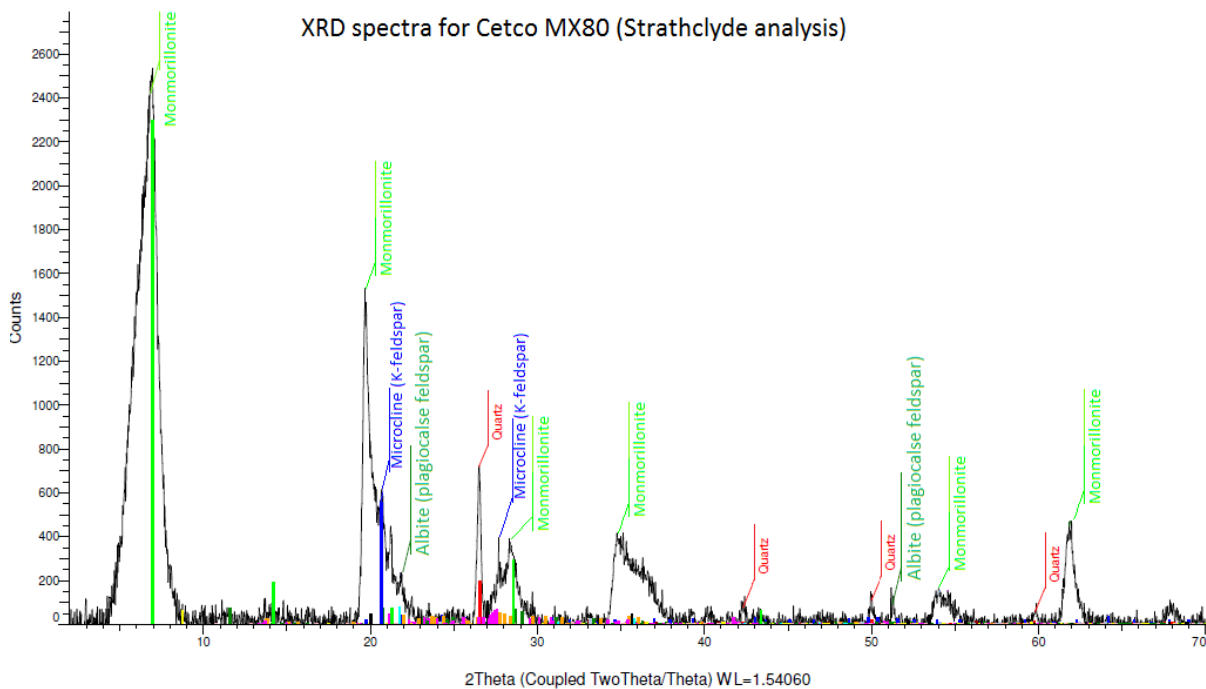
Figure 5.4: Labelled Cetco MX80 diffraction pattern for analysis undertaken at Strathclyde with background removed.

Because MX80 is predominantly montmorillonite and the crystalline accessory minerals constitute only a small proportion of its mineralogical composition, the signatures of many of the trace minerals in the diffractogram shown in Figure 5.4 may be obscured by the montmorillonite peaks. In order to show the differences in XRD spectra for montmorillonite and the accessory minerals contained within MX80, and indeed aid the identification of these minerals in subsequent analyses, the phases were separated by a series of

centrifugations and X-Ray diffraction undertaken on the accessory minerals isolated from MX80, shown in Figure 5.5. XRD was also undertaken on homoionised Na-montmorillonite isolated from MX80 provided by B+Tech, as shown in Figure 5.6.
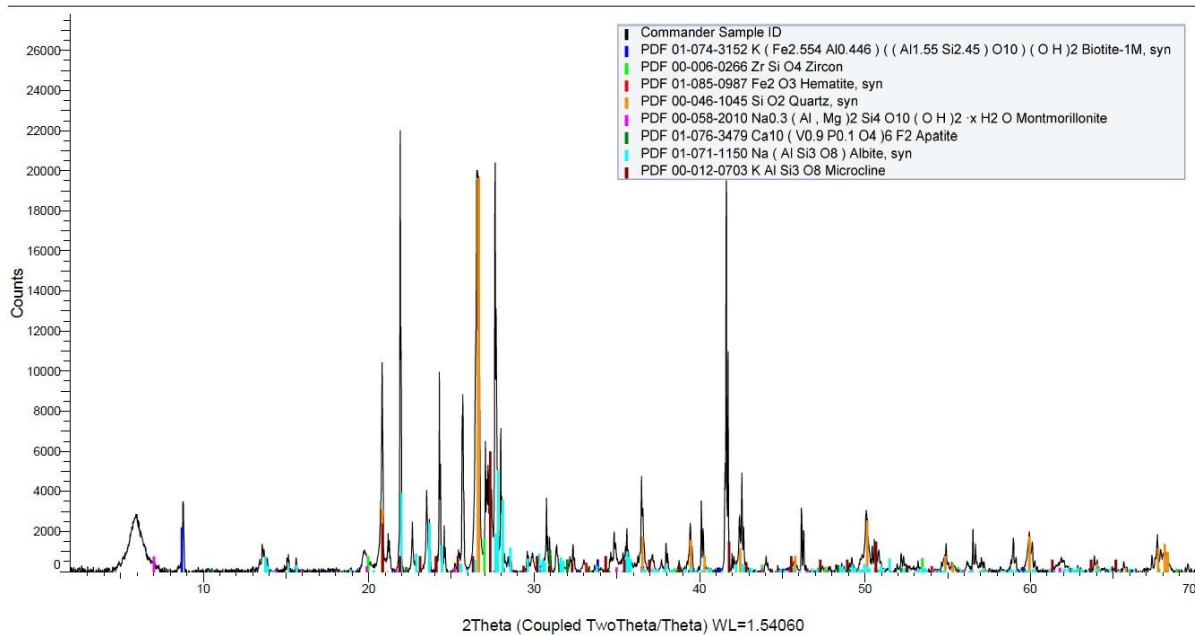
Figure 5.5: XRD spectra for accessory minerals isolated form MX80 by centrifugation.

The clay mineral montmorillonite is clearly distinguishable by its multiple, broad peaks in Figure 5.6. Whereas the crystalline minerals in the mix are characterised by the narrow, sharp peaks shown in Figure 5.5. Figure 5.3 is effectively a composite of Figure 5.5 and Figure 5.6 and it is apparent that the broad montmorillonite peaks of Figure 5.6 obscure some of the crystalline mineral peaks in Figure 5.5 over the same diffraction angles, making identification of the individual minerals in the MX80 mix difficult.

Montmorillonte isolated from MX80
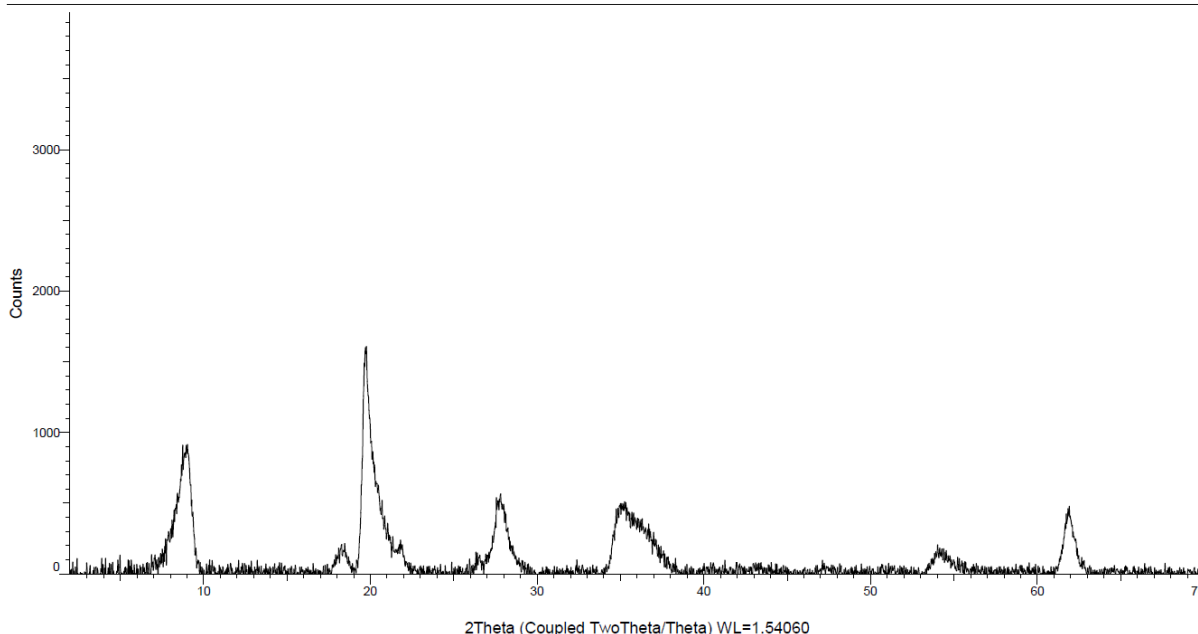
Figure 5.6: Montmorillonite isolated from MX80 and homoionised to Sodium.

Quantitative mineralogy

Despite the likely inaccuracies in peak intensities as a result of sample preparation and preferential crystal orientation, an attempt was made at quantifying the proportion of each mineral present from the scans performed at Strathclyde in order to compare with the data provided by the manufacturer. The free United States Geological Society (USGS) software *RockJock* was used for this purpose. *RockJock* is an Excel programme for determining quantitative mineralogy from X-Ray diffraction data. The software compares the integrated intensities of each peak with those of internal standards in order to calculate the weight precentage of each constituent mineral in the mix. Each mineral is analysed independently, hence the accuracy of the technique can be measured by checking how close the total is to 100%. The analysis does, however, specify the McCrone mill/ spray drying sample preparation technique in order to ensure random crystal orientation. Data is input into the spreadsheet as Intensity vs. 2Θ; each mineral which is expected to be in the mix is specified and the calculation is then performed. The results of these calculations are presented in Figure 5.7.
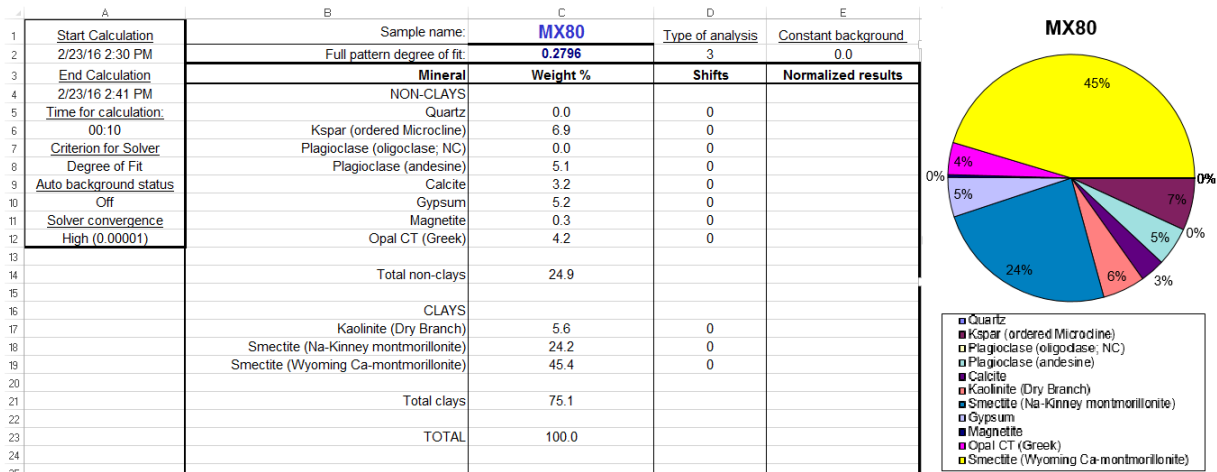
Figure 5.7: Quantitative XRD data for Cetco MX80 calculated using USGS Rockjock software.

It is apparent from Figure 5.7 that *Rockjock* estimates the quantitative mineralogy of the Cetco MX80 to comprise of 69.9% mixed Na and Ca montmorillonite, 6.9% K-feldspar, 5.6% kaolinite, 5.2% gypsum, 5.1% plagioclase, 4.2% opal, 3.2% calcite and 0.3% magnetite. It should be noted however that these are corrected weight precentages, as after summation of the weight percentage of each constituent based on comparison with the internal standards, the software initially returned a total of 126%. Furthermore, the '*full pattern degree of fit*' for the data, as noted in cell C2 in Figure 5.7, is given as 0.2796. *Rockjock* specifies a degree of fit <0.1 to represent an accurate quantitative assessment of diffraction data hence the reliability of the results has to be questioned further.

Also notable, is the apparent lack of quartz identified by *Rockjock*. Despite it being identified as the second most abundant phase in MX80 by Philips (2014) and its identification using *diffract.eva* software, depicted Figure 5.4 and Figure 5.5, the qualitative analysis undertaken at Strathclyde.

Figure 3 shows there is an excellent match between the XRD data procured at Strathclyde and the XRD analysis provided by the supplier. As a consequence, given the stringent material standards and high technical specification for MX80, it was decided that because the same phases could be qualitatively identified as being present, any discrepancies in the quantitative percentage of each mineral present was most likely a result of the sample preparation techniques. Hence, the quantitative data provided by the supplier was chosen

as a more accurate representation of the weight percentage of each phase present in as delivered Cetco MX80.

5.2 Nanocor PGN

Due to the small quantity of Nanocor PGN material provided by B+Tech consultants, the same level of material characterisation as that undertaken on Cetco MX80 material (dry-sieve grain size distribution and liquid limit test) could not be carried out. In any case, a higher level of characterisation was undertaken on MX80, due to the higher degree of variability one might expect from a material with a lower stated purity. Nanocor PGN is a high purity (>98%), polymer grade montmorillonite; it is intended for use as an additive to hydrophilic polymer suspensions, in order to create nanocomposites.

5.2.1 Water content and grain size

The manufacturer's data sheet for the material specifies a water content of ≤ 12%. Upon testing the water content of the material at Strathclyde, it was found to have a water content of 10%.

No information on the grain size distribution of Nanocor PGN is given in the data sheet provided by the manufacturer. Through correspondence with the manufacturer however, Nanocor have indicated that the material has a particle size in the range of 20 μm. This particle size was confirmed by optical microscopy on the 'as-delivered' Nanocor PGN received from B+Tech.

Figure 5.8 shows an image from the optical microscopy undertaken on a sample of the '*as delivered*' Nanocor PGN material at 40x magnification. It is apparent from Figure 5.8 that the largest particle in this sample has a maximum lateral dimension of approximately 30μm, the majority of the particles are indeed in the sub 20μm range, as stated by the manufacturer. What is not readily apparent from the optical microscopy on the 'as-delivered' material, due to how small the particles are, is which particles are montmorillonite aggregates (98%) and which are accessory minerals (2%). This shall be discussed further in section 7.5.

Figure 5.8: Optical microscopy image of a sample of 'as-delivered' Nanocor PGN at 40x magnification.

The < 30 μm particle size range of Nanocor PGN therefore is significantly different from that of MX80 material, the latter of which has approximately 95% of its particles (montmorillonite aggregates and accessory minerals) > 63 μm, as shown in Figure 5.1.

5.2.2 X-Ray diffraction
Qualitative mineralogy

No detailed quantitative XRD data was available from the manufacturer, however, the material data sheet states a montmorillonite purity of the material of >98%, the remaining <2% of the material is comprised predominantly of the accessory minerals albite (plagioclase feldspar), calcite, dolomite, orthoclase (K-feldspar) and quartz. Nanocor PGN and MX80 are therefore similar in terms of their mineralogical constituents, if not the particle size and proportions of each of these constituents.

The similarity in mineralogy between either material is clearly demonstrated in Figure 5.9, which shows the XRD spectra from analysis undertaken at Strathclyde for a) Nanocor PGN and b) MX80 with the background removed.
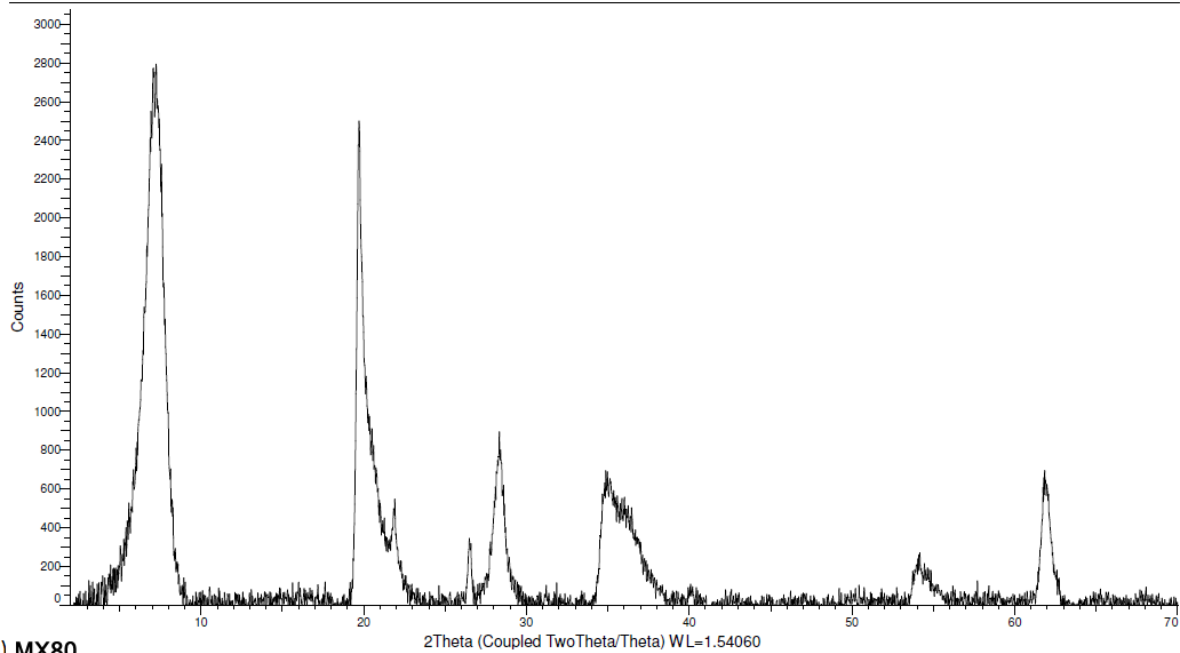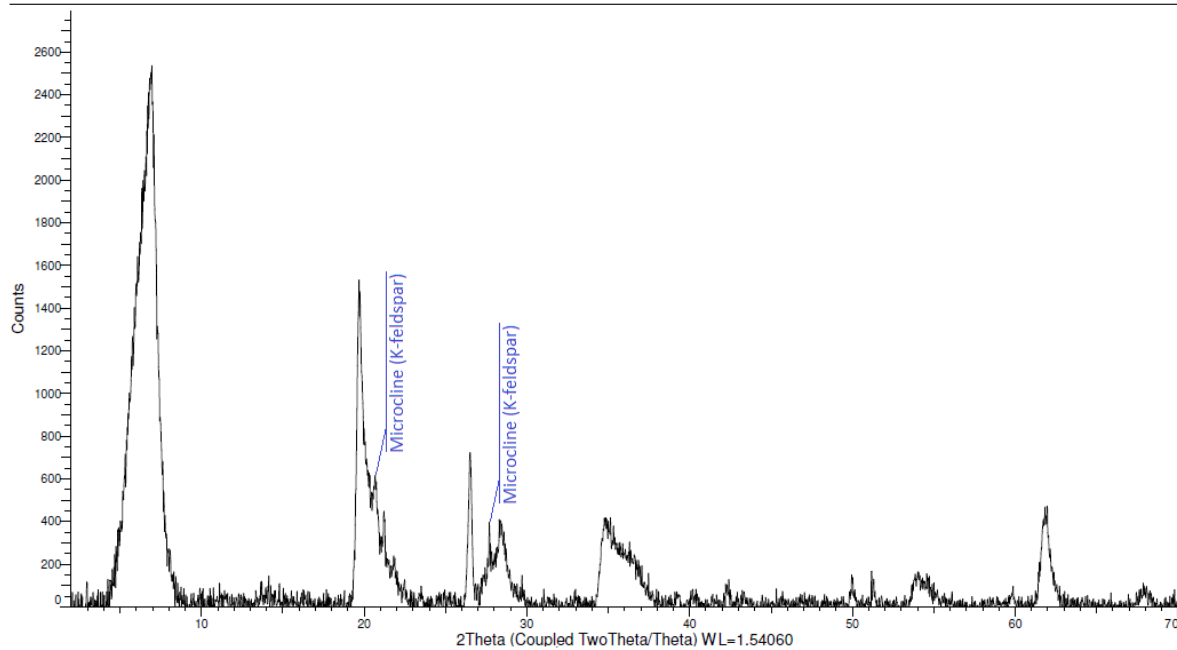
Figure 5.9: XRD spectra for a) Nanocor PGN and b) MX80. Analysis undertaken at Strathclyde.

Two key differences in mineralogy between the materials are labelled in Figure 5.9; the presence of the feldspar mineral microcline. Additional peaks which appear in the diffractogram for MX80 which are not present in the diffractogram for Nanocor PGN correspond to subsequent peaks of this mineral and quartz. The similarity in mineralogy between either material might be explained by the fact that Cetco and Nanocor are both subsidiaries of the same parent company, i.e. Nanocor PGN may be produced from MX80 as the raw material.

Quantitative mineralogy

As was performed with MX80 material, an attempt was made at quantifying the presence of each of the minerals present in Nanocor PGN using the USGS software *Rockjock*.
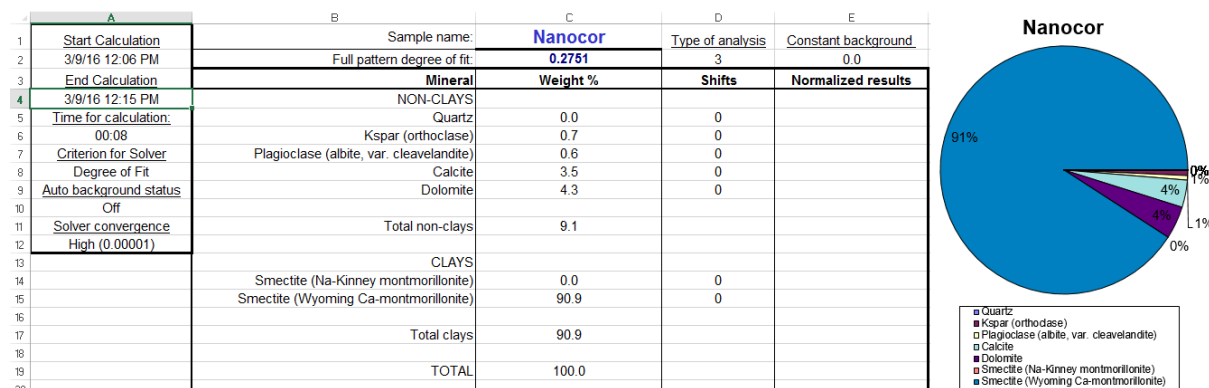
Figure 5.10: Quantitative XRD data for Nanocor PGN calculated using USGS Rockjock software.

The procedure outlined in section 5.1.2 was followed for Nanocor PGN and it is apparent from Figure 5.10 that the software estimates the sample to contain 91% montmorillonite, 4.3% dolomite, 3.5% calcite, 0.7% orthoclase (K-feldspar) and 0.6% albite (plagioclase). As was the case with the implementation of *Rockjock* with MX80 however, the software failed to recognise the presence of quartz in the sample. Despite the apparent presence of quartz in the XRD data for the sample shown in Figure 5.9a. As was also the case with MX80, the software returned a high *'full pattern degree of fit'* for the sample of 0.2751, *Rockjock* specifies a degree of fit <0.1 to represent an accurate quantitative assessment of diffraction data.

As with the MX80, it was decided that the quantitative mineralogical data provided by the manufacturer of a montmorillonite content of > 98% was likely to be the most accurate assessment. The underestimation of the montmorillonite content in the sample by *Rockjock* in the case of both MX80 (≈15%) and Nanocor PGN (≈10%) is most likely to be the result of a lack of appropriate sample preparation.

A summary of the MX80 and Nanocor PGN material properties are provided in Table 5.2 and Table 5.3.

Material Property	MX80		Nanocor PGN
Liquid limit (two methods)	475% (K&K)	360% (BS)	-
Water content	12%		10%
Max grain size	1mm		0.03mm

Table 5.2: Liquid limit, water contant and grain size characteristics of MX80 and Nanocor PGN

Material Mineralogy (Manufacturer data)	MX80	Nanocor PGN
Montmorillonite	89.7%	> 98%
Quartz	4.2%	< 2%
K-feldspar	2.0%	< 2%
Plagioclase	1.8%	-
Opal-c / Cristobalite	1.8%	-
Pyrite	0.2%	-
Kaolinite	0.2%	-
Calcite	0.1%	-

Table 5.3: Mineralogy of MX80 and Nanocor PGN - from manufacturer's data.

Chapter 6 Erosion of MX80 in a variable aperture fracture flow test

A fracture flow test was undertaken to examine the erosion behaviour of MX80 within a fracture of naturally varying aperture (Reid et al, 2015).

The test set-up is depicted in Figure 6.1. Figure 6.1 shows the variable aperture flow cell, in which the MX80 sample is installed, mounted under a DSLR camera for the purpose of image analysis of the sample extrusion process, controlled through a PC by *candylabs videovelocity* software. Data is acquired from a load cell mounted under the sample through the same PC via *labview* data acquisition software and *National Instruments* hardware. The inlet to the cell is connected to an *Ismatec* peristaltic pump delivering deionised water from a 5 litre Schott bottle.
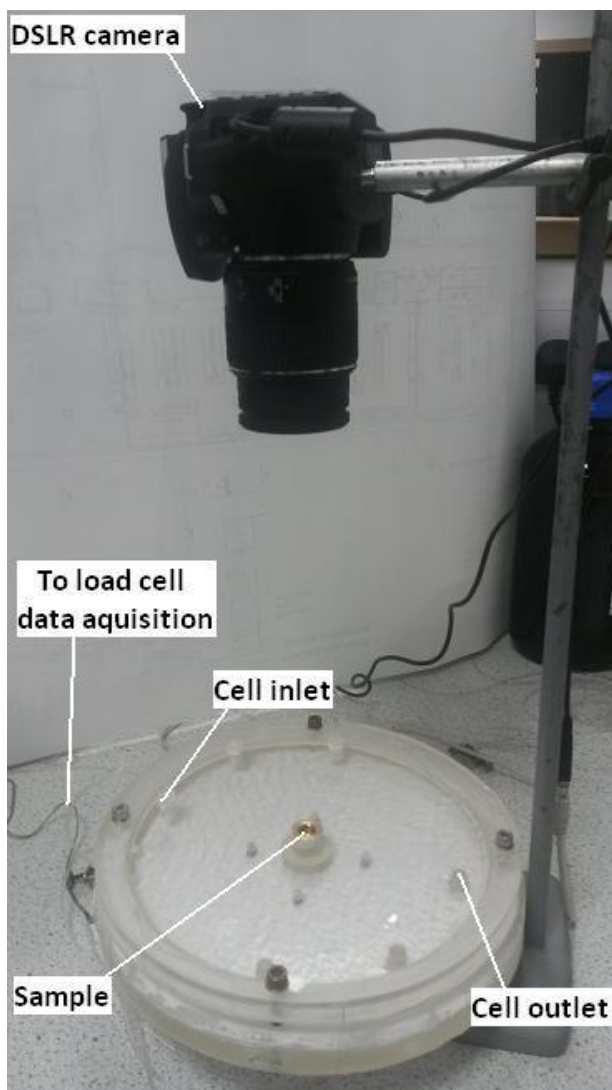
Figure 6.1: Experimental apparatus.

The outlet from the cell ran to a 2 litre conical flask which was changed daily and the effluent filtered through a 0.2µm filter paper to determine the mass loss rate from the cell. Standpipes were also T-pieced off the inlet and outlet lines to the cell and fixed vertically to the nearest wall, in order to measure the pressure drop across the cell.

Prior to commencing the flow-through erosion test, the hydraulic aperture of the cell was determined. As described in Section 4.2.2, a tracer test, using a red dye, was conducted to determine the approximate extent of the flow within the plates. An example of this process is depicted in Figure 6.2. Dye was injected into the left hand port. The presence of the central plug (containing a blank cylinder instead of the MX80 for the purpose of the tracer test) inhibits direct flow from the inlet to the outlet and clearly creates a zone of no flow in its wake (between the plug and the outlet). The dye spreads laterally within the fracture due to diffusion, so it is likely that the actual flow zone is slightly more elliptical in shape than that described by the coloured zone on the right hand image. Based on the results of the injection test and the Hagen Pouseuille equation described in 4.2.2, the hydraulic aperture was determined as being 57 microns.
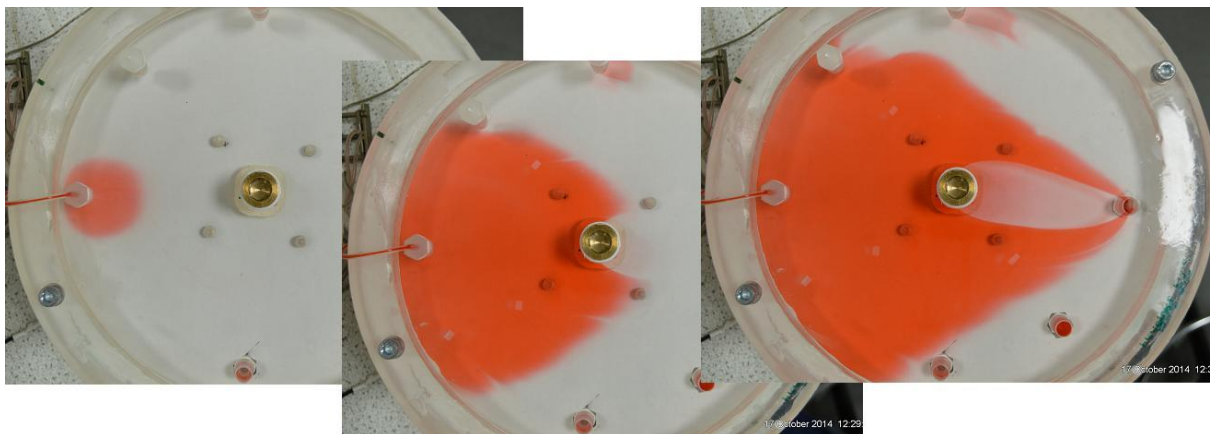
Figure 6.2: Example of dye injection process for quantitative establishment of extent of flow.

During the erosion test, flow was applied through the fracture cell at a constant rate of 1ml/min for a duration of 130 days. As saturation of the compacted bentonite plug begins to occur, the bentonite swells out of the central compartment and into the fracture.

Figure 6.3: MX80, variable aperture fracture, extrusion at day 0, 5 and 90.

Figure 6.3 shows the test on day zero, prior to swelling, and on day 5 when the bentonite is clearly visible within the fracture, as a zone of brown surrounding the central plug. By day 90 (Figure 6.3) the area of the fracture cell occupied by the bentonite has stabilised at around 6% of the fracture surface. During the test, flow rate and swelling pressure were continuously monitored, as discussed in section 4.2, the daily total mass of eroded material was also estimated, via filtration of the effluent (section 4.5) and retained for post-test analyses. Photographic images of the bentonite extrusion within the fracture cell were also recorded on a daily basis.

6.1 MX80, variable aperture, constant flow

Figure 6.4 shows the data gathered during the course of the 130 day experiment. Each of the data sets are now considered.
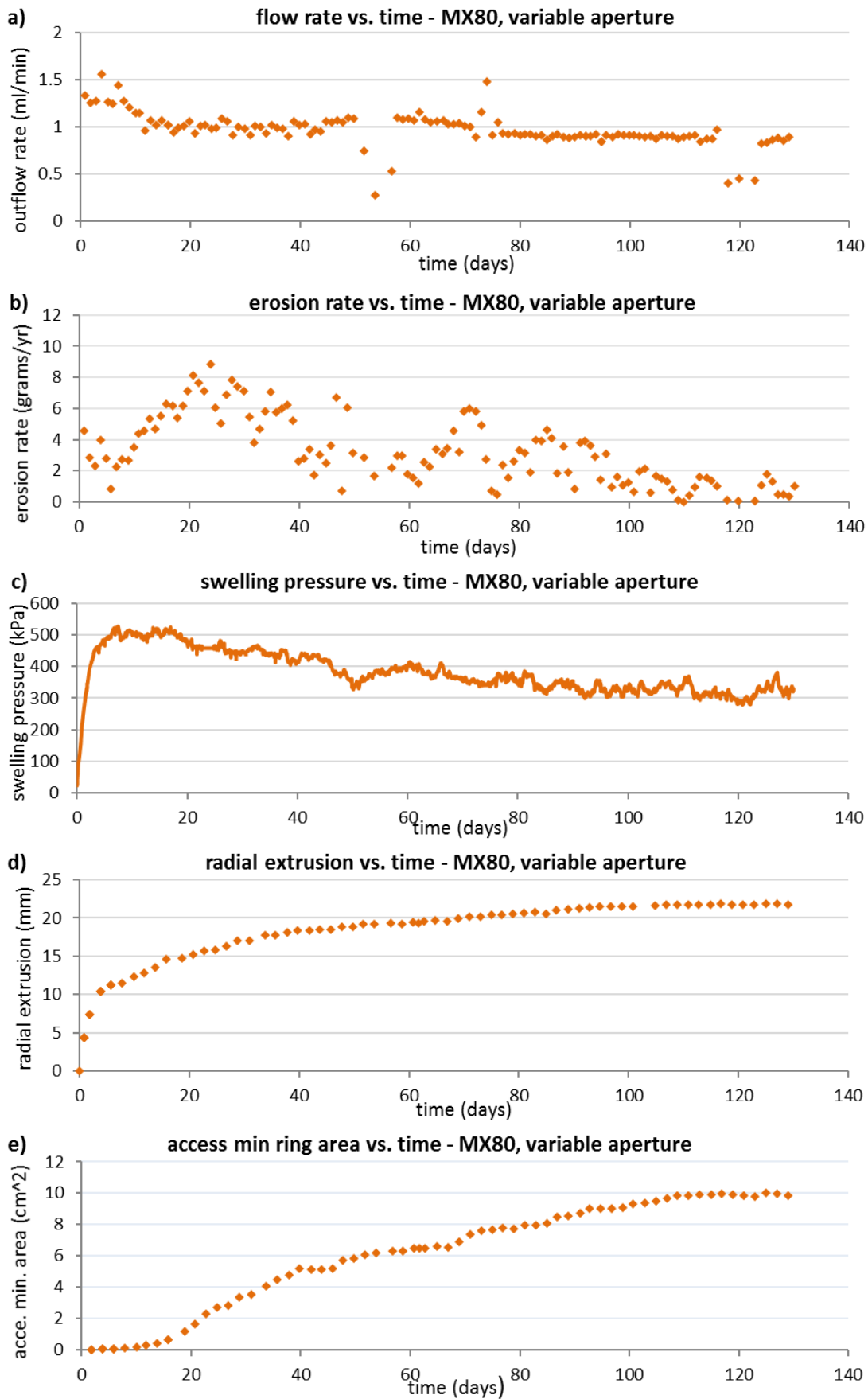
Figure 6.4: Mx80, variable aperture fracture data for a) flow rate b) erosion rate c) swelling pressure d) radial extrusion distance and e) accessory mineral ring area with respect to time

Flow rate

Flow rate data recorded over the duration of the test are shown in Figure 6.4a. The peristaltic pump was calibrated prior to commencing the test and a setting of 1ml/min on the pump was expected. However, the pump initially produced a flow rate between 1.25 and 1.5 ml/min through the system and had to be adjusted after the first 6 days of the experiment. After this adjustment the flow rate stabilised at around 0.95ml/min.

Also apparent in Figure 6.4a are three relatively short periods in which the flow rate was either increased or decreased substantially. The two periods in which the flow rate was reduced correspond to holiday periods, during which time it was not possible to change the effluent bottle on a daily basis so the flow rate was halved so that the same volume of water had passed through the fracture between consecutive samples that were collected every 2 days: days 50 to 57 and 116 to 123. During days 70 to 74, the peristaltic pump pipe was changed because of frictional wear; this led to a short period with an increased flow rate before the pump speed was adjusted back down to 1ml/min.

Closer inspection of the flow measurements in Figure 6.4a also reveals a greater variability in the flow rate during the first 42 days. This is due to the measurement technique employed. Prior to day 42, the volume of filtrate was measured using a measuring cylinder. After day 42, a more reliable method of weighing the effluent at the point of bottle change was adopted, thus providing a more accurate measurement that is not subject to error due to evaporation during the filtration process. The slight decrease in flow rate over the period from days 58 to 70 can be attributed to wear of the peristaltic pump pipe due to friction, which restricted the diameter of the pipe in contact with the rollers, gradually reducing the flow rate. The pipe was replaced at day 70 for a long-life version of the same tubing, *Tygon E-LFL.*

Mass loss

Figure 6.4b shows the daily erosion rate throughout the test. During the 130 days of the test, approximately 1.11g of the original 4.67g of dry mass of bentonite initially emplaced was eroded, i.e. 24% of the initial sample mass. Figure 6.4b shows that the erosion rate (when scaled from the measured mass lost in a 24-hour period to grams/year) increased to 8.8 grams per year during the first 23 days of the experiment and then gradually decreased over time. Most apparent in the Figure are clear and regular oscillations in the erosion rate,

which have ever decreasing magnitudes. These oscillations have a period of approximately 10 days.

The initial increase in erosion rate, up to 8.8 grams/year over a 23-day period (Figure 6.4b), is most likely to be the result of the simultaneous increase in the surface area of the bentonite in contact with the flowing water as the bentonite extrudes radially into the cell. However, it may also be a coupled chemical/ physical process because the erosion rate does not begin to increase until after 6 days, by which time the sample has extruded 12mm into the fracture, half way to its full extent. As the erosion of bentonite colloids is influenced by the presence of cations in the interlayer space, effectively acting as the glue holding the clay platelets together, the initial lag period before erosion commences may be to the result of the time taken for these ions to flush from the sample into the flowing water thus facilitating colloid release.

Interestingly, the fluctuations in erosion rate appear to be occurring independently of changes in flow rate. Specifically the period of increasing flow rate from 70 to 74 days in Figure 6.4a corresponds to a period of decreasing mass loss from 70 to 74 days in Figure 6.4b.

Swelling pressure

Data showing the swelling pressure of the sample, measured directly beneath the sample as depicted in section 4.2, Figure 4.2, over the course of the erosion experiment is illustrated in Figure 6.4c.

Figure 6.4c shows that the swelling pressure generated by the bentonite increased rapidly, corresponding with initial water uptake and saturation of the sample, to a value of 515 kPa over the course of 1 week. The observed swelling pressure is an order of magnitude less than what might be expected of a sample compacted to this dry density. The bentonite buffer, when compacted to the same density as the sample examined in this work, is expected to produce a swelling pressure in the repository of between 2 and 10 MPa, depending on the chemistry of the groundwater when fully saturated (Juvankoski 2010).

This may be because of a variety of factors, including the fact that the ratio of fracture aperture to sample height in this instance (1:100) is far removed from that expected in a repository scenario (1:90000). Thus the sample is unconfined relative to the level of

confinement we may come to expect in a full scale deposition hole; 1.75m in diameter and 9m in height, intersected by fracture apertures of the same magnitude as that examined in this work. Hence the loss of mass from the central compartment into the fracture by extrusion, may reduce the dry density and swelling pressure to a far greater extent in the experimental work than in a full scale scenario.

Another explanation for this lack of swelling pressure generation, is that the sample had free space in which to swell in the compartment before extrusion, thus increasing the void ratio of the sample to the point where the associated swelling pressure was an order of magnitude less. Cui and Tang (2013) derive a relationship (Figure 6.5) between constant volume, laboratory scale swelling tests for various bentonites and bentonite/ sand mixes and the vertical stress (P), for a range of values of the bentonite void ratio (e) of the form $P = 2.1698 \, e^{-4.111}$.
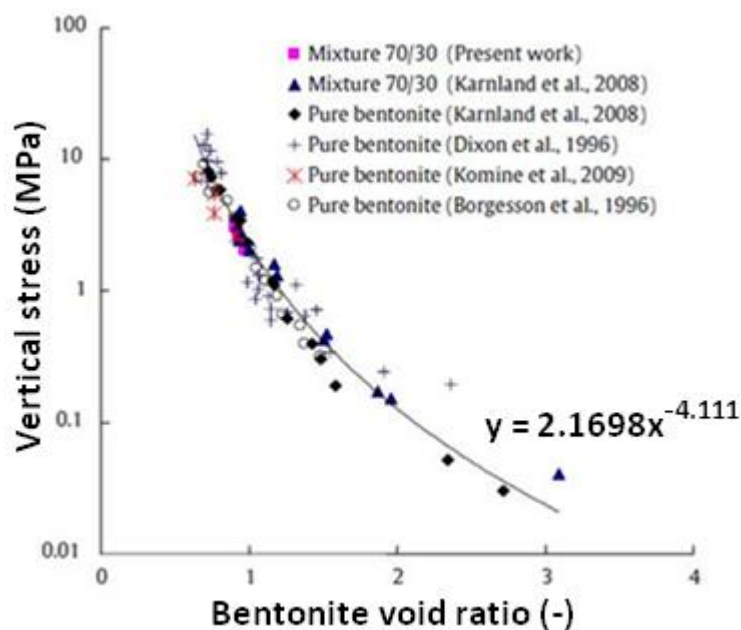
Figure 6.5: Relationship between vertical stress and void ratio for various bentonites and bentonite/sand mixes. Adapted from Cui & Tang et al (2013)

After trimming to fit the compartment, the pellet prior to installation in the cell was 18.65mm in diameter, 10.3mm in height and had a water content of 17.82%. If fully saturated and confined, based on the data of Cui and Tang (2013) the sample would be

expected generate a swelling pressure somewhere in the region of 11MPa as detailed below:

As void ratio, $e = \dfrac{G_s.V}{m_s} - 1$

Where: $G_s = specific\ gravity\ of\ MX80 = 2.78\ (Kiviranta\ and\ Kumpulainen\ 2011)$

$V = Volume\ of\ sample = 2.812\ cm^3$

and, $m_s = Mass\ of\ solids\ in\ sample = 4.672g$

$$\therefore e = \frac{2.78 \times 2.812}{4.672} - 1$$

$$\therefore e = 0.6732$$

$$\therefore P = 2.1698\ (0.6732)^{-4.111}$$

$$\therefore P = \mathbf{11.04\ MPa}$$

Now consider the case of the compartment being 1mm larger in diameter and height than the pellet i.e. 19.65mm in diameter and 11.3mm in height. Once expanded to occupy the compartment, this would result in a new volume for the pellet of 3.43 cm^3. This equates to a decrease in swelling pressure as demonstrated:

$$\therefore e = \frac{2.79 \times 3.43}{4.672} - 1$$

$$\therefore e = 1.0454$$

$$\therefore P = 2.1698\ (1.0454)^{-4.111}$$

$$\therefore P = \mathbf{1.81\ MPa}$$

Further, taking the erosion of material from the onset of the experiment into account i.e. assuming mass is lost before the sample is capable of generating its full swelling pressure, the observed maximum swelling pressure in this experiment is not unexpected.

Following the initial rise in swelling pressure (Figure 6.4c), the swelling pressure then decreased over the course of an approximately 90-day period to a value of 350kPa before stabilising around this value for the remaining 40 days. Also of note in Figure 6.4c, is that

after the initial swelling pressure rise, whilst the general trend is decreasing because of mass loss from the system, the swelling pressure exhibits regular periodic fluctuations.

Radial extrusion

Figure 6.6 illustrates the radial extrusion of bentonite (from the sample emplaced beneath the brass plug) at snapshots of 10, 50, 90 and 130 days. The quantified areas of accessory minerals at these points in time are bounded by turquoise in the right hand side of Figure 6.6. These extrusion areas were quantitatively analysed in terms of the plan view area in mm^2, using image analysis as described in section 4.8.
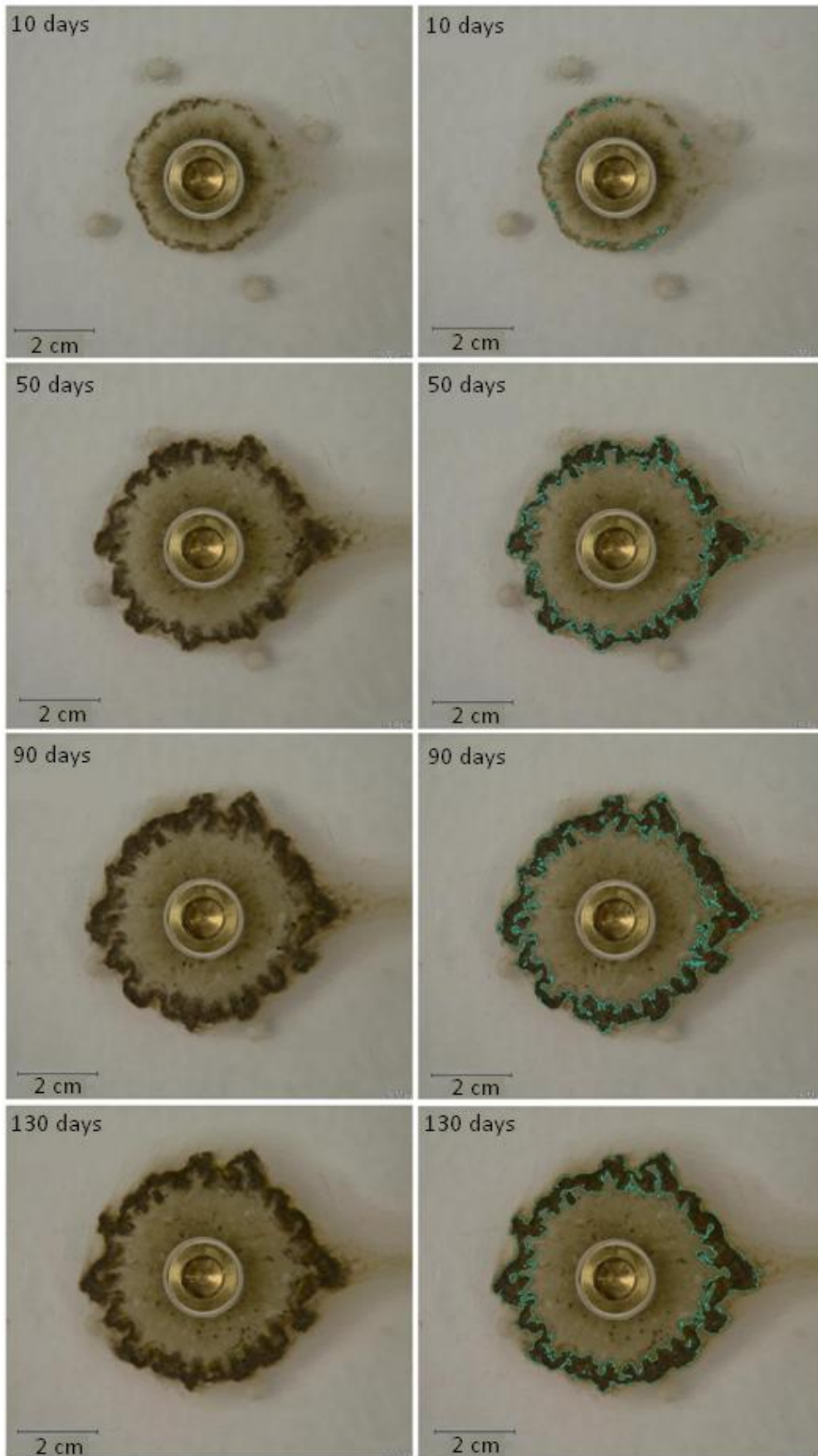
Figure 6.6: MX80, variable aperture, radial extrusion after 10, 50, 90 & 130 days. Image analysis technique with evaluated mineral ring area depicted in images on right hand side.

Figure 6.4d shows the mean radial extrusion distance plotted against time for the duration of the experiment as estimated from the image analysis.

It is apparent from Figure 6.4d that most (≈80%) of the extrusion occurs within the first 40 days, with an initial rapid extrusion period of 6 days, corresponding to the initial wetting phase. After this 40-day period, the overall zone of bentonite extrusion increases more gradually, with the final 20 days showing no apparent change.

Analysis of the images in Figure 6.6 shows that as extrusion occurs, a dark ring forms around the periphery, of gradually increasing thickness. This accumulation is the darker region of accessory minerals which is in line with observations by previous researchers, as described in section 3.8.

The extrusion of bentonite into the fracture can be summarised as follows. As bentonite extrudes into the fracture, the accessory minerals, which are predominantly darker in colour, are transported along with the lighter-coloured montmorillonite particles. This process of swelling and extrusion results in decreasing density of the bentonite with radial distance from the central plug. At the edge of the extrusion zone, where the density of the bentonite is very low and it is in contact with the flowing deionised water, the montmorillonite particles are susceptible to erosion through the formation of colloids. These colloids are eroded by the advective flow through the fracture, leaving the larger diameter accessory minerals behind. As more bentonite extrudes into the fracture from the central compartment, more accessory minerals are transported and thus the thickness of the accessory mineral ring increases.

From visual inspection of the images in Figure 6.6 it is clear that there is a radial colour change across the extruded material; i.e. the bentonite material appears more dense (darker) towards the central sample and appears less dense (lighter) moving radially outward, this is in line with the conceptual model detailed in Apted et al et al (2010) in section 3.8.1, Figure 3.16.

Early in the experiment (Figure 6.6), most apparent after day 10, there appears to be a distinct narrow zone at which the density changes across the extruded material. This is illustrated in Figure 6.7, which shows the extent of extrusion after 10 days and density

profiles along two sections (α2 – α1 and β2 – β1), using pixel gray value as a proxy for sample density. A low gray value represents the most dense material and a high gray value represents the least dense material, at the outer edge of the extruded region. Discounting aberrations caused by the presence of darker coloured accessory minerals throughout the extruded material, it is evident from Figure 6.7, that the density decreases almost linearly moving radially outward from the sample until approximately 5mm, at which point the density is consistent for the last 2mm.
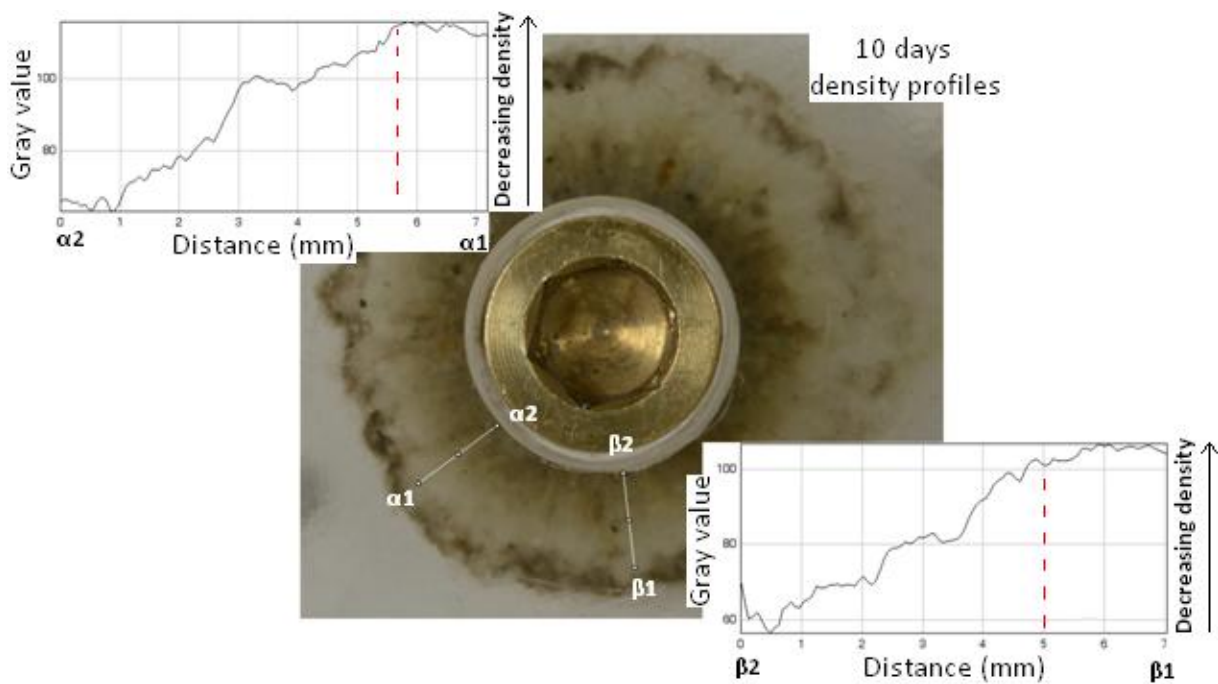
Figure 6.7: MX80, variable aperture, density profiles across two sections after 10 days.

Later in the experiment, taking 130 days as an example as detailed in Figure 6.8, the density profile appears to be more linear across the entire extent of the extruded material, with no peripheral region of constant density. This may be due to the fact that early in the experiment, when mass loss is high, the rate of water and density redistribution across the extruded material is not fast enough to balance the rate of mass loss. Later in the experiment, however, when mass loss is low, the system has time to redistribute water and mass across the extruded material.
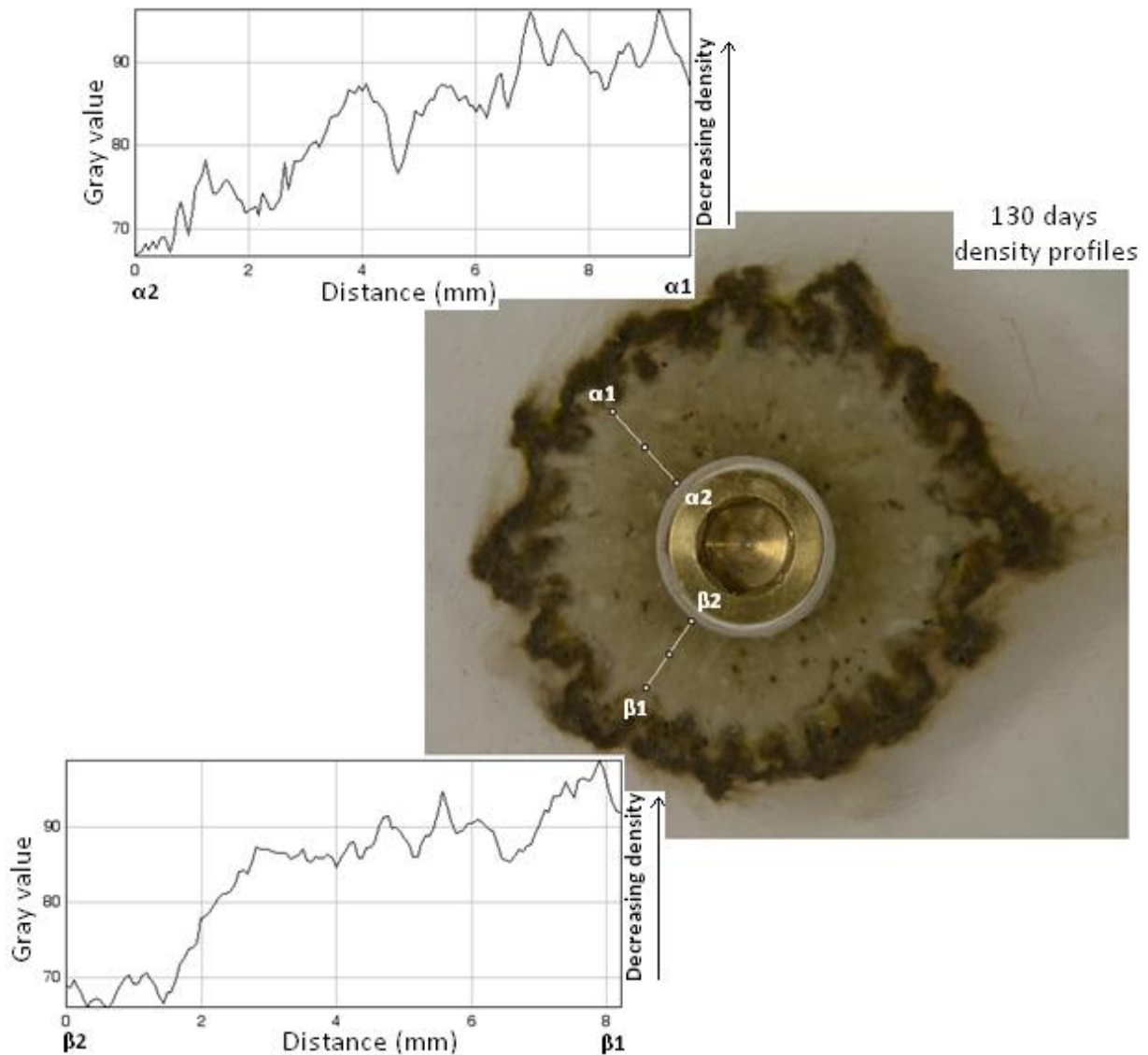
Figure 6.8: MX80, variable aperture, density gradient along two sections after 130 days.

At the outer margins of the expanded material (Figure 6.9), beyond the dark mineral ring, where the density of bentonite is extremely low, it is subject to a shear force by the flowing water. The extruded bentonite appears to curve in the direction of flow, towards the outlet port of the cell. Figure 6.9 depicts identical images, in Figure 6.9b), the areas which are subject to shear by the flowing water have been highlighted.

This shear effect of the flow is relatively minor. Analysis of Figure 6.9 shows that within the accessory mineral ring, the bentonite expands in a radially symmetric manner into the fracture i.e. the amount of expansion against the direction of flow is the same as that along

it. This indicates that the shear force imparted on the bentonite by the flowing water is insufficient to mechanically affect the bulk of the extruded material.

In summary, despite the relatively high water velocities in this experiment (in the order of 10^{-4} m/s) the influence of flow on the extrusion behaviour appears to be minimal, only affecting the material of low density at the edge of the extruded material.
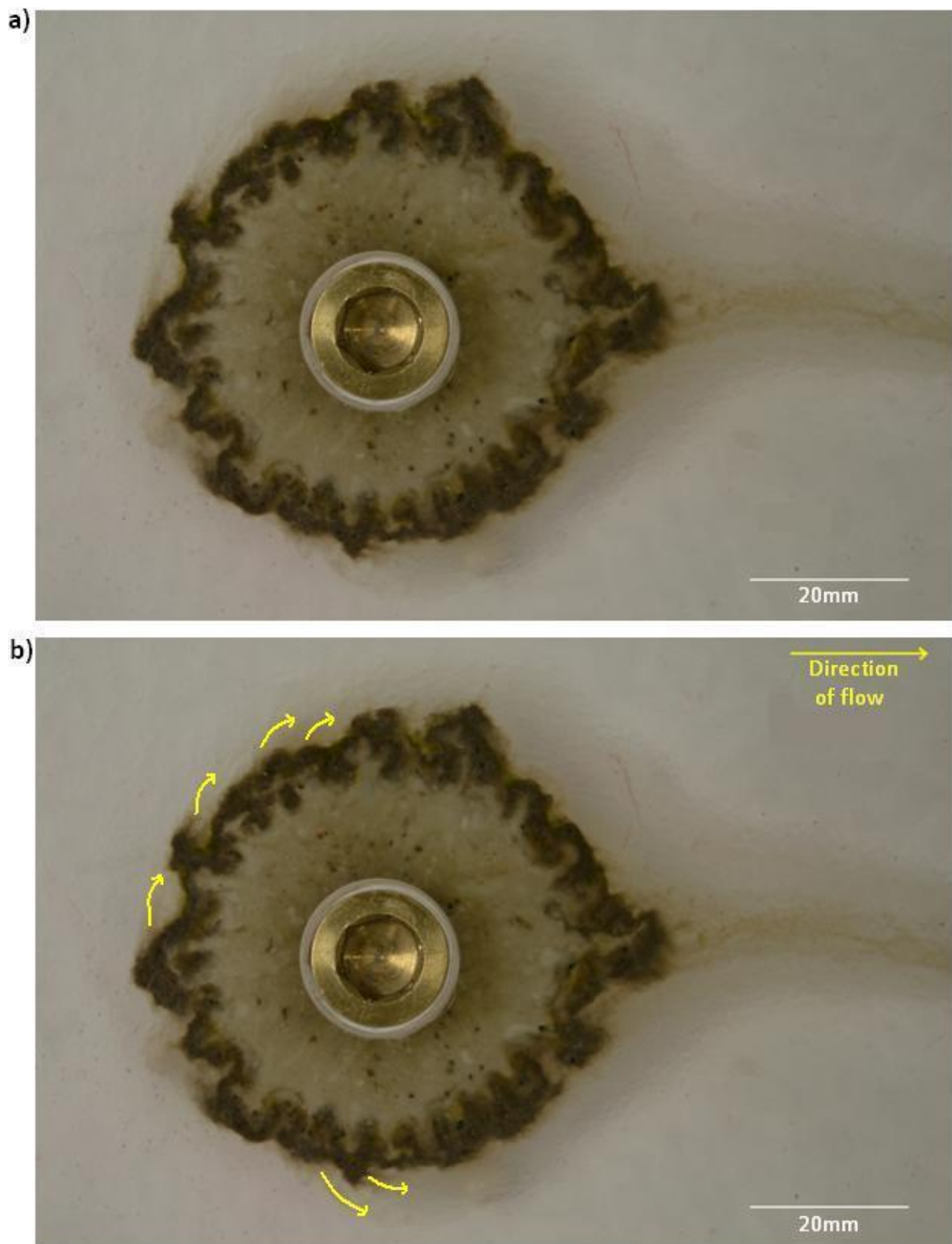
Figure 6.9: MX80, variable aperture cell, influence of flow on extruded material

Accessory mineral ring

As discussed in section 4.8, image analysis was used to estimate the total area, in plan view, containing accessory minerals. Figure 6.4e is a plot of the accessory mineral ring area with time. During the initial 40-day extrusion phase, the accessory mineral ring exhibits a period of rapid growth which, after a period of lag, commences at approximately 13 days. This continues for 27 days, to day 40, before its growth rate decreases. This period of gradual growth of the mineral ring occurs in a stepwise fashion, for approximately 60 days, with periods of relative stability and periods of increased growth rate, before it stops growing and stabilises with an area of 10cm^2.

6.2 Mass loss and accessory mineral ring image analysis data correlation

In order to assess which factors may be affecting the trends in erosion rate, correlations between mass loss data and accessory mineral ring image analysis were evaluated, so that fluctuations in erosion rate over time were compared with changes in the rate of growth of the accessory mineral ring (Figure 6.10).
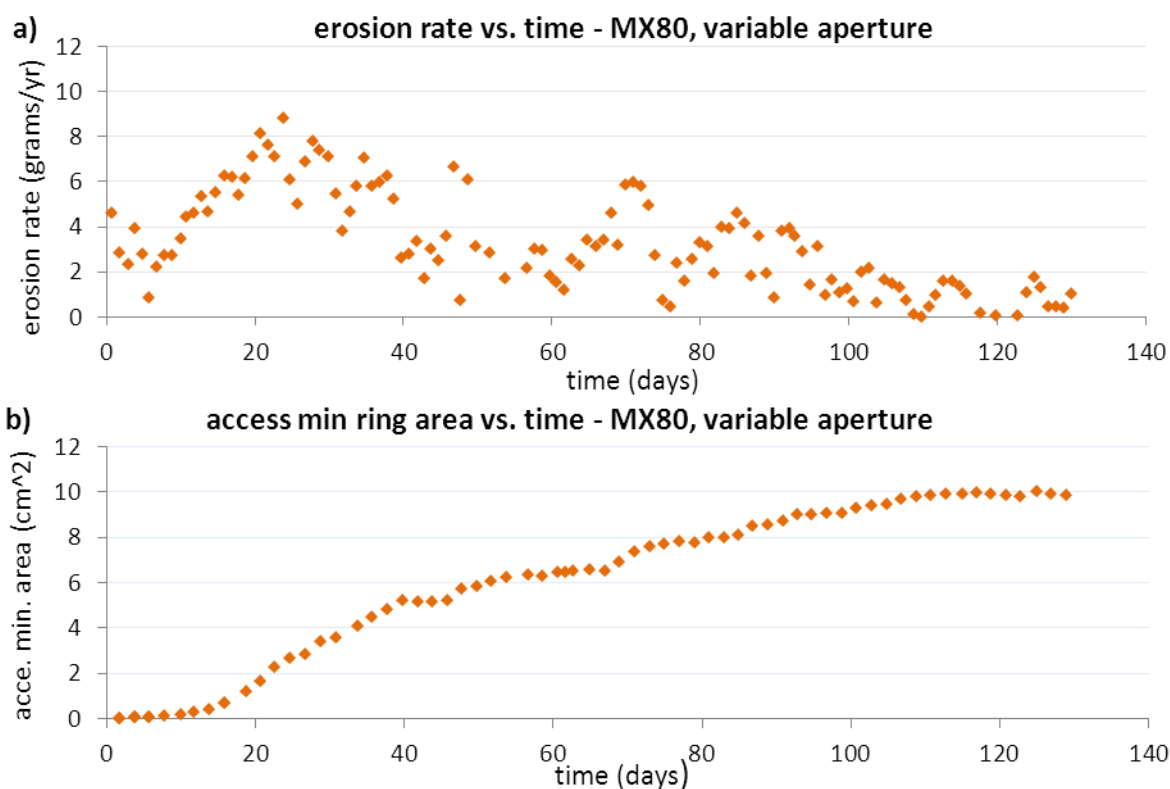
Figure 6.10: MX80, variable aperture, erosion rate, swelling pressure and accessory mineral ring area against time.

The initial rise in erosion rate up to 23 days is discussed in section 6.1. Here, the reason underlying the subsequent decrease in erosion rate is explored.

It is postulated that the growth and establishment of the accessory mineral ring at the edge of the extruded material causes the gradual decrease in erosion rates after the first 23 days. This finding would confirm the proposition of Neretnieks et al (2009) that the accessory minerals inherent in MX80 may be effective in mitigating against erosion of montmorillonite.

Apparent in Figure 6.10b is that the accessory mineral ring begins to establish itself at 13 days. There is then a 10-day period, between days 13 and 23, within which the accessory mineral ring is growing and the erosion rate is continuing to increase. It follows, therefore, that if the formation of the accessory mineral ring is responsible for the subsequent decrease in erosion rate from day 23, a critical thickness of accessory mineral ring barrier must be deposited before attenuation of the erosion rate becomes apparent. The thickness of barrier sufficient to prevent erosion will presumably will be a function of the mass of accessory minerals deposited, the extent of bentonite extrusion and the fracture aperture.

It is also apparent from Figure 6.10b that there is a stepwise growth in the accessory mineral ring between day 40 and day 100. Each step in the mineral ring growth corresponds to a period of erosion in Figure 6.10a. As the ring is supplemented by incoming accessory minerals, the thickness of the ring increases and the porosity of the ring decreases as smaller accessory minerals are strained within the accessory mineral ring matrix. This goes some way to explaining why each subsequent erosive period is of a lesser magnitude than the last as the ring becomes more resilient with each erosive period. Thus supporting the hypothesis put forward by Richards and Neretnieks (2010) that the accessory mineral ring can indeed function as a granular, porous filter medium, allowing fewer and fewer montmorillonite particles through as it grows.

6.3 Post-test analysis

Two forms of post-test analysis of the material eroded from, and remaining in, the flow cell were undertaken:

1. XRD on samples from '*points of interest*' taken from the fracture face and samples of the material eroded from the cell.

2. Optical microscopy on the same samples described in 1.

This analysis was performed with a view to understanding the deposition process of the various mineral phases within the rock fracture and to identify the minerals which were being eroded from the system. Optical microscopy can also give an insight into the particle size of the deposited mineral phases, a characteristic which is directly linked to the efficacy of granular media used in traditional filters. Evidence for potential changes in mineralogy of these mineral phases and for biological activity in the cell throughout the course of the experiment were also considered.

6.3.1 XRD analysis
Analysis of material on the fracture surface

Samples were taken from three points on the fracture face according to the methodology described in section 4.7.2, as depicted in Figure 6.11:
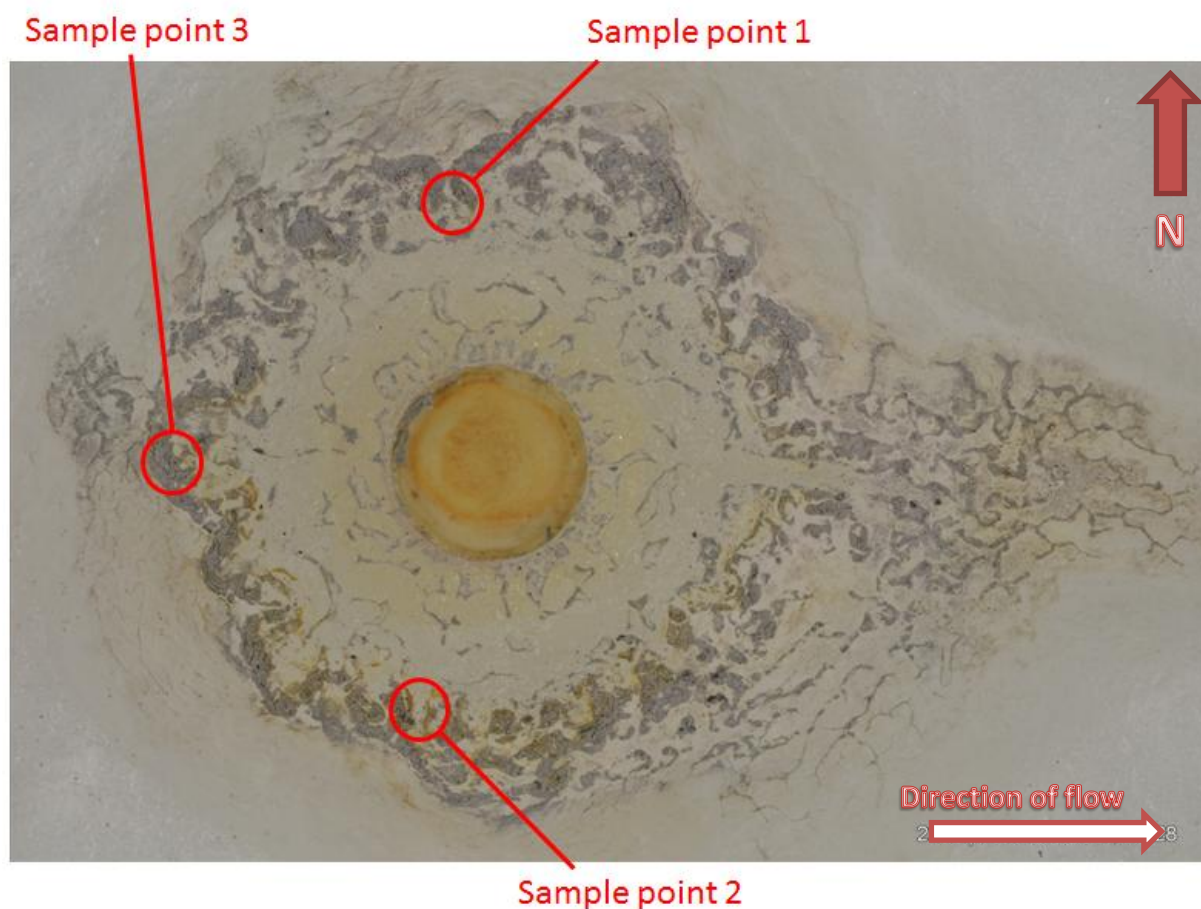
Figure 6.11: Image of bottom half of MX80 fracture cell with extruded material after drying. Sample points indicated

As discussed in section 4.7.2, because of the small size of the samples highlighted in Figure 6.11, the sample holder itself contributed significantly to the observed diffraction pattern during analysis. Consequently, the sample holder was scanned on its own first, to assess this contribution. The XRD pattern for the sample holder on its own is given in Figure 6.12. The sample holder produces three peaks of diminishing intensity: A large broad peak between 8° and 22° 2Ө and two less discernible peaks between 26° and 34° 2Ө and 41° and 24° 2Ө.
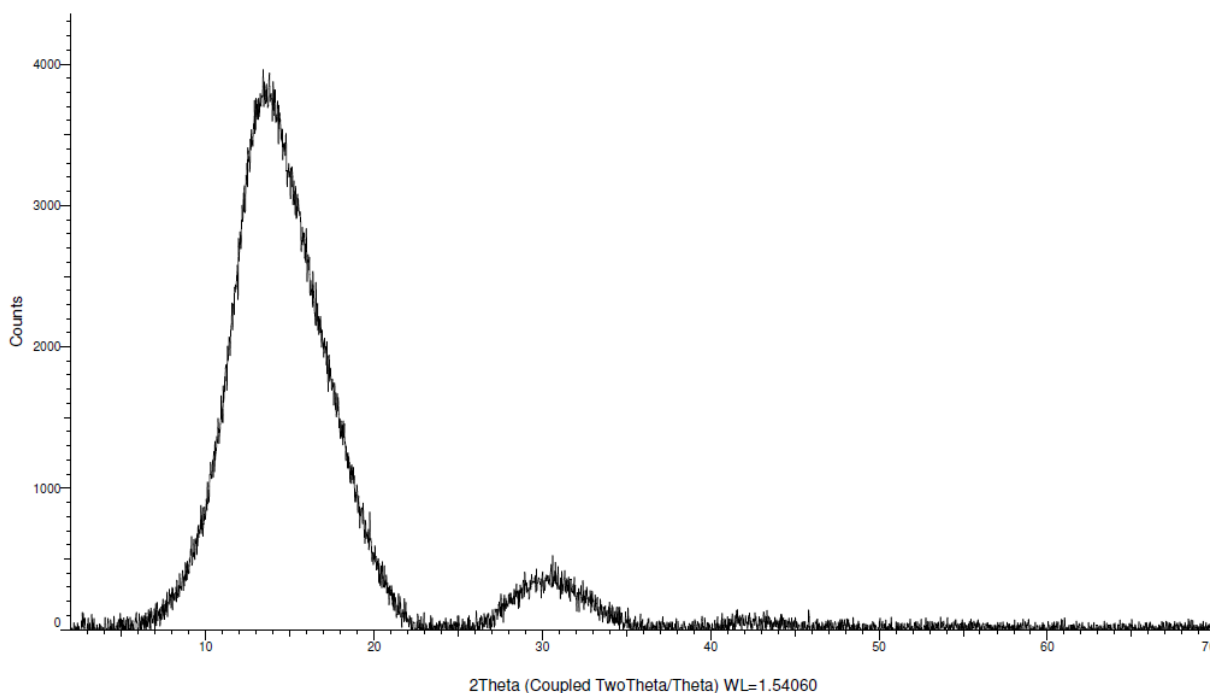
Figure 6.12: XRD pattern for empty sample holder.

Sample 1

Sample point one (Figure 6.11) corresponded to the inner region of the accessory mineral ring towards the top of the image. The results of the XRD scan with the background removed via *diffract.eva* software, and each of the minerals identified, is detailed in Figure 6.13. The diffractogram appears as various colours (magenta, green, red, black and blue) because the figure is a composite of multiple scans taken at various rotations of the sample holder, as described in section 4.7.2.
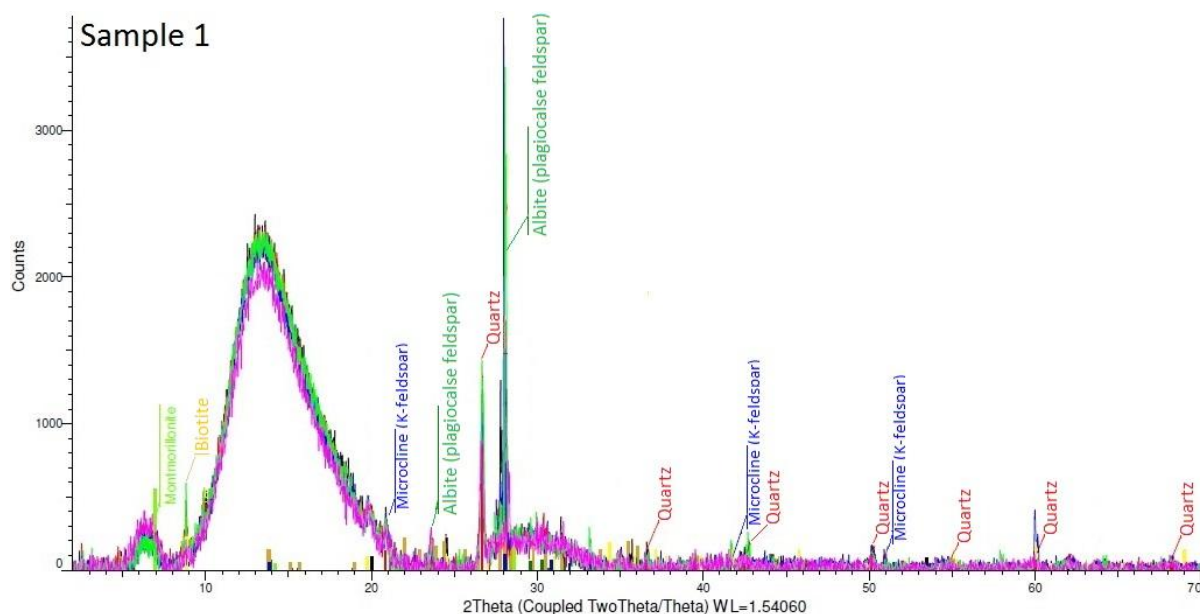
Figure 6.13: Labelled X-Ray diffraction pattern for sample 1 with background removed.

It is clear from Figure 6.13 that the mineralogy of the sample is dominated by crystalline phases. The broad peak corresponding to montmorillonite in the diffractogram for as-delivered MX80 (Figure 6.14) has been significantly reduced in intensity relative to the other peaks in the diffractogram, and the sharp peaks between 26° and 29° have increased.
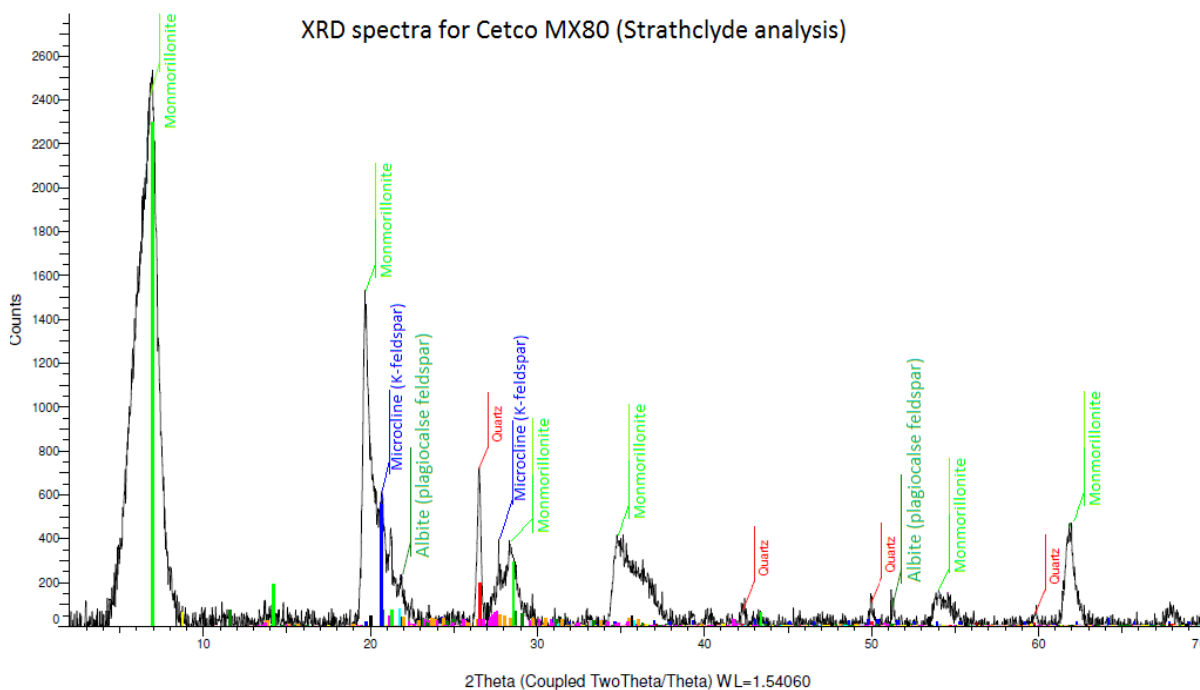
Figure 6.14: Labelled x-ray diffractogram for Cetco MX80 bentonite

The large broad peaks between 8° and 22° 2Θ and the less discernible broad peak between 26° and 34° 2Θ are from the amorphous sample holder, as also depicted in Figure 6.12.

The most significant peaks correspond to quartz at 26.5^o 2Θ and albite at 28° 2Θ. The iron rich mineral biotite is now visible at 9° 2Θ, this was not apparent in the original scan of MX-80, presumably because of its trace quantities in relation to the dominating phase of montmorillonite. Biotite was not recognised as being present by either Philips (2014) or Kiviranta and Kumpulainen (2011) through XRD analysis, however, Kiviranta and Kumpulainen (2011) did identify the mineral as being present in trace quantities in Cetco MX80 by optical microscopy.

As discussed, Figure 6.13 constitutes multiple scans of the same material with the sample holder oriented at various rotations; the 5 different coloured scans are overlain. Peaks for certain minerals, such as biotite, only appear at specific orientations of the sample holder i.e. the 9° 2Θ peak for biotite is most apparent in the green scan. Further to this, subsequent peaks which might be expected for a specific mineral do not appear to be present, such as the peak at 34.5^o 2Θ for biotite. This is because of the very small quantities of these minerals present and the resultant high signal to noise ratio between the sample holder and the sample. The fact that all crystal orientations of each mineral will almost certainly not be present with a sample of this size is also significant in this regard.

Sample 2

Sample two (Figure 6.11) corresponds to the inner region of the accessory mineral ring at the bottom of the image, specifically chosen to include a region of material which appears to have undergone some mineralogical change; there is a clearly discernible red/orange hue to the material which may correspond to an iron-rich region. The diffractogram for sample 2 is shown in Figure 6.15:
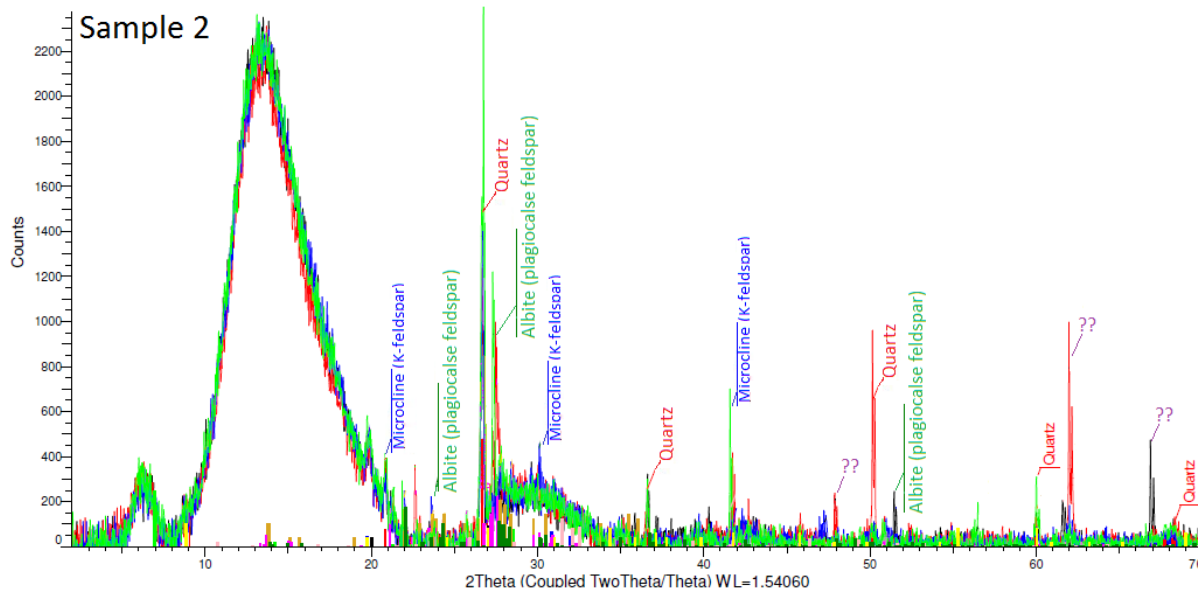
Figure 6.15: Labelled X-ray diffraction pattern for sample 2 with background removed.

As is evident in Figure 6.15, the sample is again dominated by the crystalline phases quartz, plagioclase and K-feldspar, with the same diminished peak for montmorillonite and background signal apparent. Also present is a peak for biotite at 9° 2Θ, although this has diminished relative to the biotite peak in Figure 6.13. This may be an effect of the sample size. Three additional peaks appear in Figure 6.15 at 48°, 62° and 67° 2Θ which are not in the spectra for accessory minerals isolated from MX80 (Figure 6.14) indicating that some form of mineralogical change has occurred throughout the experiment. One possible explanation for the additional peaks in Figure 6.15 is that the red/orange deposit visible in the cell is a result of oxidation of the iron-rich biotite. This would also be in keeping with the reduction in the biotite peak. Lepidocrocite (Esmeraldite or Hydrohematite) is one such reddish brown mineral which is formed as a result of the oxidation of iron bearing minerals underwater. The presence of these minerals in the samples however could not be confirmed by fitting the database spectra for these minerals to the sample data. The additional peaks at 48°, 62° and 67° 2Θ could not be identified, despite an exhaustive search of the mineral database in the *diffract.eva* software. If the mineralogical change is to the result of a chemically mediated process, one might expect that the colour change would occur in a radially consistent pattern around the circumference of extruded material. From Figure 6.11 however, it is apparent that this change in colour appears only around the bottom half of the sample.

One possible explanation for the non-uniform mineralogical change is that the process is bacterially mediated. The development of a biofilm at one particular site on the mineral ring, followed by growth around the circumference of the mineral ring, may explain the non-uniform distribution. Bacteria are certainly indigenous in MX80 (Pedersen 2000) and Fe-cycle bacteria in particular have been found to be indigenous in smectite deposits from other regions of the U.S. (Shelobolina et al 2005). Further evidence of biological activity was found throughout each experiment with MX80. For instance, a build-up of a gas was noted in the effluent bottle from the cell when left overnight with the top sealed with *parafilm*, as depicted in Figure 6.16:

Figure 6.16: Images of parafilm bulge and apparent gas build up inside effluent bottles from the cell.

As noted in section 2.2.3, biological processes in the buffer are hampered by the > 2MPa swelling pressures generated in the main body of the buffer in the deposition hole. In the extruded material however, the lack of confinement and associated swelling pressure, may facilitate microbial activity in those species indigenous in the MX80 or imported via the incoming groundwater.

In summary, the mineralogical changes evident in the accessory mineral ring may be either chemically or biologically mediated processes. With regard to implications for a GDF scenario, such processes may be favourable or detrimental. Mineralogical changes could be detrimental in the sense that the dissolution of mineral phases by chemical alteration may ultimately reduce mineral stability. However, if these processes are only occurring on the trace biotite/ hematite iron rich minerals they should not be significant, because the accessory mineral ring is predominantly comprised of quartz, plagioclase and K-feldspar.

Biological activity and microbially mediated mineralogical changes may in fact be beneficial, in the sense that bacterial adherence to a mineral surface is often facilitated by the excretion of an exopolymeric substance (Perdrial et al 2009). If the accessory mineral ring is considered to be a granular, porous media matrix, the excretion of this exopolymeric substance in the pore space of the matrix may serve to reduce its porosity, thus reducing further still the pathways through which montmorillonite colloids can migrate and erode.

Sample 3

The final sample point (Figure 6.11) corresponds to the outer edge of the accessory mineral ring in the left hand side of the image i.e. the point at which flow from the inlet port first contacts the extruded material. No mineralogical changes were evident visually in the sample. The diffraction pattern for sample 3 is illustrated in Figure 6.17. Consistent with samples 1 and 2, it is dominated by the crystalline phases quartz, plagioclase and K-feldspar.
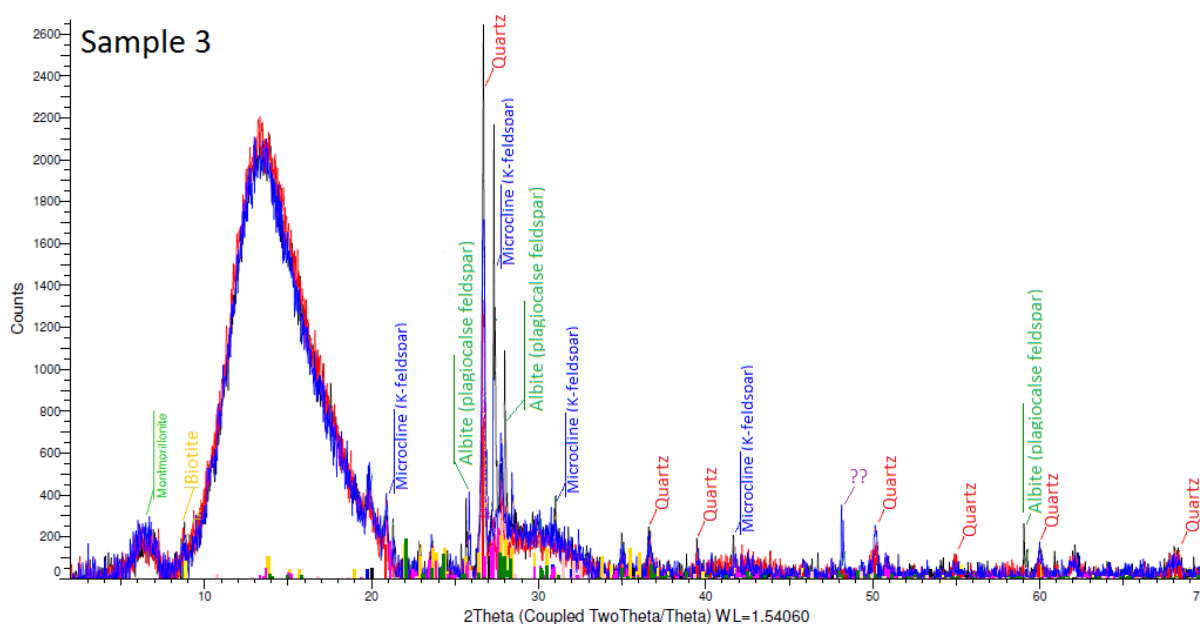
Figure 6.17: Labelled X-ray diffraction pattern for sample 3 with background removed.

The presence of biotite is more discernible in sample 3 (Figure 6.17) than in sample 2 (Figure 6.15) where the orange/red hue was observed, but not as large as the biotite peak in sample 1. Also visible in Sample 3 (Figure 6.17) is one of the peaks at 48° 2ϴ that was found in Sample 2. As noted previously, this peak is not in the spectra for the accessory minerals isolated from MX80 and may be from a mineral alteration product.

Eroded material

Two samples of the eroded material from the cell were also analysed by X-ray diffraction using the method detailed in section 4.7.3. None of the narrow, sharp peaks corresponding to the crystalline minerals in samples 1, 2 and 3 are present in Figure 6.18. The same noise artefacts from the sample holder can be identified, but to a lesser extent because the surface area of the sample holder was covered by the filter paper. From the scans depicted in Figure 6.18, it seems that only montmorillonite has been eroded.
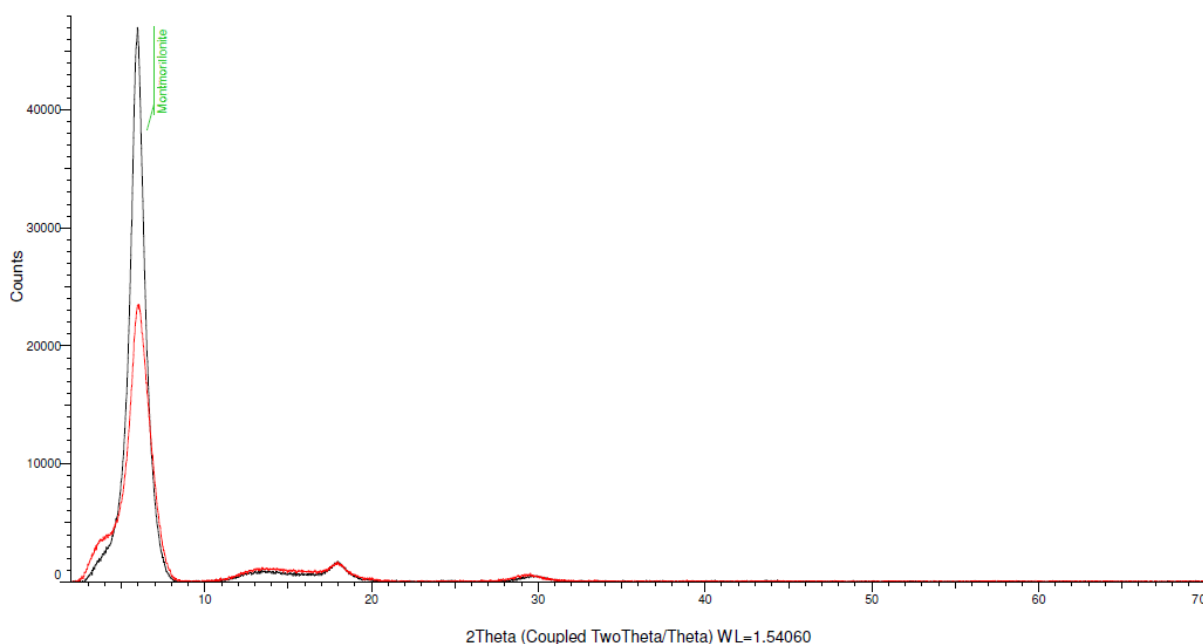
Figure 6.18: Labelled X-ray diffraction pattern for 2 eroded samples (red and black scan), background removed.

The intensities of the montmorillonite basal reflections are enhanced (the counts scale extends to 48,000 as opposed to 2000-3000 for all other XRD spectra in this chapter) in Figure 6.18 and, hence, the relative intensities of any eroded accessory minerals may have been masked. To address this, the counts axis was truncated to 2500, to enhance the intensity of any trace accessory minerals in the spectra. The resultant scan is shown in Figure 6.19 and one further peak is visible at 18° 2Θ. This additional peak is, however, likely to be the secondary peak for montmorillonite (also visible in Figure 6.20, the spectra for montmorillonite isolated from MX80 at 18° 2Θ). None of the accessory minerals present in MX80 produce a peak at 18° 2Θ. The large broad peak between 10° and 20° 2Θ and the less discernible peaks between 28° and 32° 2Θ are background peaks from the sample holder.

Material eroded from MX80, variable aperture cell, composte of two dates (truncated y-axis)
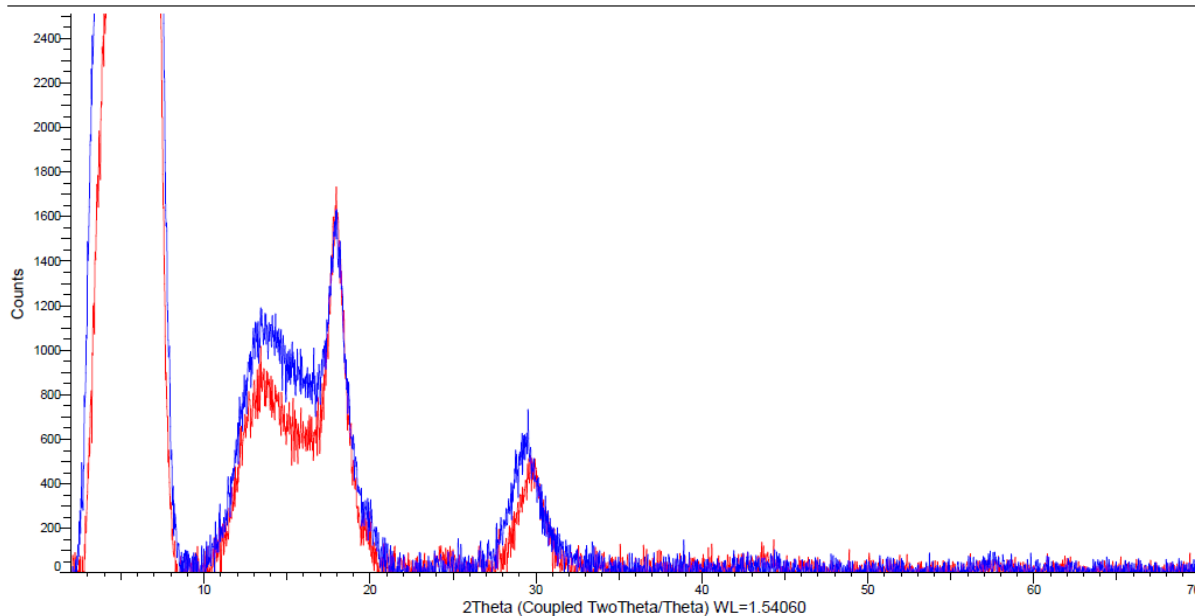
Figure 6.19: X-ray diffraction pattern for 2 eroded samples (red and blue scan), background removed, Y-axis truncated.

The slight shift in the montmorillonite peak to 6°, in Figure 6.19 from 8.5^o 2Θ in the original scan for montmorillonite (Figure 6.20) is likely to be the result of variations in the water content between samples.

Montmorillonte isolated from MX80
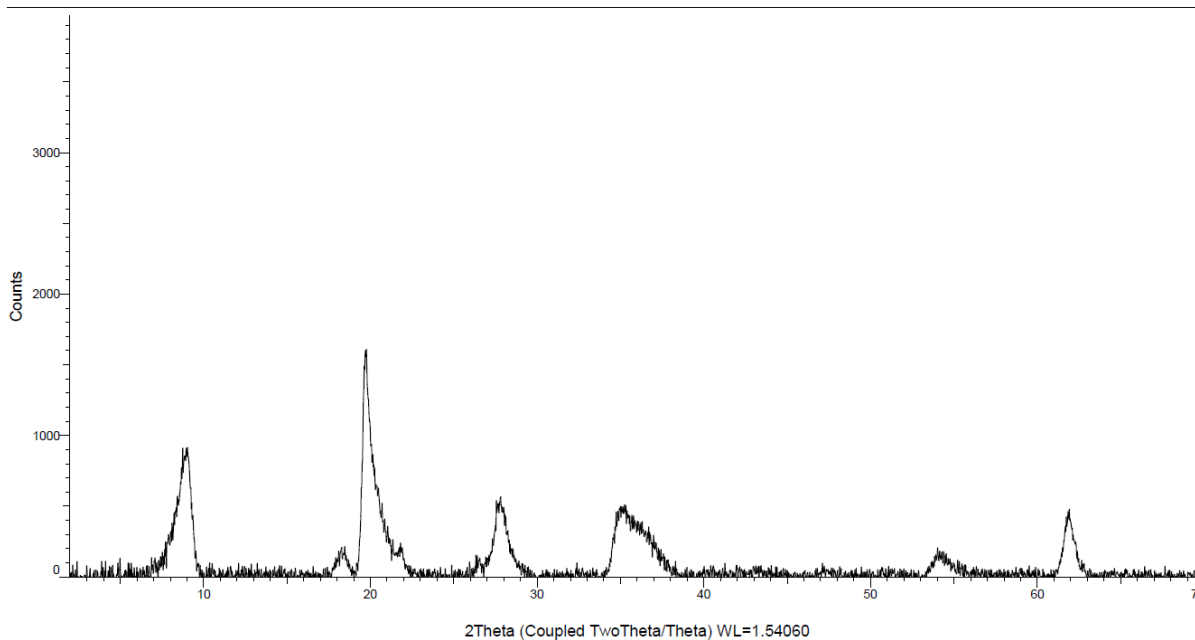
Figure 6.20 X-ray diffraction pattern for montmorillonite isolated from MX80 and homoionised to Sodium

A comparison of Figure 6.18 with Figure 6.21, an X-Ray diffractogram of oriented montmorillonite mounts in various states of hydration from the United States Geological Survey (2001) illustrates the similarity in the diffraction patterns of Figure 6.18 and the blue scan for untreated montmorillonite from Figure 6.21, to confirm that indeed, only pure montmorillonite is eroding from the system. Figure 6.21 also illustrates the effect of hydration on the diffractogram peaks for montmorillonite, explaining the slight shift in the montmorillonite peaks between the original MX80 and the eroded material.
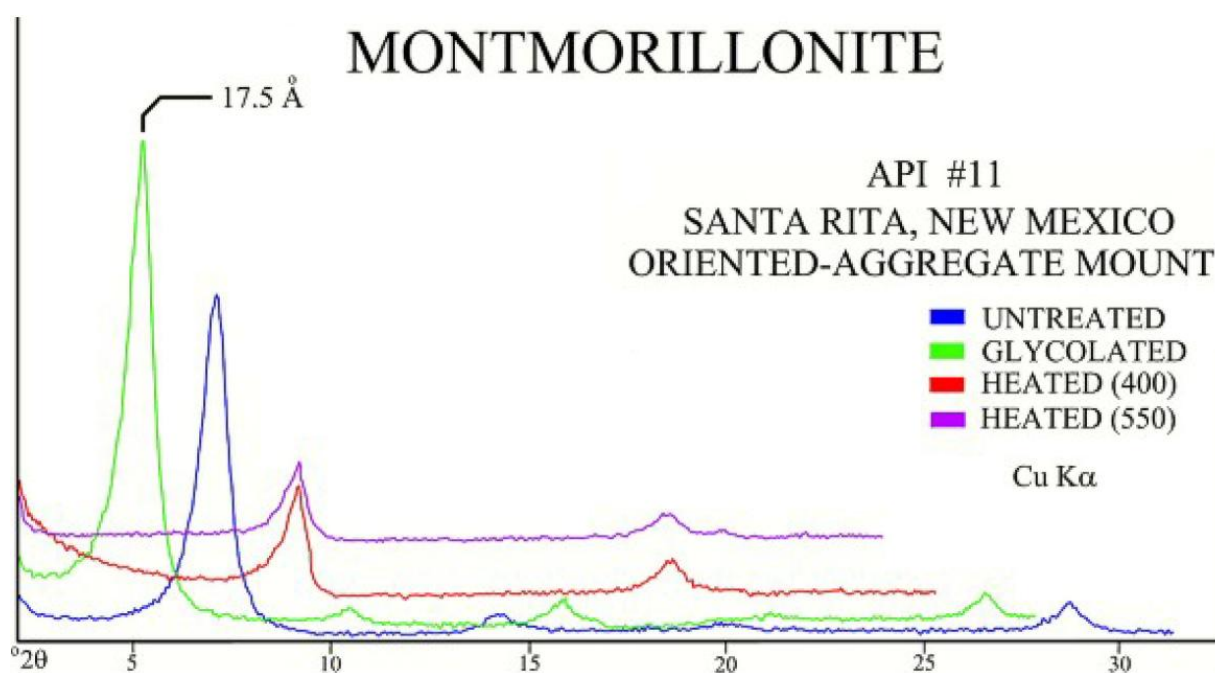
Figure 6.21: USGS XRD data for montmorillonite in various states of hydration (USGS 2001).

The over-arching message to be taken from the post-test XRD analysis is that the mineral ring is dominated by quartz, plagioclase and potassium feldspar, which are the accessory minerals most abundant in MX80. These minerals are not present in the eroded material, which is comprised of pure montmorillonite. This occurs despite relatively high water velocities in the fracture (in the order 10^{-4} m/s) relative to those that may be expected to occur in groundwater at depth. Hence, in a repository scenario, accessory minerals are highly unlikely to be eroded.

6.3.2 Optical microscopy

Optical microscopy was performed on each of the samples circled in Figure 6.11 with the aid of a *Nikon Eclipse LV100ND* optical microscope. Optical microscopy was also performed on a sample of accessory minerals isolated from bulk MX80 material by a series of centrifugations. In order to perform the microscopy, each of the 3 samples from section 6.3.1 (stored in weighing boats), was subsampled and the subsample transferred to a glass slide. 4x, 10x, 20x and 40x magnification in both bright and dark field methods were employed.

Accessory minerals isolated from the MX80

Shown in Figure 6.22 are accessory minerals that have been isolated from the *as delivered* MX80 bentonite at both 10x and 20x magnification.
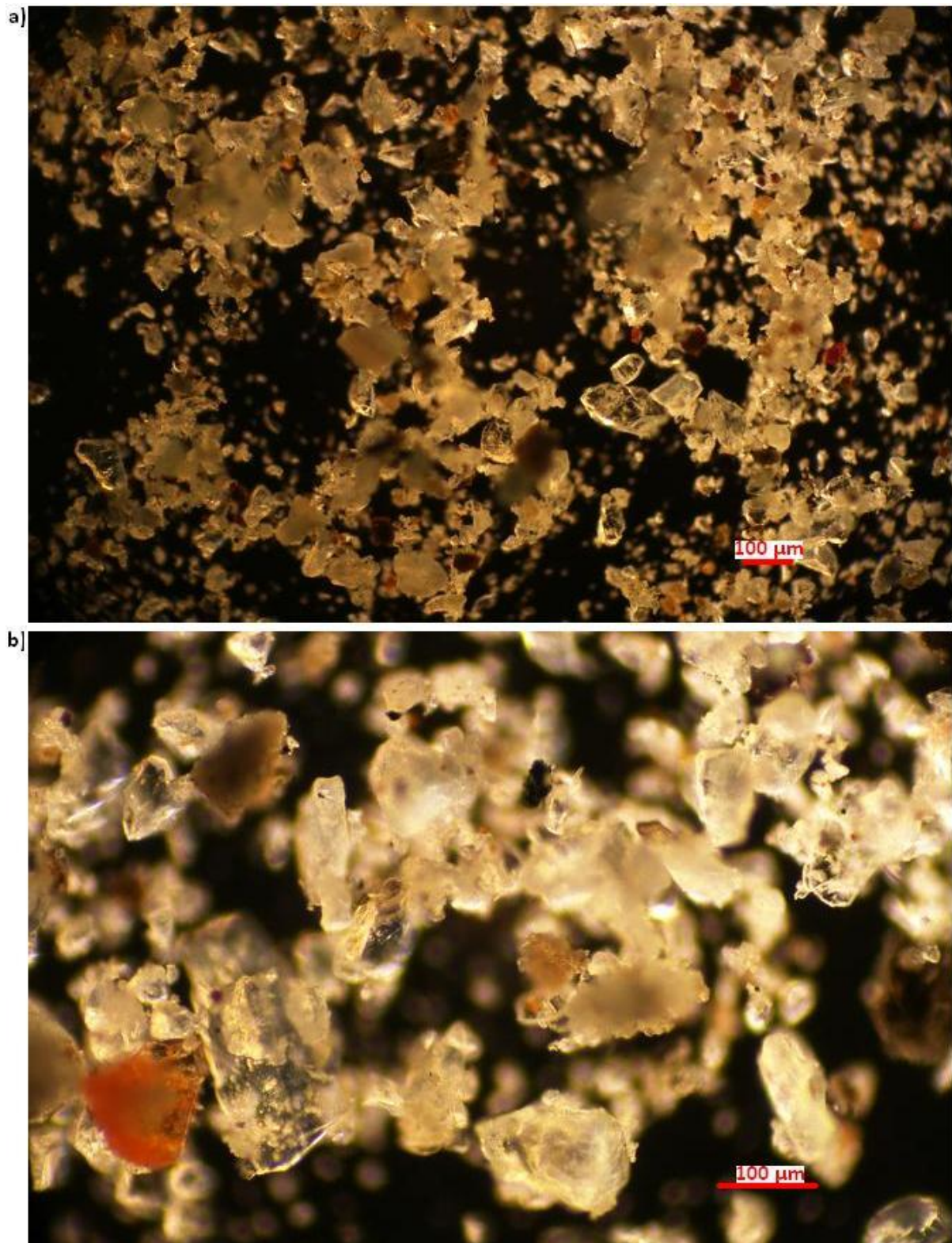
Figure 6.22: Accessory minerals isolated from MX80 by centrifugation at a) 10x magnification and b) 20x magnification

Figure 6.22 shows that the accessory minerals are mainly in the size range 10 – 200 μm. A small proportion of the minerals are larger; up to 300 μm across their widest lateral

dimension. The sample appears to be dominated by quartz, in line with the mineralogical data provided by Philips (2014) for the material, with the more opaque and red/ brown minerals visible in Figure 6.22b likely to be the feldspar and plagioclase phases. Black coloured minerals, more identifiable in Figure 6.22b, are likely to be cristobalite and/or pyrite, which were also identified by Philips (2014).

Post-test samples from experiment

Photomicrographs of sample points 1, 2 and 3 (Figure 6.11) of the material taken from the plate post-test at both 4x and 10x magnification are shown in Figure 6.23. This material appears to be mostly non-clay minerals i.e. the accessory minerals contained within the MX80, confirming the X-Ray diffraction data of the sample shown in Figure 6.13. Furthermore, the size range of these minerals is consistent with the size range of minerals from the material isolated from MX80 by centrifugation (10 – 200 μm, each vertical division in Figure 6.23a, c and e represents 100 μm). Indicating that no physical straining (exclusion) of the larger accessory minerals i.e. those up to 300 μm in diameter, at the entrance to, or indeed inside the fracture has taken place.

In order for these minerals to have entered the fracture, either they must have oriented themselves with their narrowest dimension parallel to the plane of the fracture aperture or the physical fracture aperture is substantially greater than the measured hydraulic aperture of 57μm.
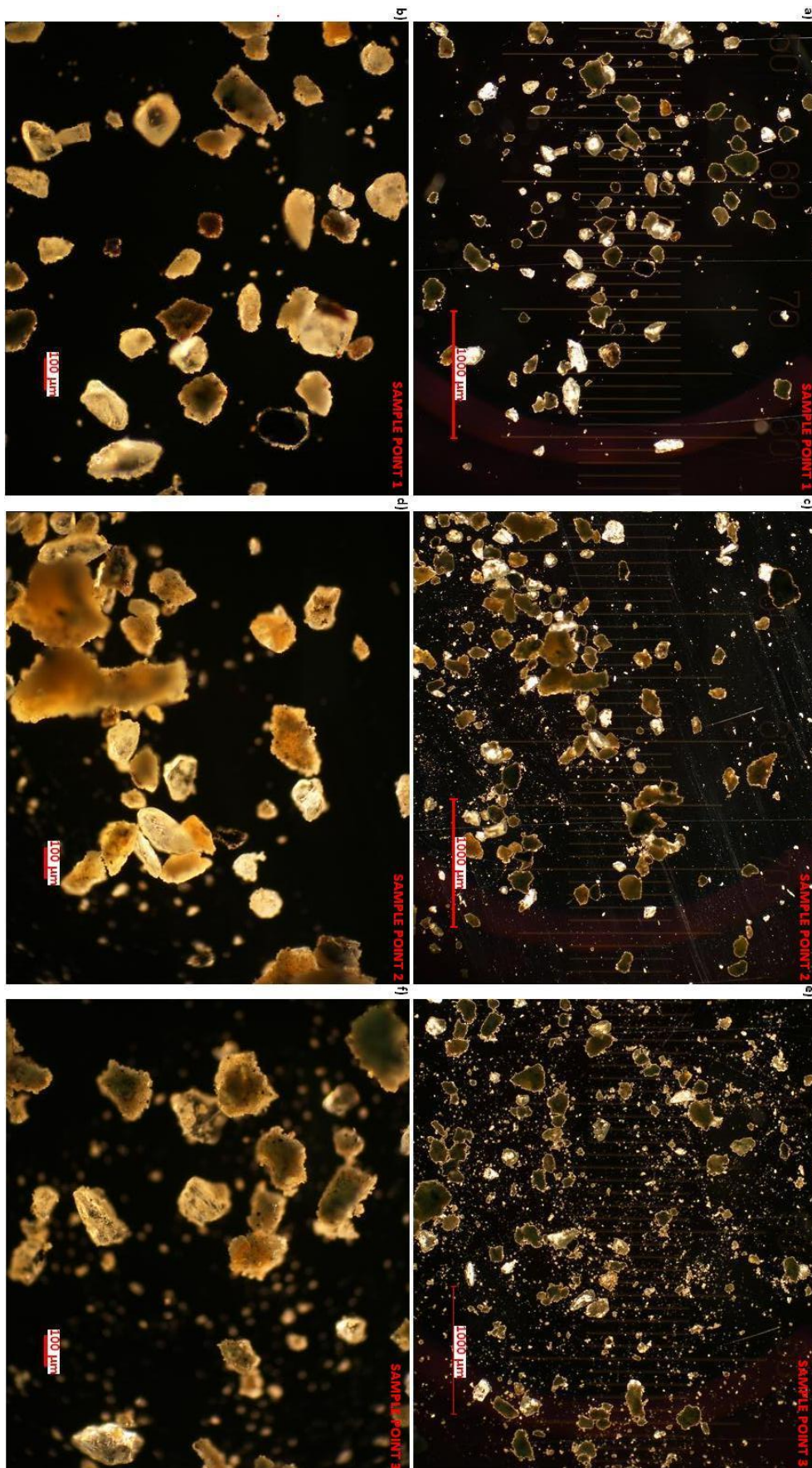
Figure 6.23: Post-test a) sample 1, 4x magnification and b) sample 1, 10x magnification c) sample 2, 4x magnification d) sample 2, 10x magnification e) sample 3, 4x magnification f) sample 3, 10x magnification

As discussed previously, Sample point 2 was selected due its red to orange hue in relation to sample points 1 and 3. However, a comparison of the images from sample point 2 (Figure 6.23c and d) to sample points 1 (Figure 6.23a and b) and 3 (Figure 6.23e and f) shows no appreciable difference in the quantities of red to orange minerals present.

What also appears to be consistent between sample points upon closer inspection of each of the images in Figure 6.23, is that the minerals appear to be coated with a fine grained material. This coating is more prevalent on the red to brown coloured minerals. This phenomenon is most noticeable in Figure 6.23d and f, and more so at 20X magnification, as shown in Figure 6.24. This fine grained material is most likely montmorillonite, which would also corroborate the presence of the clay mineral in the X-Ray diffraction data of Figure 6.13, Figure 6.15 and Figure 6.17. This differs somewhat from the images of the accessory minerals isolated from MX80 by centrifugation (Figure 6.22), which do not show the same surface coating of this fine material.
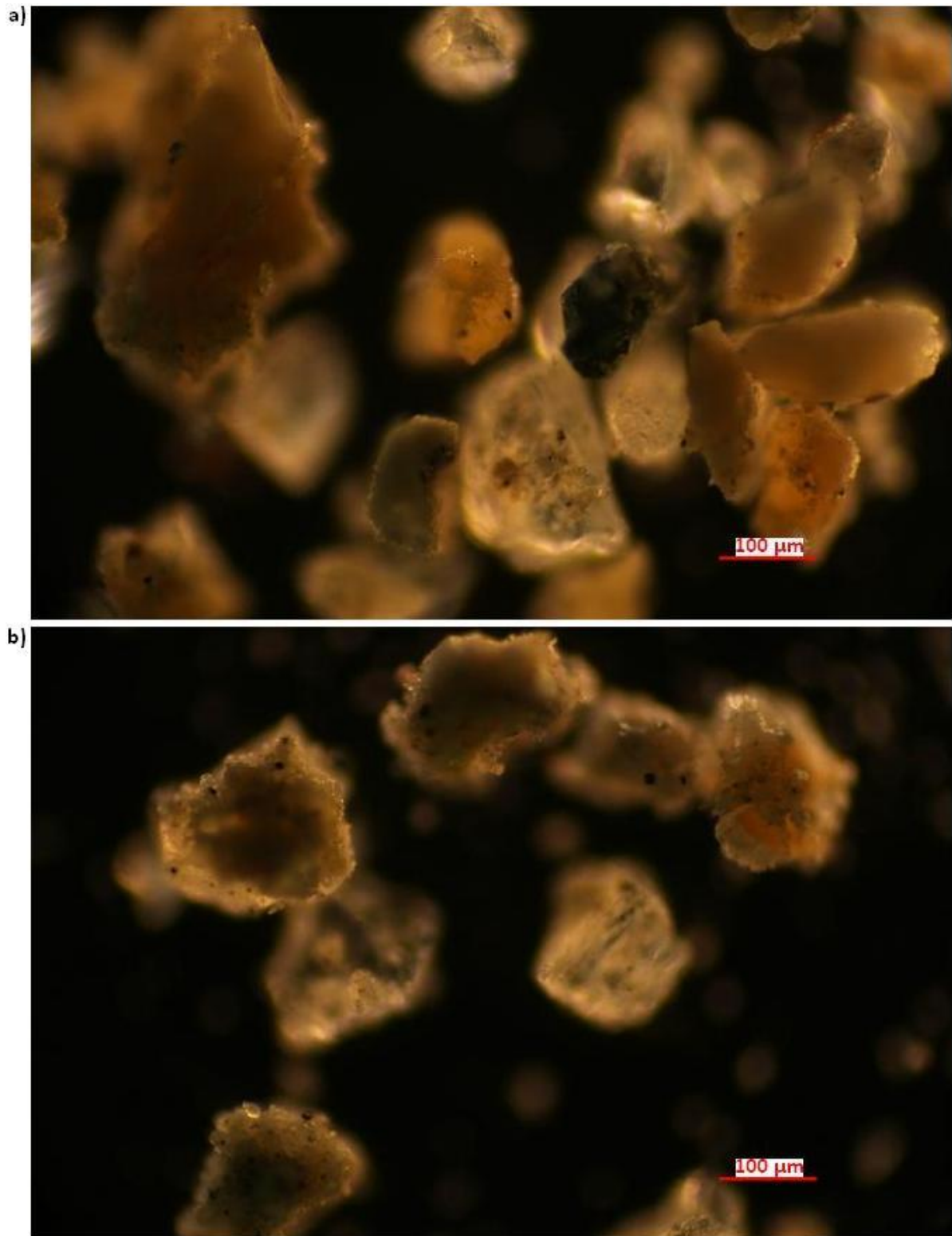
Figure 6.24: Post-test a) sample 2, 20x magnification and b) sample 3, 20x magnification

Figure 6.23 and Figure 6.24 indicate that the accessory mineral ring, which forms at the edge of the extruded bentonite, has some degree of its pore space filled by

montmorillonite. When the fracture was unsealed and dried through evaporation, these montmorillonite particles effectively bound to the larger accessory mineral surfaces.

The apparent coating of these particles compared with an apparent lack of this phenomenon on the transparent quartz particles, may in some way be due to a difference in the surface charge of either particles, causing the negatively charged montmorillonite particles to have a higher affinity for the red-brown coloured mineral. The surface charge of these darker particles may be a result of mineral alteration during the course of the experiment. Supported somewhat by lack of this surface coating on the darker minerals isolated from MX80. If this were indeed the case, it may provide capacity for the minerals deposited at the edge of the extruded material to mitigate against erosion of montmorillonite particles further still.

An example of what appears to be a particle of biotite coated with very fine particles, presumably of montmorillonite, is shown in Figure 6.25. Because of the three dimensional nature of the accessory minerals, achieving an entire mineral grain in focus within the microscope proved difficult. However, biotite has a more two dimensional, lamellar mica structure, hence, focussing on the face of the mineral was achievable. Planes of cleavage are evident at the left hand side of the mineral in Figure 6.25.
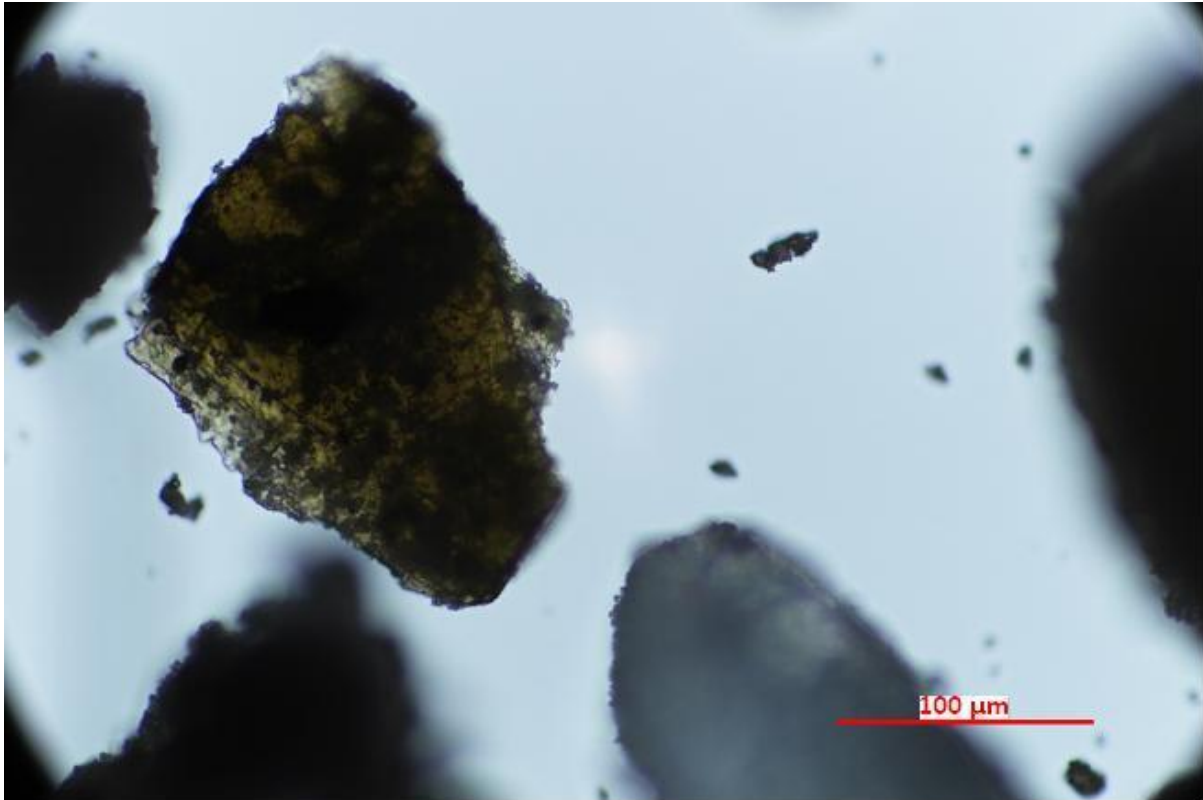
Figure 6.25: Biotite particle for post-test sample 1 at 40x magnification.

6.4 Conclusions

This erosion experiment has demonstrated that the erosion of MX80 in a variable aperture cell exhibits a cyclical nature. Rising to an initial peak value before decreasing and undergoing subsequent erosive events of a lesser magnitude. Throughout the erosion process, the darker accessory minerals are deposited at the edge of the extruded material, accumulating in a continuous ring around the extruded zone. The onset of growth of the accessory mineral ring corresponds to the first decrease in mass loss from the system, indicating that the presence of the accessory mineral ring is indeed attenuating mass loss from the system. During each subsequent mass loss event, the accessory mineral ring appears to grow, regaining its integrity.

Swelling pressure decreases to a steady state due to mass loss while exhibiting local fluctuations.

Post-test analysis on the fracture face has confirmed that the dark ring of minerals accumulated at the edge of the extruded material is dominated by the accessory minerals

quartz, plagioclase and feldspar present in the bentonite. Some chemically or biologically mediated mineralogical changes were also apparent in the deposited accessory minerals. Only montmorillonite was found in the material eroded from the cell.

The above experiment differs from those of other researchers (e.g. Schatz et al 2013) in two ways. Firstly, MX80 has been used in place of pure montmorillonite, secondly the fracture has variable aperture. In the following chapter the effects of these two differences are explored independently and the results compared with those of other researchers.

Chapter 7 The effect of a non-uniform fracture aperture and the presence of accessory minerals on bentonite erosion

In order to differentiate the effect on montmorillonite erosion of the fracture having a varying aperture from that of the presence of accessory minerals, two further tests were performed. First, an experiment was prepared using exactly the same method as detailed in the previous chapter, with the exception that a uniform fracture aperture was created by using smooth fracture surfaces separated by physical spacers. Second, a test was conducted in a uniform fracture aperture using pure montmorillonite. These tests are summarised in Table 7.1, test numbers 2 and 4 respectively. The test described in the previous chapter, experiment 1, is also summarised in Table 7.1. The results of experiments 1, 2 and 4 and data correlation for these tests shall be described in this chapter. Experiment number 3, which resulted from an aborted attempt at experiment number 4 shall also be briefly discussed in this chapter.

Exp. no.	Hydraulic fracture aperture (μm)	Rough or smooth fracture aperture?	Bentonite used	Accessory minerals present?	Flowrate 0(ml/min)	Initial saturating solution	Test duration (days)
1	57	Rough	MX80	yes	1	De-ionised	130
2	102	Smooth	MX80	yes	1	De-ionised	130
3	104	Smooth	Nanocor PGN	no	0	De-ionised	55
4	104	Smooth	Nanocor PGN	no	0.38	De-ionised	118
5	68	Rough	MX80	yes	1	Saline	14

Table 7.1: Summary table of experiments undertaken and parameters varied

7.1 MX80, uniform aperture, constant flow – experimental data

The uniform fracture aperture erosion test, experiment no. 2, was set up to be as comparable as possible to experiment 1, described in chapter 6. Employing spacers which were 150 μm thick in the uniform aperture cell, as detailed in section 4.9.1, gave rise to a hydraulic aperture of 102 μm (post-test it was noted that the spacers had indented slightly into the fracture faces, which may account for the large reduction from the physical aperture). Whilst the 102 μm is larger than the 57 μm hydraulic aperture calculated for the variable aperture cell experiment described in the previous chapter, it is more comparable to the physical aperture of the previous test, which may have a greater effect on mineral ring development.
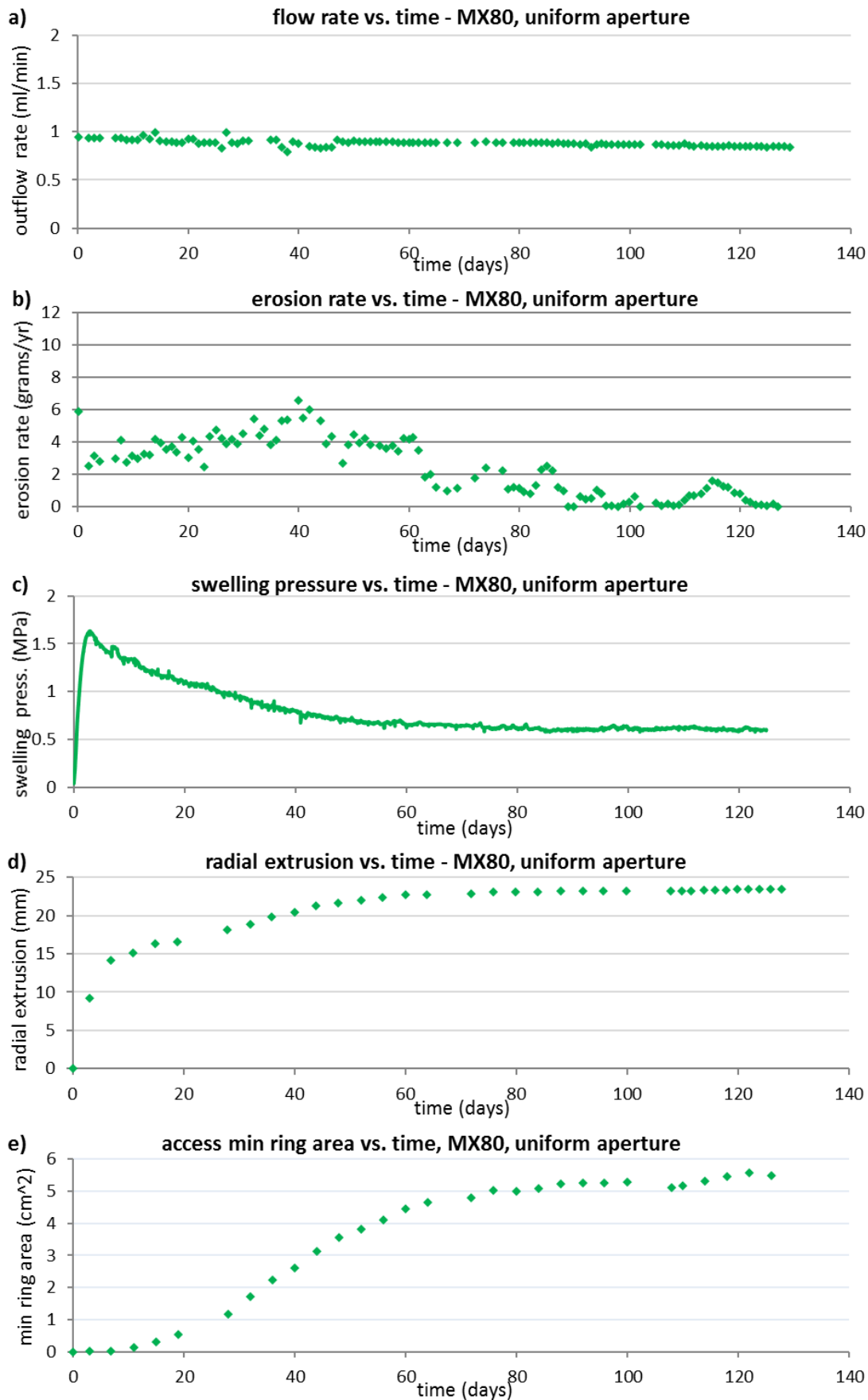
Figure 7.1: MX80, uniform aperture fracture data for a) flow rate b) erosion rate c) swelling pressure d) radial extrusion distance and e) accessory mineral ring area with respect to time

Figure 7.1 shows the data gathered during the course of the 130 day experiment. Each of the data sets shall now be considered individually.

Flow rate

To allow direct comparison between tests, the flow rate was maintained at 1ml/min throughout the test. Figure 7.1a shows that the measured flow is slightly erratic for the first 46 days, then beyond this point it stabilises. The reason for this is unknown because the same measurement method was used throughout the entire experiment.

Mass loss

The erosion rate of the MX80 in the uniform aperture cell (Figure 7.1b) exhibits similar behaviour to the variable aperture cell (Figure 6.4b). The erosion rate rises to an initial peak value of 6.6 grams/ year after 40 days, before falling away to approximately 2 grams/ year after 65 days. The initial peak in erosion rate is reached after approximately twice the time taken in the original variable aperture cell i.e. 40 days as opposed to 23 days. Cyclical erosive events are again observed, though these are of a lesser magnitude than in the initial test and have a period of approximately 10 days (Figure 7.1b).

Swelling pressure

The maximum swelling pressure generated by the sample in the uniform aperture cell (Figure 7.1c) is an order of magnitude greater than that generated in the variable aperture cell (Figure 6.4c). The value of 1.6 MPa recorded here is more in-line with the swelling pressure expected from a sample compacted to this dry density i.e. between 2 and 10MPa as described in section 2.2.3. As discussed previously, this is probably because this sample fitted more snugly into the compartment and hence there being a smaller void space remaining. After the initial rapid pressure rise evident in Figure 7.1c, the swelling pressure falls away gradually as a result of mass loss reaching a steady state after approximately 60 days. Also of note is that the fluctuations in swelling pressure, apparent in the previous experiment (Figure 6.4c), are not observed in Figure 7.1c.

Radial extrusion

Radial extrusion of the sample is plotted in Figure 7.1d. The sample extrudes further and more rapidly than in the previous test, reaching a maximum of 23mm after approximately 60 days. This is because of the greater swelling pressure generated in this test.

Figure 7.2a shows the extent of extrusion of the bentonite at 10, 50, 90 and 130 days. For comparison, images from the previous test are reproduced in Figure 7.2b. The dark ring of accessory minerals takes longer to form in the uniform aperture test and is not as wide. This may be explained by the larger extent of extrusion: for the same mass lost, the same mass of accessory minerals should be deposited; these are then distributed around a ring with a greater circumference.

Figure 7.2 also shows that the mineral ring, when formed, adopts the same distinct cog-like structure. Hence, the irregularity in the shape of the mineral ring is not as a result of the fracture aperture variability. One possible explanation is the following. The extent of extrusion is controlled, and limited by, the swelling pressure generated in the sample. This is a function of initial dry density, pore water chemistry and confinement conditions. The deposition of accessory minerals at the edge of the extruded material is governed by the mass of montmorillonite lost. Therefore, a point in time will arrive when the accumulation of further accessory minerals into the ring cannot be accommodated by the circumference of extruded material. The mineral ring will then be forced to concertina on itself to accommodate incoming minerals.
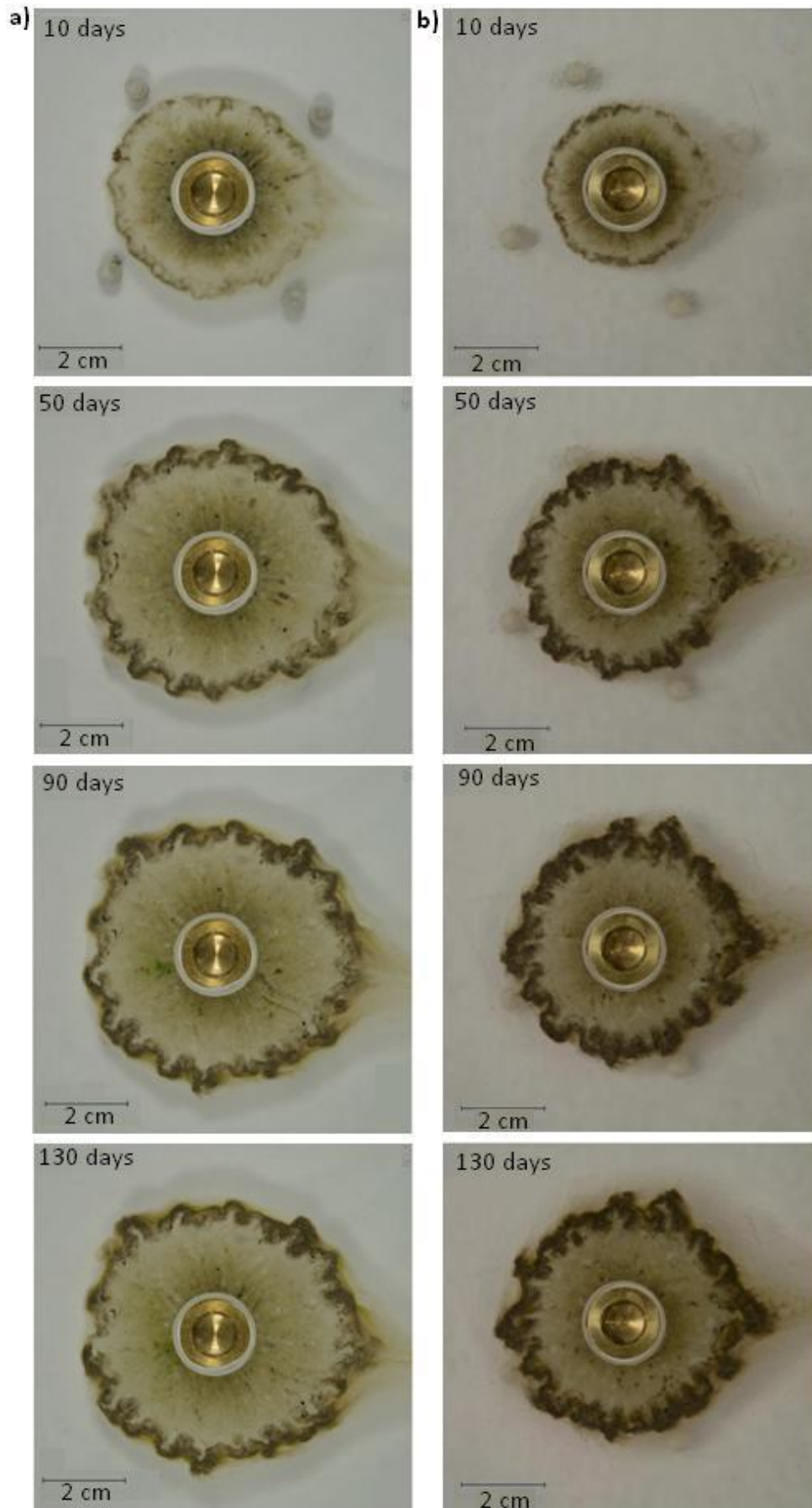
Figure 7.2: Radial extrusion after 10, 50, 90 and 130 days. a) MX80 uniform aperture b) MX80 variable aperture

As was the case in the previous test, a sharp decrease in density in the uniform aperture system occurs across the extruded material early (Figure 7.2a, 10 days) in the experiment. Figure 7.3 shows density profiles along two sections ($\alpha2 - \alpha1$ and $\beta2 - \beta1$), using pixel gray value as a proxy for sample density. At around 7mm the density profile changes from being approximately linear with increasing value to constant.
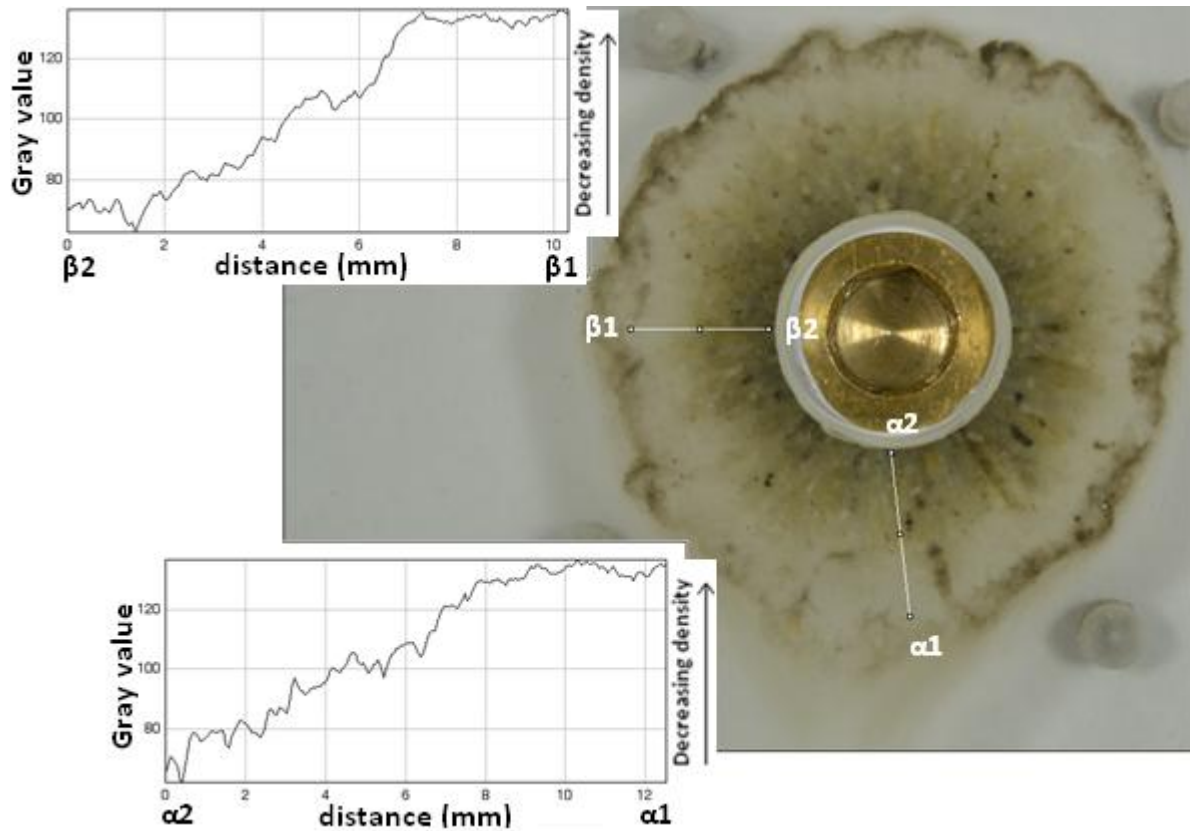
Figure 7.3: MX80, uniform aperture cell, density gradient across two sections, early in experiment

Again, as with the variable aperture cell, the sharp change in density across the extruded material disappears over time as the rate of mass loss decreases; over time the water and density gradients across the material equilibrates. This occurs at 130 days (Figure 7.2a) after which the density profile is approximately linear throughout.
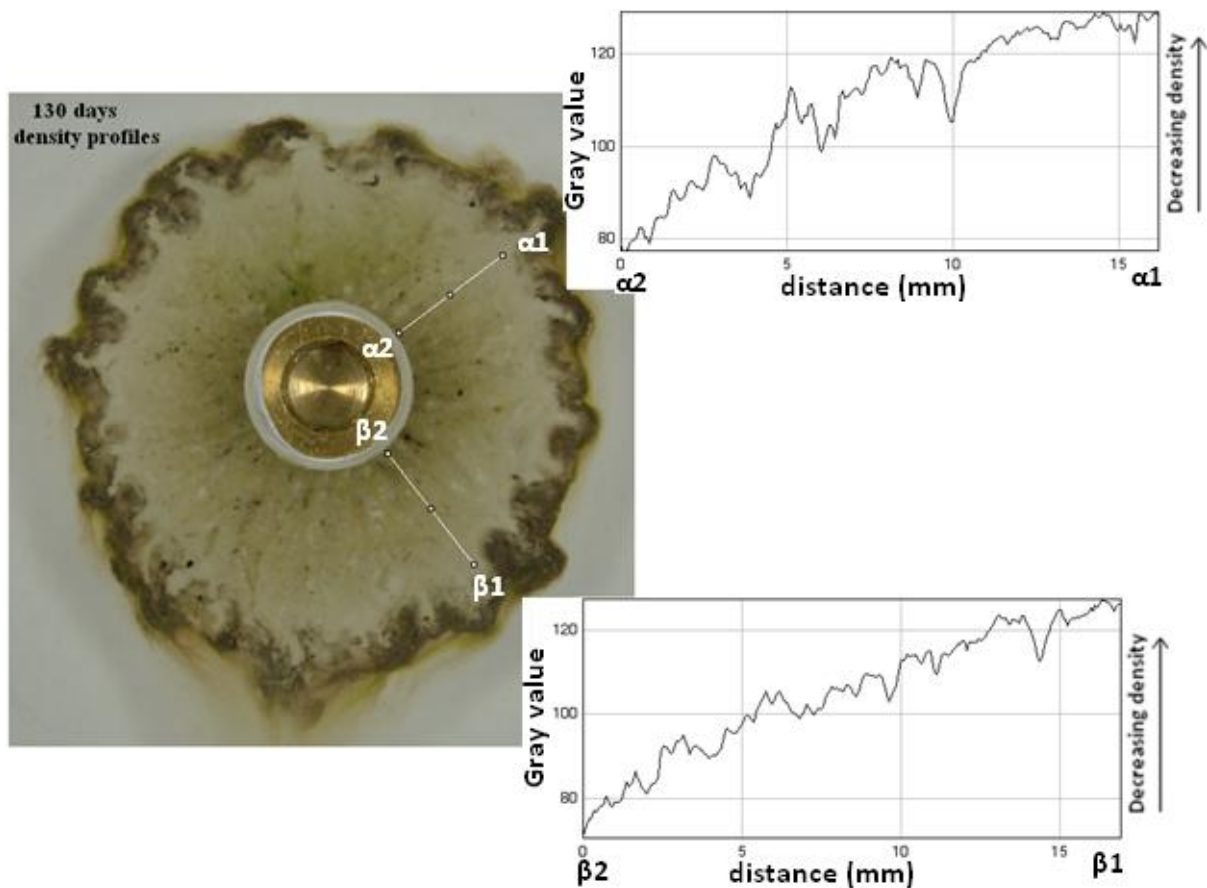
Figure 7.4: MX80, uniform aperture cell, density gradient across two sections, late in experiment

Accessory mineral ring

Figure 7.1e plots the area of the mineral ring against time. This has also been replotted in Figure 7.5a with the same data for the previous test (Figure 7.5b) for the purpose of comparison. Figure 7.5 shows that the accessory mineral ring initiates in the uniform aperture cell at the same time (after 18-20 days) as in the variable aperture cell and approaches steady state at around the same value, (approximately 5cm^2) for both the variable and uniform aperture fracture cells. The time taken to reach this value however is different. It takes approximately 70 days in the uniform aperture cell and 40 days in the variable aperture cell.
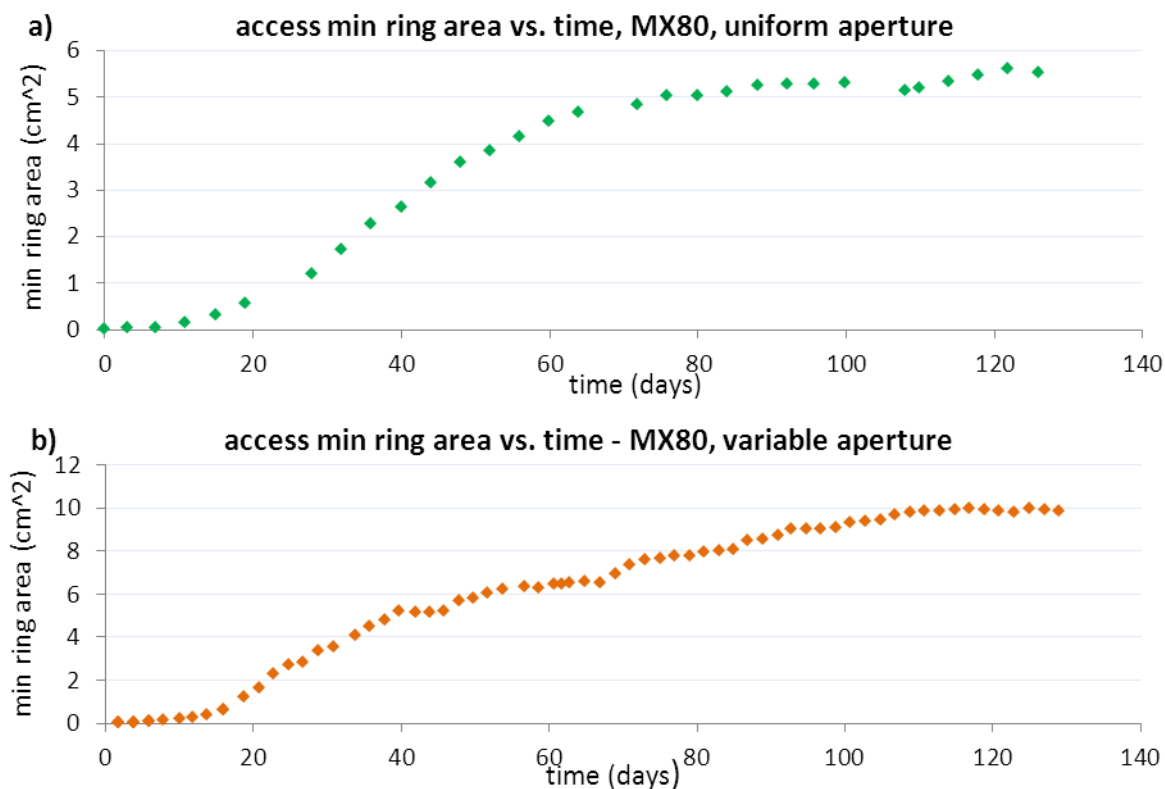
Figure 7.5: Accessory mineral ring area against time a) MX80, uniform aperture b) MX80, variable aperture

As with the variable aperture cell, the accessory mineral ring grows during each erosive period, although there is only one clear step in the rate of increase in the area of the accessory mineral ring apparent in the uniform aperture cell, occurring at around 115 days which is corresponds to a period subsequent to an erosive burst (Figure 7.1b).

7.2 Controls on formation of the accessory mineral ring and erosion rate

The accessory mineral ring, in both the variable (Table 7.1, experiment 1) and the uniform (Table 7.1, experiment 2) aperture fracture experiments, is not formed by sieving because of physical asperities in the fracture aperture, they appear to simply accumulate at the edge of the extruded material, where the montmorillonite gel density is too low to facilitate further transport. This observation is based on the similarities in ring shape between the two experiments and the fact that in the uniform aperture cell, there are no physical asperities on the fracture surface, yet the ring forms and its shape is remarkably similar.

The reaching of a steady state with the regard to the size of the accessory mineral ring area is directly linked to a slowing or cessation of mass loss of montmorillonite from the system in both experiments. This makes sense, because the mineral ring is only supplemented by

further extrusion of montmorillonite from the central compartment which is driven by mass loss from the edge of the extruded material. Common traits in the trends of the accessory mineral ring growth in both the uniform aperture and variable aperture experiments are that they begin to grow at approximately the same time and approach a steady state at approximately the same size of mineral ring area. In both experiments, a steady-state ring area corresponds to a cessation or slowing of mass loss from the system. It seems unlikely that the area of accessory minerals is the controlling factor, however, because the extent of extrusion differs between the two experiments implying that the shape of the accessory mineral ring area should also be different.

Due to the irregularity of the shape of the accessory mineral ring area, no direct measurements of the ring width, from quantitative image analysis, could be determined. However, if the irregular shape of the extruded area of material measured from image analysis data is considered as an equivalent circle of a particular circumference (Figure 7.6), the effective thickness of ring can be calculated as:

$$effective\ mineral\ ring\ thickness = \frac{accessory\ mineral\ ring\ area}{circumference\ of\ extruded\ material}$$
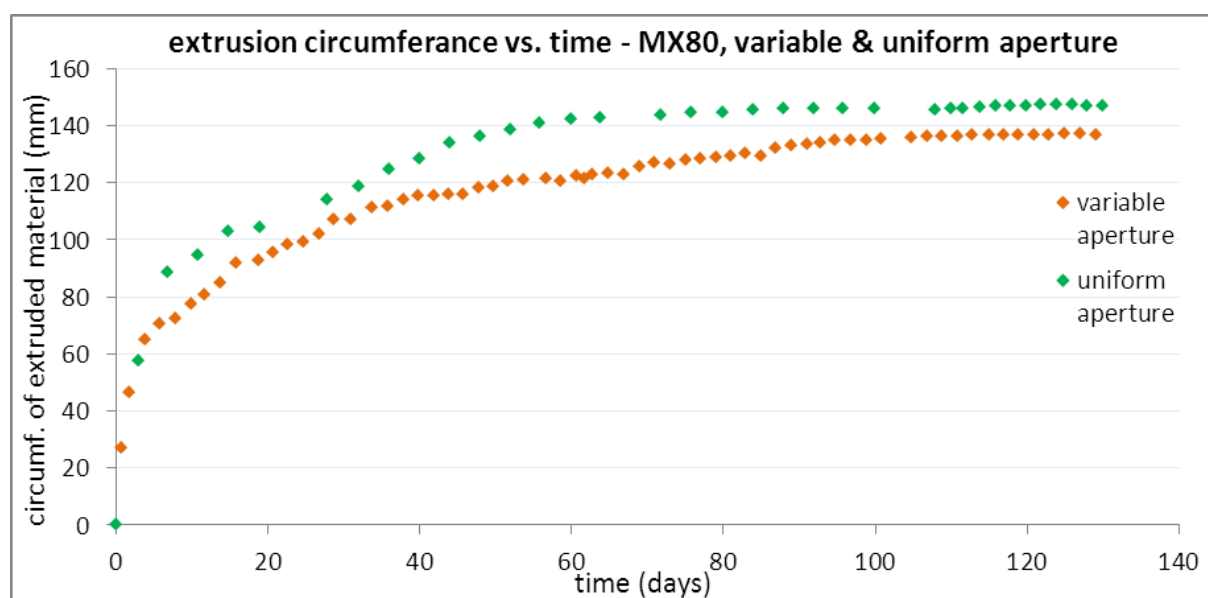
Figure 7.6: MX80, variable and uniform apertures, circumference of extruded material against time
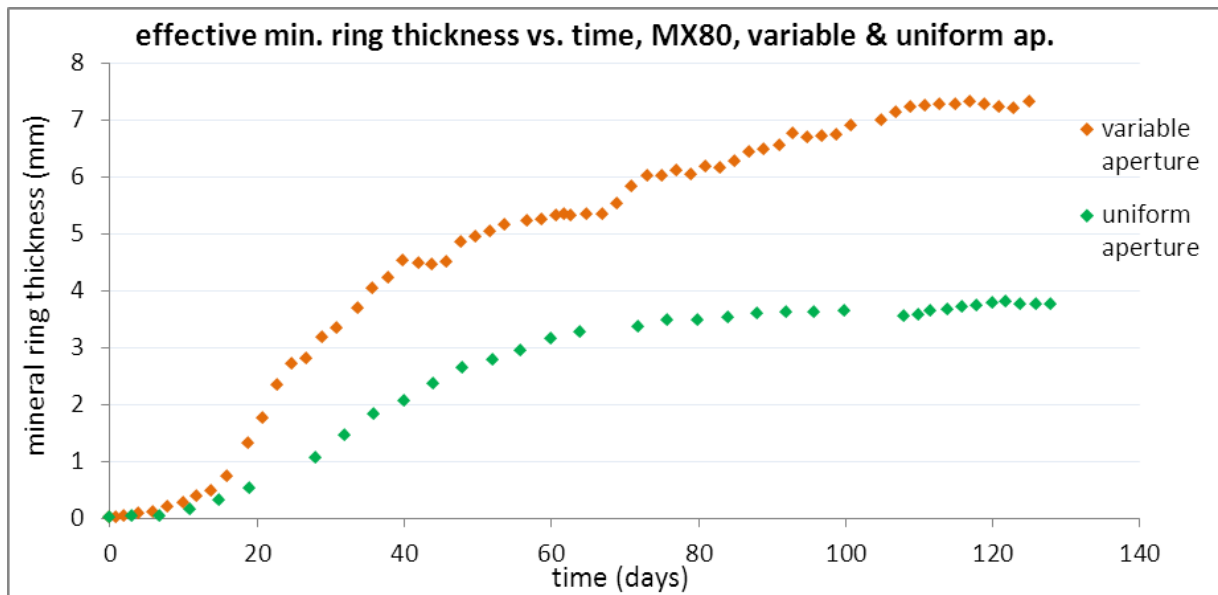
Figure 7.7: MX80, variable and uniform apertures, effective mineral ring thickness against time

The effective ring thickness plotted against time assuming a circle of equivalent mineral ring area is shown in Figure 7.7 for both experiments. The difference in the growth rate of the two mineral rings is well illustrated.

Now examining the first erosive period in both the variable and uniform aperture fractures i.e. the first increase then decrease in erosion rate in both experiments (Figure 7.8), and comparing them to the effective mineral ring thickness with respect to time in Figure 7.7, it becomes apparent that the mineral ring thickness around the circumference of the extruded material is controlling the erosion rate. The points at which the erosion rate starts to drop in each experiment (23 days in the variable aperture cell and 40 days in the uniform aperture cell) correspond to the same, critical, 2mm effective thickness of accessory mineral ring, as depicted in Figure 7.9.
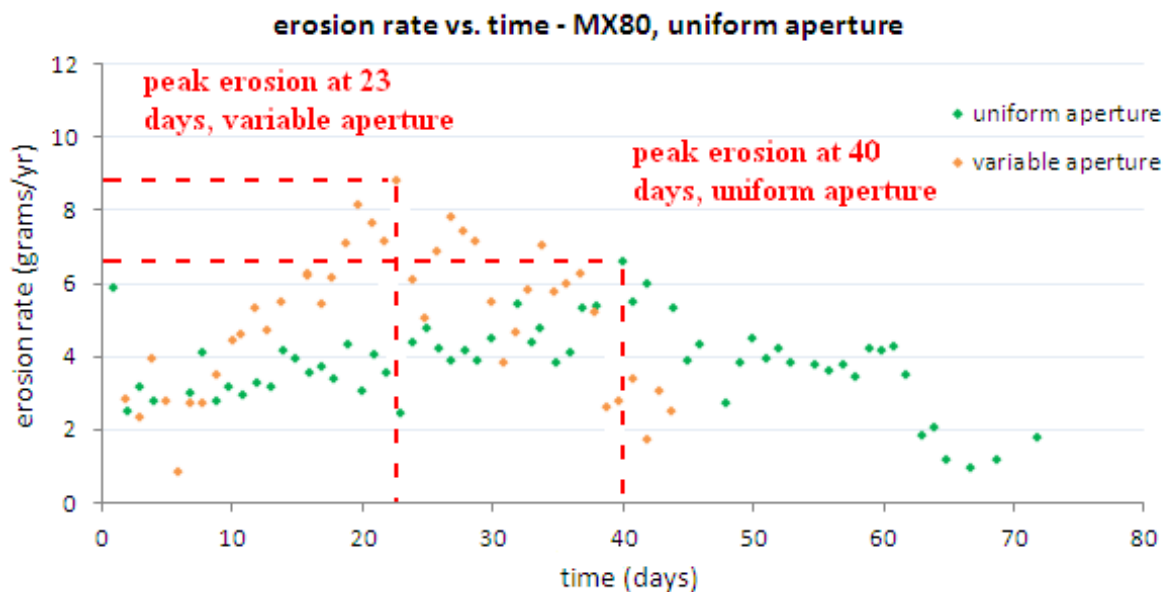
Figure 7.8: MX80, variable and uniform aperture, erosion rate (1st erosive period) against time
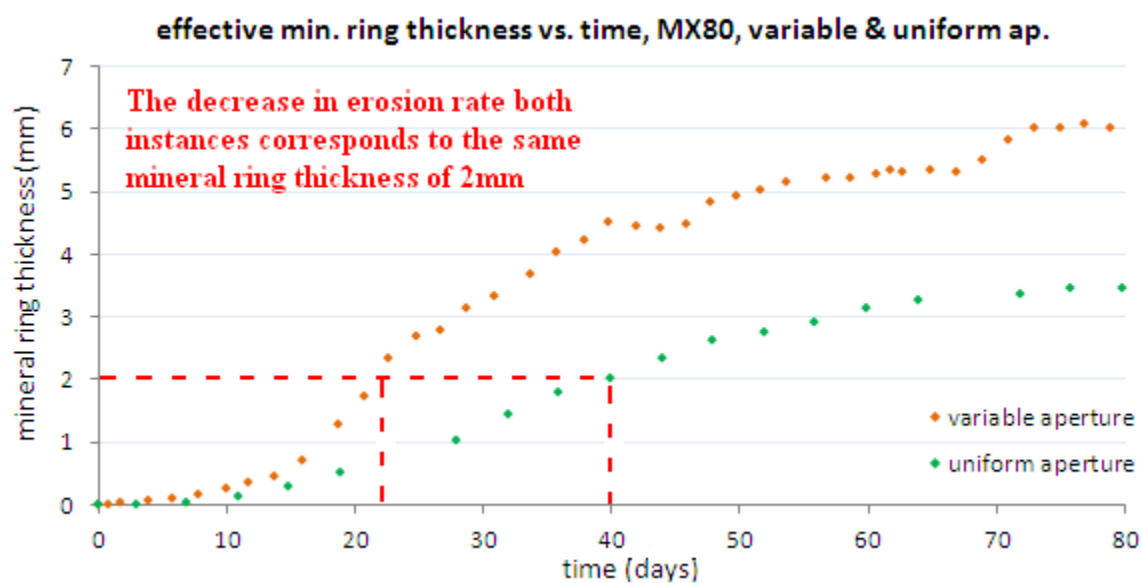
Figure 7.9: MX80, variable and uniform aperture, effective mineral thickness against time

These time points (Figure 7.8), at which the erosion rate starts to drop, are at 23 days (23/3/14) in the variable aperture and 40 days (29/11/14) in the uniform aperture. Due to a data acquisition malfunction, no images were collected from the 23/3/14 – 25/3/14 for the variable aperture experiment. An image from day 22, the 22/3/14 has been included however for comparison in Figure 7.10 which shows the respective mineral rings at this point.

Figure 7.10: MX80, variable and uniform aperture, mineral ring area, point at which erosion rate drops.

The image thresholding at these points shows the ring to still be discontinuous i.e. it is periodically interrupted by gaps and appears visually thicker at certain points than it does at others. It is important to note, however, that at the points at which breaks appear in the ring, there are enriched, darker regions of minerals visible which are not dark enough to be picked up by the detection limits of the threshold parameters employed in the image analysis.

This implies that the mineral ring, the region which is thought to be causing a decrease in erosion rate, may actually be thicker than the 2mm which is described herein based on image analysis. What is clear from a comparison of the images in Figure 7.10 is that visually, the development of the mineral accessory ring at these time points is very similar and can be described as an almost complete ring based on the thresholded value with notably darker regions of material in the gaps.

The mass of eroded material required to reach this point of ring development is 0.288 grams of montmorillonite in the variable aperture cell and 0.410 grams of montmorillonite in the uniform aperture cell. It is clear, therefore, that for a given fracture aperture, groundwater velocity and swelling pressure (as in a repository scenario) the mass of montmorillonite which would have to be eroded to accumulate a suitably thick region of accessory minerals to mitigate against further erosion may be calculated. Scaling of this mechanism to a repository scenario shall be revisited in the discussion chapter of this thesis.

It is also interesting to note that, if the velocity of groundwater is also a controlling factor in the extent of extrusion, a higher groundwater velocity may not be as detrimental as may be expected with respect to buffer erosion. Because there will be a limit to the mass of montmorillonite which can be eroded with increasing velocity, as a result of the increase in shear strength with density of the extruded material towards the central compartment. A higher velocity, while ultimately causing a higher mass loss initially, may limit extrusion to the point where it facilitates a more rapid formation of the mineral ring to a critical thickness around a reduced circumference of extruded material. Thus high, short term mass loss, as oppose to longer term, sustained mass loss of a lower quantity may be beneficial. As demonstrated, somewhat serendipitously, because of differences in sample density and

swelling pressure and not groundwater velocity, by the experiments described in the current chapter and chapter 6.

7.2 Post-test analysis

The same degree of post-test analysis as undertaken on the previous test, described in section 6.3, was not undertaken on the test described in this chapter since there is no reason to believe that they would differ from those previously identified. It is worth noting though that there was clear evidence of biological activity in the uniform aperture experiment, in the form of green organic matter which evolved over time in the accessory mineral ring (Figure 7.11).
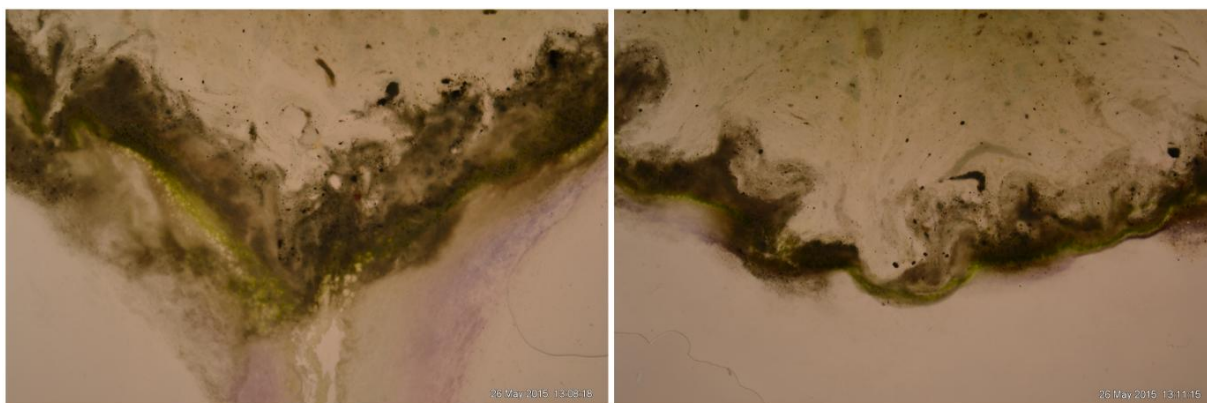
Figure 7.11: Green organic matter apparent in accessory mineral ring.

7.3 Nanocor PGN, uniform aperture, stagnant – experimental data

The following section refers to Table 7.1, experiment 3. A test was commenced with a sample of Nanocor PGN in a 104 µm uniform hydraulic aperture flow cell at the same flow rate as the previous two experiments. It soon transpired however that the system was unable to cope with the mass loss experienced at a flow rate of 1ml/min. The outflow tube repeatedly became blocked, causing restrictions to flow, a build-up of back-pressure and consequent ruptures in the sealant around the cell. As a consequence, data acquisition was abandoned after 10 days. Limited data during this 10 day period were acquired. The experimental data acquired during the period of flow (0-10 days) and under stagnant conditions (10-55 days) are shown in Figure 7.12
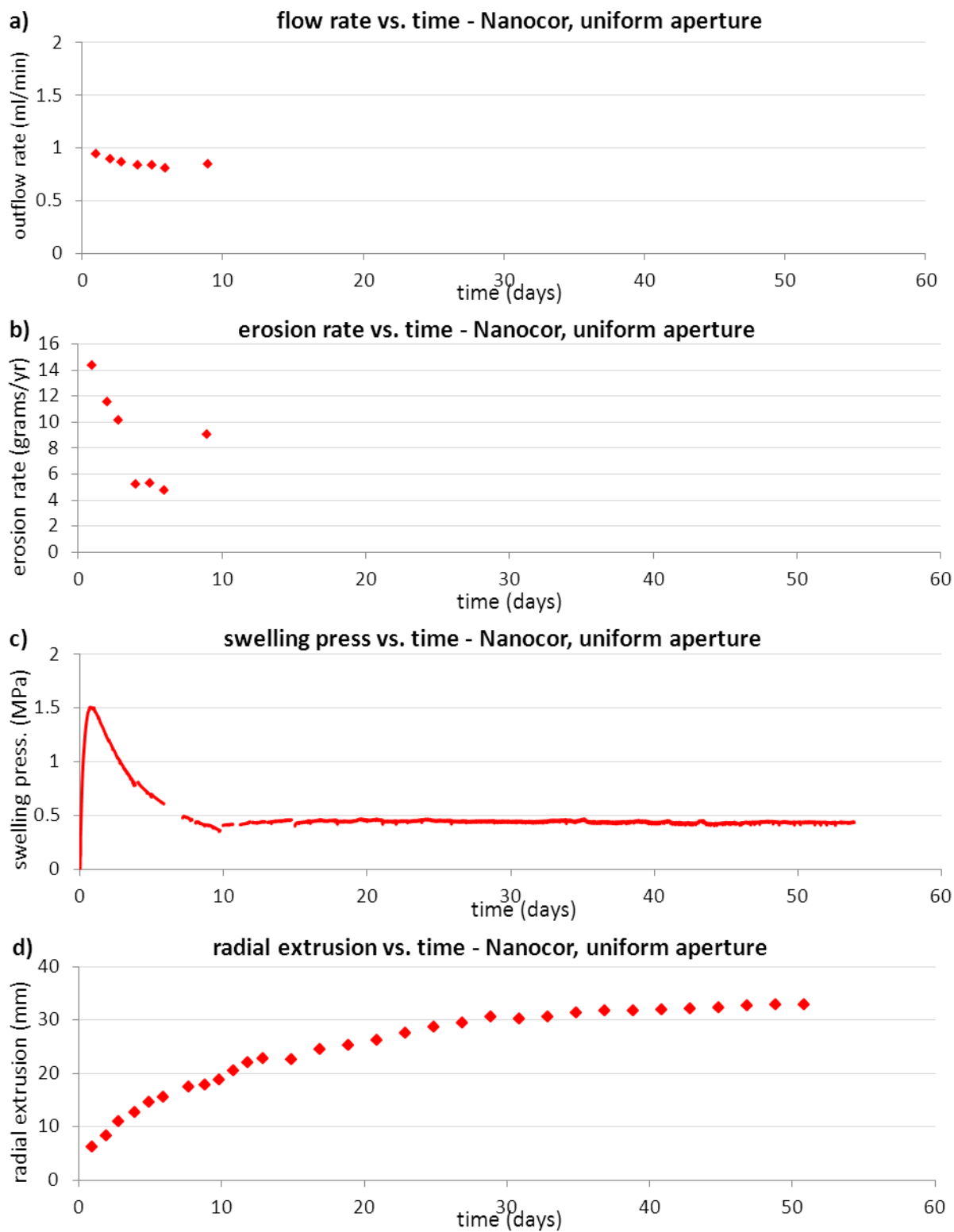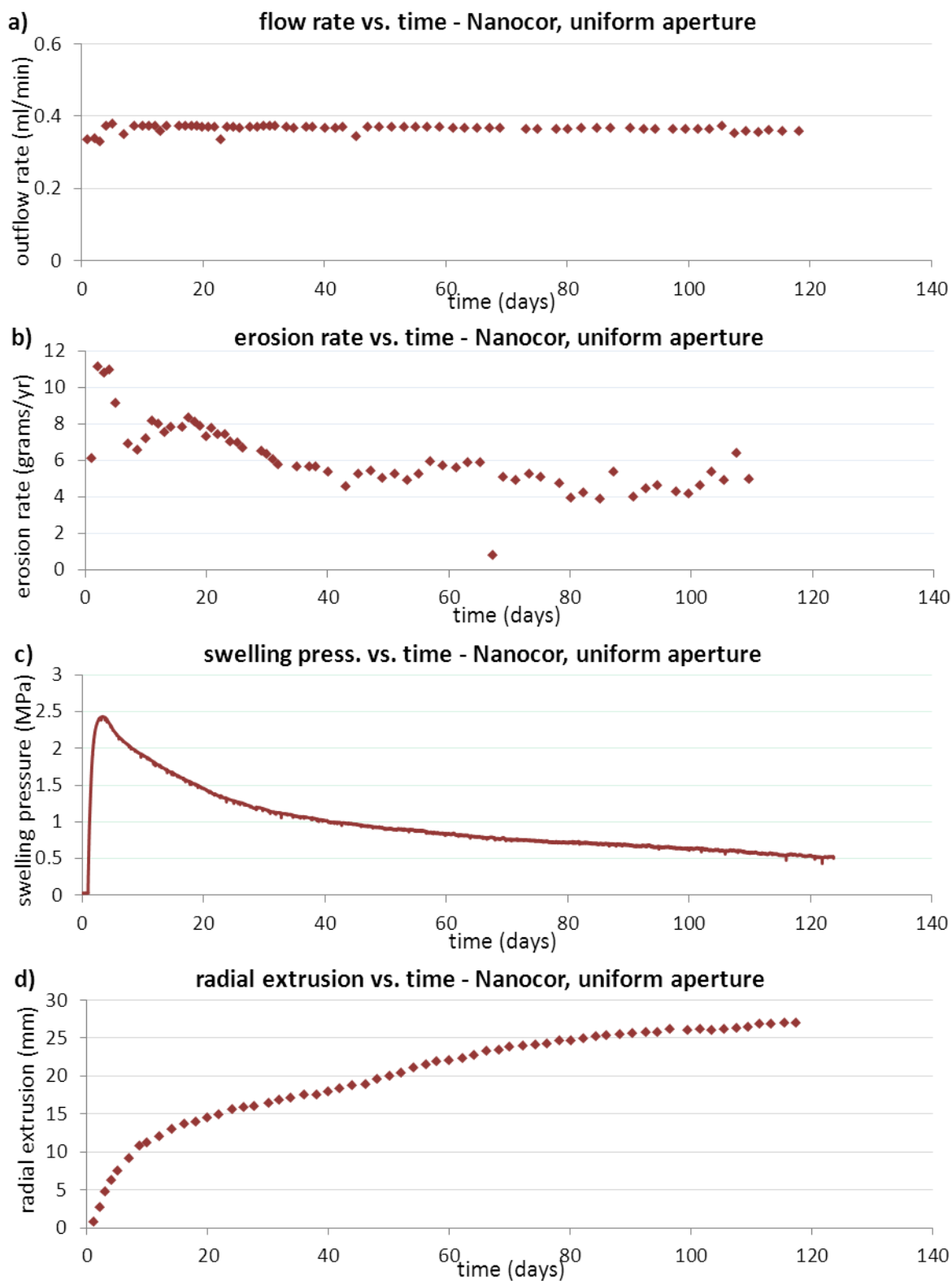
Figure 7.12: Nanocor PGN, uniform aperture fracture data for a) flow rate b) erosion rate c) swelling pressure d) radial extrusion distance with respect to time

Flow rate

Flow was commenced at 1ml/min and was continued for 10 days. The gradual decrease in flow rate evident over the 10 day period in Figure 7.12a) is because of leakage from the cell. Flow was aborted for this reason after 10 days.

Mass loss

Mass loss data were collected over this ten day period (Figure 7.12b) but are not representative of the actual mass lost, since significant mass was lost through the broken sealant around the cell.

Swelling pressure

Period of flow, 0-10 days

During the 10 day period of flow and mass loss, the swelling pressure reached a peak of 1.5MPa, followed by a dramatic decrease in swelling pressure to approximately 450 kPa as a result of the rapid mass loss (Figure 7.12c). Although the gradient of decay in swelling pressure appears to be reducing over the 10 day period, it is likely that this drop in swelling pressure would have continued to zero had the flow rate been maintained at 1ml/min for a sustained period.

Stagnant period, 10-55 days

After this first 10 days, it was decided to lower the flow rate to a negligible value in an attempt to reseal the cell once again. When this proved successful, it was decided to maintain these conditions in the cell, effectively allowing free swelling with no erosion for a period of 45 days. Swelling pressure data acquisition and image capture only were continued throughout this time period.

From day 10 to day 55, the period in which free swelling with negligible flow in the cell was run, it is evident from Figure 7.12c, which shows the swelling pressure generated by the sample over the entire 54 days of the test, that the swelling pressure remains relatively constant at a value of approximately 450 kPa.

Radial extrusion

The extrusion behaviour evident in the cell appears to be occurring independently of the presence of flow in the system. I.e. the rate of extrusion is relatively steady from 0 to 30 days before reaching a maximum extent of extrusion at approximately 32mm. The extrusion occurring beyond the period of flow (beyond day 10), quantified in Figure 7.12d, is as a result of diffusion from the extruded material already present in the fracture, as discussed herein.

Figure 7.14 plots the gray value, or intensity of pixels, along a radial line in the same direction at both 10 days, the end of flow and erosive conditions in the cell, and 50 days, the point at which the experiment was terminated. Adopting pixel intensity as a proxy for montmorillonite density, it is apparent from Figure 7.14 that montmorillonite density varies from 75 to 120 along a 10mm section after 10 days and 70 to 120 along a 25mm line after 50 days. Therefore, the same mass of material in the fracture is present at either time frame; spread over different distances, 10mm in a) and 25mm in b). Considering this to be a purely diffusion driven process, i.e. diffusion of cations from the sample to the groundwater and diffusion of groundwater from the fracture into the sample it must hold that if the system was left long enough, montmorillonite would eventually diffuse from the central compartment until no density, cation or groundwater distribution gradients existed in the system. The rapid erosion of montmorillonite during flowing conditions, therefore, occurs as a result of the least dense material at the edge of the extruded material constantly being removed by the flowing water and more material migrating from the central compartment to redress this balance.
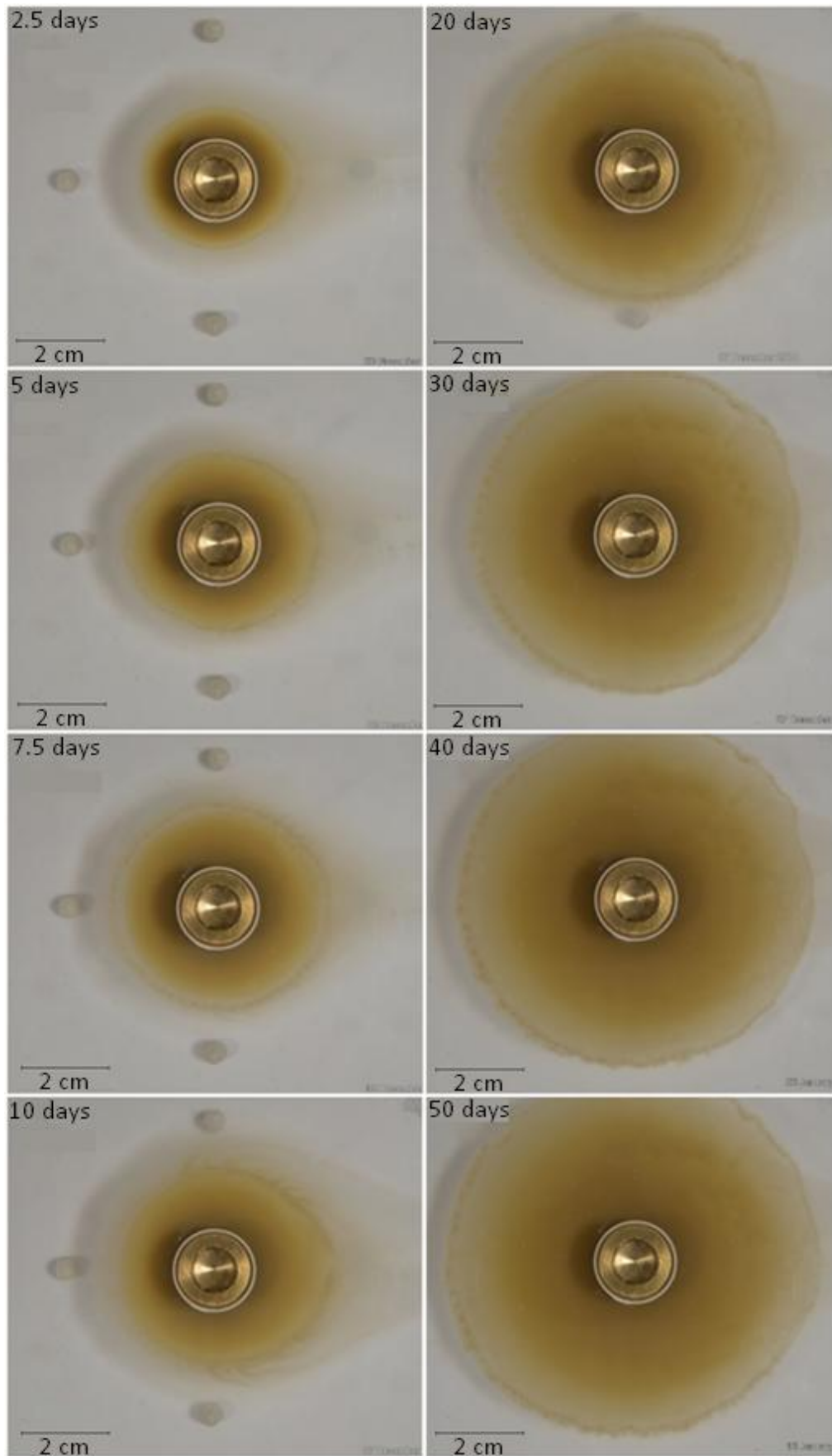
Figure 7.13: Nanocor PGN, uniform aperture cell, extrusion under flowing conditions (Day 1-10, LHS images) and no flow (Day 10-55, RHS images)
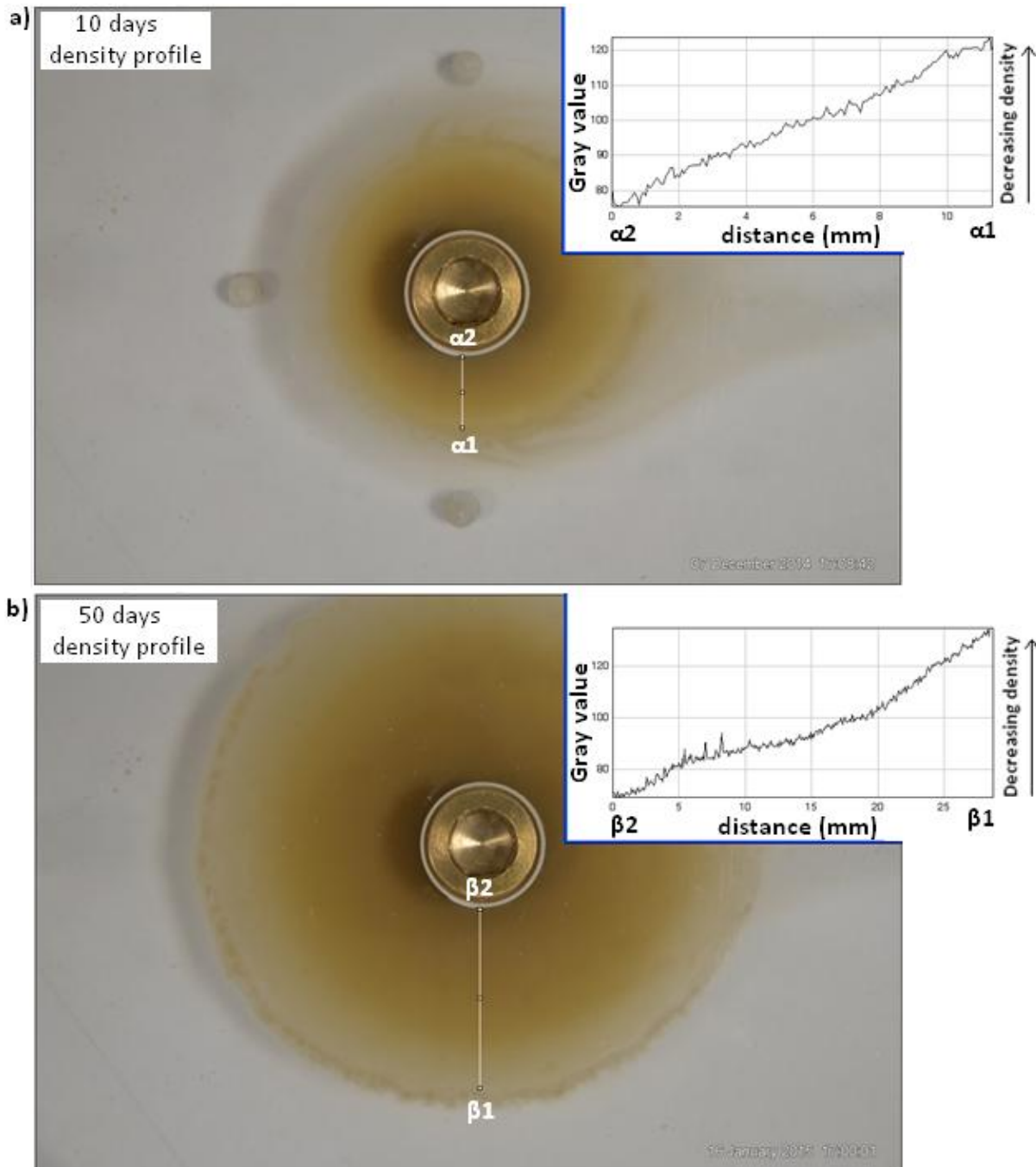
Figure 7.14: Nanocor PGN, uniform aperture cell, Gray value as a proxy for material density across extruded material at a) 10 days and b) 50 days

It should be noted that in a repository scenario, the presence of these high gradients across the buffer would be limited to periods of dilute chemical conditions of the groundwater. A buffer saturated by groundwater of high salinity, relative to dissolved salt concentrations in the buffer itself, may only experience limited swelling and extrusion into the fracture. This is because of the fact that, with a low/zero cation concentration gradient across the buffer,

the cations will remain within the buffer, thus limiting the volume water which can be accommodated between montmorillonite sheets. Hence, there would be limited extrusion into the fracture and a relatively uniform montmorillonite density profile over the extruded material.

7.4 Nanocor PGN, uniform aperture, constant flow – experimental data

Upon termination of the first test with Nanocor PGN, another test was initiated with Nanocor PGN material in a uniform aperture using a reduced flow rate and wider diameter inlet and outlet ports and pipes (according to the same protocol set forth in chapter 4). Figure 7.15 shows the data gathered during the course of the 130 day experiment. This corresponds to experiment number 4 in Table 7.1.

Flow rate

The methodology for this second test was identical to the test undertaken previously with the exception that the flow rate was reduced to 0.38 ml/min and the inlet and outlet pipes to the system were increased to 1.54 mm in diameter. Flow was maintained at a constant rate of 0.38 ml/min as illustrated in Figure 7.15a.

Mass loss

Mass loss was relatively stable over the test duration of 105 days. An initial period of high erosion, consistent with previous tests occurs from days 1 to 6 (Figure 7.15b). In line with previous tests and, as noted by Schatz et al (2012), this may be attributable to loose mass generated during the emplacement of the sample.

Figure 7.15: Nanocor, uniform aperture fracture data for a) flow rate b) erosion rate c) swelling pressure d) radial extrusion distance with respect to time

When comparing data on the magnitude of mass loss from this experiment with previous tests however, it is necessary to refer to the effluent solids concentration rather than the erosion rate, due to the lower flow rate employed in the test. Figure 7.16 shows effluent solds content vs. time for each of the tests undertaken.
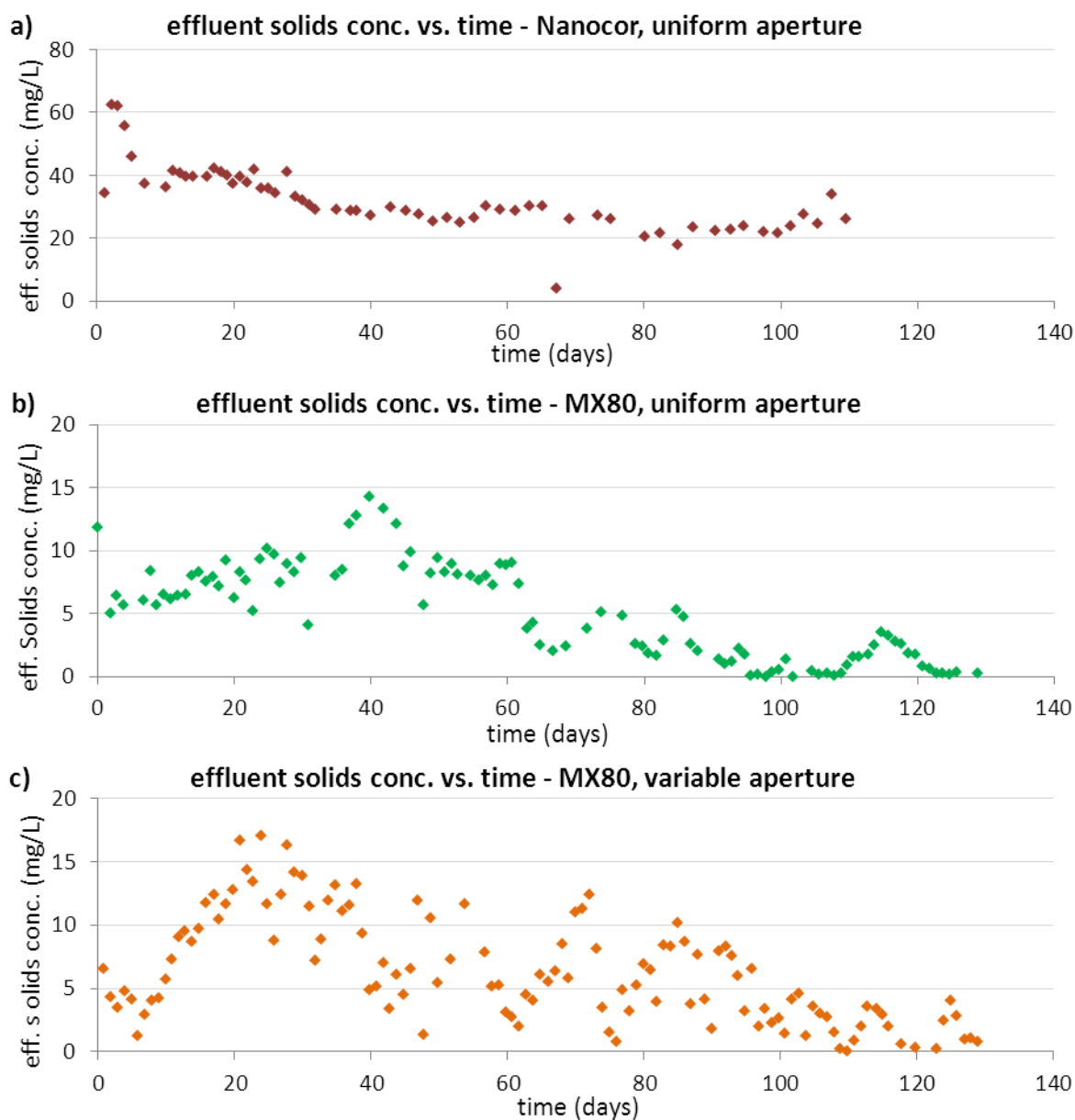
Figure 7.16: Effluent solids concentration against time for a) Nanocor, uniform aperture b) MX80 uniform aperture and c) MX80 variable aperture

Figure 7.16a shows that between days 10 and 40, the effluent solids concentration falls from 40mg/l to 30 mg/l. This period also corresponds to a decrease in the rate of swelling

pressure decay. The average effluent solids concentration over the period 40 – 105 days is 25.1mg/l (Figure 7.16a), which compares to an average concentration of 4.2mg/l (Figure 7.16b) in the test conducted using MX80 in the uniform aperture cell and 6.4mg/l (Figure 7.16c) in the test conducted with MX80 in the variable aperture cell with the same hydraulic aperture. Despite ~2.5 x the flowrate through the system in the latter two instances. A further observation is that the variability in effluent concentration is much lower in the test using Nanocor PGN.

Swelling pressure

The swelling pressure generated by the sample over the course of the experiment is shown in Figure 7.15c. Swelling pressure rises rapidly to a value of 2.4 MPa before decreasing as a result of mass loss. 2.4 MPa is significantly higher than the maximum of 1.5 MPa generated in the aborted test (Figure 7.12c), which is consistent with the higher flow rate causing substantial early mass loss.

The period of sustained mass loss beyond day 40 in this test (Figure 7.16a) corresponds to a linear reduction in swelling pressure (Figure 7.17). Extrapolating this linear trend, the system would lose mass until day 211 at which point the swelling pressure would be 0.

swelling press. vs. time - Norcor PGN, uniform aperture

$y = -0.0052x + 1.1521$
$R^2 = 0.979$
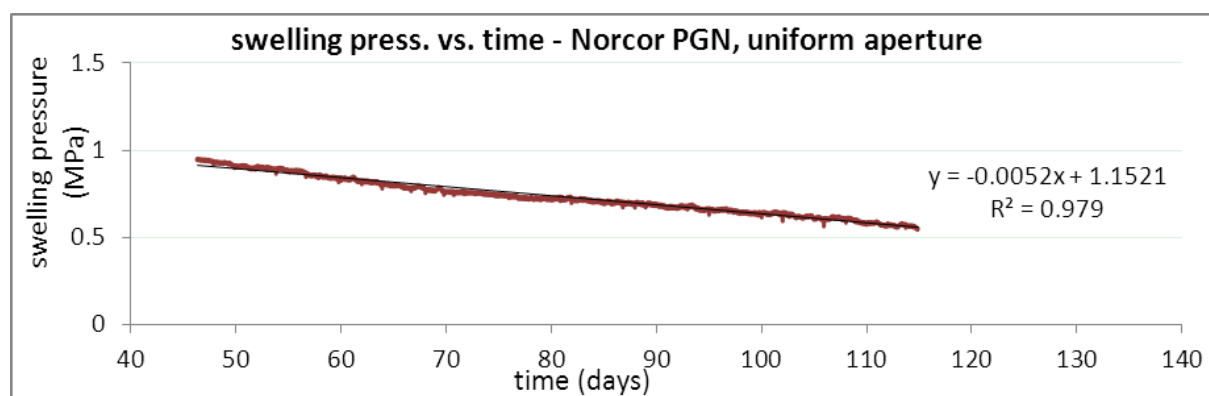
Figure 7.17: Nanocor PGN, uniform aperture cell, uniform decay in swelling pressure against time - beyond day 45

Naturally, with a higher effective dry density of montmorillonite present in the Nanocor PGN test than in the MX80, a higher swelling pressure is expected. This test did generate the highest swelling pressure, however, this may also be a function of the lower flow rate.

It may be the case that in the previous test on both MX80 and Nanocor PGN, mass loss was sufficiently high in the early phase of the experiments that it prevented the sample from generating its true potential swelling pressure.

It is apparent from Figure 7.15c that the rate of decrease in swelling pressure is more rapid towards the start of the experiment i.e. the first 40 days. Beyond 40 days, the swelling pressure decays at a relatively steady rate. This monotonic decay in swelling pressure is in line with steady mass loss from the system, and is in stark contrast to the fluctuating decay in swelling pressure exhibited in the experiments using MX80. In short, the swelling pressure continues to steadily decrease in this system as there are no mechanisms present to mitigate against mass loss.

Radial extrusion

Figure 7.18 illustrates the extrusion of the sample into the fracture throughout the course of the experiment at 10 day intervals up to 80 days. It is clear from Figure 7.18 that a rim of darker material forms at the edge of this extruded material. This is also visible to a lesser extent in the previous aborted test (Figure 7.13).

Image analysis shows smoothly increasing radial extrusion throughout the test (Figure 7.15d). This is in keeping with smoothly varying swelling pressure shown in (Figure 7.15d). There is no reduction in the rate of radial extrusion, which after the first 20 days is approximately linear. This is consistent with the steady concentration of eroded solids in the effluent (Figure 7.15b).

In Figure 7.18, the darker rim of material is more uniformly distributed around the top half (moving clockwise from 9 to 3 on the clock face) of the extruded material and adopts a different structure on the bottom half (moving clockwise from 3 to 9 on the clock face). On the bottom half, the darker material forms in discrete branches which grow by the addition of more material on their ends. This may be the result of uneven flow conditions around the sample or preferential flow around one side of the sample, creating conditions more conducive to erosion. This could occur if the inlet and outlet ports aren't perfectly in line with centre of the sample compartment.
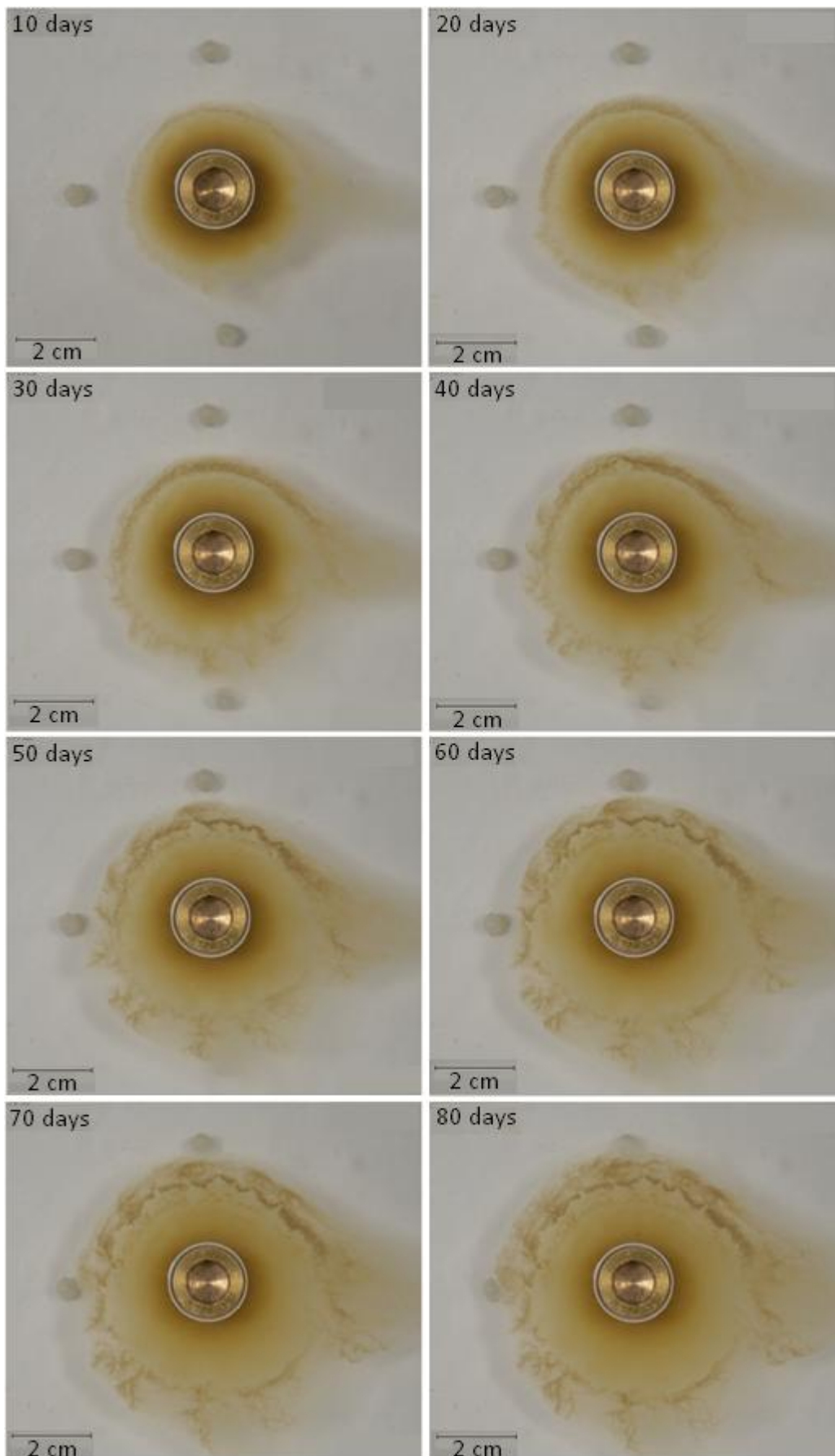
Figure 7.18: Nanocor PGN, uniform aperture cell, extrusion evolution up to 80 days

The difference in structure of the darker rim of material between the flowing test Figure 7.18 and the static test (Figure 7.13) is illustrated at the same time point in Figure 7.19.

Figure 7.19: Nanocor PGN, uniform aperture cell, comparison between 42 days with no flow (LHS) and 42 days with flow (RHS)

The left hand side of Figure 7.19 depicts extrusion under conditions of no flow after 42 days and the right hand side represents 42 days of extrusion and erosion under flowing conditions. Discounting the extent of extrusion, it is evident that a 'branch-like' darker rim of material occurs as a consequence erosion. The zone of darker material grows radially over time by the addition of new material on the end of the branches, hence it may be to the result of flocculation of non-visible colloidal material which form attractive edge/face card-house interactions when collisions between particles occurs.

The Nanocor PGN montmorillonite is graded to a purity of >98%, hence does contain a small proportion of accessory minerals, as described in section 5.2.2. The formation of this darker rim of material, however, is not occurring by the same process as the formation of the mineral ring in the previous experiments with MX80 i.e. visible migration from the central

compartment followed by deposition at the edge of the extruded material, supplementing the ring from behind. No transportation of darker minerals is observed and the ring of darker material appears to grow gradually wider by supplementation at its outer edge.

The very gradual decrease in mass loss rate over time (Figure 7.15b) could be attributable to the formation of the darker zone of material at the edge of the extruded sample; as this non-erosive region of material grows, the area of montmorillonite exposed to eroding groundwater may diminish.

7.5 Post-test analysis

Post-test X-Ray diffraction analysis and optical microscopy was undertaken on sample points from the fracture face after completion of the experiment, according to the procedure set-out in section 4.7. As with the experiment with MX80, this was with a view to understanding the mineralogy, grain size and morphology of various regions of interest on the fracture face.

7.5.1 XRD analysis

Analysis of material on the fracture surface

Once the water had evaporated from the cell, samples were taken from 4 points on the fracture face as illustrated in Figure 7.20. Sample points 2 and 4 corresponded to the outer region of the extruded material, which is darker in colour. Sample points 1 and 3 corresponded to the inner region of the extruded material. This material, though uniformly distributed around the full rotation of the extrusion zone during the experiment, contracted into lines when dried. As with the post-test analysis conducted in section 6.3.1, because of the small size of samples 1 – 4, the background scan of the sample holder discussed in section 6.3.1 contributed significantly to the diffractograms for each sample.
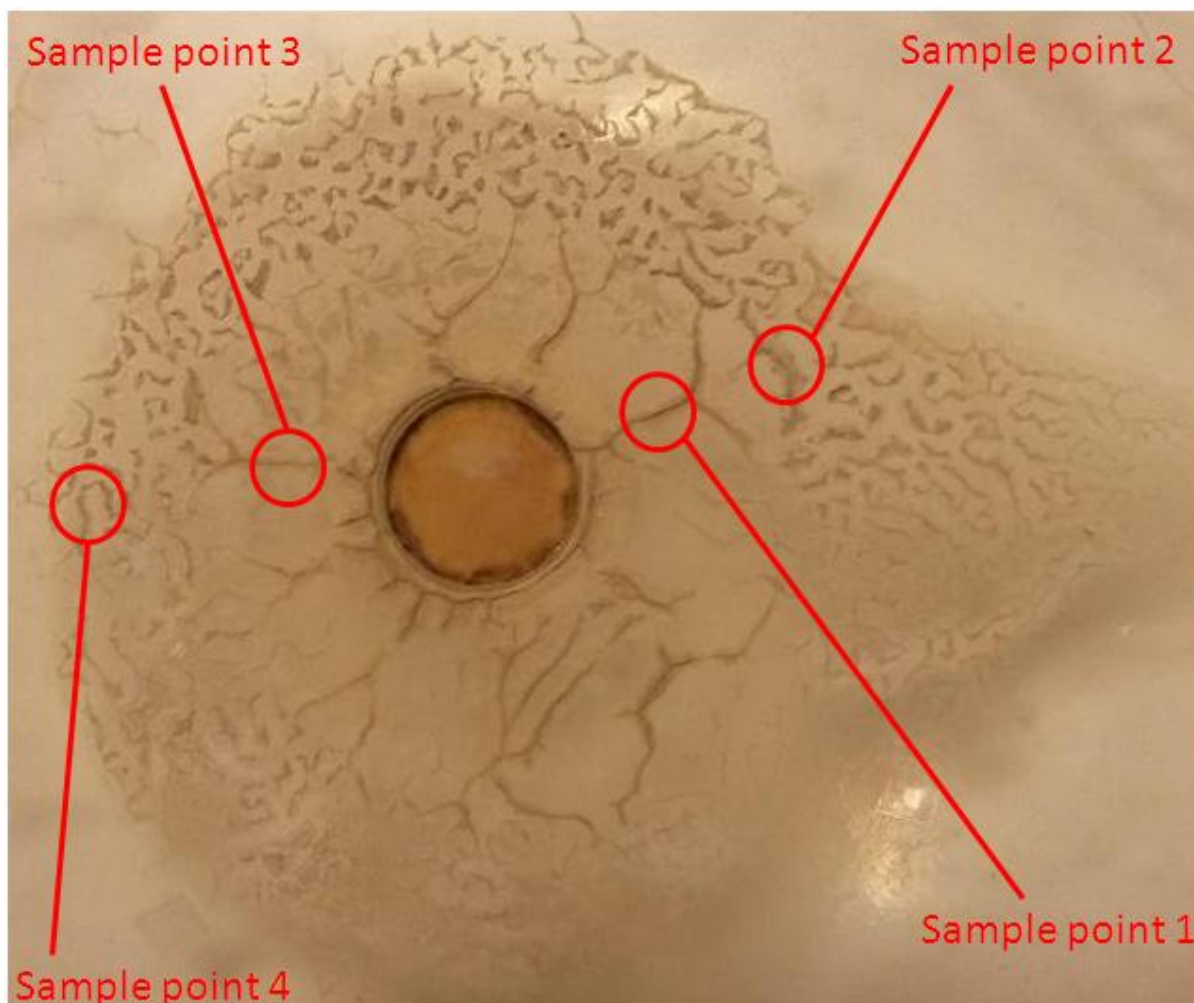
Figure 7.20: Image of bottom half of Nanocor PGN fracture cell with extruded material after drying. Sample points indicated

Sample points 1 and 2

The X-Ray diffractograms for samples 1 and 2 are displayed in Figure 7.21. Disregarding the background signal from the sample holder (Figure 6.12) , it is clear that each sample has a different mineralogical make-up. The inner region of the extruded material is predominantly monmorillonite, sample 1, Figure 7.21a. Whereas the outer region, sample 2, Figure 7.21b, is enriched with quartz, and has a diminished peak for montmorillonite in relation to the inner region sample. The inner region sample does show a small presence of quartz at 26.5° 2θ, however, this reflection is far weaker in this sample than the outer one. Hence, quartz is migrating through the inner region and being deposited at the outer region where the enriched zone of quartz occurs.
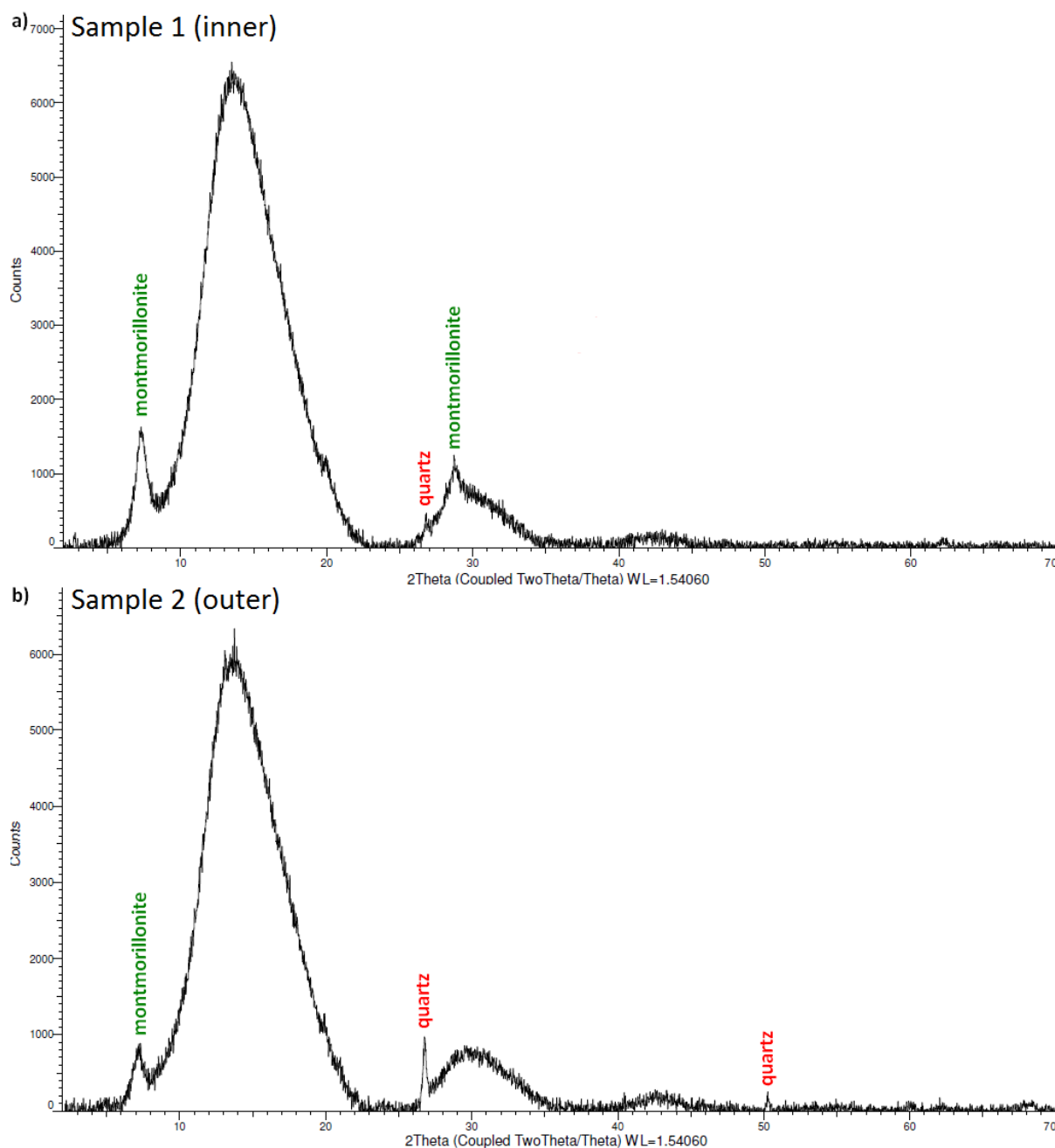
Figure 7.21: Post-testX-ray diffraction data for Nanocor PGN experiment. a) Sample 1 (inner) and b) Sample 2 (outer).

The secondary peak for montmorillonite at 28.5^o 2θ is not discernable in the outer sample, Figure 7.21b, most likely because of it being present in far lower quatities relative to the inner region.

Sample points 3 and 4

This apparent difference in mineralogy i.e. an enriched region of quartz at the edge of the extruded zone and an apparent lack of it in relation to montmorillonite in the inner region of

material is also consistent with samples 3 and 4. The X-ray diffractograms for samples 3 and 4 are displayed in Figure 7.22:
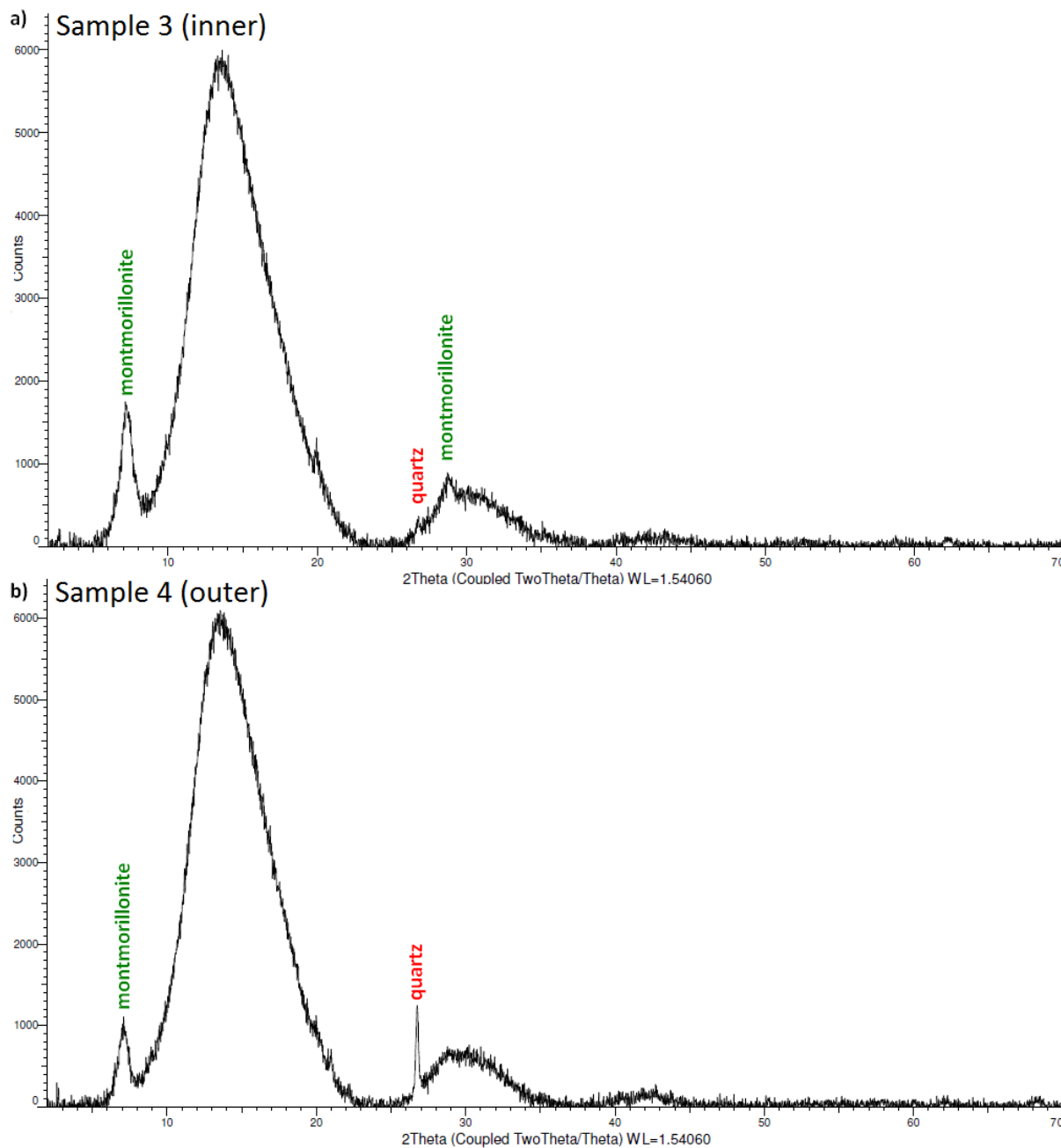
Figure 7.22: Post-test X-ray diffraction data for Nanocor PGN experiment. a) Sample 3 (inner) and b) Sample 4 (outer).

Again, in Figure 7.22 the outer region, sample 4, which appears as the dark coloured material at the edge of the extrusion zone in Figure 7.18, is enriched with quartz and depleted in montmorillonite relative to the inner region, sample 3, Figure 7.22a.

The XRD data shown in Figure 7.21 and Figure 7.22 are in stark contrast to the equivalent results from the MX80 shown in Figure 6.13, Figure 6.15 and Figure 6.17, in which the quantities of crystalline minerals deposited in the mineral ring were sufficient to render the montmorillonite undetectable. The results do indicate, however, that a similar process is occurring with the small percentage of quartz present in the Nanocor PGN system. Although the accumulation of quartz in the fracture is not sufficient to mitigate against erosion over the timescale of this test.

Eroded material

A sample of the eroded material from the cell was also analysed by X-ray diffraction according to the method detailed in section 4.7.3. It is apparent from the scan depicted in Figure 7.23, which shows the diffractogram for the eroded material on the filter paper, that, similar to the eroded material from the cell containing MX80 depicted in Figure 6.18, the basal reflection for montmorillonite at 7° 2Θ has been enhanced by being effectively analysed as an oriented mount rather than random powders as a result of the vacuum filtration process.

On this occasion, the noise artefact from the sample holder has been reduced to one broad peak between 13° and 21° 2Θ. Presumably the background manifests itself at different diffraction angles to previous examples, such as in Figure 6.12 and Figure 6.19, because of the degree to which it is exposed to the X-ray source.

Nanocor PGN cell - material eroded
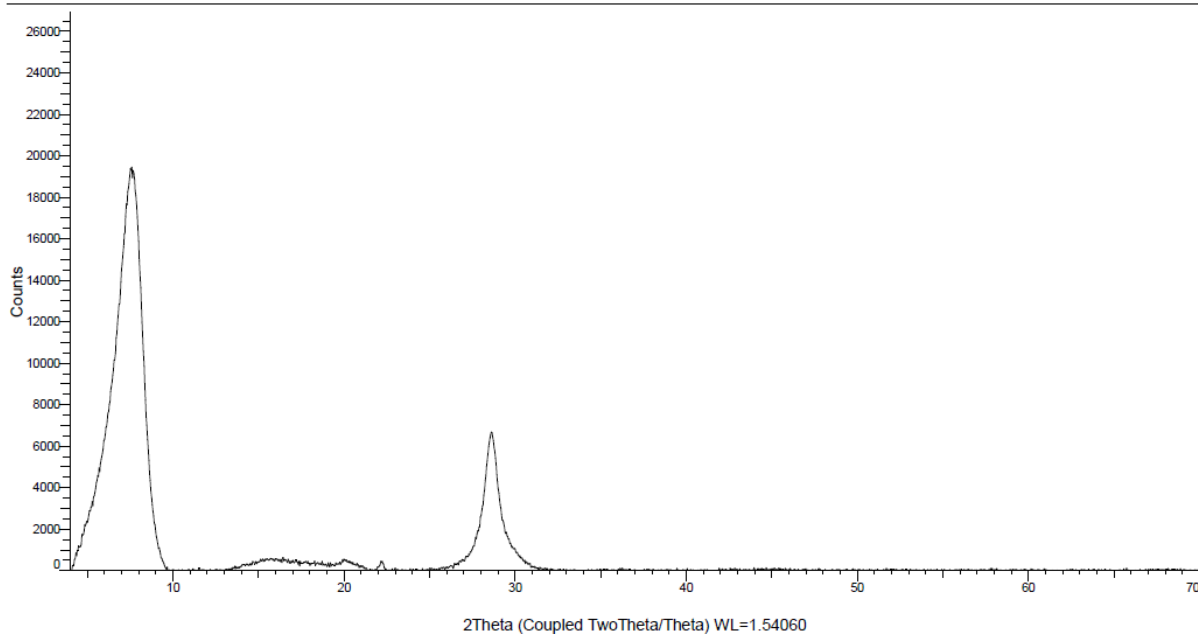
Figure 7.23: X-ray diffraction pattern for eroded sample from Nanocor PGN cell, background removed.

One characteristic of the diffractogram shown in Figure 7.23 does not occur in the diffractograms for the eroded material from the cell containing MX80 (Figure 6.18 and Figure 6.19); the peak at 22° 2Θ. This peak is more readily discernible when the Counts axis for the diffractogram shown in Figure 7.23 is truncated, as revealed in Figure 7.24.

Figure 7.24: X-ray diffraction pattern for eroded sample from Nanocor cell, background removed, Y-axis truncated

The small distinct peak at 22$^\text{o}$ 2Ɵ in Figure 7.24 corresponds to the plagioclase albite, as also shown in the X-ray diffractogram for accessory minerals isolated from MX80 in Figure 5.5, and, as stated by the manufacturer, is present in Nanocor PGN. This suggests that the particle size of this mineral in the Nanocor PGN clay is small enough to facilitate its removal from the system by the shear force generated by the flowing water.

7.5.3 Optical microscopy

Optical microscopy was performed on each of the samples described in 7.5.1 with the aid of a *Nikon Eclipse LV100ND* optical microscope. In order to perform the microscopy, each sample from 7.5.1 (stored in weighing boats), was subsampled and the subsample transferred to a glass slide. 4x, 10x, 20x and 40x magnification in both bright and dark field methods were employed.

Sample points 1 and 3 – Inner regions of fracture face

Photomicrographs of sample point 3, from the inner region of extruded material, at 4x and 10x magnification are shown in Figure 7.25. The sample appears to be exclusively composed of montmorillonite clay particles, that are very different in appearance from the transparent and varied colours of crystalline minerals in the size range 10 – 300 μm present in the samples taken post-test from the MX80 experiment, shown in Figure 6.23.

These particles in Figure 7.25 are large, up to 500 μm in breadth. The size of these particles is most likely a result of the sampling technique employed, which involved physically removing the sample from the fracture face to which it had adhered, causing it to break into random sized aggregates. The clay aggregates are characterised by their dark centres and opaque edges, at which broken bonds have resulted in the lamellae being thinner, allowing more light to pass through. Despite the presence of a small quantity of quartz in this material, according to the mineralogical data in Figure 7.21a and Figure 7.22a, no quartz is visibly present at 4x magnification (Figure 7.25a) or 10x magnification (Figure 7.25b). This is perhaps due to the fact that, as the sample had effectively formed a film on the fracture face and had to be removed by mechanical force, any quartz within the sample may be confined within the larger montmorillonite aggregates. As detailed in section 5.2.1 these quartz particles are in the size range <30 μm.
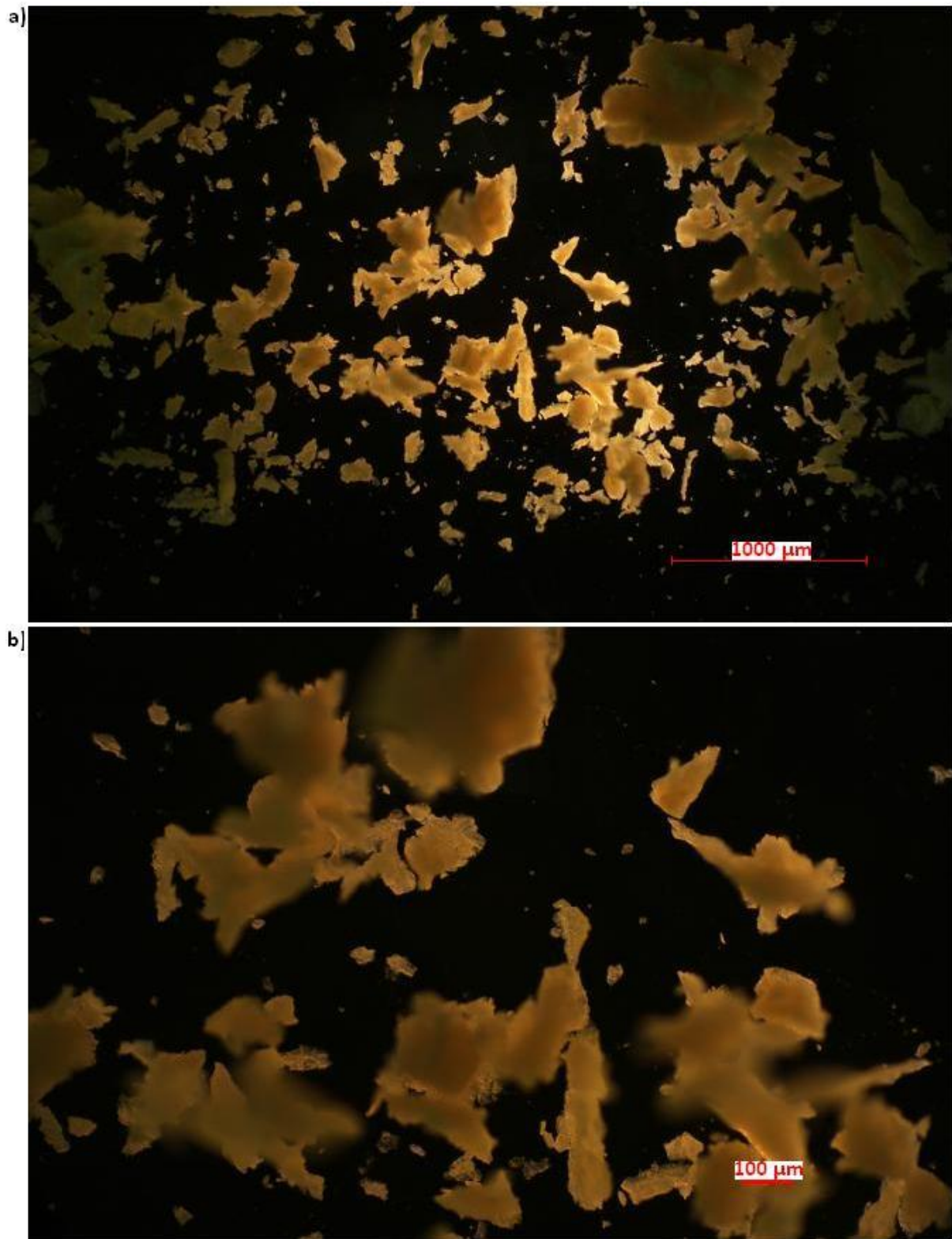
Figure 7.25: Post-test inner region sample at a) 4x magnification and b) 10x magnification
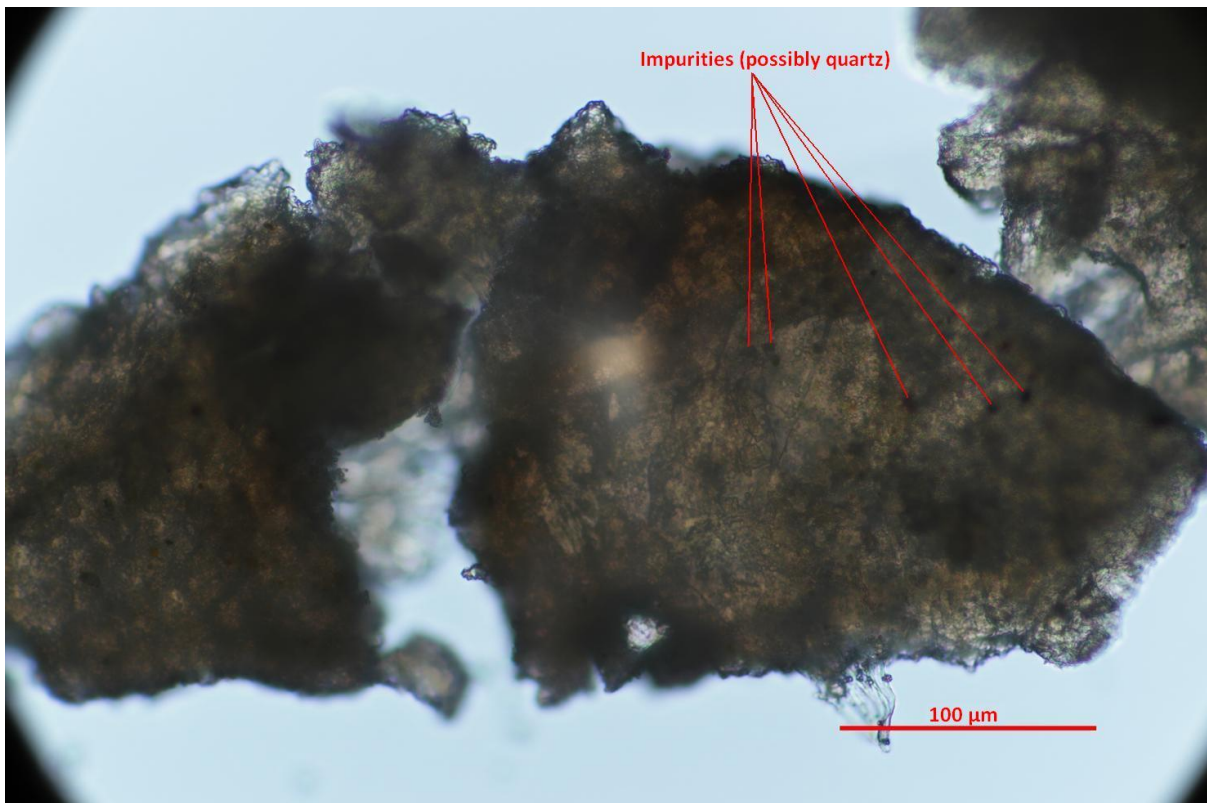
Figure 7.26: Post-test inner region clay aggregate (1) at 40x magnification.

Closer inspection of the particles (Figure 7.26 and Figure 7.27) confirms their resemblance to small clay aggregates; lamellar in appearance and thin enough to allow light to pass through. This implies that any quartz which was in the sample must be very fine grained, because even at 40x resolution, when focussing on individual clay aggregates, no quartz is visible. Dark spots (5 µm in diameter) within the aggregates in Figure 7.26 and Figure 7.27 could correspond to fine-grained quartz particles.
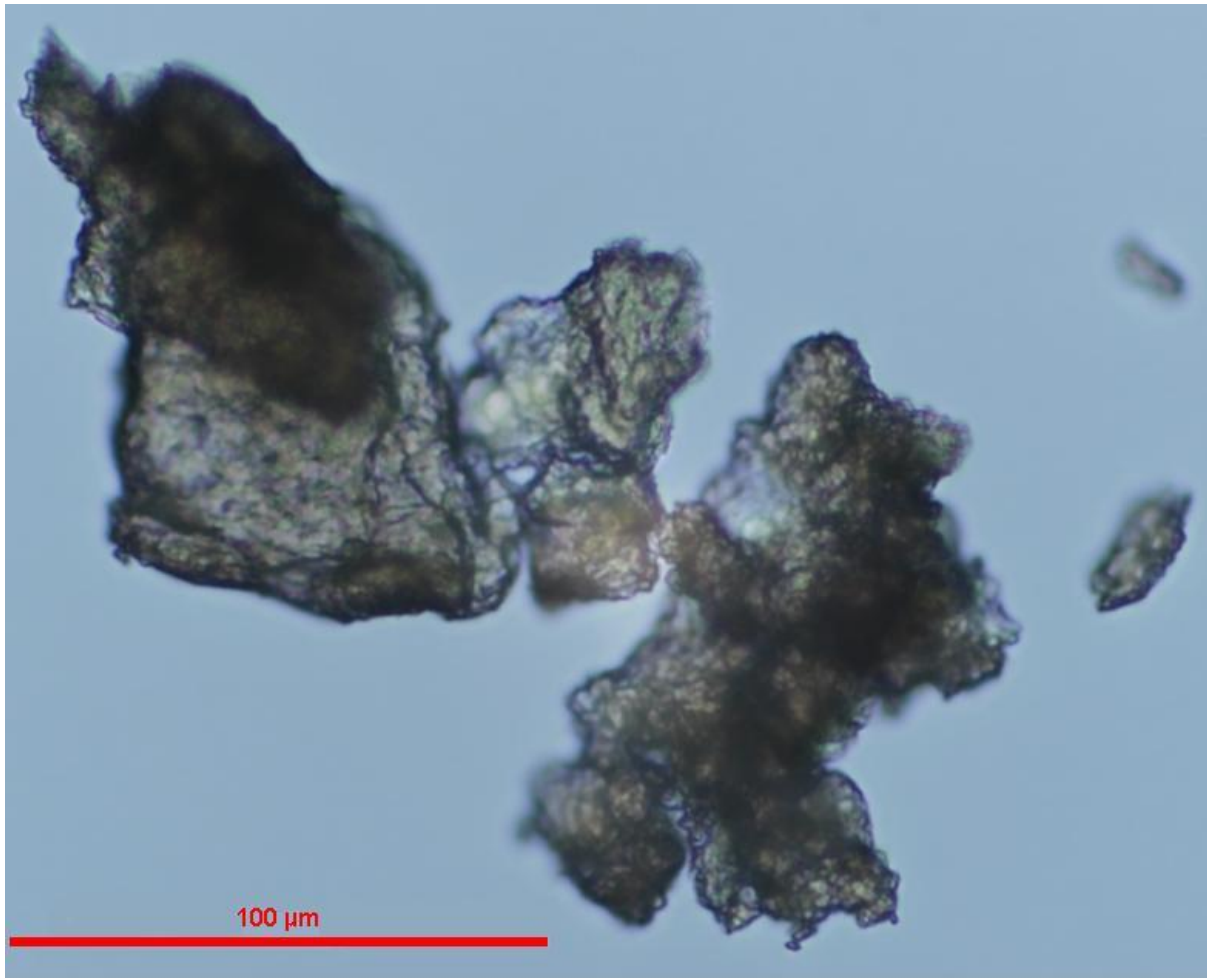
Figure 7.27: Post-test inner region clay aggregate (2) at 40x magnification.

Sample points 2 and 4– Outer regions of fracture face

Sample points 2 and 4 are similar in appearance to the inner region of material. Optical microscope images of sample point 4, from the outer region of extruded material, at 4x magnification and 10x magnification are shown in Figure 7.28. With relatively large clay particles, whose size is most likely determined by the sampling technique, interspersed with particles in the <50 µm range as shown in Figure 7.28. One particle does stand out as being quartz like in Figure 7.28a and is brought shaper in to focus in Figure 7.28b in the centre right hand side of the image, approximately 200 µm in diameter, revealing it to resemble a quartz particle surrounded by clay aggregates.
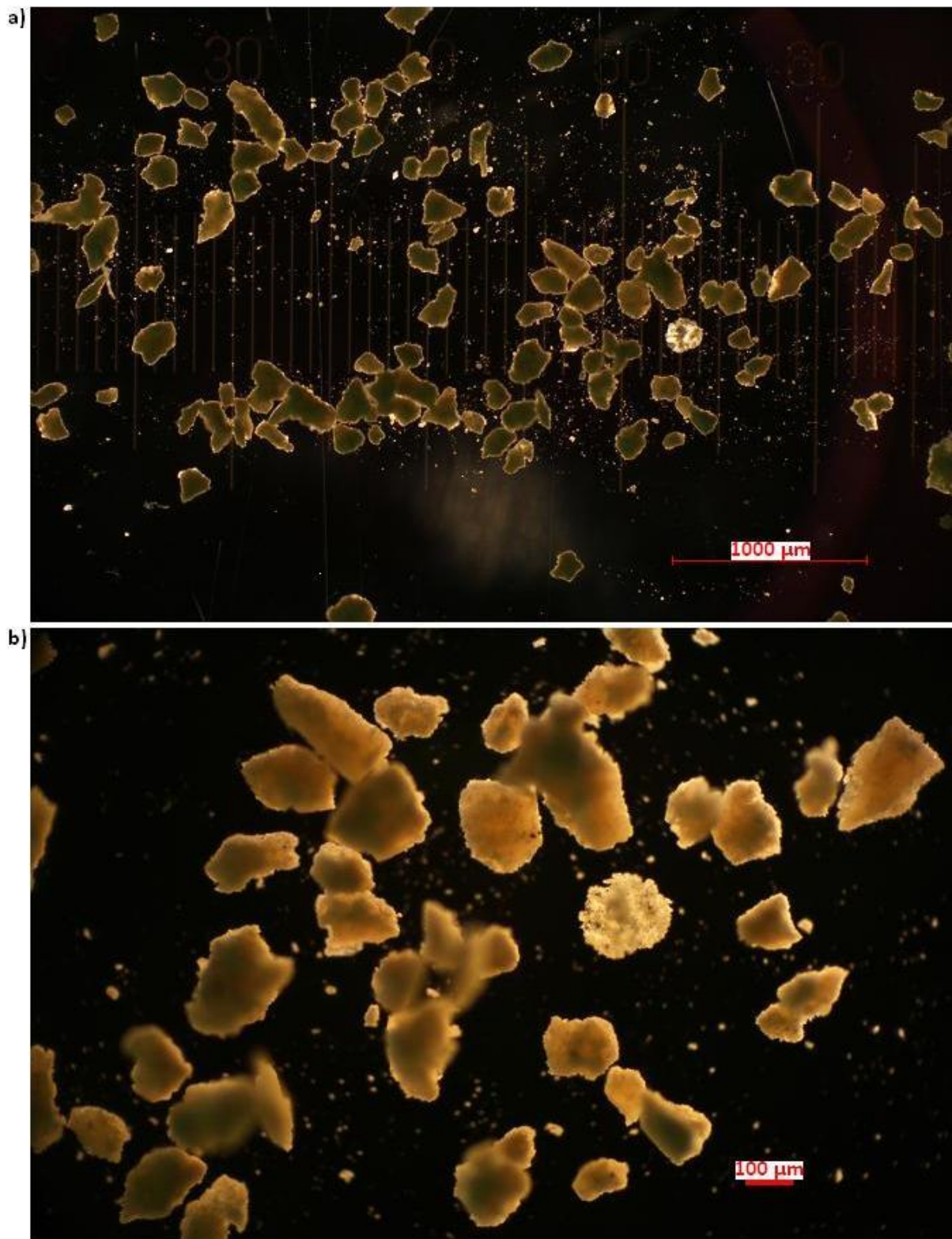
Figure 7.28: Post-test outer region sample at a) 4x magnification. and b) 10x magnification

Again, despite the outer region of material being enriched in quartz, as determined from the XRD, visualising it under optical microscopy at up to 40x magnification proved difficult.

At 40x magnification, the breakdown of the large clay particles into small stacks of montmorillonite lamellae, <5 μm in diameter is visible. These particles bear some resemblance to the '*as-delivered*' state of Nanocor PGN shown in Figure 5.8. Again however, no quartz particles are visible at this magnification.

Figure 7.29: Post-test outer region clay aggregate, broken down into stacks of lamellae, at 40x magnification.

7.6 Conclusions

The experiments described in this chapter has confirmed that the accessory minerals are effective in mitigating against erosion, irrespective of whether a variable aperture or a uniform fracture aperture are present. A comparison of results identifies a critical thickness of the accessory mineral ring of 2 mm, at the edge of the extruded material, at which the ring becomes effective in erosion mitigation. This value was consistent in both the uniform and variable aperture experiments.

In the case of the uniform aperture fracture experiment described in this chapter, no increases in swelling pressure were apparent after the formation of the accessory mineral

ring to the critical thickness, at which point erosion reduced and the swelling pressure reached a steady state.

This chapter has also shown that, without the accessory minerals present in MX80, there is no mechanism to mitigate against erosion, resulting in a steady mass loss and swelling pressure decay throughout the course of the experiment.

It was evident from the post-test analysis on experiment number 3 that quartz, occurring as <2% of the Nanocor PGN, was deposited at the edge of the extruded material as a consequence of the montmorillonite erosion. Its presence however was not sufficient to mitigate against erosion. Both montmorillonite and the accessory mineral albite were found in the material eroded from the cell.

A more detailed examination of the way in which mass loss, the accessory mineral ring and swelling pressure of the system correlate for MX80 bentonite will be discussed in the discussion chapter of this thesis.

Chapter 8 The effect of initial saturation with a saline solution on bentonite erosion

One final test was undertaken on MX80 in a variable aperture cell, using a saline solution as the initial saturating fluid, to be followed by deionised water. This was with a view to reproducing the conditions present in a repository. Early in repository evolution, after emplacement of the buffer and backfilling of the tunnels, any groundwater saturating the repository will most likely be saline to briny in nature, however, later (perhaps many millennia later) the intrusion of fresh glacial melt water may occur. The aim of the experiment was to establish what effect, if any, initial saturation with a saline solution would have on MX80 erosion. The following test corresponds to experiment number 5 in Table 7.1.

8.1 MX80, variable aperture, constant flow, initial saturation with saline solution – experimental data

As with previous tests, the methodology outlined in chapter 4, for MX80 in a variable aperture fracture cell was followed. The salinity of the saturating solution was the only parameter changed. The initial saturating solution comprised of a 50:50 mix (by weight) of NaCl and $CaCl_2$ at a concentration of 35g/L. Sea water typically has a total dissolved solids concentration of 35 g/L, though the concentration of calcium ions relative to sodium ions used in this solution is high relative to seawater concentrations. There are instances however, throughout a repository evolution, which may serve to increase the concentration of calcium ions in the groundwater, such as leaching from cement plugs and seals. The solution chemistry was chosen on the basis of being sufficiently saline to prevent chemical erosion during sample saturation though the high calcium:sodium ratio, relative to a typical groundwater (e.g. Table 3.1) may have affected the extent to which the sample could extrude into the fracture.

The solution was prepared by weighing 35g of reagent grade Sodium Chloride and 35g of reagent grade Calcium Chloride into a 2 litre volumetric flask, filling to 2 litres with deionised water and stirring until mixed.

The test was run for two weeks before it had to be abandoned because the peristaltic pump pipe on the inlet line ruptured and drew air in to the flow cell. The cell was dismantled and a

further attempt at undertaking the test also met with difficulties because of the accumulation of a dark material, presumably organic matter, in the inlet and outlet pipes to the cell causing the system to become blocked. Despite fully disinfecting the cell, pipework and inlet bottle with *Virkon* disinfectant, a further attempt at running the test resulted again in the formation of the dark matter. Alas, the test was aborted entirely because of time constraints.

Despite the limited duration of the test, some meaningful data was collected which suggests that the effect of initial saturation with a saline solution may not influence the development of the mineral ring or the mode of erosion witnessed in previous experiments with MX80 for a number of reasons which shall be elaborated upon. The experimental data gathered over the course of the experiment is shown in Figure 8.1.
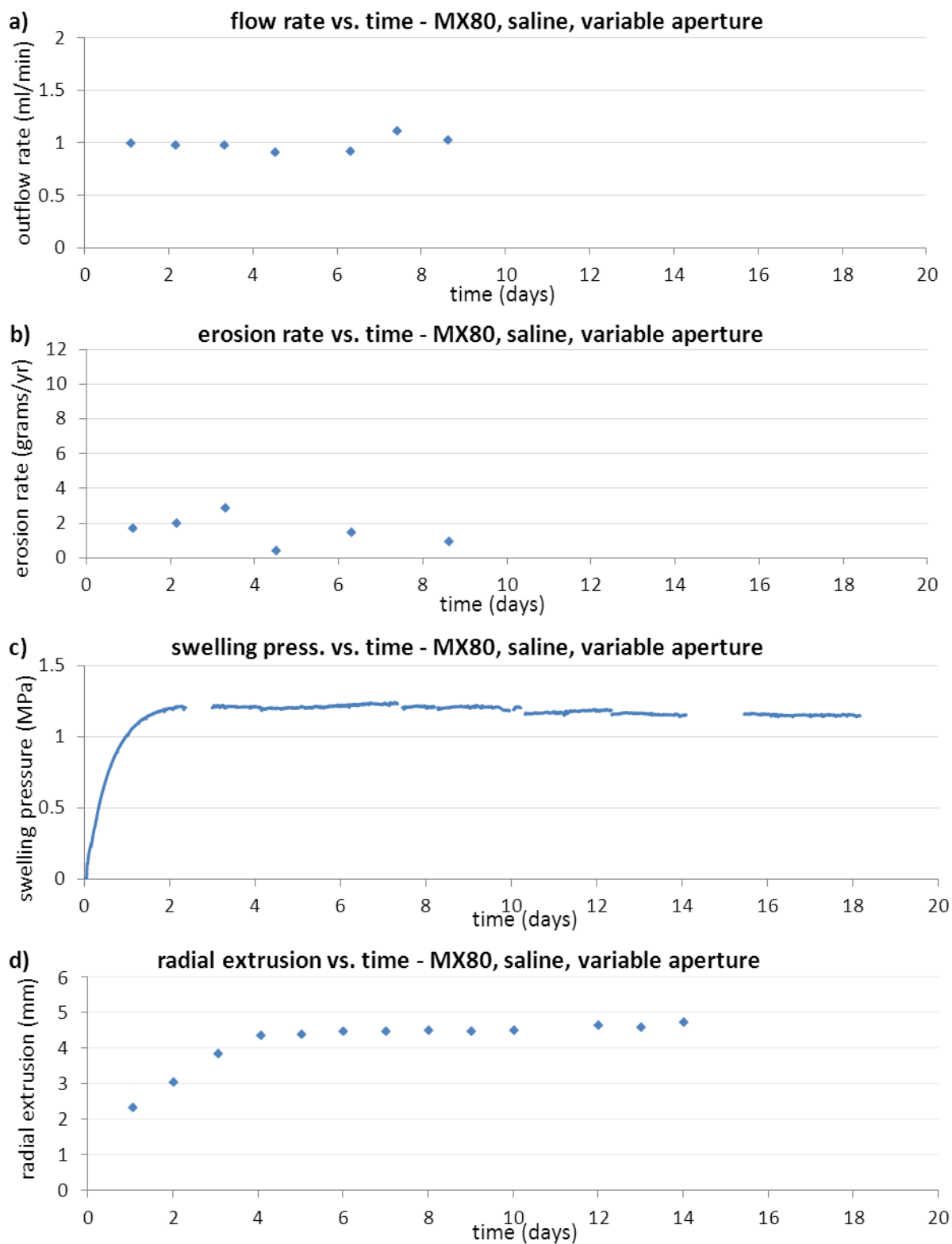
Figure 8.1: MX80, saline, variable aperture fracture data for a) flow rate b) erosion rate c) swelling pressure and d) radial extrusion distance with respect to time

Flow rate

The 50:50 NaCl:CaCl$_2$ was pumped through the system at a flow rate of 1ml/min as illustrated in Figure 8.1a, which shows the flow rate over the short duration of the

experiment. When the influent bottle was running empty, another solution was prepared in the same fashion.

Mass loss

The limited mass loss data which were collected over the 10 day period are shown in Figure 8.1b. It is clear from Figure 8.1b that insignificant mass is being lost from the system, relative to those which had been undertaken previously. Any mass which was recorded on the filter papers after filtration appeared to be evaporated salts from the water flowing through the system and not from the montmorillonite.

Swelling pressure

Figure 8.1c shows the swelling pressure, which rises to a value of approximately 1.2 MPa before remaining relatively stable for twenty days. Saturation with a saline solution should not generate as significant a swelling pressure as with a dilute solution (as long as the dilute solution does not immediately initiate erosion). This is because of the limit in the basal spacing, or volume of water which can be accommodated, between clay platelets when specific cations are also present. The test described in chapter 9, for dilute waters, measured a peak value of 1.6 MPa (Figure 7.1c), as compared to 1.2 MPa (Figure 8.1c) when saturating with a saline solution.

The very slight decrease in swelling pressure over the 18 day period may be attributable to the limited extrusion into the fracture, i.e. a decrease in mass of sample held in the central compartment. Maintenance of the swelling pressure at this value of 1.2 MPa is consistent with little-to-no mass loss from the system. This behaviour is as expected, with the non-erosive (i.e. non colloidal sol forming conditions) present during this early saturation phase in a repository scenario.

Radial extrusion

The material approaches a maximum extrusion distance of 4mm as depicted in Figure 8.1d, which shows the radial extrusion of the sample throughout the course of the experiment determined from image analysis, and Figure 8.2. Initial extrusion occurred quite rapidly to 4 days, beyond which time limited extrusion was observed in the cell.
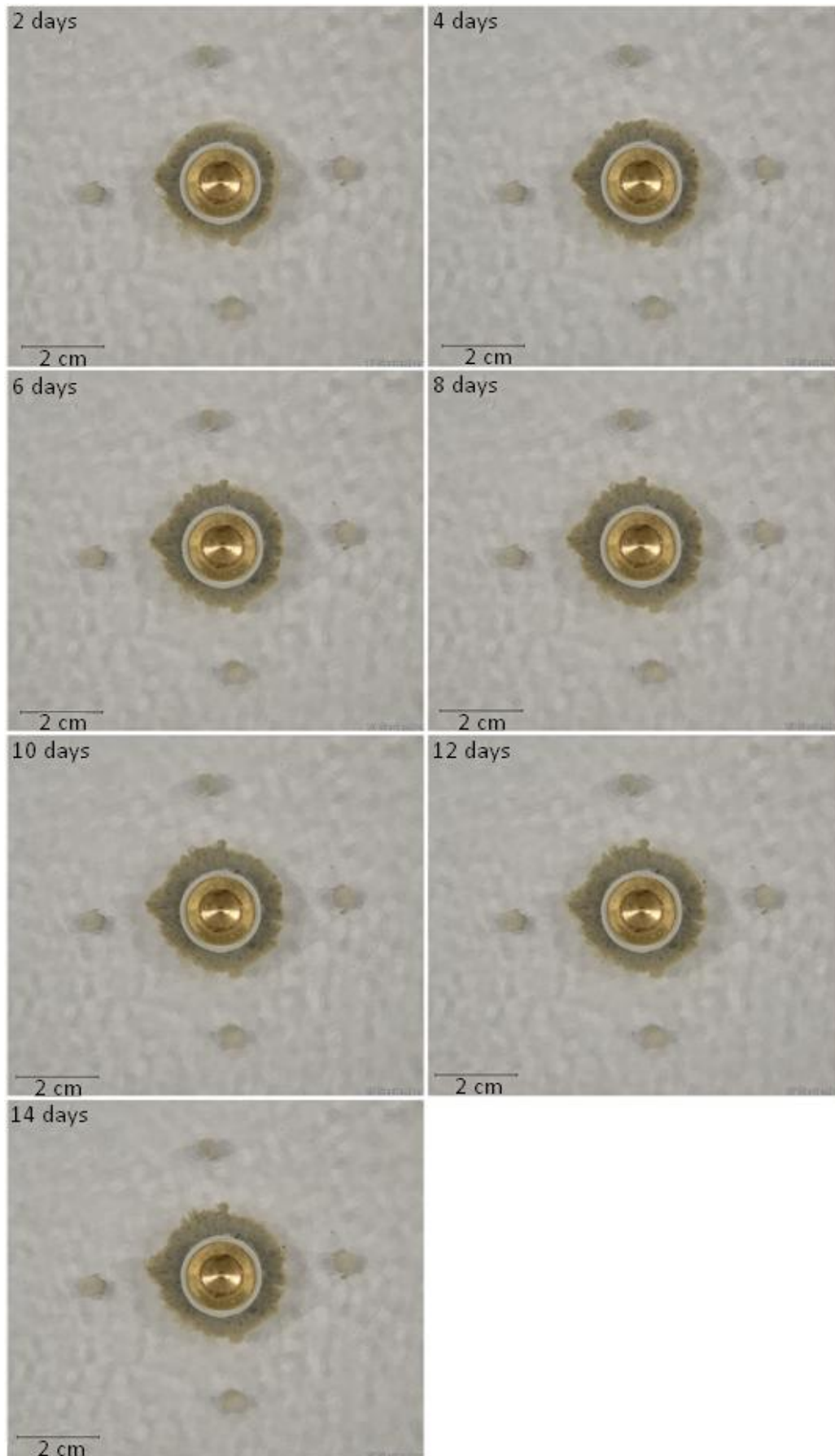
Figure 8.2: MX80, variable aperture cell, saline conditions, extrusion up to 14 days in 2 day increments

The extrusion of the material at 14 days is also shown in Figure 8.3, which illustrates the difference when saturating with a dilute solution. The extent of extrusion is much smaller than when saturating with a dilute, erosive solution at the same time frame.
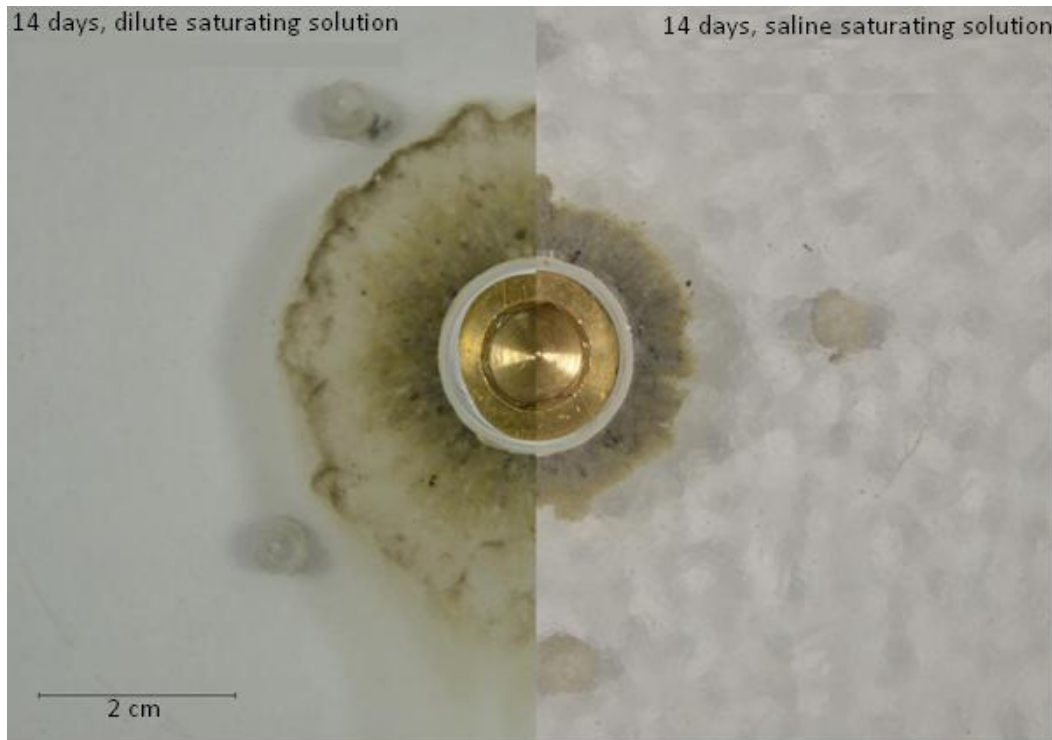
Figure 8.3: MX80, comparison pf dilute (LHS) and saline (RHS) saturating conditions at the same 14 say time point in the experiment

The most notable observations from Figure 8.3 include:

1. The extent of extrusion when saturating with saline water is less than half of that when saturating with deionised water.

2. There is no visually discernible density gradient across the extruded material when saturating with a saline solution.

3. The accessory minerals are interspersed evenly throughout the extruded material and don't accumulate at its edge.

4. The extruded material did not behave in the same dynamic fashion: there was no visible accessory mineral transportation.

Density gradient of extruded material

Intuitively, observations 1 - 4 above are what we may come to expect of these conditions. As previously stated, the basal spacing between clay platelets is limited to a set distance in a saline system, this in turn will limit the extent of extrusion from the central compartment but also explains the lack of a visually discernible density gradient across the extruded material. There is in fact a density gradient present over this extruded material as illustrated in Figure 8.4 which illustrates gray value as a proxy for material density across two sections, $\beta2 - \beta1$ and $\alpha2 - \alpha1$.
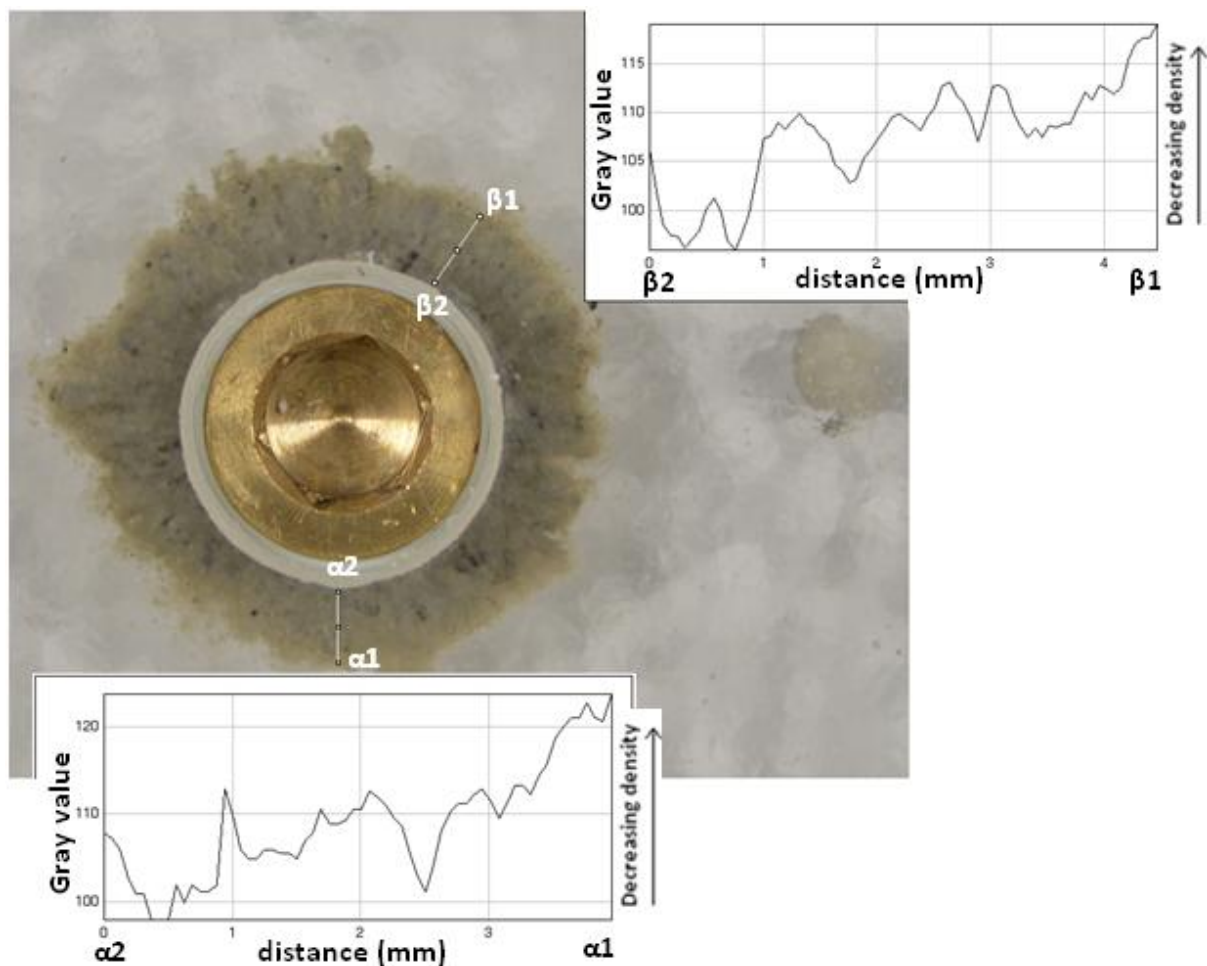
Figure 8.4: MX80, variable aperture cell, saline conditions. Pixel gray value as a proxy for material density across two sections of extruded material

The limit to the basal spacing across this material means that when, in the outer most regions of the extruded material the clay has reached its full capacity to absorb water, water

is forced to migrate by diffusion further into the extruded material. Thus a density gradient is less discernible by eye. The clearly discernible density gradient is present in the deionised system, due to the fact there is no limit to the basal spacing between clay platelets so the material is free to expand.

Discounting slight lighting variations between experimental apparatus, the sharp change in density occurs around a gray value of approximately 130 under dilute saturation. Under saline saturation conditions the extruded material, at its maximum extent of extrusion, has a gray value beyond 120, approaching 130.

8.2 Discussion on the effect of initial saturation and extrusion with a saline solution on a cyclic erosion mechanism.

To reiterate, neither of the experiments undertaken with a saline solution as saturating fluid ran for a long enough time frame to introduce dilute erosive conditions. Had erosive conditions been introduced however, likely effects are:

s) The initial mass loss recorded from the system may be higher than experiment 1, described in chapter 6. This is because there will be a larger surface area of montmorillonite in contact with the groundwater from the onset of the dilute erosive conditions.

t) There may be some ageing artefacts present when deionised water is introduced, in that, it may take time for the now saline pore water of the bentonite to be flushed out of the pore space.

It is clear from Figure 8.1c, that the sample had reached its full extent of extrusion at 4.5mm into the fracture. This equates to an increase of ≈50% of interfacial surface area in contact with the eroding solution had erosive conditions been initiated in the saline cell at 4.5 mm extrusion relative to erosive conditions being present from the start of the test. Using data on mass loss presented in Figure 8.5 it is possible to calculate the likely initial erosion rate.
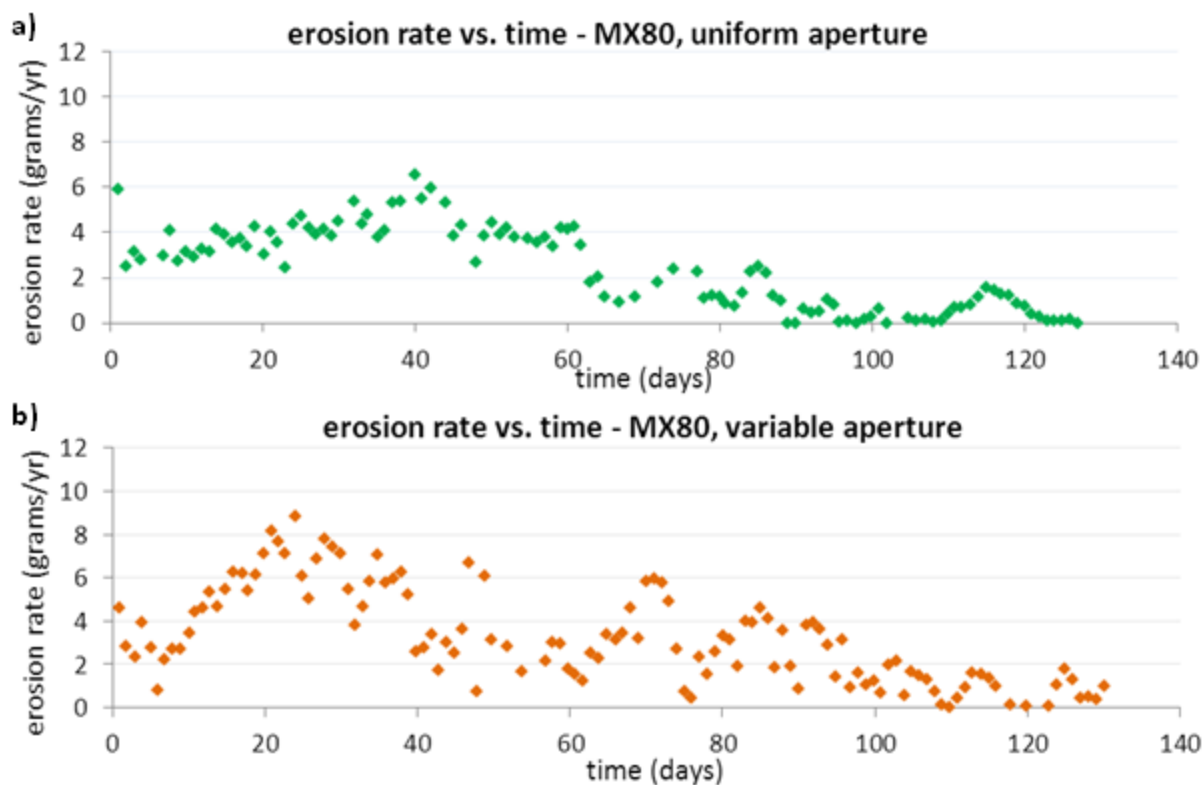
Figure 8.5: Erosion rate vs. time for MX80 in a) uniform aperture cell and b) variable aperture cell

Figure 8.5 shows that the initial rate of erosion in both experiments using MX80 (discounting mass loss because of sample disturbance during emplacement) is approximately 3 grams/year. Assuming that this figure is directly proportional to the interfacial surface area between the sample and the eroding water, an increase in surface area of 50% might be expected to produce an initial erosion rate in the region of 4.5 grams/year. It has been shown, however, that the rate of mass loss is not only proportional to the interfacial surface between sample and groundwater but is also affected by the pore water chemistry of the sample. This is because of the fact that the increase in erosion rate to a peak in Figure 8.5a and Figure 8.5b occurred relative linearly whereas the extrusion behaviour of the samples over the same time period did not, as shown in Figure 8.6.
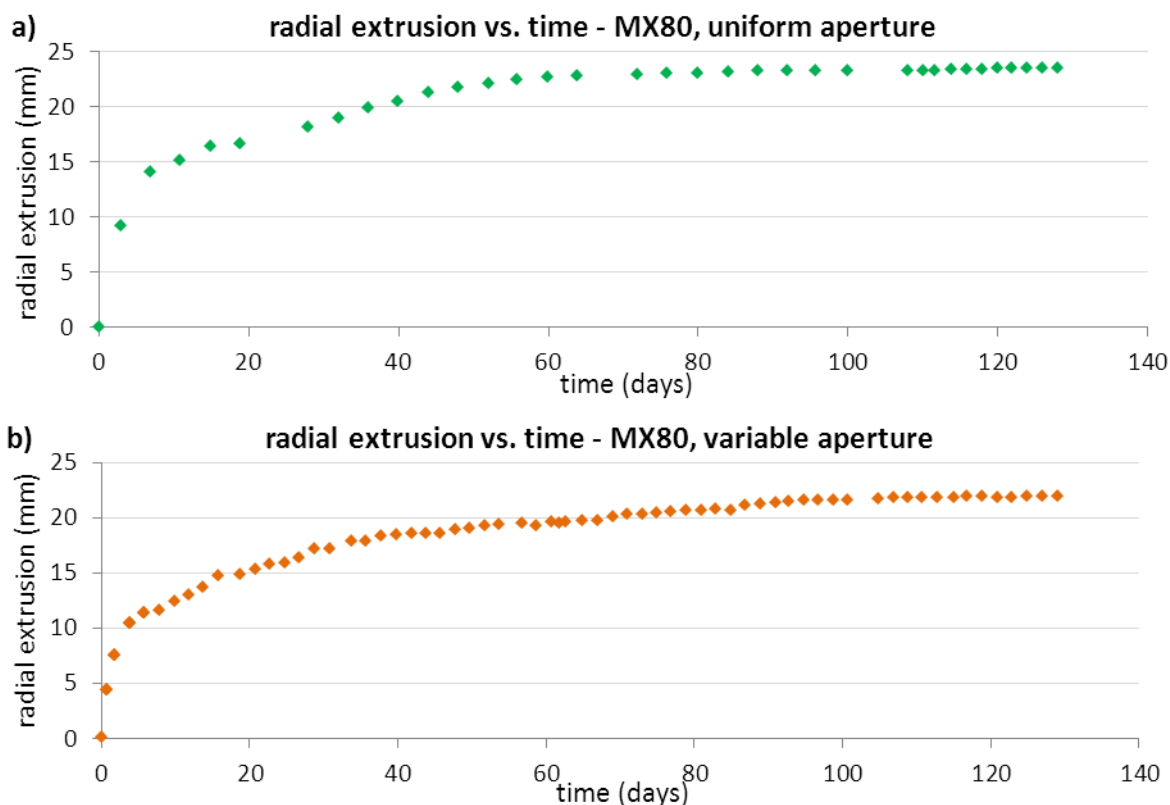
Figure 8.6: Radial extrusion vs. time for MX80 in a) uniform aperture cell and b) variable aperture cell

The increase in dissolved salts in the pore water of the sample, because of saturation with a saline solution, may offset the larger magnitude of initial erosion rate one might expect due to the increase in interfacial surface area.

Further to this, the 4.5 mm maximum extent of extrusion of the sample under saline saturating conditions is only ~20% of the maximum extent of extrusion observed in both the uniform and variable aperture cell tests under erosive conditions. This indicates that the majority of bentonite extrusion (~80%) would only occur if dilute, erosive conditions were introduced into the cell. At this point, one might expect the erosive behaviour of the sample to exhibit a similar nature to that depicted in Figure 8.5a and Figure 8.5b.

8.3 Conclusions

Insufficient data was gathered from the tests described in this chapter to say conclusively whether initial saturation and extrusion with a saline solution may have any effect on the erosion process. However, based on the data which was gathered and the experiments

described in chapters 6 and 7 for erosion of MX80, an increase in the initial mass loss from the system upon the introduction of deionised water might be expected.

Chapter 9 Discussion

This chapter proposes a new mechanism for buffer erosion based on the data gathered from the erosion experiments with MX80.

The practical implications of the research are also addressed i.e. how the mass loss data and erosion mechanism presented compares with SKB's current quantitative safety case assessment, and how the data may scale to a repository scenario, to ultimately be incorporated into future quantitative safety case assessments of buffer loss from a fracture intersecting a deposition hole in the KBS-3V concept.

Similar filtration systems for erosion prevention, from engineered systems out-with the context of buffer erosion in radioactive waste disposal, are also briefly explored.

9.1 The cyclic erosion mechanism

It has been demonstrated in chapter 8 that once the accessory mineral ring at the edge of the extruded material reaches a critical thickness, it is effective in mitigating against erosion in both the variable and uniform aperture fracture cells. This process is now considered in more detail, taking into account the swelling pressure behaviour in both the uniform and variable aperture fracture tests.

Figure 9.1 reproduces the observations of erosion rate for MX80 in both the variable (Figure 9.1a-c) and uniform aperture (Figure 9.1d-f) flow cells. Both tests demonstrate the same underlying behaviour. Initially, there is a rise in erosion rate, during which time the accessory mineral ring forms at the perimeter of the extruded material and then thickens. Once the thickness of the ring has reached a critical value (~22 days in the variable aperture cell and ~40 days in the uniform cell, Figure 9.1 a and d respectively) the mineral ring begins to inhibit erosion. For the remainder of the test, the erosion rate displays a periodic behaviour with a gradually decreasing magnitude.
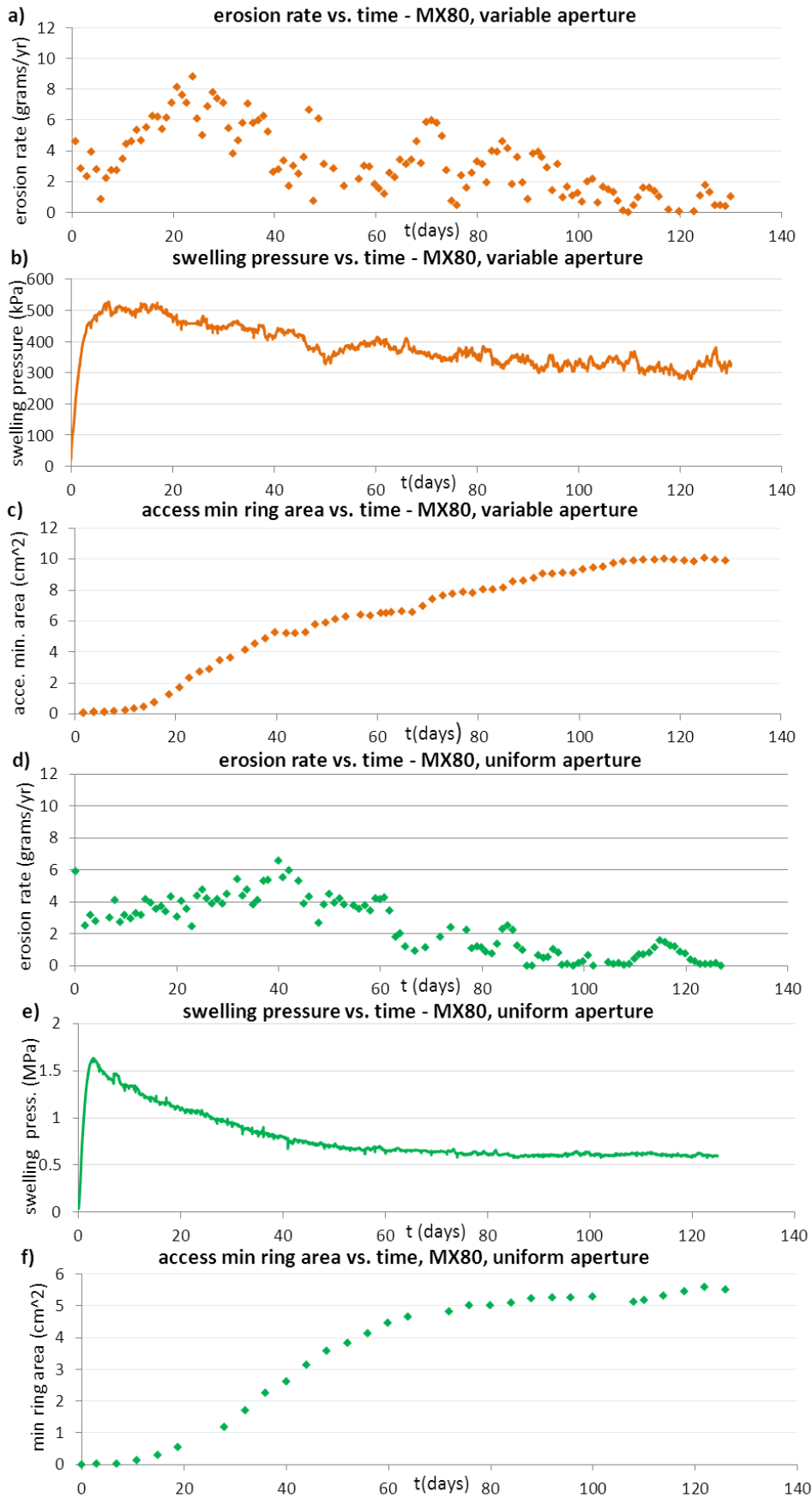
Figure 9.1: MX80 experimental data w.r.t. time a) erosion rate, var aperture b) swelling pressure, var aperture, c) min ring area, var aperture d) erosion rate, uni aperture e) swelling pressure, uni aperture, f) min ring area, uni aperture

Figure 9.2 reproduces, in more detail, the erosion rate swelling pressure and mineral ring area for two consecutive periodic cycles (between 48 to 84 days on Figure 9.1a) for MX80 in the variable aperture flow cell. Each periodic cycle can be considered to occur in 2 stages. In stage 1, the pressure rises, the accessory mineral ring thickens gradually and the erosion rate decreases. Figure 9.3a shows a conceptual model of this stage during which bentonite is being exported at a slow rate to the edge of the mineral ring, which is corrugated in shape. Once at the edge, the montmorillonite diffuses through the ring at a low rate, leaving behind additional accessory minerals that thicken the ring. Stage 1 ends when the mineral ring is breached (Figure 9.3b) which occurs when the swelling pressure behind the ring becomes large enough to induce failure. This failure occurs at a concave part of the ring, where the ring is structurally weak, and acts to release the swelling pressure. Hence, in Stage 2 of each cycle, the swelling pressure drops, the erosion rate rises because of the breach and, as a consequence, the mineral deposition rate rises which, in turn, increases the area of the mineral ring (Figure 3c). Once sufficient accessory minerals have been deposited, the breach is healed (Figure 3d) and the whole process begins again. Video examples of breaches in the accessory mineral ring are included in the appendix of this thesis.

Over repeated cycles (Figure 9.1a) the magnitude of each peak in the erosion rate gradually decreases. This is a result of both the gradual thickening of the accessory mineral ring and to bentonite mass loss which causes a gradual decrease in swelling pressure once the pellet is fully saturated.
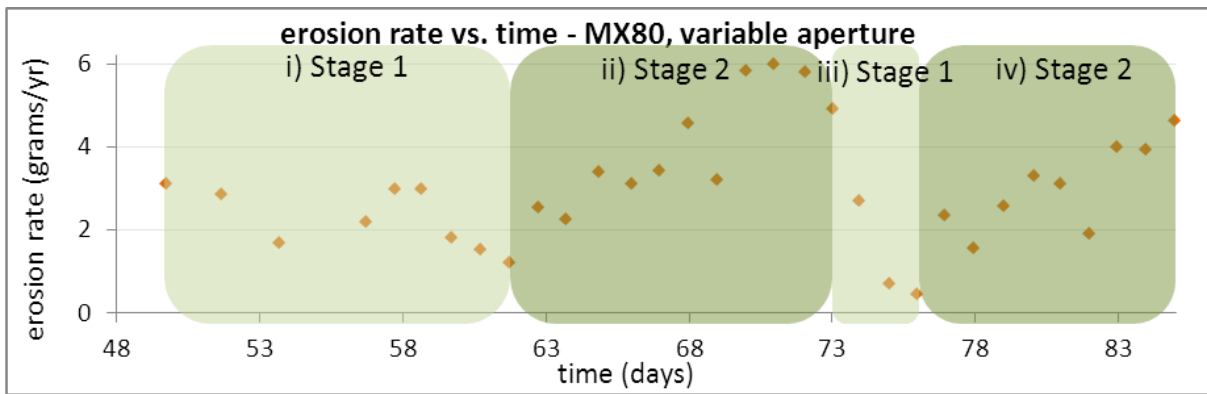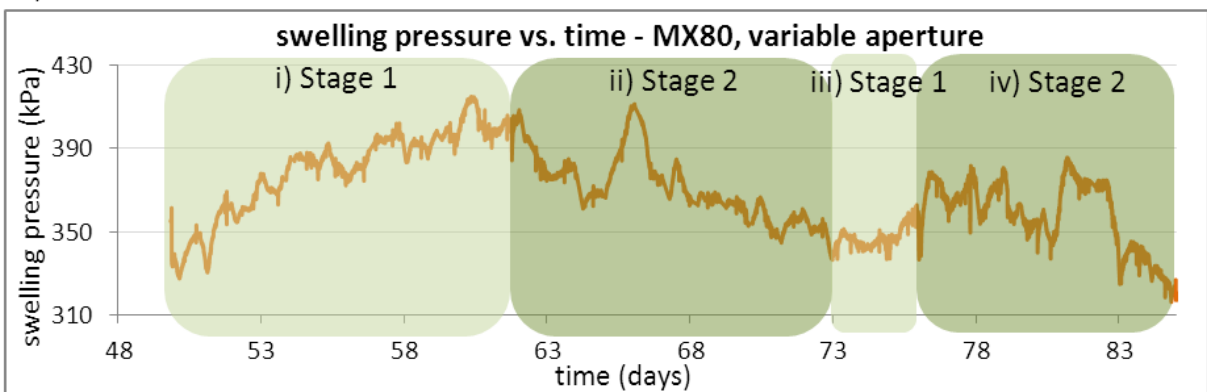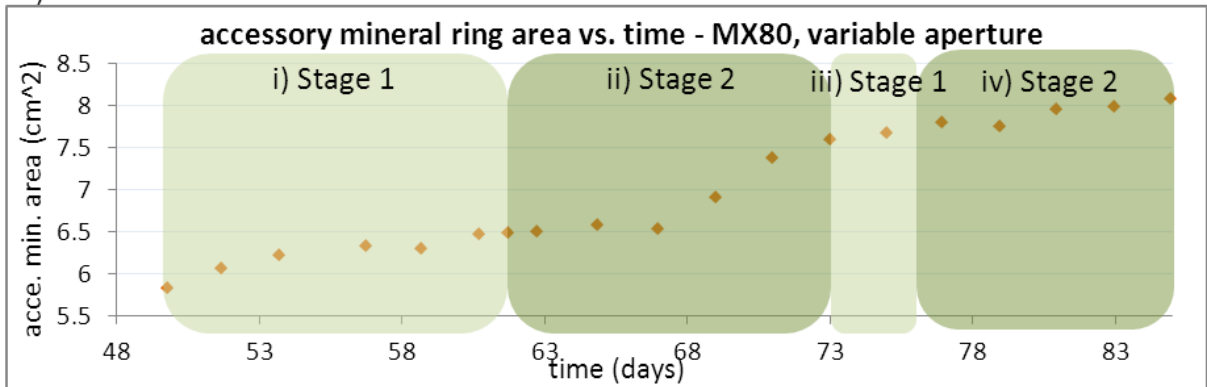
Figure 9.2: MX80, variable aperture, erosion rate, swelling pressure and accessory mineral ring area against time. For the period 48 - 86 days.
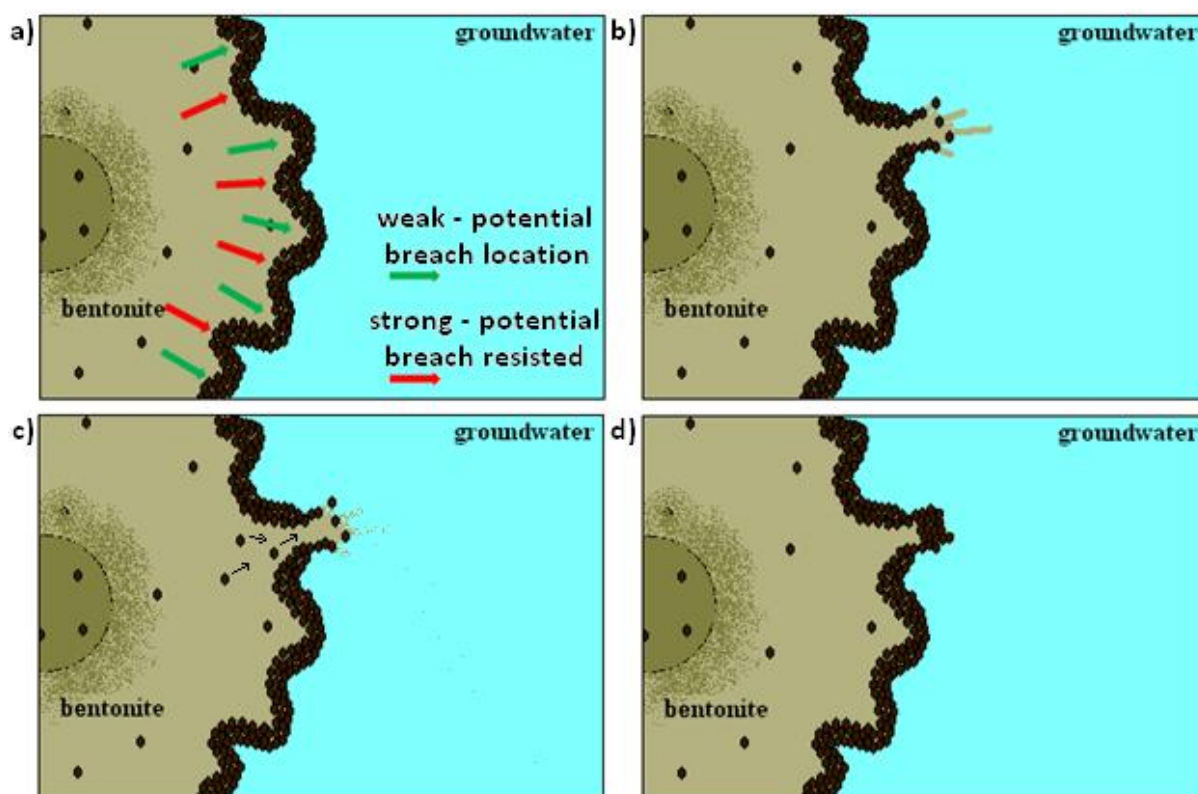
Figure 9.3: Conceptual model of accessory mineral ring breach as a result of water uptake / rise in swelling pressure and auto-healing

9.2 Effect of aperture variability on proposed erosion mechanism

As discussed previously, the uniform aperture cell data exhibits erosive periods of a lesser magnitude than those experienced in the variable aperture cell (Figure 9.1 a and d). This behaviour can be explained, as follows, in terms of the aperture wall roughness.

Firstly, it is likely that, because the accessory mineral ring has the same morphology in both the uniform and variable aperture fractures, no physical sieving of accessory minerals has occurred in either cell. That is to say, the fracture aperture in both cells is larger than the largest accessory mineral grain in the system. In both experiments, the accessory minerals are transported within the montmorillonite as it swells and are deposited at the location that the montmorillonite erodes in colloidal form – leaving the accessory minerals behind.

The accessory minerals deposited at the swelling front form constraining arches between the two fracture walls as a result of force chain development; this must occur in order to resist the swelling pressure of the montmorillonite behind (otherwise the ring would continue to move). The development of such force chains and a constraining arch within a

granular media upon vertical flow (under gravity) through an orifice is well known – an example is shown in Figure 9.4.
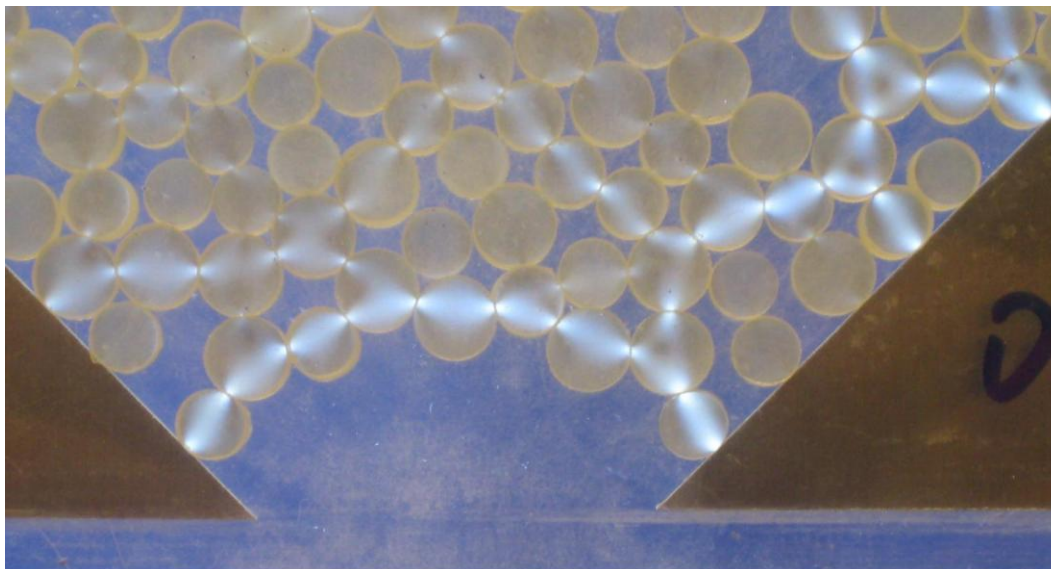
Figure 9.4: Example of force chain development and jamming in granular material during flow through a constriction (Tang 2012)

A conceptual model of the way these force chains may occur for both a variable aperture fracture (again, assuming all accessory minerals are smaller than the fracture aperture) and a uniform aperture fracture are illustrated in Figure 9.5 and Figure 9.6 respectively.

In the variable aperture cell (Figure 9.5a), particles in the accessory mineral ring that are part of the convex sections of the ring (Figure 9.5a) may be subject to force chain development because of two arching mechanisms; one perpendicular to the fracture plates (as detailed in Figure 9.5b) and the other in the convex parts of the ring (i.e. in the plan view in Figure 9.5a).

In the case of the uniform aperture cell, the constraining mechanism due to the concertina effect is still present in the convex sections of the ring (Figure 9.6a). However, because of the smooth cell walls, the force chain will take longer to develop in cross-section (due to lack of friction and undulations on the upper and lower fracture surfaces) and as a consequence, the ring is likely to be less uniform in thickness over depth.

For purified montmorillonite systems in uniform aperture fractures, previous work by Eriksson and Schatz (2015) has shown that gravity plays a significant role in shaping the structure of the buffer-groundwater interface at the edge of the extruded material. The illustration in Figure 9.6b assumes a similar shape to those observed in their work. The slower development of force chains between particles in the uniform aperture cell is in keeping with the experimental observations where the initial accessory mineral ring takes almost twice as long to develop.
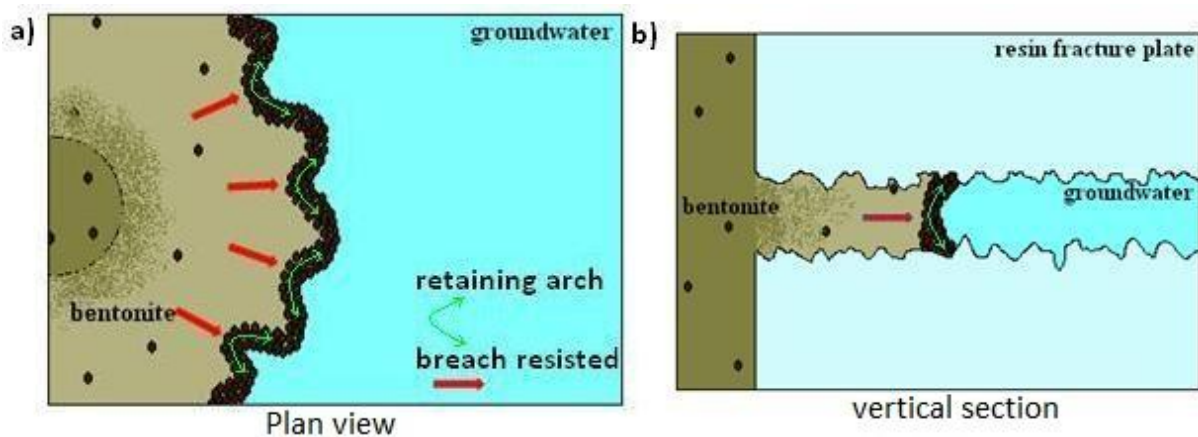
Figure 9.5: Dual arch retaining mechanism in variable aperture system

In the uniform aperture system,
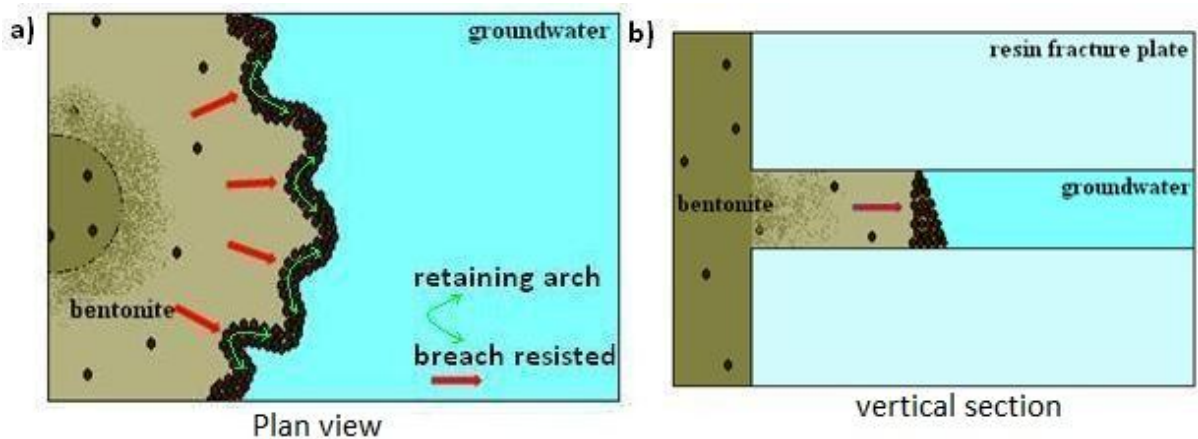
Figure 9.6: Single arch retaining mechanism in uniform aperture system

In summary, the dual constraining mechanism present in the variable aperture cell permits swelling pressure generation to the point where the yield strength of the weakest part of the ring is exceeded, resulting in erosive events of a relatively large magnitude.

It may be the case that the concertina shape of the accessory mineral ring is an artefact of the small spatial scale in these experiments, further investigation of this phenomenon is a topic for future investigations.

9.3 Comparison of experimental work in this thesis with SKB's 2012 safety case model to quantify buffer erosion from a fracture intersecting a deposition hole, as proposed by Neretnieks et al (2009).

As discussed in the literature review, SKB's current quantitative safety case model is predicated on the buffer being comprised of 100% purified sodium montmorillonite. SKB's model quantifies the montmorillonite release rate from a conductive fracture intersecting a 1.75m diameter deposition hole according to equation 1.

$$R_{Erosion} = A \times \delta \times v^{0.41} \qquad\qquad\qquad\qquad \textit{equation 1}$$

Where: $R_{Erosion}$ = release rate (kg/year), A = constant 27.2, δ = fracture aperture (m) and v = groundwater velocity (metres/year).

A dynamic force balance model is employed to estimate radial extrusion of the buffer into the fracture for various groundwater chemistries. This takes into account all forces acting on each montmorillonite particle, which are: gravity and buoyancy, diffusional, Van der Waals attraction, diffuse double layer repulsion and friction forces (Moreno et al 2010).

For dilute groundwater chemistries (<4mM), advective erosion of the buffer from the buffer-groundwater interface is modelled by simultaneously solving the Darcy flow equation (for two dimensional flow in a fracture), the solute diffusion equation and the dynamic force balance equations for the expansion of the gel (Neretnieks et al 2009).

Equation 1 results from this method, which calculates a constant mass loss rate from the buffer-groundwater interface in the fracture once a steady state has been reached between extrusion and erosion, for a given groundwater chemistry, velocity and fracture aperture.

Moreno et al (2010) also looked at the way in which deposition hole diameter affected the rate of montmorillonite release rate, by both increasing the deposition hole to 5m, and decreasing the deposition hole to 0.5m in their simulations. The results of these simulations are shown in Figure 9.7.
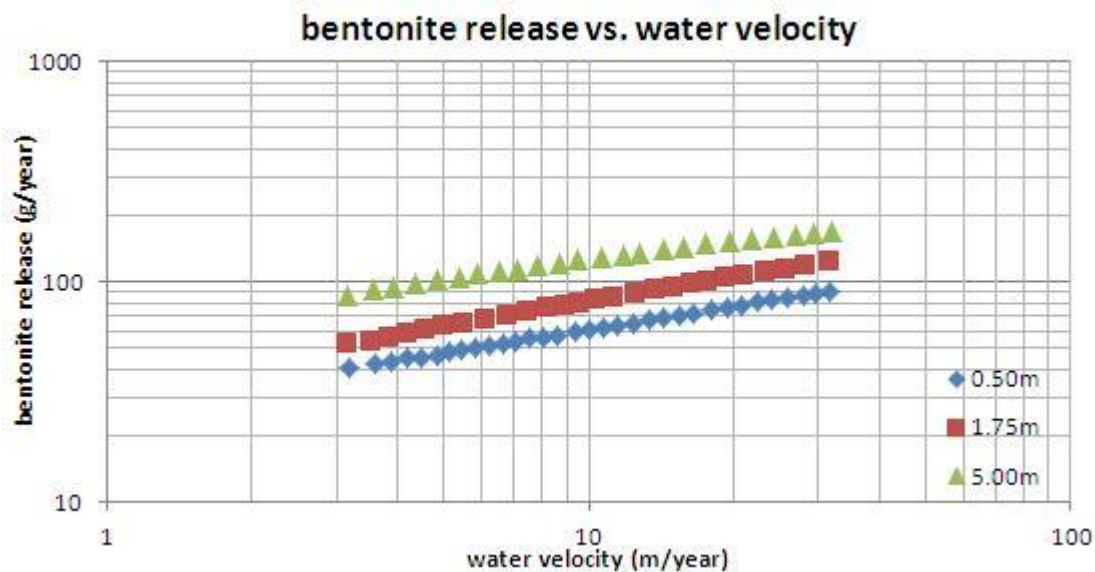
Figure 9.7: Montmorillonite mass loss against water velocity for various deposition hole diameters. 1mm fracture aperture. Moreno et al (2010)

Considering that the 'deposition hole' diameter used in the experiments detailed in this thesis was 20mm (0.02m), the diameter of the central compartment, an approximation was made of the effect of reducing the deposition hole diameter to 0.02m on the bentonite release rate in the simulations.

This was achieved by using the free software *graphgrabber,* downloadable from *Quintessa.org,* which allows raw data to be extracted from publication figures. *Graphgrabber* was used on Figure 9.7, in order to evaluate the relationship between bentonite release and deposition hole geometry for various flow velocities. The results of which are shown in Figure 9.8.
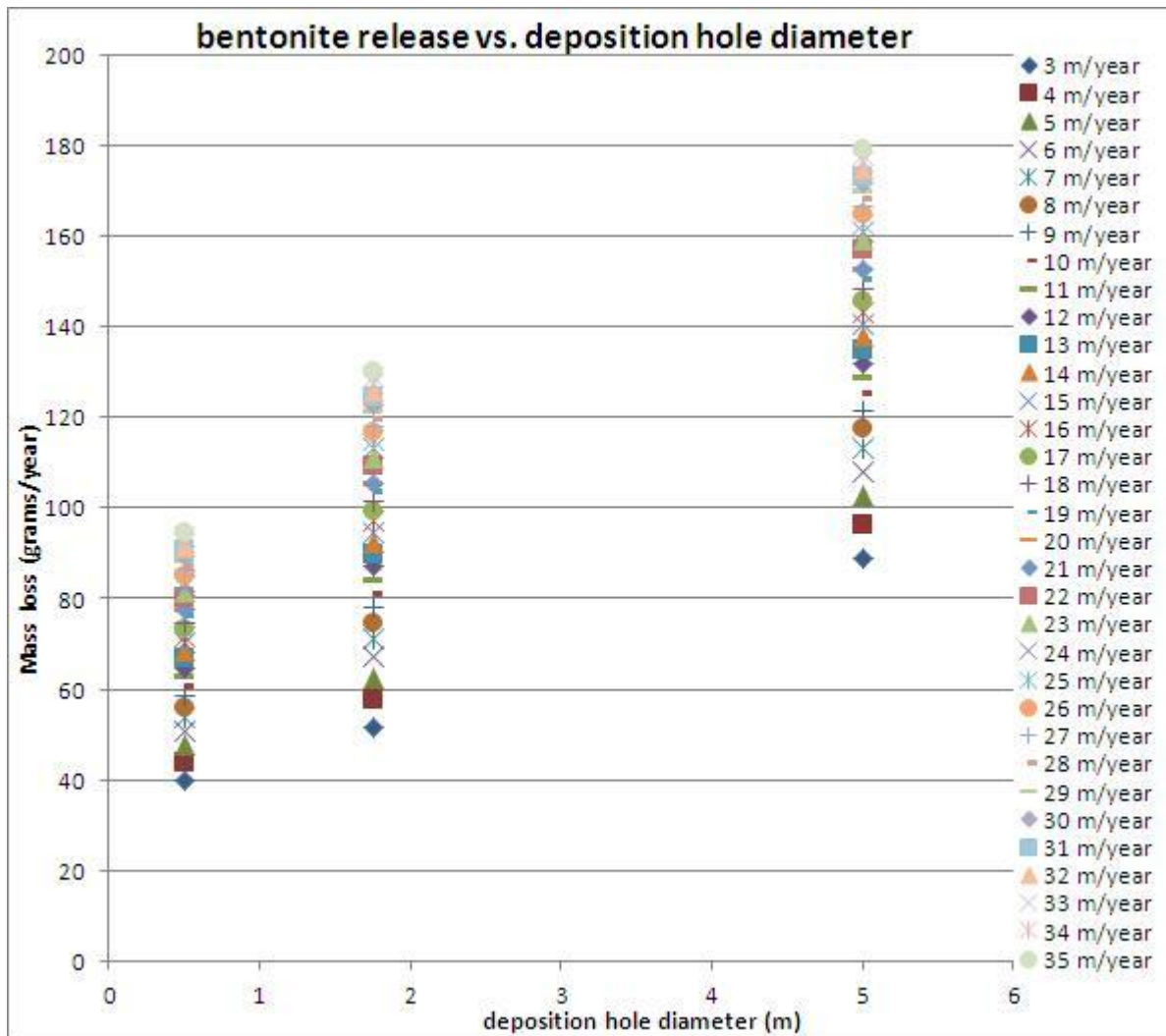
Figure 9.8: Montmorillonite release against deposition hole diameter at various flow velocities.

A 2nd order polynomial relationship was established for each flow velocity in Figure 9.8, and each relationship was used to approximate the mass loss for a deposition hole diameter of 0.02m (Figure 9.9).
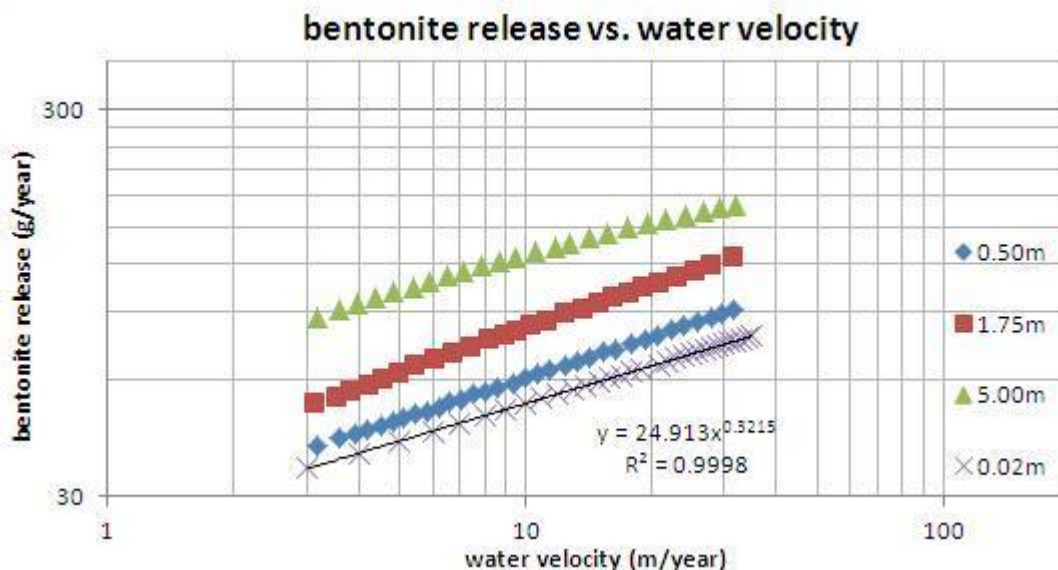
Figure 9.9: Montmorillonite release against water velocity at various deposition hole diameters.

The flow velocities examined in this work for both MX80 and purified montmorillonite are 1-2 orders of magnitude greater than those simulated in Figure 9.9: 2×10^3 m/year in the cells with Nanocor PGN and in the order 10^4 m/year in the cells using MX80. Hence, extrapolating from the 0.02m diameter deposition hole data in Figure 9.9, montmorillonite release rates of 286.88 g/year are estimated for the cell run with Nanocor PGN and 481.311 g/year for the cell run with MX80.

The modelled results plotted in Figure 9.9 correspond to a 1mm fracture aperture. According to *equation 1*, mass loss scales directly with fracture aperture. Hence, for the uniform aperture fracture experiment for Nanocor PGN, with an aperture of 104 μm, the expected montmorillonite release rate is [(0.104/1) x 155.89] = 29.83 g/year.

Because *equation 1* has been derived for a purified montmorillonite with a constant fracture aperture, the prediction of 29.83 g/year should be comparable to the experiment using Nanocor PGN. Figure 9.10 reproduces the erosion rate of Nanocor PGN with a fracture of constant aperture; the erosion rate exhibits a maximum value of 11 grams/year at the beginning of the test, the same order of magnitude as the model prediction, with an average over the course of the test of approximately 6 grams/year.

The experimental erosion rates are also relatively constant once a steady state between erosion and extrusion is reached, hence the experiment is broadly in agreement with the model, particularly considering the velocity extrapolation that was required.

Also, given the fact that the Nanocor PGN material used in the experiments wasn't 100% pure, and the accumulation of impurities at the erosion interface may go some way to explaining the gradual decrease of erosion rate over the course of the experiment. Had the sample installed in the experiment been 100% pure, the observed mass loss would most likely have been closer to the modelled predictions.
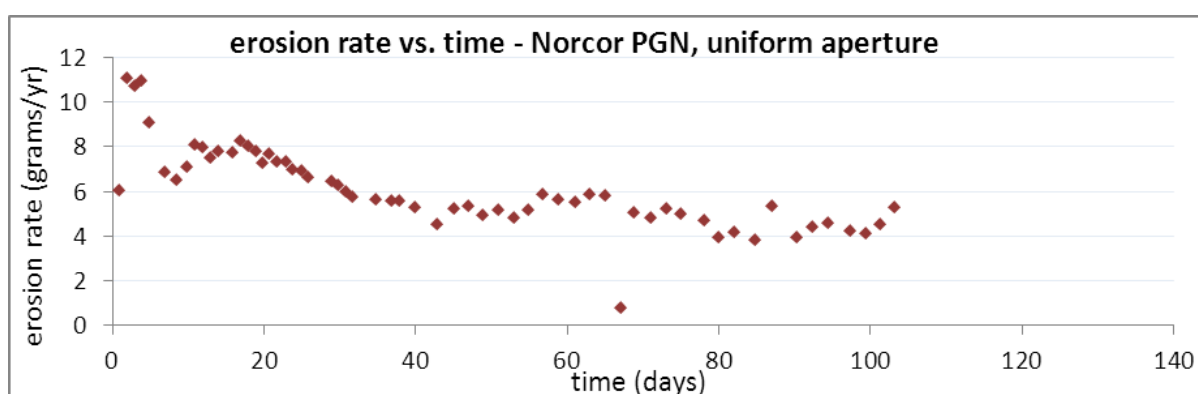
Figure 9.10: Nanocor PGN, uniform aperture cell, erosion rate against time.

To compare the model predictions for purified montmorillonite with the erosion rates observed from MX80 in the test conducted in the uniform aperture, the model was used to estimate montmorillonite mass loss assuming a hydraulic aperture of 102 μm and a water velocity in the plate of 10^4 m/year. This resulted in an estimated mass loss of [(0.102/1) x 481.311] = 48.13 grams/year. The mass loss from the MX80 experiment with a uniform fracture aperture is reproduced in Figure 9.11; the maximum erosion rate was 6.6 grams/year, dropping to an average value of approximately 2 grams/year. Further, the erosion rate isn't constant as the model predicts.
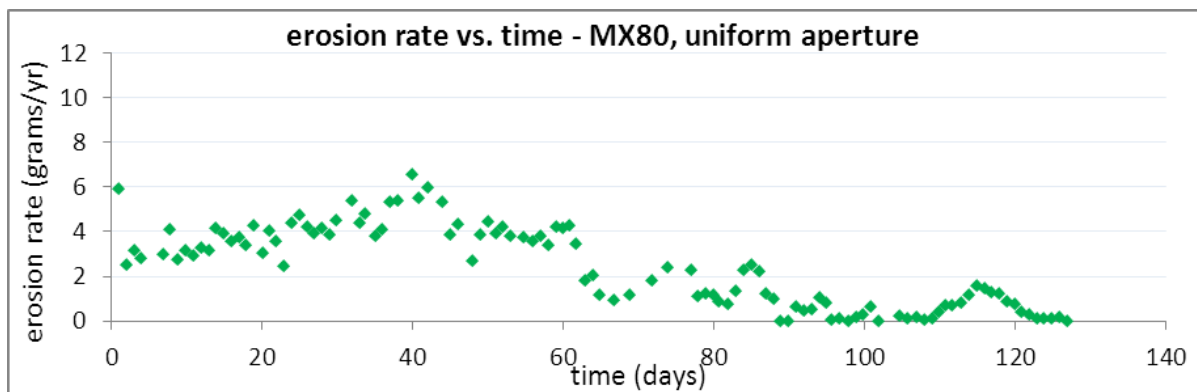
Figure 9.11: MX80, uniform aperture cell, erosion rate against time.

The experiments undertaken here demonstrate that erosion rates from MX80 are at least an order of magnitude less than those predicted based on experiments using pure montmorillonite. This highlights the high level of conservatism currently employed in the SKB license application.

9.4 Considerations in scaling experimental results to repository scenario

Based on the data for the MX80 erosion presented in this thesis, it is proposed that quantitative assessments of buffer loss may be augmented to take into account the mitigating effect of accessory minerals against buffer erosion. As discussed, Neretnieks et al's (2009) work assumes a constant mass loss rate of buffer from the fracture intersecting the deposition hole at a fixed extrusion distance once a steady state has been reached between extrusion and erosion. Experimental data from previous researchers (e.g. Schatz et al 2013), and the work presented in this thesis, shows this to be the case when purified montmorillonite is used. However, when MX80 is used and accessory minerals are present, this is not the case, and this work demonstrates that MX80 buffer erosion reduces with time as the system stabilises.

It is proposed here, based on the tests undertaken on MX80 presented in this thesis in variable and smooth apertures, that for the purpose of estimating MX80 erosion at a repository scale, the erosive period should be split into 3 distinct periods. These are shown in Figure 9.12 and are described in more detail below.
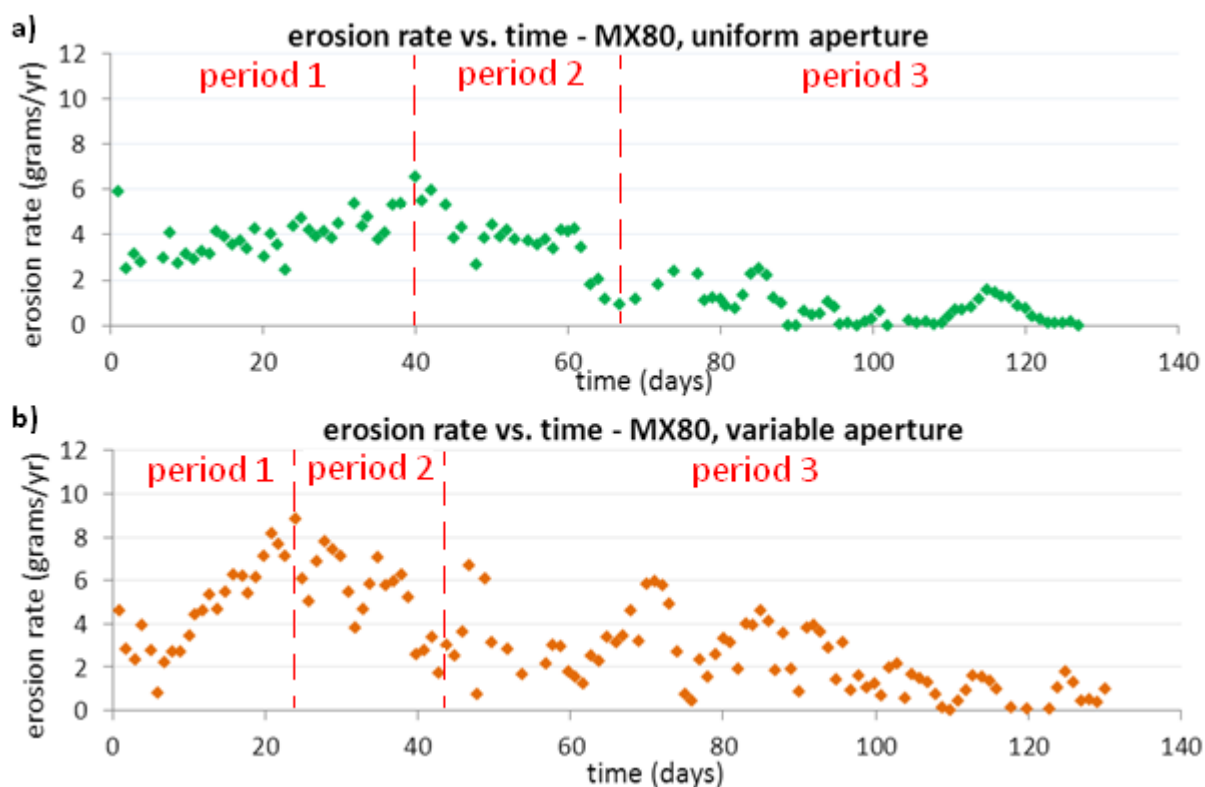
Figure 9.12: Mass loss data for a) erosion of MX80 in a uniform aperture and b) erosion of MX80 in a variable aperture. With erosion periods highlighted

Period 1: The time taken and mass of buffer lost before a sufficiently thick bed of accessory minerals are deposited to begin to mitigate against erosion

Period 1 in the experiments corresponds to an increase in erosion rate to a peak value, over 40 days in the case of the uniform aperture test (Figure 9.12a) and over 23 days in the case of the variable aperture test (Figure 9.12b). In either case, the rise in erosion rate is as a result of the coupled phenomena of the elution of soluble accessory minerals from the sample and a gradual increase in the surface area of the groundwater – bentonite interface.

As discussed in chapter 8 of this thesis, a comparison between initial saturation with a saline solution (more reflective of a natural scenario) and initial saturation with deionised water, suggests that ≈ 80% of extrusion is still likely to occur with the introduction of fresh, glacial water, ≈ 20% having occurred during saline conditions. Hence, despite the fact that no initial extrusion under saline conditions occurred in these experiments, period 1 will still be largely representative of early conditions with dilute groundwater in a repository scenario with regard to extrusion behaviour.

In terms of the equilibration of the dissolved salts in the system during period 1 however, the process may unfold differently at repository scale compared to these experiments. An accompanying conceptual stage diagram and the corresponding erosion behaviour is illustrated in Figure 9.13.

Figure 9.13i depicts the initial phase of limited extrusion, associated with buffer saturation under the initially saline groundwater conditions. Subsequent to this, glacial meltwater intrusion will cause a gradual dilution of the local groundwater. This will result in further extrusion into the fracture and washing of the soluble salts in the bentonite pore water to equilibrate with the prevailing groundwater, Figure 9.13ii.

The rate at which this process might occur will be dependent on the local hydrogeochemical conditions. The diffusion rate of ions across the buffer - groundwater interface will depend on the dispersion and advection of ions through the groundwater.

No erosion will occur until the cation concentration of the groundwater falls below 4mM, as described by Birgersson et al (2009). When this occurs, the bulk of extrusion will be initiated. Once erosion is initiated, a period of increasing extrusion distance and erosion rate, in line with any further dilution of the groundwater below 4mM, will occur (Figure 9.13iii). During this time, the accessory minerals will begin to accumulate at the bentonite-groundwater interface.

In the repository, erosion behaviour during period 1 may differ from the experiments for two reasons:

a) The bulk of equilibration of dissolved salts in the buffer with the groundwater will have occurred under non-erosive conditions over long time frames.

and

b) Because of the increased extrusion distance, the accessory minerals will be required to travel a greater distance from the central compartment and accumulate around a far larger bentonite groundwater interface. As a consequence, it is possible that a steady state may be reached between extrusion and erosion of the buffer (Figure 9.13iv) before the accessory

minerals accumulate to a critical thickness around this interface and mitigate against erosion (Figure 9.13v).

This was not the case in either experiment performed with MX80. The accumulation of accessory minerals occurred rapidly, from the onset of the extrusion process. Period 1 ends when a 2mm bed of accessory minerals had been deposited at the bentonite – groundwater interface in the fracture.
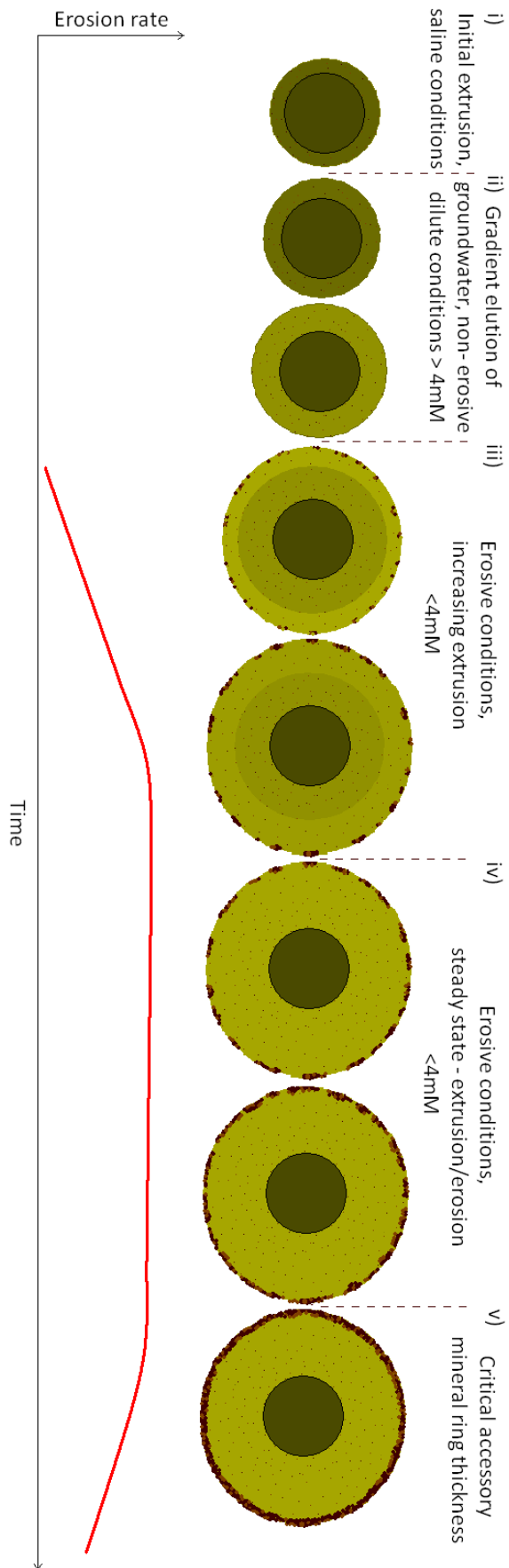
Figure 9.13: Conceptual phases of extrusion and erosion from a fracture intersecting a deposition hole, repository scenario.

Period 2: The time taken and mass of buffer lost before a sufficiently thick bed of accessory minerals are deposited to reduce erosion rates to low levels.

Period 2 represents the time taken before a sufficiently thick bed of accessory minerals are deposited to reduce erosion rates to low levels. Chosen as ≤ 2 grams/year here based on the mass loss data presented in Figure 9.12**.**

≤ 2 grams/year was chosen as a low level of mass loss due to 2 grams/year being the maximum magnitude of the erosive events which appear beyond day 70 in the uniform aperture cell (Figure 9.12a) and beyond day 100 in the variable aperture cell (Figure 9.12b) I.e. the points in either test at which the accessory mineral ring appears to be stable against breaches and erosive events > 2 grams/year. The uniform aperture MX80 test shows that the erosion rate is reduced to 1.79 grams/year after 63 days. In the case of the variable aperture test, the erosion rate is reduced to 1.71 grams/year after 43 days (Figure 9.12b).

Figure 9.14 shows the effective mineral ring thickness for both MX80 experiments as a function of time. At 43 days in the variable aperture test, the accessory mineral ring thickness is approximately 4.5mm and at 63 days in the uniform aperture test, the accessory mineral ring thickness is approximately 3.3mm. Thus, the mineral ring thickness at the point at which the erosion rate begins to drop (period 1) in either test is the same, however, it is different at the point at which erosion rates are reduced to low levels (period 2). Therefore the thickness of mineral ring when erosion rates are reduced to low levels in either test can't be used to accurately predict the duration of period 2.
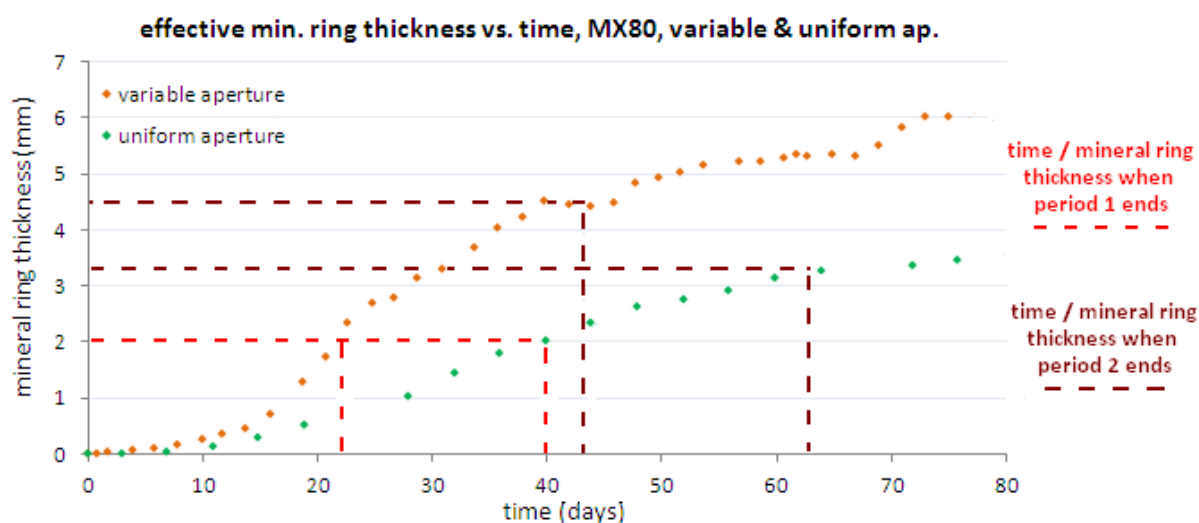
Figure 9.14: Accessory mineral ring thickness against time for uniform and variable aperture fractures.

Based on these results, an approximation of the length of time this may take to occur in a repository scenario can be made. In the variable aperture test, it took [(43-23)/23]*100% = 87% of the time taken to begin to mitigate against erosion for erosion to reduce to low levels. In the case of the uniform aperture test, it took [(63-40)/40]*100% = 58%. Therefore, between the two tests it took an average of 72% longer, after the 2mm accessory mineral ring barrier had formed, for erosion to reduce to low levels.

Period 3: Period corresponding to subsequent erosive periods as a result of mineral ring breach and erosion rates of ≤ 2 grams/year.

As detailed in section 9.1, it has been proposed that erosive events of regular periodicity with diminishing peaks occur as a result of rises in swelling pressure in the sample causing breaches of the accessory mineral ring. In order to assess whether or not the same phenomena may occur at a repository scale two points are worth considering:

1) The sample used in this experiment was not fully saturated upon installation, whereas in a repository scenario, the buffer will most likely be fully saturated before the start of Period 1 i.e. at the onset of glacial meltwater intrusion at depth. Therefore, any significant rises in swelling pressure caused by further saturation would not occur.

2) In a repository scenario, the majority of elution of the soluble salts in the buffer will occur before erosion is initiated. Therefore, the system may not have the same capacity for the swelling pressure increases that occur when the mineral ring is intact (i.e. before the periodic breaches).

The small periodic mass loss events associated with Period 3 are what might be expected of a system approaching chemical equilibrium. It is not clear whether, because of the diffusion of dilute waters into the bentonite, it will still have the capacity for rising swelling pressure at this time in the repositories evolution. Hence, for estimation of repository mass loss in the following section, a conservative approach of a constant mass loss of 2 g/year has been assumed.

9.4.1 Scaling assumptions for calculation of repository scale erosion rates

In order to upscale and estimate the mass loss in each period and the time taken for periods 1 and 2 to occur for a repository scenario, a number of assumptions have to be made, based on the way in which the process may develop at full scale:

Based on the idea that in a repository scenario, a steady state between extrusion/erosion will be reached before the accessory mineral ring forms at a critical thickness, the first assumption, is that during period 1, the accessory minerals are deposited during a period of constant mass loss.

In the case of the experiments undertaken, this loss rate was calculated by taking the average mass loss over period 1. For example, in Figure 9.12b 0.319 grams of montmorillonite were eroded over 23 days, resulting in a constant mass loss estimate of 0.0139 grams/ day (before a sufficiently thick bed of accessory minerals are deposited to start to mitigate against erosion).

The second assumption based on steady state extrusion/erosion is that this period of constant mass loss occurred at a fixed extrusion distance, in both the variable and uniform aperture fracture experiments, this distance was chosen as the extrusion distance at which the erosion rate first starts to drop. For example, at 23 days in the variable aperture test (Figure 9.12b), the total extruded area determined by image analysis (plan view including the central brass plug) was 1912.645 mm^2. Therefore, assuming the extruded material to be a circle, the average radius of extrusion = $\overline{\frac{1912.645}{\pi}}$ = 24.68mm. Hence, the circumference of extruded material, the length of the interface between the extruded material and groundwater, therefore = $\pi\ 2 \times 24.68$ = 155.07mm. With a 100μm fracture aperture, this implies an interfacial surface area of $155.07\ mm \times 0.1\ mm$ = 15.51 mm^2.

As is apparent from the image analysis, Figure 6.4d), the rapid period of extrusion occurs early in the experiment and the maximum extent of extrusion is almost reached by 23 days.

The mechanism detailed in this thesis can be scaled to a repository scenario by augmenting the theoretical model proposed by Neretnieks et al (2009), which captures the chemical aspect of the erosion of the montmorillonite constituent of the buffer *(equation 1)*. In order

to incorporate the physical aspect of the erosion process, which occurs when accessory minerals are present, as described in this thesis.

In order to achieve this, it is also assumed that the purified montmorillonite, on which Neretnieks' model is based, contains the same proportion of insoluble accessory minerals as the MX80 examined in this thesis.

Finally, it is assumed that the rate of deposition of these accessory minerals at the erosion interface is directly proportional to the mass of montmorillonite eroded per unit interfacial surface area between the groundwater and the extruded material, and that this relationship between the deposition of accessory minerals and montmorillonite mass loss is independent of groundwater velocity.

9.5 Validation of this scaling approach using the experiment with the uniform aperture

Before attempting to scale the experimental results to a repository scenario, the above assumptions and approach were validated using the existing experiments: the results from the variable aperture test, which has a smaller extent of extrusion, were used to predict the mass of montmorillonite lost and time taken for a 2mm bed of accessory minerals to be deposited in the uniform aperture fracture test, which has a larger extent of extrusion.

From the variable aperture fracture experiment, it took 23 days to deposit a 2mm deep bed of accessory minerals at an average mass loss of 0.0139 grams/day around an interfacial surface area of 15.51 mm^2. Hence we can pose the questions:

> How long will it take to deposit a 2mm deep bed of accessory minerals at a mass loss of 0.01 grams/day around an interfacial surface area of 19.14 mm^2? What mass of montmorillonite in total would have to be eroded to deposit this thickness of accessory minerals?

Taking a 1mm^2 portion of bentonite - groundwater interfacial surface area in the variable aperture experiment, the mass loss rate over this surface area is 0.0139/15.51 = 0.00090 grams/day/mm^2.

Taking a 1mm^2 portion of surface are in the uniform aperture experiment, the mass loss rate over this surface area is 0.01/19.14 = 0.00052 grams/day/mm^2. I.e. the mass loss rate per

unit surface area is 0.00090/0.00052 = 1.73 times faster in the variable aperture experiment than the uniform aperture.

Again, assuming the rate of deposition of accessory minerals is directly proportional to the mass of montmorillonite eroded per unit interfacial surface area, it should take 1.73 x 23 days = **39.8 days** for a 2mm deep bed of accessory minerals to form in the uniform aperture test over a larger extent of extrusion and mitigate against erosion. Further, in order to deposit this bed of accessory minerals, 39.8 days x 0.01grams/day = **0.398 grams** of montmorillonite should have to be eroded.

In practice, **0.401 grams** of montmorillonite was eroded over a **40 day** period to deposit a 2mm thick bed of accessory minerals in the uniform aperture fracture, which began to mitigate against erosion, as shown in Figure 9.11.

9.6 Scaling from bench to repository scale.

Montmorillonite loss rate as a function of groundwater velocity and fracture aperture is given by *equation 1* for a fresh groundwater, and is represented by the red square tick marks in Figure 9.7 for a deposition hole 1.75m (repository scale). Table 9.1 shows the steady state buffer release rate from a 1mm aperture fracture intersecting a deposition hole calculated using *equation 1*, for various groundwater velocities from 0.1 m/year to 315 m/year, examined for the purpose of SKB's safety case.

Water velocity, [m/yr]	Smectite release for 1 mm fracture aperture, [g/yr]	Penetration into the fracture at the centre, [m]
0.10	11	34.6
0.32	16	18.5
0.95	26	11.5
3.15	43	7.0
31.50	117	2.1
315.00	292	0.5

Table 9.1: Loss of smectite by advective flow. Neretnieks et al (2009).

9.6.1 Scenarios considered

Data from the erosion of MX80 experiments undertaken in this thesis was used in conjunction with the modelled mass loss rates and extrusion distances for purified

montmorillonite in a 1mm aperture fracture from SKB's 2012 safety case application to scale to 4 repository scenarios. Two of which were the first and last scenarios in Table 9.1.

Two additional hypothetical scenarios for 100µm fracture apertures were also examined. For the latter two scenarios, *Equation 1* was used to estimate mass loss for two different groundwater velocities. However, because no equivalent fracture penetration data (as in Table 9.1) has been published for a 100 µm aperture fracture, the extrusion distances were approximated for these scenarios.

Scenario 1 – 0.1 m/year water velocity, 11 g/year mass loss, 34.6m penetration, 1mm aperture

Corresponds to the first scenario in Table 9.1.

Scenario 2 – 315 m/year water velocity, 292 g/year mass loss, 0.5m penetration, 1mm aperture

Corresponds to the last scenario in Table 9.1.

Scenario 3 – 315 m/year water velocity, 29.2 g/year mass loss, 2m penetration, 100µm aperture

As above with a 100 µm aperture and assumed 2m penetration.

Scenario 4 – 1 x 10^4 m/year water velocity, 118.7 g/year mass loss, 0.5m penetration, 100µm aperture

Corresponds to the groundwater velocity and fracture aperture from the experiments on MX80 examined in this thesis.

Each of the scenarios to be evaluated are summarised in Table 9.2.

Scenario *Data*	*1* *Safety case*	*2* *Safety case*	*3* *Hypothetical*	*4* *Hypothetical*
Fracture aperture (mm)	1	1	0.1	0.1
Water velocity (m/year)	0.1	315	315	1 x 10^4
Mass loss rate (eqn. 1) (grams/year)	11	292	29.2	118.7
Extrusion dist. (m)	34.6	0.5	2 assumed	0.5 assumed
Buffer – groundwater interface (mm^2)	222,959	8,639	1,812	870

Table 9.2: Summary table of scenarios to be evaluated for scaling experiments to repository

As demonstrated, period 1 in the experiment undertaken with MX80 in the variable aperture cell is scalable to the larger extent of extrusion in the uniform aperture cell experiment. Hence, when scaling from the bench to a repository scenario, either experiment would give the same outcome. The variable aperture experiment data were chosen.

A detailed analysis of the scalability of the bench scale experiments to repository scenario 1 is included below for illustration purposes. The results of subsequent analyses for scenarios 2, 3 and 4 are presented as summaries in Table 9.3.

9.6.2 Quantitative assessment of mass loss for repository scale.
Upscaling from bench to repository – Scenario 1, period 1.

It takes 23 days to deposit a 2mm deep bed of accessory minerals at a mass loss rate of 0.0139 grams/day around an interfacial surface area of 15.51 mm^2 in the variable aperture experiment with MX80. Hence, the question can be posed:

> For a repository scenario, how long will it take to deposit a 2mm deep bed
> of accessory minerals at a mass loss rate of 11 grams/year (0.03
> grams/day) around an interfacial surface area of 222959 mm^2? What mass
> of montmorillonite in total would have to be eroded to deposit this
> thickness of accessory minerals?

Taking a 1mm^2 portion of surface area in the experimental set-up, the mass loss rate over this surface area is 0.0139/15.51 = 0.00090 grams/day/mm^2. Taking a 1mm^2 portion of surface area at repository scale, the mass loss rate over this surface area is 0.03/222959 = 0.000000135 grams/day/mm^2. I.e. the mass loss rate per unit surface area is 0.00090/0.000000135 = 6689 times faster in the experiment than at repository scale in scenario 1.

Again, assuming that the rate of deposition of accessory minerals is directly proportional to the mass of montmorillonite eroded per unit interfacial surface area, it would take 6689 x 23 days = **153841 days (421 years)** for a 2mm deep bed of accessory minerals to form in this instance and mitigate against erosion.

In order to deposit this bed of accessory minerals, 153841 days $\times 0.03$ grams/day = **4615 grams** of montmorillonite would have to be eroded.

Upscaling from bench to repository – Scenario 1, period 2.

As discussed, data from both experiments with MX80 in the uniform and variable aperture tests suggest that the average time taken for erosion rate to fall to the low levels defined, subsequent to the ring forming at a critical thickness, is 72% of the duration of period 1. Based on these results, a rough approximation of the length of time this may take to occur in a repository scenario can be made.

In period 1, for scenario 1, it took 422 years for an effective barrier to form, based on the approximation above, it would take a further (0.72*422) = **303.84 years f**or erosion to fall to < 2 grams/year

The initial mass loss rate in scenario 1 was 0.03 grams/day (11 grams/year). Assuming the mass loss rate decays steadily over this period from 11 grams/year to 2 grams/year, the average mass loss rate throughout this period is (11+2)/2 = 6.5 grams/year. Over the subsequent 303.84 year period this equates to a further mass loss of **1974.96 grams**.

In total therefore it would take 422+303.84 years = **725.84 years** with a mass loss of 4622 + 1975 = **6.60kg** before erosion rates were reduced to < 2 g/year.

Upscaling from bench to repository – Scenario 1, period 3.

SKB's reference glacial cycle assumes that approximately 2% of deposition holes may be exposed to fresh glacial water for a duration of 30,000 years during each 120,000 year glacial cycle (SKB 2011, Vol II). SKB's entire repository assessment period is 1 million years, hence it follows that a repository may undergo up to (1,000,000/120,000) = 8 glacial cycles during this assessment period. This equates to (8 x 30,000) = 240,000 years of buffer exposure to dilute water during the 1 million year assessment period.

For the purpose of scaling, it is assumed that the barrier is formed during the first 120,000 year glacial cycle and remains in place during subsequent glacial cycles, maintaining erosion rates at ≈ 2 grams/year. The duration of period 3 will therefore be 240,000 years – (duration

of period 1 + duration of period 2). In the case of scenario 1 this equates to period 3 lasting 239,274 years.

In scaling the mass loss rates from the experiments to a deposition hole geometry in periods 1 and 2, mass loss was scaled per unit interfacial buffer-groundwater surface area. For period 3 however, if we consider that perturbations in the accessory mineral ring at discrete locations are responsible for mass loss during this period, then mass loss rates from the experiments should be equivalent to those in a repository scenario.

This is because of the fact that the accessory mineral ring spans the full circumference of the extruded material at both the laboratory and repository scale, and these breaches occur locally on the accessory mineral ring. In other words, mass loss due to a perturbation on a ring of 5 cm circumference should produce the same mass loss as the same perturbation occurring on a ring 5m in circumference.

The total mass of montmorillonite lost from the system during period 3 for scenario 1 will therefore be (239,274 x 2 g/year) = 478.55 kg.

Upscaling from bench to repository – Scenarios 2, 3 and 4.

Similar analysis for scenarios 2, 3 and 4 was undertaken yielding the results in Table 9.3

9.6.3 Scaling summary

Table 9.3 shows a summary of the scaling calculations undertaken for the four scenarios analysed. It includes the time frames, and the masses of montmorillonite eroded before the 2mm bed of accessory minerals was deposited. The time taken to reduce erosion rates to low levels and subsequent montmorillonite mass loss are also reported.

The equivalent mass losses for a buffer comprised of purified montmorillonite over the same timeframe, with no accessory minerals present, have also been included in Table 9.3 for direct comparison.

Scenario / Data	1 Safety case	2 Safety case	3 Hypothetical	4 Hypothetical
Fracture aperture (mm)	1	1	0.1	0.1
Water velocity (m/year)	0.1	315	315	10^4
Mass loss rate (eqn. 1) (grams/year)	11	292	29.2	118.7
Extrusion dist. (m)	34.6	0.5	2 assumed	0.5 assumed
Buffer – groundwater interface (mm^2)	222,896	8,639	1,812	870
Scaling from experiments to repository scenarios				
Period 1 duration (years)	422	0.62	12.9	0.15
Mass eroded during period 1 (kg)	4.62	0.18	0.38	0.018
Period 2 duration (years)	304	0.45	9.3	0.11
Mass eroded during period 2 (kg)	1.978	0.07	0.14	0.007
Period 3 duration [240,000 years – (period 1 + period 2)] (years)	239,274	239,999	239,978	239,999
Mass eroded during period 3 (kg)	478.55	480	479.96	480
Total mass eroded over 240,000 year period (kg) **with** accessory minerals	**485.15**	**480**	**480.45**	**480.03**
Total mass eroded over 240,000 year period (kg) **without** accessory minerals	**2,640**	**70,080**	**7,008**	**28,488**

Table 9.3: Approximations for scaling experimental results to hypothetical repository scenarios

SKB specify in their safety case that an inability to generate a sufficient swelling pressure and advective conditions may be induced in the buffer upon the loss of 1,200kg of buffer from the ≈20,000kg of buffer in a single deposition hole (SKB 2011, Vol II).

Consider scenario 1 in Table 9.3, with no accessory minerals present. 240,000 years of exposure with a release rate of 11 grams/year would result in 2,640kg of buffer being lost over the assessment period from a single 1mm fracture intersecting the deposition hole i.e. mass loss would be unacceptable. This is discounting the fact that multiple transmissive fractures might be expected to intersect some deposition holes.

Now consider scenario 1 with accessory minerals present, based on the experiments described in this thesis, a barrier of accessory minerals, effective at mitigating against erosion, would have formed after 422 years in the first glacial cycle. It would take a further 304 years to reduce erosion levels to low levels, or 726 years in total from the onset of

erosion to reduce erosion to low levels during the first 30,000 year exposure to fresh glacial water. Subsequent mass loss at ≈ 2 grams/year for the remainder of the first glacial cycle, and the seven successive 30,000 year glacial cycles over the repository assessment period, results in a total mass loss from the system of 485.15 kg over the entire assessment period. Mass loss from the single fracture would be less than 1,200 kg and hence acceptable. If two such conductive water features intersect the deposition hole, this would still result in less than 1,200 kg of buffer being lost.

Similarly, as is evident in Table 9.3, unacceptable quantities of mass loss are predicted for scenarios 2, 3 and 4 using the current quantitative safety case assessments based on purified montmorillonite. In scenarios 2 and 4, the entire buffer would be lost from the deposition hole if comprised of pure montmorillonite. When accessory minerals are present however, mass loss over the entire assessment period falls well below the 1,200 kg threshold set by SKB.

From the data displayed in Table 9.3, it is also apparent that total mass loss from the system is similar across the 4 scenarios when accessory minerals are present. This is because the period of time over which the accessory mineral ring forms (periods 1 and 2) is short relative to the duration of period 3, which accounts for the most mass lost from the system. In addition, based on the results of this research, the mass loss rate does not appear to be linked to the groundwater velocity when a protective accessory mineral ring is in place (Reid et al, 2015).

Over repository timescales, the accessory mineral ring, which protects the bentonite barrier, may be subject to other physical/chemical processes, such as reciprocating isostatic uplift and depression from multiple glacial cycles, tectonic activity or indeed reciprocating exposure to dilute and saline groundwater causing the buffer to contract and expand. These processes are not expected to significantly affect mass loss, however, because this research has also demonstrated that the ring has a capacity to self-heal.

The accessory mineral ring may also be subject to biological and/or chemical processes that serve to enhance its effectiveness. Suarez (2012) discusses in his thesis the ageing of granular soils and the ways in which their engineering properties may be enhanced over time through such processes as cementation caused by microbial activity and precipitation

of soluble phases at particle contacts. These, and similar processes, may serve to enhance the stability of an accessory mineral ring over the longer term.

9.7 Engineered filter optimisation

If the montmorillonite filter mechanism proposed in this thesis were to be engineered for optimal barrier protection as suggested by Neretnieks et al (2009), instead of relying on the accessory minerals inherent in MX80, the composition, grain size and percentage of accessory minerals would need to be considered.

9.7.1 Engineered filter analogues

Engineers out with radioactive waste disposal regularly utilise granular filter media in order to protect or retain base soils. To explore the opportunities for engineered erosion mitigation, through the addition of accessory minerals, it is useful to explore practise in other fields of engineering.

Dam filters

In many ways, the process of filter bed formation mitigating against erosion can be considered as being analogous to the process of filtration as a means of protecting dams from erosion. Granulated filters are installed in earth dams in a variety of configurations, specifically engineered to prevent erosion and piping of the base soil by allowing water to pass freely while restraining the base soil.

In dams, the granular fill is graded to a suitable particle size distribution and compacted to a specific density to best prevent erosion. I.e. conditions which aren't representative of the way in which a filter of accessory minerals may form in a fracture; while their particle size distribution could be engineered, their deposition and degree of compaction in the fracture would occur in an uncontrolled manner.

Another way in which filters are utilised to prevent dam erosion is in the use of upstream crack-stoppers: these are regions of granular material, upstream of the dam core designed to wash into, and clog, any cracks that form. This is directly relevant to the work detailed in this thesis: the crack in the dam core is analogous to a fracture intersecting a deposition hole; the crack stoppers are analogous to the accessory minerals contained within the buffer; and the base soil of the dam is analogous to the erosive montmorillonite constituent

of the buffer. The main point of relevance in this instance is the stochastic nature of the way in which the filter media seals the crack/ rock fracture.

Park (2003) demonstrated in a series of flow through experiments designed to mimic flow through cracked dam cores and filters that the granular material from the filter may be washed from the bulk filter material into the crack, successfully clogging it and reducing erosion of the dam core. The majority of Park's tests were done on the ability of a filter to slump, under gravity and fill a crack, not entirely relevant under repository conditions. However, Park (2003) also conducted a small number of tests in which the filter media was washed into the crack under the influence of flowing water and observed a reduction in the erosion of the dam core material, observable through changes in the turbidity of the effluent water.

This is analogous to the process detailed herein in the sense that, although the dam filter is initially installed as a graded and compacted engineered barrier, displacing material from the barrier and re-depositing it elsewhere in the system does not appear to negate its ability to perform its intended function.

What was most notable from this work was that:

> *''It was found that the process of erosion and clogging*
> *during the tests often occurred episodically.''*

That is, after reaching a stable condition in terms of lack of erosion, breakthrough was observed and erosive conditions reinitiated, before a stable condition was again achieved by the reestablishment of the mineral bed. Hence, as was also observed in the work detailed in this thesis, Park's filter displayed an ability to self-heal after breakthrough.

Groundwater well filters

Groundwater wells are another such engineered structure which requires the use of filters to prevent soil from the aquifer travelling up the well with the fluid. In many cases they are emplaced, in other instances however they are formed naturally around the well casing, utilising the granular material in the aquifer strata (Johnson 1963). This is achieved by

careful selection of screen opening size of the well casing based on the grain size distribution of the aquifer material.

9.7.2 Engineered filter design
Particle size distribution for an accessory mineral filter capable of straining montmorillonite colloids.

In conventional filter design, the performance of a filter is closely related to the size of the D_{15} particles. D_{15} corresponds to the particle size such that 15% of the particles in the size distribution are smaller than that size. The ability of a filter to perform its required function is naturally related to the pore size in the filter and, based on extensive testing by Sherard et al (1984), the average pore size of a filter media has been found to be well represented by the D_{15} value.

The recommendations for suitable filter performance are that $(D_{15})_f / (D_{85})_s < 5$, where the subscripts *f* and *s* correspond to *filter* and *soil* (particle being filtered) respectively. The groundwater chemistry in a repository system will ultimately govern the size of particle to be filtered i.e. montmorillonite floc size $(D_{85})_s$.

Missana et al (2011) conducted tests on the erosion of a compacted bentonite in 1mM sodium chloride solution, measuring the size of colloids released from the sample by photon correlation spectroscopy. They found a relatively uniform montmorillonite floc size, in the order of 400nm (0.4µm), was observable over the course of their experiment. Therefore, based on Sherard et al's (1984) criteria, 15% of particles in the size distribution of the filter media would need to be ≤ 2 µm in order to be most effective in straining these colloids. The D_{15} value of the particle size distribution would therefore ≤ 2 µm, which places a lower bound on the particle size distribution of the filter media.

The upper bound on the particle size distribution of the filter to be designed will be dictated by the apertures of the fractures intersecting the deposition hole. I.e. the largest particle in the filter media should be small enough to enter the fracture, and not be strained at the fracture mouth upon the extrusion of buffer from the deposition hole. For the purpose of illustration, a fracture aperture of 100 µm is chosen in this instance. The D_{100} value of the particle size distribution would therefore ≤ 100 µm.

The United States Department of Agriculture (1994) state that a filter should be as well graded (contain particles of a wide range of sizes) as possible while still fulfilling the above criteria, in order to provide the most desirable filtration characteristics. The general grading of a particle size distribution can be described by its coefficient of curvature (C_z) where $C_z = D^2_{30}/(D_{60} \times D_{10})$. For a well graded filter, $1 \leq C_z \leq 3$. Therefore, after considering all of the above criteria, a particle size distribution can be constructed for a filter media, which would be effective at straining montmorillonite colloids in the order of 400nm, in fracture apertures of the order 100 µm, as shown in Figure 9.15.
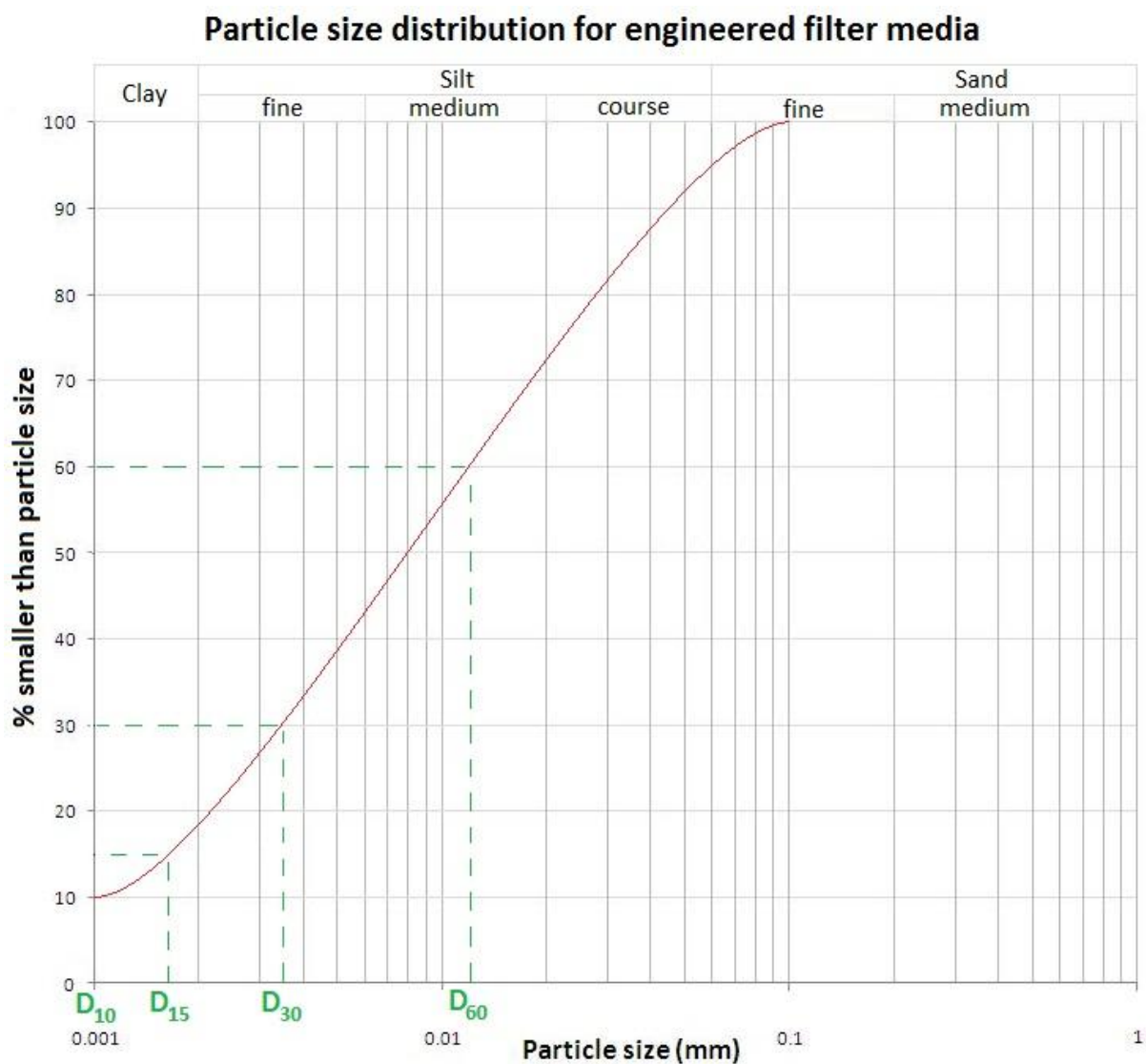
Figure 9.15: Engineered particle size distribution for filter media effective at straining 400nm colloids

Figure 9.15 shows that the criteria $D_{15} \leq 2$ µm is satisfied as $D_{15} = 1.6$ µm and $C_Z = 3.4^2/(11 \times 1) = 1.05$. I.e. as $1 \leq C_Z \leq 3$, the filter media is classed as well graded. Figure 9.15 also shows that 100% of the particles in the filter media are < 100 µm, hence all particles would be able to enter the fracture. This same method may be applied to create a suitable filter particle size distribution, tailored to site specific fracture apertures and potential montmorillonite colloid sizes.

In a process known as self-filtering, most filters rely on some of the protected material moving in to the filter to make it effective (Vaughan & Bridle 2004). It is interesting to note here, that the small proportion of accessory minerals contained within Nanocor PGN material were not well graded; this may go some way to explaining its inefficiency in filtering montmorillonite colloids in the experiment, despite its apparent deposition at the edge of the extruded material (based on the XRD data presented in chapter 7). Had the test been left to run long enough, perhaps some mitigating effect against erosion may have eventually been realised.

To reiterate, engineered filters designed by the above criteria are emplaced in a controlled manner during construction, whereas in the repository scenario described here, natural transportation and deposition of the minerals is required to form a filter bed. Transportation and deposition relies on the minerals accumulating and consolidating in such a way as to function like an engineered, emplaced filter. This thesis shows that the process is viable with the accessory minerals inherent within MX80, however, more rapid filter formation may be achievable through engineering the particle size distribution of the bentonite buffer.

Granular media particle jamming

The process of particle jamming may also be engineered to some extent. The science of granular media rheology and jamming has significance in fields out-with earth sciences and soils. The chemical, food and agricultural industries, in particular, utilize particle media rheology research to prevent undesirable instances of jamming, such as in grain flow through silos or the flow of particulate media through pipes.

As each accessory mineral travels from the central compartment to the buffer-groundwater interface, as long as its diameter is smaller than the fracture aperture, it will be relatively

free to move. Where these accessory minerals congregate at this interface, however, because of the close proximity of the particles to each other they are subject to frictional and cohesive forces. Coupled with the roughness of the rock fracture wall, this may facilitate force chain development within the granular media matrix and jamming of the particles as illustrated in Figure 9.4 and Figure 9.5b.

In granular media rheology studies conducted by Mort (2015), particle size distribution has been found to play a significant role in the onset of jamming of granular media when flow is undertaken through an orifice. Mort (2015) found that jamming onset increased with widened grain size distribution. Hence, an engineered filter media being well graded may not only aid its filtration effectiveness but the ability of the media to jam in the fracture and create a filter bed in the first place.

Mort (2015) also found that particle shape played a significant role, with elongated granules being more likely to induce jamming. Kyrylyuk & Philipse (2011) also showed through simulation that the density of such a packed, jammed solid is optimised by using slightly elongated particles. Halloysite is one such clay mineral, whose particles exhibit an elongated, needle like shape, and whose inclusion in such an engineered filter media may thus be beneficial with regard to particle jamming.

To summarise, there is a wealth of knowledge, both within geotechnical engineering applications and out-with, which may be utilised in order to best design such a filter, suitable for straining montmorillonite colloids in the context of a GDF. In general, the filter media should be well graded and contain a certain degree of particles with an elongated shape to aid the processes of both jamming in the fracture and montmorillonite colloid straining.

Augmenting KBS-3V disposal concept to include engineered filter media.

In designing this filter media, it need not necessarily have to be mixed in to a pure montmorillonite, which from a logistical point of view, considering the vast quantities of buffer in question (20,000kg x 6000 deposition holes = 120,000 tonnes of buffer for a typical repository), may prove difficult.

As discussed in section 2.2, the Nordic KBS-3V concept includes a 50mm annular gap around the circumference of the deposition hole, designed to aid the emplacement of buffer disks and rings over the waste canister. Upon emplacement of these discs and rings, it is proposed that this gap shall be gravity filled with bentonite pellets, this design is illustrated in Figure 9.16a), in which the pellet space has been made larger relative to the deposition hole geometry for illustration purposes.
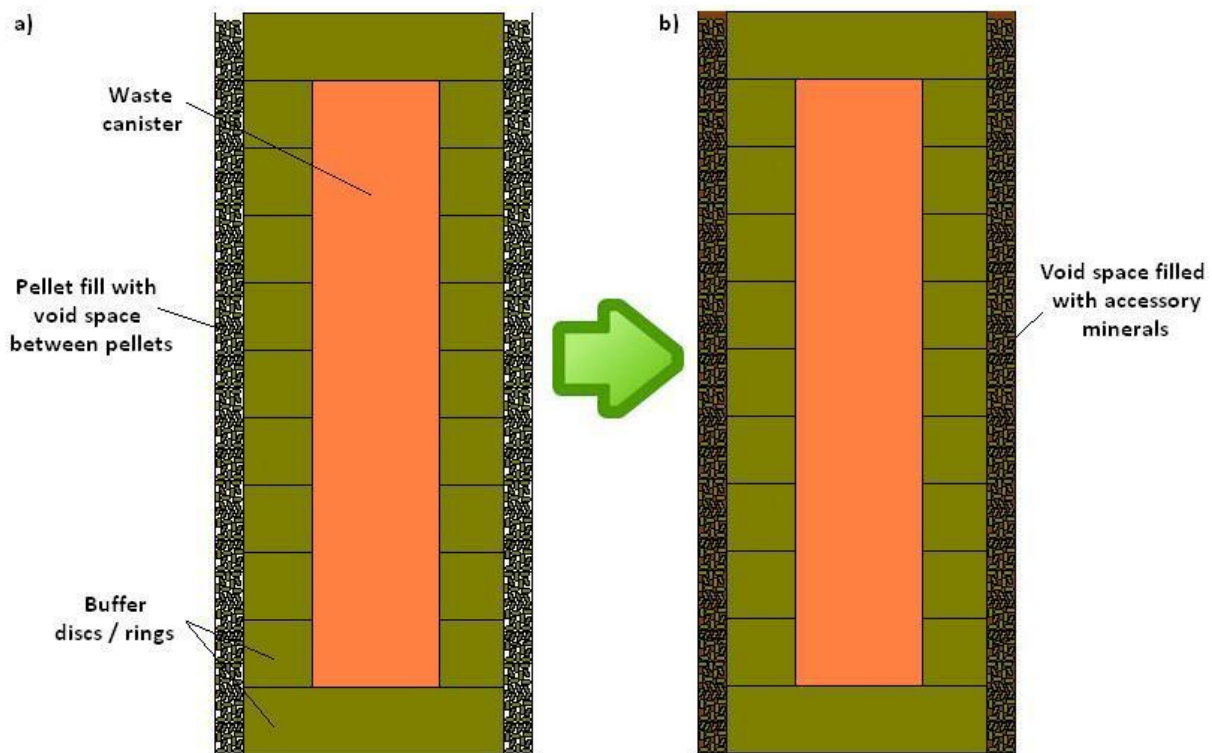
Figure 9.16: Vertical section through deposition hole in a) original KBS-3V concept and b) pellet fill void space filled with accessory minerals

As shown in Figure 9.16a), there will be a volume of exploitable voids between each of the pellets in this space. The exact volume of void space between pellets in this gap can be calculated as follows (based on reference pellet data from Juvankoski et al 2011):

- Based on a 50mm annular gap in a 1.75m diameter, 8.25m deep deposition hole, the volume of this space is 1.11m^3.

- The density of the bulk pellet fill (pellets + void space between pellets), ρ_b = 1075kg/m^3, therefore the mass of pellets in this annular gap = 1193.25 kg

- The density of each individual pellet, ρ = 1805kg/m^3, therefore the volume of the annular gap occupied by the pellets = 0.66 m^3

- The volume of void space between pellets therefore = 1.11 – 0.66 = 0.45 m^3

- Assuming the accessory minerals to have a ρ = 2650 kg/m^3

- Therefore, mass of accessory minerals to fill void space between pellets = 1192.5 kg

I.e. there is the potential to supplement the current reference KBS-3V design to include over a tonne of accessory minerals per deposition hole in the void space between pellets. Granted, the emplacement of this fill would require careful consideration with regard to ensuring this void space is filled. An assessment would also have to be made with regard to the effect this may have on target buffer saturated dry density.

There is also scope for changing the proportion of compacted pellets to granular filter media in this gap, augmenting the system to aid the presence of the inherent accessory minerals within MX80.

9.7.3 Zeolite as an additive to aid the filtration process

If the process of accessory mineral deposition in a repository scenario occurred in the same fashion as observed in these experiments, i.e. providing a relatively uniform ring around the extruded material, in doing so, it would provide another barrier which would have to be traversed by a radionuclide before migration to the biosphere. Therefore, if the accessory minerals were to be engineered in the buffer, in addition to a suitable particle size distribution, they may also be chosen based on their ability to sorb radionuclides. Zeolite, in particular clinoptilolite, is one such micro and nanoporous mineral which is extensively utilised in the nuclear remediation industry (because of its affinity for retention of specific radionuclides) and as a filter media in general. Its addition to a buffer could serve the dual role of functioning in a physical filtration capacity by mitigating against montmorillonite erosion, as well as forming an ion sieve should any escaped radionuclide traverse the buffer in the deposition hole and travel through the extruded material in the fracture.

Many advocates cited the abundance of zeolite at the Yucca Mountain site in the U.S. as a reason for its suitability to house a GDF. However, natural zeolites are more suited to the sorption of short-lived, cationic radionuclides (Vaniman & Bish 1993), whose radioactivity

will have long since decayed by the time a canister may potentially have breached and a radionuclide diffused across the buffer. Zeolites can be synthesised, however, to be selective of specific ions (Yu 2007), thus providing scope for a variety of zeolites to be synthesised and employed in this context. These could be tailored to capture a specific radioactive waste inventory, and associated decay products, over the longer term. Many natural zeolites are chemically and mechanically stable e.g. some Australian clinoptilolites are over 300 million years old with a hardness of 5/6 Moh; the stability of synthesized zeolites over the longer term would also have to be assessed before their employment in this capacity may be deemed practicable.

9.8 BELBaR benchmark test.

As part of this thesis, participation was made in a series of cross laboratory bentonite erosion benchmark tests, the results of which are given in appendix 2 of this thesis.

The results of each of the three benchmark tests were relatively consistent between the three groups in terms of extrusion behaviour, discounting the presence of air bubbles in the cell at Strathclyde. Extrusion distances were within 15% of each other over the course of the three tests.

Mass loss data was also consistent between the tests conducted at Strathclyde and B+Tech. Discrepancies in the mass loss data between the these two tests and the test undertaken at CIEMAT may have been as a result of the different measurement techniques employed by each of the groups to calculate mass lost from their respective systems.

Chapter 10 Conclusions

The environmental regulator, SSM, tasked with assessing the competency of the first globally compiled safety case to dispose of high level radioactive waste in a geological disposal facility have, in June 2016, endorsed SKB's licence application with the proviso that further work will be undertaken around a number of technical issues relating to long-term safety. One such technical issue, which was identified in a preliminary review of the safety case by an International review team, was for a more complete understanding of the bentonite buffer erosion process during periods of fresh, glacial meltwater intrusion to repository depth.

Currently, buffer erosion predictions are based on the buffer being comprised of 100% purified sodium montmorillonite, resulting in estimates of mass loss which are unacceptable under the scenarios of fracture aperture, groundwater velocity and the assessment period considered in the safety case. In some instances, these assessments result in the entire deposit of buffer being eroded from the deposition hole over the assessment period from a cross-cutting rock fracture. At the time of publication of the safety case, buffer erosion was a process which SKB conceded directly required further attention. Therefore, there is a need for informing less conservative mass loss assessments, based on empirical data from more realistic experiments into buffer erosion.

Upon commencing this thesis, the primary aims and objectives were steered based on the outcomes of this review and previous research into bentonite buffer erosion phenomena. These aims and objectives were to:

- Determine the effect of the presence of inherently present impurities or 'accessory minerals' within the bentonite and the effect they have on the erosion rate of the buffer from a horizontal fracture intersecting a deposition hole for disposal concepts in fractured crystalline rock.
- Investigate the effect of fracture aperture variability on the erosion process of buffer material from a horizontal fracture intersecting a deposition hole.

In order to understand the effect of fracture aperture variability, bespoke flow-through erosion cells were created by taking a mould of a natural fracture present in a granite core. Comparator cells repeated this process using planar surfaces. This approach allowed simulation of extrusion and erosion of the buffer in naturally rough and planar rock fractures.

The effects of the presence of accessory minerals was explored by undertaking erosion tests in both the variable and planar rock fracture cells with MX80 bentonite ($\approx$ 20% accessory minerals) and Nanocor PGN montmorillonite ($\approx$ 2% accessory minerals). The latter material also provided a benchmark with which to compare this research with similar experiments published by other researchers. Deionised water was used as a proxy for glacial meltwater in these 3-4 month duration tests with the mass loss rate from the cells and swelling pressure of the installed sample monitored throughout. Time-lapse image capture was undertaken for the purpose of quantitative image analysis of the extrusion/ erosion process also.

The key discovery presented within this thesis has been that of a new cyclical mechanism governing the erosion process of MX80 buffer material upon extrusion into a horizontal, variable aperture rock fracture intersecting a deposition hole, which can be summarised as follows:

Throughout the extrusion process of the sample, the erosion rate increases as the interfacial surface area between the sample and the flowing water increases in line with the dissolved salts contained within the bentonite washing from the sample. The swelling pressure of the sample decreases as a result of this mass loss. As the montmorillonite portion of the MX80 erodes, the crystalline accessory minerals are deposited in the fracture at the extrusion front. Results from XRD analysis of the eroded material and fracture face post-test indicate that only the montmorillonite portion of MX80 is erodible, with the accessory minerals being entirely non-erodible under the groundwater velocities examined (10^{-4} m/s).

The accessory minerals, accounting for approximately 20% of MX80, are effective in mitigating against further erosion of the montmorillonite constituent of the material when deposited at a critical thickness (2mm in fracture apertures of the order 100 µm) around the

buffer extrusion / water interface. Upon the formation of the accessory mineral ring at this critical thickness, the erosion rate of montmorillonite subsequently decreases.

During periods of decreasing or low mass loss from the system, the swelling pressure of the sample increases as a result of the rate of water uptake into the system exceeding the rate of mass loss. In a natural system this may occur because of one or more reasons. For instance, further dilution of the bounding groundwater into the system may result in the diffusion of dissolved salts from the bentonite pore water, facilitating water intake into the bentonite and a subsequent rise in swelling pressure.

The swelling pressure rises in the sample until the mineral ring is breached, when the yield strength of the force chain within accessory mineral ring is exceeded by the swelling pressure. From image analysis data, these breaches occur at discrete locations, at the concave areas of the accessory mineral ring. An erosive period then ensues as a result of this breach as more montmorillonite comes into contact with the advective groundwater flow. As montmorillonite is eroded from the breach location on the ring, more montmorillonite is transported from the central compartment, across the extruded material to redress this balance, transporting accessory minerals as it does so and depositing them at the breach location until the mineral ring regains its integrity.

Fracture aperture variability plays a role in this mechanism, in that a rough fracture provides a higher capacity for force chain development within this accessory mineral ring, resulting in a higher yield strength and resistance to breach than in a planar aperture fracture. The rough fracture aperture surface was effective in constraining the expanding bentonite and facilitating a rise in swelling pressure. Behaviour which wasn't evident in the uniform aperture cell experiment with MX80. This cyclical mineral ring breach / erosive behaviour would continue in a natural system until such time as there was no further capacity for a rise in swelling pressure of the system. I.e. the bentonite was fully saturated and the bentonite pore water was in chemical equilibrium with the bounding groundwater.

A test undertaken with Nanocor PGN material (98% pure montmorillonite) did not show the same cyclical erosion behaviour, but exhibited a steady mass loss from the system, in line

with work by other researchers, along with a concomitant decrease in swelling pressure of the sample. Post-test XRD analysis of this experiment revealed that the small proportion of quartz present in this sample was deposited at the extrusion / erosion interface as the montmorillonite eroded, via the same process as the tests conducted with MX80. Their presence was not, however, sufficient to facilitate a decrease in mass loss from the system over the time-frame examined.

The time taken for the accessory mineral ring to form and mass of montmorillonite lost to achieve this were up-scaled from the tests conducted with MX80 to repository scale. In terms of extents of buffer extrusion, mass loss rate scenarios and time frames currently considered in SKB's safety case. The main assumptions for this method of scaling are that the rate of deposition of accessory minerals at the buffer extrusion / groundwater interface is directly proportional to the mass of montmorillonite lost from this interface (in $g/mm^2/day$) and that this rate of deposition is scalable from bench scale to repository scale extrusion distances. An assumption which has been verified by scaling accurately between different extents of extrusion in the test conducted with MX80 in variable and uniform apertures. A further assumption is that when this protective mineral ring is formed, buffer loss from the fracture is reduced to an average of 2 grams/year for the remainder of the assessment period. Assuming that the buffer is exposed to erosive groundwater conditions for eight 30,000 year periods (within eight 150,000 year glacial cycles in a 1,000,000 year repository assessment period) and the mineral ring forms within the first 30,000 year exposure to erosive groundwater

Scaling these experiments indicates that the mass of buffer material lost per deposition hole over the course of a repository assessment period, should remain within acceptable limits. When compared to current quantitative mass loss assessments from a single horizontal fracture interesting a deposition hole. Simplified scaling assumptions based on the data presented in this thesis, reduce mass loss estimates over a repository assessment period by 1 – 2 orders of magnitude from a single fracture.

This work has provided further scope for adaptation of the KBS-3V concept to include the inclusion of a suitably well-graded filter media, into the buffer to enhance the efficiency of

the barrier in terms time of formation time and filtration capacity. The upper bound of the particle size distribution of this filter media may be chosen based on the fracture aperture data from the fractures intersecting the deposition holes. The lower bound may be chosen based on the size of the particle being filtered, that is the size of montmorillonite colloid, employing traditional engineering filter media theory. Should this filter media also be selected based on its radionuclide retention capacity, it may provide a further barrier to radionuclide migration to the biosphere.

This research has advanced scientific understanding of buffer erosion by providing empirical data of the erosion characteristics of the reference buffer material of the most advanced global radioactive waste disposal concept in crystalline rock, MX80, in naturally variable rock fractures. The experiments undertaken in this thesis do fall short in capturing all of the phenomena which will ultimately affect the buffer erosion process, such as non-uniform extrusion because of the presence of fracture contact points, different fracture orientations and the presence of multiple fractures intersecting deposition holes. They do however ultimately inform more realistic mass loss assessments than are currently employed and, in doing so, are a stepping stone towards a more complete understanding of the buffer erosion process before any facility to house radioactive waste is finally sanctioned.

The scalability of this mechanism and validity of the scaling assumptions over the longer extrusion distances, geological time-frames and less-dilute groundwater chemistry gradients should be verified.

Chapter 11 Recommendations for further work

Following the work presented in this thesis, several areas of interest have been identified that merit consideration for further research. These are:

1. The process of accessory mineral filter bed formation, during buffer extrusion and erosion, should be examined at a larger scale, in order to ascertain whether the predictability of the mineral ring's thickness at which it mitigates against erosion and the mass of montmorillonite lost are consistent / modelable. Scalability of the effect needs to be confirmed.

2. The effects of aperture variability and surface roughness on the critical thickness of accessory mineral bed.

3. Non-uniform access to water and extrusion of the buffer into the fracture may also be of interest, in terms of the way in which this may affect the deposition of accessory minerals and erosion process. Non-uniform extrusion may also be influenced by the presence of asperities in the fracture aperture or partially filled fracture apertures because of the presence mineral precipitates and/or rock grout.

4. The way in which cyclical saline/dilute conditions affect this process is also of interest. If a repository is expected to experience multiple glacial cycles throughout its typical 1,000,000 year assessment period. Moving from non-erosive to erosive condition over multiple cycles may cause fluctuations in swelling pressure because of chemical variability in the buffer pore water. Which in-turn may have an effect on the presence of the accessory mineral ring and the erosion process.

5. The ability to make the process of the mineral ring formation more efficient by augmenting the system with a suitably chosen engineered filter media.

6. The effect of larger perturbations on the system, i.e. shearing of the fracture surface, an earth tremor or isostatic uplift on the accessory mineral ring and its ability to regain its integrity following such an event should be investigated.

If the tests detailed in this thesis were to be repeated, pre-saturation with a saline solution before erosion is initiated could be employed in order to be fully representative of repository conditions. It is not thought this would have a great influence on the proposed process for reasons detailed in chapter 8. As part of the post-test analysis, X-ray CT scanning of the accessory mineral ring in situ, within the fracture aperture, could also be of great interest. This analysis would facilitate the acquisition of a 3D model of this granular mineral matrix and provide details on such as aspects as its' pore size distribution and density. Ion Chromatography (IC) analysis to potentially correlate cation concentrations in the effluent water with mass loss and the washing of soluble accessory minerals could also be undertaken as part of post-test analysis of the experiments.

References

Alexander, W.R. & Neall, F. B. (2011) *NDA RWMD Colloid strategy review.* 1st ed. [pdf] Harwell: NDA document library. Available at: https://rwm.nda.gov.uk/publication/colloid-strategy-review/?download [Accessed 20 Apr 2013]

ANDRA (2005) *Dossier 2005 Argile – Evaluation of the feasibility of a geological repository in an argillaceous formation – Meuse/ Haute-Marne site.* 1st ed. [pdf] Châtenay-Malabry. Available at: https://www.andra.fr/download/andra-international-en/document/editions/266va.pdf [Accessed 20 Jun 2012]

ANDRA (2005) *Dossier 2005 Granite - Assets of granite formations for deep geological disposal.* 1st ed. [pdf] Châtenay-Malabry. Available at: https://www.andra.fr/download/andra-international-en/document/editions/267va.pdf [Accessed 20 Jun 2012]

Apted, M.J. et al (2010) *Buffer erosion: An overview of concepts and potential safety consequences.* 1st ed. [pdf] Stockholm. SSM report 2010:31. Available at: https://www.iaea.org/inis/collection/NCLCollectionStore/_Public/42/040/42040088.pdf [Accessed 13 May 2012]

Baik, M-H. et al (2007) *Erosion of bentonite particles at the interface of a compacted bentonite and a fractured granite.* Engineering Geology, 91 (2-4), pp 229–239

Bath, A. et al (2006) *Geochemical indicators of deep groundwater movements at Sellafield, UK.* Journal of Geochemical Exploration, 90 (1-2), pp 24-44

Beard, R. (2013) *Treatment of colloids and related issues in the safety case.* 1st ed. [pdf] Harwell. Available at: http://www.skb.se/belbar/wp-content/uploads/2015/06/D1.3.pdf [Accessed 2 Jan 2014]

Birgersson, M. et al (2009) *Bentonite erosion, final report.* 1st ed. [pdf] Stockholm. SKB report TR-09-34. Available at: http://www.iaea.org/inis/collection/NCLCollectionStore/_Public/41/030/41030209.pdf [Accessed 15 Jan 2012]

Börgesson, L. & Sanden, T. (2006) *Piping and erosion in buffer and backfill materials. Current knowledge. .* 1st ed. [pdf] Stockholm SKB report: R-06-80. Available at: http://www.iaea.org/inis/collection/NCLCollectionStore/_Public/38/005/38005877.pdf?r=1 [Accessed 16 Feb 2012]

Clark, I. D., Douglas, M., Raven, K., and Bottomley, D., (2000) *Recharge and preservation of Laurentide glacial melt water in the Canadian Shield*. Ground Water, 38 (5), pp 735 – 742

Cuadros, J. (2008) *Clay as a sealing material in nuclear waste repositories.* Geology today, 24(3), pp99-103

Cui, Y. & Tang, A., M. (2013) *On the chemo-thermo-hydro-mechanical behaviour of geological and engineered barriers.* Journal of Rock Mechanics and Geotechnical Engineering, 5 (3), pp 169-178

Cuss, R.J., Harrington, J.F. & Noy, D.J (2010) *Large Scale Gas Injection Test (LASGIT) performed at the Äspö Hard Rock Laboratory, summary report 2008.* 1st ed. [pdf] Stockholm. SKB report: TR-10-38. Available at: http://www.skb.se/publikation/1995067/TR-10-38.pdf [Accessed 19 May 2012]

DECC (2014) *Implementing Geological Disposal – A framework for the long-term management of higher activity radioactive waste.* 1st ed. [pdf] London. Available at <*https://www.gov.uk/government/publications/implementing-geological-disposal*> [Accessed 20 Jan 2015]

DECC (2011) *Waste Transfer Pricing Methodology for the disposal of higher activity waste from new nuclear power stations.* 1st ed. [pdf] London. Available at: https://www.gov.uk/government/uploads/system/uploads/attachment_data/file/42629/3798-waste-transfer-pricing-methodology.pdf [Accessed 24 May 2012]

DEFRA, BERR and the devolved administrations of Wales and Northern Ireland, (2008) *Managing radioactive waste safely – A framework for implementing geological waste disposal.*1st ed. [pdf] Norwich. The Stationary Office. Available at https://www.gov.uk/government/uploads/system/uploads/attachment_data/file/228903/7386.pdf [Accessed 24 Jan 2012]

DEFRA & NDA (2011) *Radioactive wastes in the UK: A summary of the 2010 inventory.* 1st ed. [pdf] Cumbria. NDA publication. Available at https://ukinventory.nda.gov.uk/wp-content/uploads/sites/18/2014/02/2010-UK-Radioactive-Waste-Inventory-Summary-of-the-2010-Inventory.pdf [Accessed 2 Jan 2012]

Dixon, D. et al (2008) *Half scale tests to examine water uptake by bentonite pellets in a block-pellet backfill system.* 1st ed. [pdf] Stockholm. SKB report: R-08-132 Available at: http://www.skb.se/publikation/1882680/R-08-132.pdf [Accessed 30 Sep 2012]

Eriksson, R., and Schatz, T. (2015) *Rheological properties of clay material at the solid/ solution interface formed under quasi-free swelling conditions.* Applied clay science 108 (May 2015) pp 12-18

Evans, J. and Ryan, C. (2005) *Time-Dependent Strength Behavior of Soil-Bentonite Slurry Wall Backfill.* In: GeoFrontiers 2005. Austin, Texas: American Society of Civil Engineers. pp 1-9. Available at: http://ascelibrary.org/doi/abs/10.1061/40789%28168%2945 [Accessed 3 Jun 2015]

Garcia-Garcia, S. (2010) *Generation, stability and migration of montmorillonite colloids in aqueous systems.* Doctoral Thesis. KTH Royal Institute of Technology , Stockholm.

Hanshaw, B., B. (1964) Cation exchange constants for clay from electrochemical measurements. In: National conference on cxlays and minerals. Atlanta pp 397-421

Holmboe, M. (2011) *The Bentonite Barrier: Microstructural properties and the influence of γ-radiation.* Doctoral Thesis. KTH Royal Institute of Technology, Stockholm

Ichikawa, Y., Kawamura, K., Fujii, N., & Kitayamac, K. (2004) *Microstructure and micro/macro-diffusion behaviour of tritium in bentonite.* Applied Clay Science 26 (2004) pp 75– 90

Jansson, M. (2009) *Bentonite erosion, Laboratory Studies .* 1st ed. [pdf] Stockholm. SKB report:. TR-09-33 Available at http://www.skb.se/publikation/1968609/TR-09-33.pdf [Accessed 17 Apr 2015]

Johnson, A., I. (1963) *Filter-pack and well-screen design.* Denver, Colorado. United States department of the interior geological survey. Available at: http://pubs.usgs.gov/of/1963/0060/report.pdf [Accessed 29 Nov 2015]

Juvankoski, M. (2010) *Description for basic design for buffer.* 1st ed. [pdf] Eurajoki. Posiva report 2009-131. Available at: http://www.posiva.fi/files/1277/WR_2009-131_rev2.web.pdf [Accessed 2 Nov 2014]

Juvankoski, M., Ikonen, K., & Jalonen, T. (2012) *Buffer production line 2012: Design, production and initial state of the buffer.* 1st ed. [pdf] Eurajoki. Posiva report 2012-17. Available at: http://www.posiva.fi/files/3071/POSIVA_2012-17.pdf [Accessed 1 May 2013]

Juvankoski, M. & Marcos, N. (2010) *Design basis for buffer components*. 1st ed. [pdf] Eurajoki POSIVA work report 2009-132, Available at <http://www.posiva.fi/files/1312/WR_2009-132.web.pdf> [Accessed 5 Jun 2013]

Karnland, O. (2010) *Chemical and mineralogical characterisation of the bentonite buffer for the acceptance control procedure in a KBS-3 repository.* 1st ed. [pdf] Stockholm. SKB Report TR-10-60. Available at <http://www.skb.com/publication/2137257/> [Accessed 9 Aug 2013]

Karnland, O. et al (2011) *Long term test of buffer material at the Aspo HRL, LOT project.* 1st ed. [pdf] Stockholm. SKB report TR-09-31 Available at: http://www.iaea.org/inis/collection/NCLCollectionStore/_Public/40/109/40109509.pdf [Accessed 1 Sep 2014]

Karnland, O. et al (2011) *Selectivity coefficient for Ca/Na ion exchange in highly compacted bentonite.* Physics and chemistry of the earth. 36(17-18) pp 1554–1558

Keller, W., D. (1964). *Processes of origin and alteration of clay minerals.* In soil clay mineralogy. Univ. North Carolina press.

Keto, P. et al (2009) *Assessment of Backfill Design for a KBS-3V Repository*. 1st ed. [pdf] Stockholm. SKB report R-09-52 Available at: http://www.iaea.org/inis/collection/NCLCollectionStore/_Public/41/033/41033792.pdf [Accessed 10 Mar2012]

Kiviranta, L. & Kumpulainen, S. (2011) *Quality control and characterisation of bentonite materials. .* 1st ed. [pdf] Eurajoki. POSIVA report 2011-84, Available at: http://www.iaea.org/inis/collection/NCLCollectionStore/_Public/43/108/43108887.pdf [Accessed 10 Sep 2012]

Kyrylyuk, A., V. & Philipse, A., P. (2011) *Effect of particle shape on the random packing density of amorphous solids.* Physica Status Solidi. 208(10) pp 2299-2302

Limieux, J-M., & Sudicky, E.A. (2011) *Glaciations and groundwater flow systems.* In: Encyclopaedia of snow, ice and glaciers. Springer publishing pp372-376. Avaialable at: http://link.springer.com/referenceworkentry/10.1007%2F978-90-481-2642-2_654 [Accessed 14 Nov 2013]

Matsumoto, K., & Fujita, T. (2011). *Extrusion and Erosion of Bentonite Buffer.* 1st ed. [pdf] Ibaraki. Japan Atomic Energy Agency Report number: 2011-14. Available at: https://inis.iaea.org/search/search.aspx?orig_q=RN:43061089 [Accessed 13 Jul 2012]

Meunier, A. (2005) *Clays.* Springer-Verlag Berlin and Heidelberg pp

Missana, T. et al (2003) *Generation and stability of bentonite colloids at the bentonite/granite interface of a deep geological radioactive waste repository*. Journal of Contaminant Hydrology . 61 (2003) pp 17– 31.

Missana, T. et al (2011) *Analysis of colloids erosion from the bentonite barrier of a high level radioactive waste repository and implications in safety assessment.* Physics and Chemistry of the Earth. 36 (17–18) pp 1607-1615

Michell, J.K. & Soga, K. (2005) *Fundamentals of soil behaviour.* Third edition. New Jersey. John Wiley and Sons.

Mort, P (2015) *Characterizing flowability of granular materials by onset of jamming in orifice flows.* Papers in Physics, Vol 7 (070004 - 2015)

Moreno, L., Neretnieks, I., & Liu, L. (2010) Modelling of erosion of bentonite gel by gel/sol flow. 1st ed. [pdf] Stockholm. SKB report: TR-10-64 Available at: http://www.iaea.org/inis/collection/NCLCollectionStore/_Public/42/008/42008360.pdf [Accessed 12/4/13]

Murray, H. H. (2007) *Applied clay mineralogy.* Amsterdam. Elsevier science

Nagra (2012) *Mont Terri Underground Rock Laboratory, .* 1st ed. [pdf] Meiringen Nagra. Available at <http://www.eurosafe-forum.org/files/sem4_1.pdf> [Accessed 12/3/13]

Natural Analogue Working Group (NAWG) (2012). Web page. Available at: http://www.natural-analogues.com/ [Accessed 1/12/12]

Neretnieks, I., Moreno, L., & Liu, L. (2009) *Mechanisms and models of bentonite erosion .* 1st ed. [pdf] Stockholm. SKB report: TR-09-35 Available at: http://www.iaea.org/inis/collection/NCLCollectionStore/_Public/41/043/41043239.pdf [Accessed 12/7/2012]

Nuclear Energy Agency – Radioactive Waste Management Committee (2012) *The post closure radiological safety case for a spent fuel repository in Sweden. An International peer*

review of the SKB license application of March 2011. Available at:
http://www.stralsakerhetsmyndigheten.se/Global/Slutf%C3%B6rvar/NEA/SSM%202010-4132-95%20Final%20Report_NEA_RWM_PEER_2012_2.pdf%20564893_1_1.pdf [Accessed 1/2/2013]

Olsson, S. & Karnland, O. (2009) *Characterisation of bentonites from Kutch, India and Milos, Greece – some candidate tunnel backfill materials* SKB report: TR-09-53. 1st ed. [pdf] Stockholm. Available at:
https://www.iaea.org/inis/collection/NCLCollectionStore/_Public/41/038/41038317.pdf [Accessed 7/4/2010]

Park, Y. (2003) *Investigation of the Ability of Filters to Stop Erosion through Cracks in Dams*. Doctoral Thesis. Virginia Tech, Virginia.

Pedersen, K. (2000) *Microbial processes in radioactive waste disposal* . 1st ed. [pdf] Stockholm. SKB report: TR-00-04. Available online at <
https://www.researchgate.net/profile/Karsten_Pedersen4/publication/264450697_Microbial_processes_in_radioactive_waste_disposal/links/53dfb7250cf27a7b8306a646.pdf>
[Accessed 2/11/2013]

Perdrial, J. N., Warr, L. N., Perdrial, N., Lett, M.C., & Elsass, F. (2009) *Interaction between smectite and bacteria: Implications for bentonite as backfill material in the disposal of nuclear wast.* Chemical Geology 264 (2009) pp 281–294

Prikryl, R. & Weishauptova, Z. (2010) *Hierarchical porosity of bentonite-based buffer and its modification due to increased temperature and hydration.* Applied clay science. 47 (2010) pp 163-170.

Pusch, R. (2008) *Geological storage of radioactive waste.* Berlin: Springer.

Reid, C., Lunn, R., El Mountassir, G. & Tarantino, A. (2015) *A mechanism for bentonite buffer erosion in a fracture with a naturally varying aperture.* Mineralogical magazine,79 (6) pp 1485-1494

Richards, T. & Neretnieks, I. (2010) *Filtering of clay colloids in bentonite detritus material.* Chem. Eng. Technology, 33(8), pp 1303–1310

Riikonen, E. (2009) *Flow-Through and Wetting Tests of Pre-Compacted Backfill Blocks in a Quarter-Scale Test Tunnel.* 1st ed. [pdf] Eurajoki. Posiva report 2008-89, Available at:
http://www.posiva.fi/files/1304/WR_2008-89.web.pdf [Accessed 12/12/12]

Robinson, P. & Bath, A. (2011) *Workshop on copper corrosion and buffer erosion.* 1st ed. [pdf] Stockholm. SSM report 2011-08. Available at:
http://www.iaea.org/inis/collection/NCLCollectionStore/_Public/42/040/42040099.pdf [Accessed 17/4/2012]

Sanden, T. & Borgesson, L. (2010) *Early effects of water inflow into a deposition hole. Laboratory test results* 1st ed. [pdf] Stockholm. SKB report: R-10-70. Available at:

http://www.iaea.org/inis/collection/NCLCollectionStore/_Public/43/035/43035578.pdf [Accessed 1/8/2011]

Schatz, T., and Kanerva, N. (2012) *Formation of accessory mineral bed layers during erosion of bentonite buffer material*. Poster Presentation. Clays in natural and engineered barriers for radioactive waste confinement conference. 5th International meeting. Montpellier, France.

Schatz, T., Kanerva, N., Martikainen, J., Sane, P., Olin, M., Seppälä, A. & Koskinen, K. (2013) *Buffer Erosion in Dilute Groundwater.* 1st ed. [pdf] Eurajoki. Posiva report 2012-44 Available at:
http://www.posiva.fi/en/databank/posiva_reports/buffer_erosion_in_dilute_groundwater.1871.xhtml?xm_freetext=schatz&xm_col_type=4&cd_order=col_report_number&cd_offset=0#.VeXHGn3Rb6g [Accessed 12/1/14]

Scottish Government (2011) *Scotland's Higher Activity Radioactive Waste Policy* 2011. 1st ed. [pdf] Edinburgh. The Scottish Governement. Available at <http://www.scotland.gov.uk/Resource/Doc/338695/0111419.pdf> [Accessed 30/9/2012]

Serco (2012) *Treatment of colloids in post-closure safety assessment.* 1st ed. [pdf] Didcot. Report for NDA RWMD

Shelobolina, E. S., Pickering, S. M., Lovley, D. R., (2005) *Fe-cycle bacteria from industrial clays mined in Georgia, USA*. Clays and Clay Minerals, 53 (6), pp 580-586

Sherard, J., L. Dunnigan, L., P. and Talbot, J. R. (1984) *Filters for silts and clays.* Journal of the ASCE, 110 (No. GT6) pp 684-700.

SKB (2011) *Long-term safety for the final repository for spent nuclear fuel at Forsmark Volume I*. 1st ed. [pdf] Stockholm. SKB Report TR-11-01. Available at http://www.iaea.org/inis/collection/NCLCollectionStore/_Public/43/003/43003620.pdf [Accessed 13/7/13]

SKB (2011) *Long-term safety for the final repository for spent nuclear fuel at Forsmark Volume II*. 1st ed. [pdf] Stockholm. SKB Report TR-11-01. Available at https://www.stralsakerhetsmyndigheten.se/Global/Slutf%C3%B6rvar/KTL/KTL%203/01_vol 2.pdf [Accessed 13/7/13]

SKB (2015) *The authorities review – The government decides.* Web page. Available at: http://www.skb.com/future-projects/the-spent-fuel-repository/the-review-process/ [Accessed 13/1/2016]

Sparks, D. (1995) *Environemental soil chemistry.* San Diego. Academic Press Inc.

Suarez, N., R. (2012) *Micromechanical Aspects of Aging in Granular Soils.* Doctoral Thesis. Virginia Tech, Virginia

Tang, j. (2012) *Flow and jamming of granular material in a two-dimensional hopper*. Doctoral Thesis. Duke University

Tournassat et al (2011) *Influence of montmorillonite tactoid size on Na-Ca cation exchange reactions.* Journal of colloid and interface science. 364 (2011) pp 443-454

USDofA (1994) *Gradation design of sand and gravel filters.* Part 633 – National Engineering Handbook. 1st ed. [pdf] Washington. Available at http://directives.sc.egov.usda.gov/OpenNonWebContent.aspx?content=18397.wba [Accessed 13/7/15]

USDoE (2013) *Strategy for the management and disposal of used nuclear fuel and high-level radioactive waste.* 1st ed. [pdf] Washington. Available at <http://energy.gov/sites/prod/files/Strategy%20for%20the%20Management%20and%20Disposal%20of%20Used%20Nuclear%20Fuel%20and%20High%20Level%20Radioactive%20Waste.pdf> [Accessed 13/7/14]

USGS (2001) *A Laboratory Manual for X-Ray Powder Diffraction – Smectite group.* U. S. Geological Survey. 1st ed. [pdf] Washington. Open-File Report 01-041. Available online at < http://pubs.usgs.gov/of/2001/of01-041/htmldocs/clays/smc.htm> [Accessed 13/8/15]

Vaniman, D., T. and Bish D. L. (1993). *The importance of zeolites in the potential high-level radioactive waste repository at Yucca Mountain, Nevada.* In: Zeolite '93 conference. Los Alamos Available online at http://pbadupws.nrc.gov/docs/ML0037/ML003749365.pdf [Accessed 13/7/14]

Van Olphen, H. (1966) *An Introduction to Clay Colloid Chemistry.* New York. Interscience Publishers.

Vaughan, P., R. & Bridle, R., C. (2004). *An update to perfect filters.* Long-term benefits and performance of dams. In: Long term benefits and performance and performance of dams. Thomas Telford, London, 2004. Available at: http://www.icevirtuallibrary.com/doi/abs/10.1680/lbapod.32682.0043 [Accessed 13/9/12]

Velde, B., & Meunier, A. (2008) *The origin of clay minerals in soils and weathered rocks.* Heidelberg. Springer- Verlag.

Vilks, P. & Miller, N.H. (2010) *Laboratory bentonite erosion experiments in a synthetic and a natural fracture.* 1st ed. [pdf] Toronto. Atomic energy of Canada limited. NWMO technical report: TR-2010-16 Available at <http://www.nwmo.ca/publications?media_file_id=1734> [Accessed 13/9/14]

Weaver, C.E. & Pollard, Lin.D. (1973) *Developments in Sedimentology 15 - The Chemistry of Clay Minerals.* Amsterdam. Elsevier Scientific Publishing.

Welch, G. and Neville, R. (2012) *Should Cumbria take part in the search for a geological disposal facility site.* Ipsos MORI survey. Available online at https://www.ipsos-mori.com/Assets/Docs/Polls/Cumbria%20Managing%20Radioactive%20Waste%20Presentation%20220512.pdf [Accessed 13/9/14]

West Cumbria: MRWS (2012) *The Final Report Of The West Cumbria Managing Radioactive Waste Safely Partnership.* 1st ed. [pdf] Cumbria. doc no. 285 Available at

<http://www.westcumbriamrws.org.uk/documents/306-The_Partnership%27s_Final_Report_August_2012.pdf> [Accessed 13/10/13]

Wilson, J. et al (2011) *Bentonite – A review of key properties, processes and issues for consideration in the UK context.* 1st ed. [pdf] Harwell. NDA document number QRS-1378ZG-1.1. Available at www.nda.gov.uk/documents/biblio/upload/Bentonite-A-Review-of-key-properties-processes-and-issues-for-consideration-in-the-UK-context.pdf [Accessed 17/2/13] [Accessed 1/2/13]

Yariv, S. & Cross, H. (1979) *Geochemistry of Colloid Systems for Earth Scientists*. Berlin. Springer- Verlag.

Yu, J. (2007) *Synthesis of Zeolites.* Chapter 3 in Introduction to Zeolite science and practice – 3rd revised edition. Amsterdam. Elsevier.

Zaoui, A. & Sekkal, W. (2014) *Can clays ensure nuclear waste repositories?* Nature, Scientific Reports 5, Article number: 8815 (2015). Available at http://www.nature.com/articles/srep08815?WT.ec_id=SREP-704-20150310 [Accessed 3/10/15]

Table of Figures

Table of Tables

Appendices

Appendix 1 – CD rom

Video of experiment 1 extrusion / erosion process

Video of experiment 2 extrusion / erosion process

Video of experiment 3 extrusion / erosion process

Video of experiment 4 extrusion / erosion process

Video of experiment 5 extrusion process

Video of breaches in accessory mineral ring triggering erosive periods.

Appendix 2 – Data from cross-laboratory BELBaR benchmark erosion experiments undertaken.

Appendices

BELBaR, bentonite buffer erosion benchmark experiments.

As part of the EC project, Bentonite Erosion**:** effects on the Long term performance of the engineered Barrier and Radionuclide Transport (BELBaR**),** a series of cross-laboratory benchmark artificial fracture tests have been undertaken with a view to predictively modelling the results. The tests were conducted by three laboratories:

a) CIEMAT in Spain (Alonso and Missana)

b) B+Tech in Finland (Schatz)

c) Strathclyde University (this work)

The detailed protocol for the series of experiments is included at the end of this appendix. The same experimental premise as examined in this thesis, of a flow through cell housing a compacted bentonite sample intersected by a fracture at its mid-point was used. Each of the three groups however used custom apparatus of different dimensions and different sample dimensions were also used.

The parameters which were kept constant throughout each experiment were:

- Nanocor PGN montmorillonite was used compacted at a dry density of 1400 kg/m^3.

- Fracture aperture was set at 100 µm.

- De-aired, 1mM NaCl solution was used as a groundwater simulant.

The experiments were undertaken for a period of 60 days in total split into three phases:

1. Phase 1 corresponded to a 30 day stagnant period of no flow.

2. Phase 2 corresponded to a 14 day period of flow at 10^{-6}m/s. (10^{-5}m/s was used at Strathclyde because this corresponded to the minimum flow rate which could be achieved with the peristaltic pump)

3. Phase 3 corresponded to a 14 day period of flow at 10^{-4}m/s.

Data acquisition during the course of the experiments and post test included:

- Radial extrusion distance.

- Effluent solids content.

- Post test: eluted mass, penetrated mass, mass remaining in sample compartment.

- Swelling pressure of the sample was also monitored at Strathclyde.

Radial extrusion

Snapshots from the same stage in each phase of the experiment across the three different groups are shown in Figure 1. It is apparent from Figure 1 that the extrusion behaviour of the material in each phase of the test over the three groups was very similar. Phase 1, shown in Figure 1ai, bi and ci, corresponded to the stagnant phase and was characterised by uniform radial extrusion in the fracture. During phase 2, the period of reduced flow, shown in Figure 1aii, bii and cii, the outer rim of the extruded material began to break down. In the final phase of flow at a higher velocity, shown in Figure 1aiii, biii and ciii, the extruded material begins to breaks down further towards the central compartment and a tail of eroded material is deposited downstream of the sample.
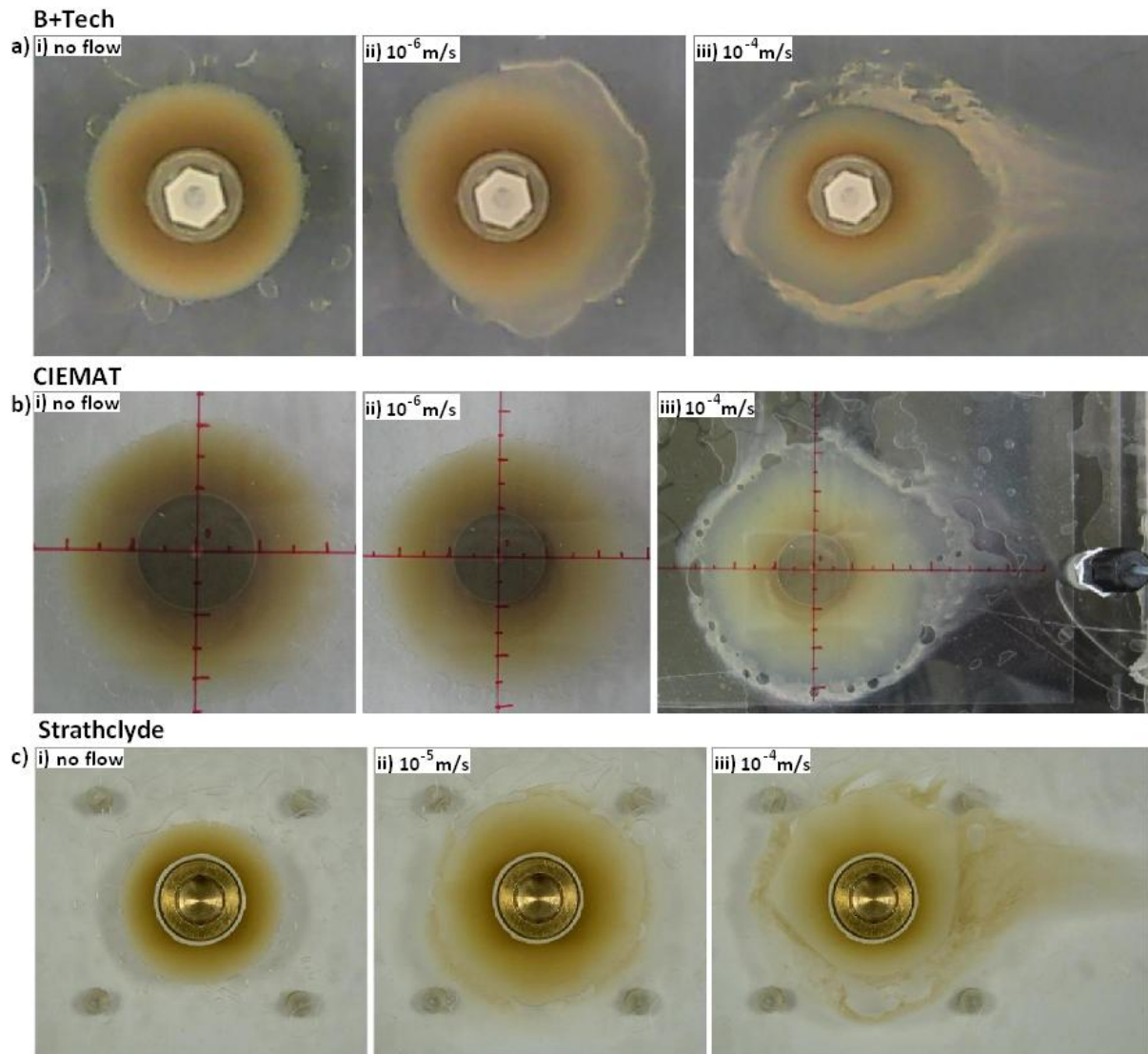
Figure 1: Radial extrusion distance at the same time point in each stage of experiment. a) B+Tech b) CIEMAT c) Strathclyde

Data regarding the radial extrusion distance of the samples over each of the three phases throughout the tests is shown in Figure 2. It is evident from Figure 2 that over phases two and three of the experiment, each of the three groups achieved a relatively consistent set of results in terms of the quantitative extrusion distance of the sample. Over the course of phase 1, it is apparent from figure 2, that the sample appeared to extrude to a lesser extent in to the fracture during phase one in the test undertaken at Strathclyde relative to the tests performed by B+Tech and CIEMAT.
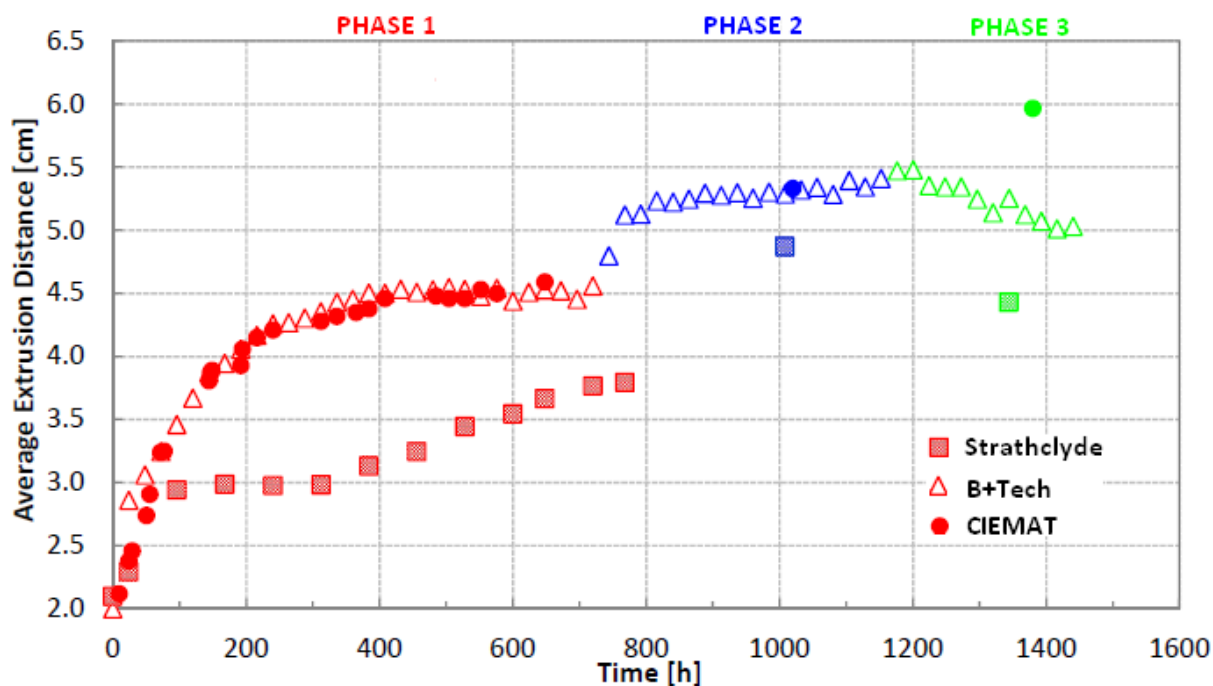
Figure 2: Radial extrusion distance against time for the sample across each phase of the experiment.

This was to the result of air bubble formation around the sample during the stagnant phase, which limited access of the sample to water around its circumference, thus reducing its ability to swell into the fracture.

Swelling pressure

This is demonstrated by the swelling pressure data for the sample from the test undertaken at Strathclyde, shown in Figure 3. It is apparent from Figure 3, that the period in which limited extrusion occurs (from 100 to 300 hours in Figure 2), also shows a decrease in swelling pressure (from 5 to 13 days in Figure 3). Indicating that the sample had have limited access to water because of the presence of air bubbles around its circumference. When the air bubbles were removed from around the sample (by tilting the fracture to displace them) the sample began to absorb water again, the swelling pressure began to rise and the sample continued to extrude in to the fracture (from 300 hours in in Figure 2 and day 13 in Figure 3).
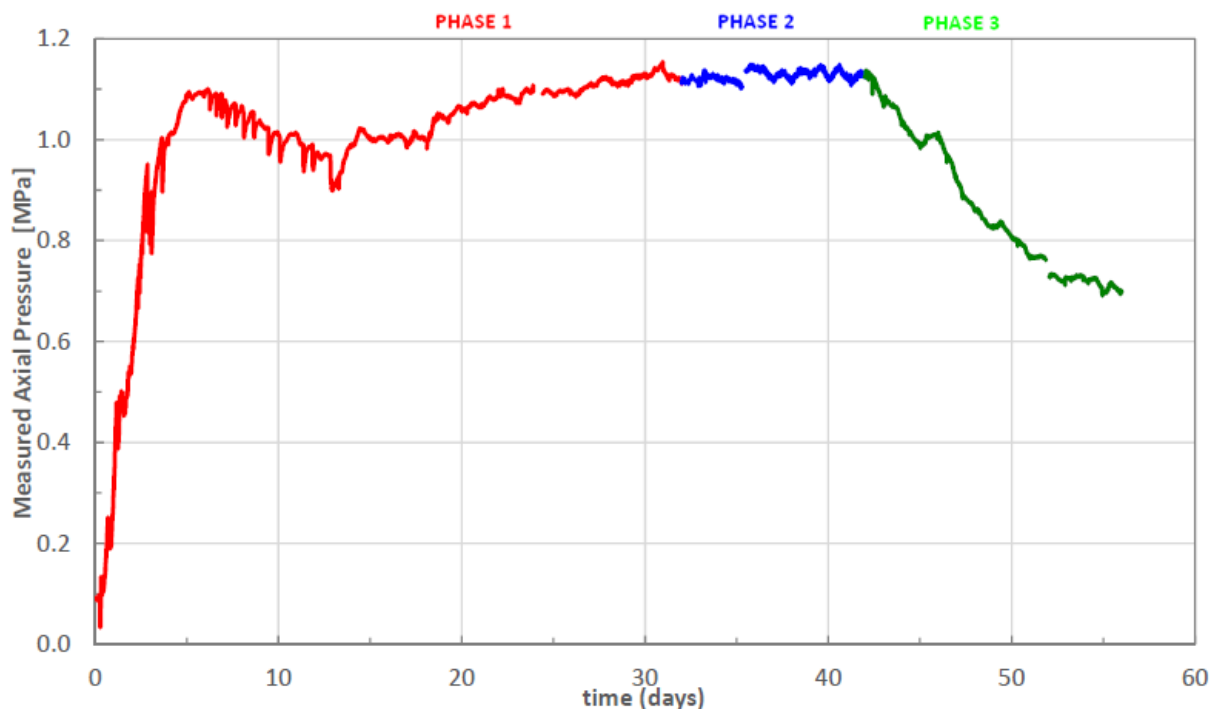
Figure 3: Swelling pressure against time over three phases of BELBaR benchmark test.

Mass loss

Despite these apparent discrepancies in the swelling behaviour between the samples, and despite each of the groups commencing with different dimensions of sample (emplaced mass). The respective extruded mass, upon termination of the tests, appeared to be relatively similar between each of the three groups as shown in Table 1, which shows the mass loss and post-test data for each of the experiments. The mass remaining in the compartment on completion of the test also appeared to be comparable between each of the groups, ranging from 75% at Strathclyde to 88% at CIEMAT of the initial mass emplaced in the cell.

Total mass loss from the system (eluted mass in Table 1) was consistent between the tests undertaken at B+Tech and Strathclyde, which were within 1% of each other. The total eluted mass from the test undertaken at CIEMAT however was approximately 80% less than that the tests from B+Tech and Strathclyde.

The eroded mass data row from Table 1, given as [emplaced mass − (remaining mass + extruded mass)] is an order of magnitude less for the test undertaken at CIEMAT than the tests undertaken at B+Tech and Strathclyde.

BELBaR	CIEMAT	B+Tech	Strathclyde
Emplaced mass (g)	3.8554	7.7023	4.3000
Extruded mass (g)	0.3640	0.3090	0.3137
Remaining mass (g)	3.4040	6.4977	3.2479
Eroded mass (g)	0.0874 (2.3%)	0.8956 (11.6%)	0.7384 (17.2%)
Eluted mass (g)	0.1180	0.5622	0.5576

Table 1: Mass loss data from each of the BELBaR bench mark tests

Conducting an overall mass balance for each of the systems:

Emplaced mass = Extruded mass + Remaining mass + Eluted mass

CIEMAT: Emplaced = 3.8554 g

　　　　Extruded mass + Remaining mass + Eluted mass = 3.882 g

　　　　Difference = + 0.0266 g (+ 1% more mass than emplaced)

B+Tech: Emplaced = 7.7023 g

　　　　Extruded mass + Remaining mass + Eluted mass = 7.3689 g

　　　　Difference = - 0.3334 g (- 4% less mass than emplaced)

Strathclyde: Emplaced = 4.3000 g

　　　　Extruded mass + Remaining mass + Eluted mass = 4.1192 g

　　　　Difference = - 0.1808 g (- 4% less mass than emplaced)

BELBaR: Artificial Fracture Benchmark Tests Protocol

Tim Schatz

B+Tech Oy

tim.schatz@btech.fi

August 2014

Introduction

This document provides an overview of the artificial fracture benchmark tests which are to be carried out and predictively modeled within the BELBaR Project. The benchmark tests will be carried out and the results disseminated under work package 2; predictive modeling will be performed under work package 5.

Method

Artificial fracture benchmark tests will be conducted using the custom-designed, small-scale, flow-through artificial fracture currently operated by the BELBaR partners normally performing such experiments in work package 2. Although the test cells vary in design from one laboratory to another, all will feature the same fracture aperture, the same initial dry density of (the same) compacted sample material and the same solution composition for the purposes of benchmark testing.

Test Parameters

Fracture Aperture: 0.1 mm

Fracture Plane Size: This parameter will vary according to the design of the various test cells but is not expected to influence test results.

Compacted Sample Size: This parameter will vary according to the design of the various test cells; anticipated dimensions are as follows

          1. height = 10 mm, diameter = 35 mm

          2. height = 20 mm, diameter = 20 mm

          3. height = 50 mm, diameter = 50 mm

Sample Material: sodium montmorillonite (PGN, Nanocor Inc.)

Sample Dry Density: 1400 kg/m^3

Due to concerns over whether a sample at this density will generate sufficient swelling pressure to deform, e.g., bulge the test apparatus, resulting in a nonuniform aperture distribution, it is proposed that each participant monitor, if possible, any vertical displacement of the fracture planes over the course of the tests.

Solution: deaired, 1 mM NaCl in deionized water

Flow Rate: no flow, stagnant conditions for 30 days followed by flow conditions for 30 days – two separate flow velocities will be examined, 14 days at 10^{-6} m/s followed by 10^{-4} m/s

Test Protocol

Sample Presaturation: samples will be presaturated with test solution prior to test

Test Duration: 60 days

Measured Data

penetration distance of solid phase interface into fracture as a function of time

effluent solids concentration during active flow periods as a function of time

possibly, post-test analysis of penetrated mass, mass remaining in emplacement volume and dispersed mass

any additional measurement data (e.g., $\rho(r)$, P_{sample}) is welcome for collection

In an effort to crosscheck the results as much as possible, identical methods should be used to produce measurement data. This concern presumably applies mainly to determination of effluent solids concentration. Additionally it should be ensured that sampling periods overlap as well; maximum 24 hour sampling periods are proposed, i.e., penetration distance and effluent solids concentration (when applicable) should be measured at least every 24 hours from the start of the test.

Dissemination

benchmark test results will be communicated and discussed and compared to predictive modeling efforts in a BELBaR meeting upon completion (by November 2014)